

**Development of in-vitro  $\mu$ -channel devices  
for continuous long-term monitoring of  
neuron circuit development: Device  
fabrication, biophysics of signal generation  
and large scale data analysis and  
visualization.**



UNIVERSITAT POLITÈCNICA  
DE CATALUNYA  
BARCELONATECH



Departament  
d'Enginyeria  
Electrònica



ibec Institut de bioenginyeria  
de Catalunya

**Michael Riss**

Departament d'Enginyeria de Sistemes,  
Automàtica i Informàtica Industrial (ESAI)  
Universitat Politècnica de Catalunya

Supervised by Dr. Enric Claverol Tinturé

Biomedical Engineering PhD Program  
Departament d'Enginyeria Electrònica  
Escuela Técnica Superior de Ingeniería Industrial de Barcelona (ETSEIB)

May 2013

Thesis presented to obtain the qualification Doctor of Philosophy from the  
Universitat Politècnica de Catalunya.



---

## Abstract

In this thesis various methods are presented towards long-term electrophysiological monitoring of in-vitro neuron cultures in  $\mu$ -channel devices.

A new  $\mu$ -channel device has been developed. The StarPoM device offers multiple culture chambers connected with  $\mu$ -channels allowing to study communication between neuron populations. For its fabrication an advanced multi-level SU-8 soft-lithography master was developed that can mold  $\mu$ -channels and culture wells simultaneously. The problem of aligning features across a thick SU-8 layer has been solved by integrating a chrome mask into the substrate and then using back-side exposure through the chrome mask.

A long-term monitoring of neuron electrophysiological activity has been conducted continuously during 14 days in the StarPoM device. For the analysis of the recorded dataset a new software tool-chain has been created with the goal of high processing performance. The two most advanced components - `OlPlot` and `ISI viewer` - offer high performance visualization of time series data with event or interval annotation and visualization of inter-spike interval histograms for fast discovery of correlations between spike units on a device. The analysis of the 14 day recording revealed that signals can be recorded from day 4/5 onwards. While maximum spike amplitudes kept rising during the 14 days and reached up to 3.16 mV, the average spike amplitudes reached their maximum of 0.1-0.3 mV within 6 to 8 days and then kept the amplitudes stable.

To better understand the biophysics of signal generation in  $\mu$ -channels, the influence of  $\mu$ -channel length on signal amplitude was studied. A model based on the passive cable theory was developed showing that spike amplitude rises with channel length for  $\mu$ -channels  $< 250 \mu\text{m}$ . In longer  $\mu$ -channels, further growth of spike amplitude is inhibited by cancellation of positive and negative spike phase. Also, clogging of the  $\mu$ -channel entrances by cells and debris helps to enhance signal amplification.

---

## **Preface**

### ***Introduction***

This work was conducted in the context of basic research on  $\mu$ -channel technology and on long-term neuron monitoring. Specifically the subjects of signal generation within a  $\mu$ -channel, the application of  $\mu$ -channel devices for in-vitro neuron circuit research and engineering and the development of algorithms for long-term electrophysiology data display have been investigated.

### ***Acknowledgments***

I want to thank my supervisor Dr. Enric Claverol-Tinturé who gave me the opportunity to enter the field of Neuroengineering, Ling Wang and Ricardo Morales Carbajal for their collaboration in projects and publications, Dr. Dobryna Zavidia for support and advice, Jennifer Olmos Buitrago, Miriam Funes Luque, Berta Novella for dissections and help with cell culture. Outside of our group I want to thank Prof. Ramón Alcubilla for the opportunity to use the clean room of the electronic engineering department (EEL-UPC) and the clean room crew for their support: Miguel Garcia Molina, Xavier Fermín Quesada, Gema López Rodríguez and also Dr. Trifon Trifonov for additional advice. At IBEC I thank Dr. Isabel Oliveira and Laura Gómez Rubio for running the lab and thanks go also to Raúl Pérez Rodríguez for helping me in the PCB clean room.

I'm grateful towards AGAUR/Generalitat de Catalunya for granting my scholarship, towards el ministerio de ciencia e innovación and the European Union for funding our research.

On the private side thanks go to my family and friends that supported me in these rather difficult years.

And of course this all wouldn't have been possible without all the giants on which shoulders we stand (Alt, Jeunesse, Buitrago-Téllez, Wächter, Boës, and Pichler, 1997; Y. S. Erdal and Ö. D. Erdal, 2011).

# Contents

<b>1</b>	<b>Introduction</b>	<b>13</b>
1.1	State of the art . . . . .	15
1.1.1	In-vitro neuron recording methods . . . . .	15
1.1.2	Microfabrication/Lithography . . . . .	18
1.1.3	Simulation . . . . .	19
1.1.4	Data Processing . . . . .	20
1.2	Outline of the thesis . . . . .	21
<b>2</b>	<b>Spike sorting of <math>\mu</math>-channel signals</b>	<b>23</b>
2.1	Abstract . . . . .	23
2.2	Introduction . . . . .	24
2.2.1	Rationale of the device . . . . .	24
2.3	Materials and Methods . . . . .	25
2.3.1	Microfabrication (Fig. 2.2) . . . . .	25
2.3.2	Cell culture . . . . .	25
2.3.3	Cell imaging . . . . .	27
2.3.4	Recording . . . . .	29
2.3.5	Spike sorting . . . . .	29
2.4	Results . . . . .	29
2.5	Conclusion . . . . .	30
<b>3</b>	<b>O1Plot data viewer</b>	<b>35</b>
3.1	Abstract . . . . .	35
3.2	Introduction . . . . .	36
3.3	Materials and methods . . . . .	38
3.3.1	Overview . . . . .	38

---

3.3.2	Time series data . . . . .	38
3.3.3	Event data . . . . .	42
3.3.4	Interval data . . . . .	46
3.3.5	Performance tuning parameters . . . . .	47
3.3.6	Hiding the hard disk latency by double buffering . . . . .	48
3.3.7	Implementation . . . . .	48
3.3.8	Benchmarks . . . . .	49
3.4	Results . . . . .	52
3.4.1	Benchmark results . . . . .	55
3.4.2	Storage overhead . . . . .	59
3.4.3	Optimal tuning parameters . . . . .	60
3.5	Discussion . . . . .	60
<b>4</b>	<b>The StarPoM device</b>	<b>63</b>
4.1	Abstract . . . . .	63
4.2	Introduction . . . . .	63
4.2.1	Methods that were developed in this project . . . . .	64
4.3	Materials and methods . . . . .	65
4.3.1	MEA fabrication . . . . .	66
4.3.2	SU-8 soft-lithography master fabrication . . . . .	67
4.3.3	PDMS film fabrication . . . . .	70
4.3.4	The aligner . . . . .	70
4.3.5	Device assembly . . . . .	71
4.3.6	Cell Culture . . . . .	73
4.3.7	Recording Setup . . . . .	75
4.3.8	Recording . . . . .	75
4.3.9	Phase Contrast Images . . . . .	76
4.3.10	Data Analysis . . . . .	76
4.3.11	De-Interleaving and concatenation . . . . .	78
4.3.12	Visual Inspection with O1Plot . . . . .	78
4.3.13	Common Signal Elimination . . . . .	78
4.3.14	Channel 6 Artifact Elimination . . . . .	78
4.3.15	Base line drift Elimination (Wavelet Filter) . . . . .	82
4.3.16	Spike Detection . . . . .	82
4.3.17	Elimination of Overlapping Spikes . . . . .	84
4.3.18	Fine-tuning Spike Position . . . . .	84
4.3.19	Sweep Cutting . . . . .	84
4.3.20	K-Means Spike Sorting . . . . .	84
4.3.21	ISI Analysis . . . . .	86
4.4	Results . . . . .	88
4.4.1	Fabrication results . . . . .	88
4.4.2	Phase contrast image of the device with cells . . . . .	88
4.4.3	Osmolarity measurements results . . . . .	88

---

4.4.4	Data analysis results . . . . .	88
4.5	Discussion and conclusion . . . . .	109
4.5.1	Notes on the methods . . . . .	112
4.5.2	Caveats . . . . .	113
4.5.3	Findings . . . . .	114
4.5.4	Unexpected observations . . . . .	116
4.5.5	Contribution to the field . . . . .	117
4.5.6	Outlook . . . . .	117
<b>5</b>	<b>Biophysics of the <math>\mu</math>-channel</b>	<b>119</b>
5.1	Abstract . . . . .	119
5.2	Introduction . . . . .	120
5.3	Materials and Methods . . . . .	120
5.3.1	Device Fabrication . . . . .	120
5.3.2	Neuron Culture . . . . .	122
5.3.3	SEM Imaging . . . . .	122
5.3.4	Recording and Data Analysis . . . . .	122
5.3.5	Theoretical models . . . . .	123
5.4	Results . . . . .	125
5.5	Discussion and Conclusion . . . . .	126
<b>6</b>	<b>Conclusions</b>	<b>133</b>
6.1	Summary of results . . . . .	133
6.2	Outlook . . . . .	135
6.3	Publications and Presentations . . . . .	137
<b>7</b>	<b>Bibliography</b>	<b>143</b>
<b>A</b>	<b>Cluster Spike Amplitudes</b>	<b>163</b>

## List of Figures

2.1	PDMS-on-Polystyrene Biophysics . . . . .	24
2.2	PDMS-on-Polystyrene Fabrication . . . . .	26
2.3	Phase contrast images of neuron culture . . . . .	28
2.4	Fluorescent images of the neuron culture . . . . .	28
2.5	Spike Sorting - 2 clusters . . . . .	31
2.6	Spike Sorting - 9 clusters . . . . .	32
2.7	Cluster shape matrix . . . . .	33
3.1	O1Plot overview . . . . .	39
3.2	Time series data reduction . . . . .	40
3.3	Time series data reduction pyramid . . . . .	42
3.4	Event and interval data storage structure . . . . .	43
3.5	Bit tricks for event and interval data handling . . . . .	44
3.6	Event data reduction example . . . . .	45
3.7	O1Plot UI screenshots . . . . .	53
3.8	O1Plot screenshots . . . . .	54
3.9	O1Plot performance comparison . . . . .	56
3.10	O1Plot display list generation benchmark results . . . . .	57
4.1	StarPoM design . . . . .	65
4.2	StarPoM composition . . . . .	65
4.3	StarPoM Electrode Mask . . . . .	66
4.4	SU-8 StarPoM soft-lithography master fabrication . . . . .	67
4.5	Masks used for the SU-8 soft lithography master . . . . .	68
4.6	Aligner setup . . . . .	71
4.7	PDMS attachment . . . . .	72



4.8	Extending PDMS . . . . .	72
4.9	PDMS fence and lid dimensions . . . . .	73
4.10	CO <sub>2</sub> cavity fill method . . . . .	74
4.11	Co-culture areas . . . . .	74
4.12	Final StarPoM device . . . . .	75
4.13	StarPoM amplifier setup . . . . .	76
4.14	Common Artifact Elimination . . . . .	80
4.15	Exponential Artifact Elimination . . . . .	81
4.16	Wavelet Filter Example . . . . .	82
4.17	Spike detection heuristics . . . . .	83
4.18	Sweep Viewer Screenshot . . . . .	85
4.19	ISI Viewer . . . . .	86
4.20	ISI Viewer Conditions . . . . .	87
4.21	StarPoM SU-8 master SEM . . . . .	89
4.22	StarPoM PDMS film SEM . . . . .	90
4.23	StarPoM phase contrast high contrast . . . . .	91
4.24	StarPoM Center Section . . . . .	92
4.25	StarPoM PDMS Surface . . . . .	93
4.26	StarPoM Bubble Section . . . . .	94
4.27	14 Day Time Series Plot . . . . .	97
4.28	Sweep Plots . . . . .	100
4.29	Channel 0 Sweeps . . . . .	101
4.30	Channel Spike Amplitude . . . . .	102
4.31	Channel Spike Frequency . . . . .	103
4.32	Cluster Spike Frequency . . . . .	104
4.33	Day 12 Incident . . . . .	105
4.34	Raster Plot Examples . . . . .	107
4.35	ISI Example Spike Area . . . . .	108
4.36	ISI Example 1 sec width . . . . .	108
4.37	ISI Example 10 sec width . . . . .	109
4.38	ISI Asymmetric Hat . . . . .	110
4.39	Sub-noise ISI values . . . . .	111
4.40	ISI Histogram . . . . .	112
5.1	Biophysics Experiment Setup . . . . .	121
5.2	Channel clog model . . . . .	123
5.3	Compartment model . . . . .	125
5.4	Resistance vs $\mu$ -channel length . . . . .	127
5.5	Spike amplitude vs $\mu$ -channel length . . . . .	128
5.6	1st device SEM image . . . . .	129
5.7	2nd device SEM image . . . . .	130
5.8	ElectrodeStreet MEA . . . . .	131
6.1	MNE 2006 Poster . . . . .	138

*LIST OF FIGURES*

---

6.2	IBEC Symposium 2007 Poster . . . . .	139
6.3	IBEC Symposium 2009 Poster . . . . .	140
6.4	IBEC Symposium 2010 Poster . . . . .	141
6.5	Neural Interfaces 2010 Poster . . . . .	142
A.1	Channel 0 Cluster Spike Amplitudes . . . . .	164
A.2	Channel 1 Cluster Spike Amplitudes . . . . .	165
A.3	Channel 2 Cluster Spike Amplitudes . . . . .	166
A.4	Channel 3 Cluster Spike Amplitudes . . . . .	167
A.5	Channel 4 Cluster Spike Amplitudes . . . . .	168
A.6	Channel 5 Cluster Spike Amplitudes . . . . .	169
A.7	Channel 6 Cluster Spike Amplitudes . . . . .	170
A.8	Channel 7 Cluster Spike Amplitudes . . . . .	171

## List of Tables

2.1	Maximum amplitude of the averaged spike shapes for each cluster and the corresponding signal to noise ratio. . . . .	30
3.1	Time series data overhead . . . . .	59
3.2	Event and Interval data overhead . . . . .	59
4.1	Spike Detection Thresholds . . . . .	84
4.2	Noise Values . . . . .	96
4.3	Spike and Cluster numbers . . . . .	99
4.4	Day 12 time course . . . . .	106
5.1	Parameters used by the clogged channel model . . . . .	123
5.2	Parameters used by the compartment model . . . . .	124

## Nomenclature

PoM	Polymer-on-MEA
PoP	Polymer-on-Polystyrene
KiB	Kibibyte, corresponds to $2^{10}$ bytes (IEC, 2000)
MiB	Mebibyte, corresponds to $2^{20}$ bytes (IEC, 2000)
GiB	Gibibyte, corresponds to $2^{40}$ bytes (IEC, 2000)
TiB	Tebibyte, corresponds to $2^{30}$ bytes (IEC, 2000)
CT	Computer tomography
MRI	Magnetic resonance imaging
PDMS	Polydimethylsiloxane
AP	Action potential
PB	Phosphate buffer
SEM	Scanning Electron Microscope
PCA	Principal component analysis
RMS	Root mean square

## Chapter 1

### Introduction

Amongst the scientific challenges that humanity is facing today, understanding how the brain works is probably one of the greatest. The brain plays a central role in our lives. We perceive the world with it, we reason and feel with it and we coordinate our actions with it. Many even consider the brain to be the "actual self" of a human being. Yet, we don't know how the brain works.

Apart from the pure academic interest to know how our cognition works, better knowledge about the functioning of the brain will very likely have far-reaching practical effects on our lives. These could range from health care (treatment of neuro degenerative diseases, spinal cord and brain traumata) over applications such as optimized learning through improved didactics and maybe even the use of pharmaceuticals (Agay, Yechiam, Carmel, and Levkovitz, 2010; Lynch, Palmer, and Gall, 2011), to changes of our ideas about humanism and social contracts such as e.g. the concept of free will and legal culpability (Burns and Bechara, 2007). Some even speculate about modifications of the human brain to improve cognition (Decker and Fleischer, 2008; Saniotis and Henneberg, 2011).

One of the main difficulties of researching the brain is its complexity. A human adult brain has about  $10^{11}$  neurons (Lent, Azevedo, Andrade-Moraes, and Pinto, 2012) which are connected by an enormous amount of synapses (the amount of synapses in the neocortex alone is already estimated with  $10^{14}$  synapses - Pakkenberg, Pelvig, Marnier, Bundgaard, H. J. G. Gundersen, Jens R Nyengaard, and Regeur 2003; Y. Tang, J R Nyengaard, De Groot, and H. J. Gundersen 2001). Additionally neurons emit and react to neuro transmitters (chemical substances such as adrenaline or dopamine) that are transmitted through the interstitial fluid.

That makes the brain a highly interconnected system where - without better knowing the functioning the brain - the activity of any neuron could influence the activity of any other neuron.

Currently, research follows two main approaches to tackle this complexity. One approach works top-down, starting with the top level organization of the brain - categorizing different brain regions and assigning functionality to them - and then advancing into the details of mid and low level brain organization. This research is traditionally conducted by medical scientists as brain trauma patients and observations during brain surgery yielded the first useful results (C. G. Gross, 1999; Alt, Jeunesse, Buitrago-Télliez, Wächter, Boës, and Pichler, 1997; Y. S. Erdal and Ö. D. Erdal, 2011). Nowadays, also imaging methods such as computer tomography (CT) and magnetic resonance imaging (MRI) (Benveniste and Blackband, 2006; Bridge and Clare, 2006) are in use to noninvasively obtain information about e.g. brain activity during certain states and tasks (Phan, Wager, S. F. Taylor, and Liberzon, 2002; Calhoun and Pearlson, 2012) and to learn how brain regions are interconnected (Le Bihan, Mangin, Poupon, Clark, Pappata, Molko, and Chabriat, 2001; Hagmann, Kurant, Gigandet, P. Thiran, Wedeen, Meuli, and J.-P. Thiran, 2007; Gong, Y. He, Concha, Lebel, D. W. Gross, Evans, and Beaulieu, 2009; Sporns, 2011; Lichtman, Livet, and Sanes, 2008).

The other approach works bottom-up, starting with one neuron or with a small group of neurons, studying the behavior of these basic elements and then advancing to higher organization levels. While experiments on single neurons can be done in-vivo (Brecht, Fee, Garaschuk, Helmchen, Margrie, Svoboda, and Osten, 2004), these experiments face the aforementioned problem that neurons in a living organism underlie complex interaction with other neurons, wake/sleep cycle, hormones, etc.

Such interfering influences can be avoided when conducting experiments in-vitro. Neurons are extracted from the brain either as brain slice or as dissociated cells to study them within an artificial life support system (Triaud, Clenet, Cariou, Le Neel, Morin, and Truchaud, 2003). The life support system allows to control environmental parameters such as temperature, medium composition (pH, osmolarity, drug compounds, neuro transmitters, gas concentration), electrical/chemical stimulation, so that they can be adapted according to the requirements of the specific experiment. The improved control also allows to automate experiments, enabling high-throughput experimentation as it is proposed for e.g. drug screening (Steller, Kreir, and Salzer, 2012; Dittrich and Manz, 2006).

By neglecting the complexity of the real organism, the results gained during such an experiment may not directly be transferred back to the in-vivo context; further in-vivo experiments are needed to confirm the results in-vivo. However, the staged approach - first conducting experiments in-vitro and then confirming interesting findings in-vivo - promises to accelerate the knowledge discovery while lowering the costs (both monetary and of animal lives).

This thesis focuses on engineering aspects of in-vitro neuron culture devices that utilize  $\mu$ -channels both to confine/pattern the growth of the neuron culture and also to amplify the extra-cellular neuron signals. The covered aspects include microfabrication, biophysics of the signal generation in the  $\mu$ -channel, long-term monitoring of neuron electrophysiological activity and large scale time-series signal processing and visualization.

In the following a short overview of some common methods for in-vitro experiments on neurons will be given.

## 1.1 State of the art

### 1.1.1 In-vitro neuron recording methods

The signal transmission between neurons happens mainly via action potentials (AP) (Bean, 2007; Bezanilla, 2006) and synaptic transmissions. Electrophysiology measures the electrical component of action potentials and is the most common method for recording neuron activity.

#### *Patch-Clamp Method*

A versatile instrument for recording neuron activity is the patch-clamp method (Neher, 1992). An electrode gets isolated with a glass pipette which has a small opening ( $\sim 1 - 20\mu m$ ) that acts as the recording site. There are various ways to use the pipette electrode.

In the loose patch configuration the pipette opening is placed onto the cell membrane so that with (gentle) pressure the distance between the rim of the opening and the membrane can be reduced to  $\sim 200nm$  (Stühmer and Almers, 1982). This effectively isolates the ion solution inside the pipette from the extra-cellular medium outside, the electrical resistance (seal resistance) rises up to  $10^8\Omega$ . The setup can be used to record extra-cellular potentials or - with a certain noise component - even record ion channel activity of the small membrane patch under the pipette opening (Strickholm, 1961; Forti, Bossi, Bergamaschi, A. Villa, and Malgaroli, 1997; Perkins, 2006).

In the cell-attached configuration additional weak negative pressure is applied inside the glass pipette so that the cell membrane gets sucked firmly to the pipette orifice. This further increases the seal resistance, so that it rises up to  $10^9\Omega$ , into the  $G\Omega$  range (Gigaseal). The increased seal resistance allows the recording of single ion channel activity with improved signal to noise ratio. (Hamill, Marty, Neher, B Sakmann, and Sigworth, 1981; Perkins, 2006).

For the whole-cell recording configuration a tight seal configuration is created similar to the cell-attached method, but then the membrane is ruptured by applying a short, strong negative pressure pulse inside the pipette. Intracellular fluid and the saline solution in the pipette get connected and the electrode inside the pipette

is now recording the intra-cellular potential (Margrie, Brecht, and Bert Sakmann, 2002; Sah, Hestrin, and Nicoll, 1990).

The patch-clamp method allows a very detailed investigation of single cell/single ion channel activity. However, approaching the pipette tip to the cells and to make contact is a cumbersome process and does not allow high throughput experimentation.

*Patch-Clamp on a Chip* Therefore, an evolution of the patch-clamp method tries to automate the positioning process of the cells in front of the pipette opening. A common approach is to move a cell in suspension in front of a fixed micro-hole in the device which can be either on the bottom of the device (Fertig, Blick, and Behrends, 2002) or in the side walls (Seo, Ionescu-Zanetti, Diamond, Lal, and L. P Lee, 2004; Lau, Hung, A. R. Wu, and Luke P Lee, 2006; Ong, K.-C. Tang, Agarwal, Nagarajan, Luo, and Yobas, 2007). Once a good seal is obtained cell-attached patch and whole cell recording are possible. A limitation of this approach is that neurons in suspension cannot have neurite outgrowths connecting them to other cells. That means that with these devices measurements on neuron networks are not possible.

The versatility and signal quality made the patch-clamp method the "gold-standard" of electrophysiology. New methods are often compared to the patch-clamp method for comparison. In the context of this thesis, the  $\mu$ -channel devices we used could best be compared to a loose patch configuration on the axon with a low seal resistance so that extra-cellular signal can still be recorded but no single ion channel activity.

### ***Multi Electrode Arrays (MEA)***

Multi Electrode Arrays (MEA) consist of a culture chamber (similar to a petri dish) that has several planar recording/stimulation electrodes embedded in the bottom surface. Originally developed for recording from heart cells (Thomas, Springer, Loeb, Berwald-Netter, and Okun, 1972) they are also used to monitor neuron activity (Shtark, Ratushnyak, Voskresenskaya, and Olenov, 1974; G.W. Gross, Rieske, Kreutzberg, and Meyer, 1977). Dissociated neurons can be cultured on top of the electrodes and survive for months (Steve M. Potter and DeMarse, 2001). The extra-cellular potentials generated by the neurons are recorded by the electrodes; stimulation is also possible (Wagenaar, Jerome Pine, and Steve M Potter, 2004). Using glass slides as bottom substrates and transparent conductors such as thin ITO leads for the connection to the electrodes, allows optical inspection of the neurons parallel to electrical recording (G W Gross, Wen, and J. W. Lin, 1985). Due to these properties MEAs are suitable for long-term studies of neuron network development. However, as neurons migrate during network growth, assigning individual neuron units to specific electrodes is difficult. In comparison



to patch-clamp-recorded intra-cellular potentials that are in the range of mV the extra-cellular potentials recorded by MEAs are in the range of  $\mu\text{V}$ .

*Multi Transistor Array* MEAs have typically around 60 electrodes. Going to a higher number of electrodes is difficult because of the connection routing on and off the device. Therefore efforts have been made to further increase the number of electrodes by using a silicon chip as substrate that integrates the first amplification stage and multiplexers so that the high number of electrodes map to a manageable amount of connections off the chip (Eversmann, Jenkner, Hofmann, Paulus, Brederlow, Holzapfl, Fromherz, Merz, Brenner, Schreiter, et al., 2003; Berdondini, Imfeld, Maccione, Tedesco, Neukom, Koudelka-Hep, and Martinoia, 2009).

### ***Patterning***

When growing a neuron culture on a flat substrate, a uniform cell layer with apparently random neuron connections develops. Axons and dendrites exert tensile stress on the somas leading to unpredictable neuron migration relative to MEA electrodes. The movement leads to changes of the recorded waveforms and a reliable assignment of recorded spikes to specific neurons becomes difficult. Therefore, to achieve a stable neuron-electrode interface, an improved control over neuron growth is desirable. This furthermore benefits neuron circuit analysis where control over network topology is advantageous.

Different solutions have been developed for patterning neurons:

*Chemical Patterning* Neurons need to attach to a surface for proper growth. Therefore culture chambers are coated with a protein layer that enables neurons to attach and to grow. Patterning this layer and complementing it with coatings that are known to repel neurons, allows to force the neuron growth into a desired pattern (James, Spence, Dowell-Mesfin, Hussain, Smith, Craighead, Isaacson, Shain, and Turner, 2004; Nam, Chang, Bruce C Wheeler, and Brewer, 2004).

*Physical Confinement* A more direct approach to influence the neuron growth is to force the neurons into the desired shape by physical confinement (Suzuki, Sugio, Jimbo, and Yasuda, 2005; Erickson, Tooker, Y.-C. Tai, and Jerome Pine, 2008; Merz and Fromherz, 2005; Mahoney, R. R. Chen, Tan, and Saltzman, 2005).

*$\mu$ -channel Devices* This device class not only uses physical confinement for guiding neuron growth but also uses the signal augmenting properties of narrow channels ( $\mu$ -channels) to improve the recording of extra-cellular potentials (A. M. Taylor, Blurton-Jones, Rhee, Cribbs, Cotman, and Jeon, 2005).

A further application is the compartmental application of drugs. Neurons are

cultured in several chambers that are only connected by  $\mu$ -channels. As the  $\mu$ -channels leave only few space around the neurites the flow of extracellular medium through the channel is very limited. Together with a slight pressure difference between the chambers a “liquid barrier” can be created. Drugs that are applied to the low pressure chamber cannot diffuse “upstream” to the other (high pressure) chamber. Depending on the geometry drug application can be restricted either to the somas and initial neurites or to the far axons and dendrites (Campenot, 1977; Shi, Nedelec, Wichterle, and Kam, 2010; Berdichevsky, Staley, and Yarmush, 2010).

In-vivo equivalents to  $\mu$ -channel devices are cuff electrodes and neurotropic electrodes. Cuff electrodes are placed around peripheral nerve bundles and can be used for recording nerve signals or for functional electrical stimulation (FES). (Fitzgerald, Lacour, McMahon, and Fawcett, 2008; Sujith, 2008; Stieglitz, 2010). Neurotropic electrodes need to be protruded by sprouting neurites before their signals can be picked up by the integrated electrodes (P. R. Kennedy, 1989; Bartels, Andreasen, Ehirim, Mao, Seibert, E. J. Wright, and P. Kennedy, 2008). These electrodes provide both longevity and long-term neuron-electrode stability.

In our group two technologies for  $\mu$ -channel devices have been developed. The Polymer-on-MEA (PoM) device consists of a custom fabricated ITO-on-glass-MEA which is combined with a polymeric film or block which defines the geometry of the device. The advantage of this design is that the electrodes can be placed inside the channels and enable the monitoring of neuron signals in high spacial resolution. This design is also in use in other groups (Dworak and Bruce C. Wheeler, 2008).

Another variant is the Polymer-on-Plastic (PoP) device. It’s a simplified design where the MEA is replaced by a standard petri dish. It features a polymeric block for confining the neuron growth. Recording is done by lowering Ag/AgCl electrodes into the culture chambers from the top. These electrodes pick up potential differences across the  $\mu$ -channels (Morales, Riss, Wang, Gavin, Rio, Alcubilla, and Enric Claverol-Tinture, 2008).

### 1.1.2 Microfabrication/Lithography

To fabricate the micro-structured devices for the use with neurons, methods are necessary that can produce features in the  $\mu\text{m}$  range. Common fabrication methods are based on lithography/soft-lithography (Acikgoz, Hempenius, Huskens, and Vancso, 2011).

A substrate gets coated with a photo active resist. The resist gets exposed (usually with UV light) through a photomask that contains the desired pattern for the specific device layer. The exposure causes a chemical reaction in the photoresist which either makes the resist soluble in the photoresist developer (positive photoresists) or - in the contrary - changes the exposed resist areas from soluble to

non-soluble (negative photoresists). This process can be repeated several times by successively spinning and exposing multiple layers of photoresist. The height (Z) of the fabricated features depends on the thickness of the photoresist layers (which depends on photoresist type, solvent percentage, spinning speed) and the dimensions in X and Y on the pattern of the photo mask. Care needs to be taken as the exposure of the last layers also exposes all the layers before. In the end the substrate gets submerged into developer solution where the exposed (positive photoresist) or non-exposed (negative photoresist) areas of the photoresist layers are dissolved.

In this thesis lithography/soft-lithography processes based on SU-8 (Campo and Greiner, 2007), PDMS and metal wet etching were used.

### 1.1.3 Simulation

Beside practical experiments theoretical models are necessary to understand the experimental results and to help predict neuron behavior. Numerous neuron models have been developed over the years.

#### *Passive Cable Model*

The passive cable model simulates the propagation of an action potential along an axon or dendrite. The axon is modeled by a chain of resistors for the interior of the axon and a combination of resistance and a capacitance across the membrane (Rall, 2009).

#### *Hodgkin/Huxley Model*

The model of Hodgkin and Huxley (Hodgkin and Huxley, 1952) describes the dynamics of the Na<sup>+</sup> and K<sup>+</sup> ionic currents across the cell membrane. This model has been refined over the years to account for additional ion currents (channels), different temperatures and cells (Gold, Henze, Koch, and Buzsáki, 2006).

#### *Compartment Model*

While it is possible to calculate the passive cable and Hodgkin/Huxley models analytically for very simple geometries this approach reaches its limits with more complex topologies. The compartment model divides the neuron in several connected units/compartments and uses a time-discrete numeric simulation. Typically the soma is modeled as a single compartment, the axon as a chain of compartments and the dendrites as a tree of compartments.

This approach offers the possibility to model some components passively (normally the dendritic tree) and other components with the Hodgkin/Huxley model (the soma and the initial part of the axon) (Enric Claverol-Tinture and Jerome Pine, 2002; Gold, Henze, Koch, and Buzsáki, 2006).

### ***Lattice Model***

The Lattice Model extends the space discrete nature of the compartment model into the extracellular space. The intra- and extracellular volume is fully discretized into a lattice. This allows the simulation of extracellular signal propagation (Stewart, Gowrishankar, and Weaver, 2006).

### ***Finite Element Model***

The Finite Element Model further refines the Lattice Model. Instead of partitioning the space into a regular lattice the space gets partitioned into a grid that is irregular and adapted to the geometry. The irregular adaption provides accurate results while keeping the computational cost down. Care needs to be taken for the modeling of the membrane, as the membrane is too thin for efficient FEM simulation (Moulin, Glière, Barbier, Joucla, Yvert, Mailley, and Guillemaud, 2008).

In general the choice of the model depends on the application. It's necessary to find a trade-off between accuracy of the model and computational effort. Another aspect is the determination of the model parameters such as intra- and extracellular resistivity, membrane capacity and HH-model parameters ( $g_{Na}$ ,  $g_K$ ). Although a lot of work has been done in this area the process of fine-tuning the model parameters to new cell types and conditions of specific experiments is still ongoing. While automatic methods are available (Van Geit, De Schutter, and Achard, 2008) the fine-tuning is often done manually by an expert.

#### **1.1.4 Data Processing**

Processing electrophysiological data includes data format conversion, data compression, digital filtering, visualization, spike detection and spike sorting. Due to the large size of electrophysiological data a very common approach is blockwise data processing. Data is stored in large files on the hard disk. For processing the data is split into blocks that can fit into the physical working memory of the computer. Each block is then separately read, processed and written back to the hard disk. While this approach is necessary on computers with small (32 bit) address space, it can cause additional complexity if the processing of the data blocks is not independent and context information needs to be transferred between the different block processing steps (e.g. history or padding for filter operations). Today's 64 bit operating systems offer memory mapping functionality that allows to map large files continuously into the process address space. This simplifies algorithm design and in many cases also improves performance by performing computation and I/O simultaneously.

In this thesis 64 bit memory mapped data processing was used where applicable.

### *Spike Sorting*

When recording neural activity an electrode often records from more than one neuron, resulting in dataset that is a superposition of the activity of several neurons. Spike sorting tries to reverse this process and to extract the activity of the individual neurons from the superposed recording (Lewicki, 1998; Quiroga, 2007).

Spike sorting algorithms can be classified into offline and online algorithms. Offline algorithms work on complete recordings and can therefore only be used after the experiment has been finished. Online algorithms can be used during the experiments (Franke, Natora, Boucsein, Munk, and Obermayer, 2010). They work based on the recordings of the past, present and probably with a short look-ahead into the future, i.e. the spike sorting trails a few seconds behind the recording. Standard k-means based offline spike sorting was used in thesis chapter 2 and 4.

## **1.2 Outline of the thesis**

This thesis comprises chapters that describe my own core thesis projects (chapters 3 and 4) and chapters documenting my contributions to group projects (chapters 2 and 5).

Chapter 2 covers the spike sorting that I have done in the context of a group project that focused on the development of cost-effective PoP (PDMS-on-Polymer)  $\mu$ -channel devices (Morales, Riss, Wang, Gavin, Rio, Alcubilla, and Enric Claverol-Tinture, 2008). The objective was to evaluate whether standard spike sorting methods can be applied to signals from  $\mu$ -channel devices and how many separable spike units can be identified. The spike sorting used both the traditional approach of sorting PCA-processed spike sweeps but also applied the k-means algorithm directly on the raw spike sweeps. Up to 9 spike clusters were identified, showing that per  $\mu$ -channel and per electrode several units can be distinguished.

Chapter 3 was inspired by the surprising difficulty we encountered during the PoP project in chapter 2 with plotting time series data of 10 minutes or longer. As data display is an essential element of the data analysis process, this problem needed to be solved before moving on to long-term neuron monitoring. Therefore I proposed and conducted a project which applied advanced computer visualization methods such as hierarchical data reduction, LoD (Level of Detail) Visualization and Out-of-Core processing to speed up time series display from an algorithmic complexity of  $\mathcal{O}(n)$  to  $\mathcal{O}(1)$ . This is an important, qualitative improvement as the `OlPlot` software now allows to display datasets of arbitrary size within  $<20\text{ms}$ , enabling smooth, interactive data navigation. The `OlPlot` software component could be used as a standard visualization method for long-term experiments in the future.

My second core project in chapter 4 focused on long-term monitoring of neuron development. Several methods that were developed in the context of this effort are documented. The StarPoM device marked the step from

1D PoM (Polymer-on-MEA) device geometries (E. Claverol-Tinture, Cabestany, and Rosell, 2007) to more complex 2D PoM devices. The necessary alignment accuracy was achieved by integrating both  $\mu$ -channel and culture well features on a multi-level SU-8 soft-lithography master using a substrate-embedded chrome mask and backside exposure.

The StarPoM device was then used to continuously monitor electrophysiological activity of a neuron culture during its first 14 days of development. After the recording, the data was analyzed offline using a newly developed tool-chain, which was performance optimized to cope with the large datasets. While spike sorting turned out to be surprisingly difficult due to lack of spike shape distinguishability (compared to the relative ease of spike sorting in chapter 2) the newly developed `ISI viewer` seems to be a promising tool to quickly discover correlated neuron activity.

In chapter 5 the first iteration of our group effort to understand the biophysics of signal generation in  $\mu$ -channels (Wang, Riss, Buitrago, and Claverol-Tintur , 2012) is documented. It focused on the influence of  $\mu$ -channel length on the measured signal amplitude. Experimental data from 59 devices with varying  $\mu$ -channel lengths has been analyzed. The obtained signal amplitudes were related to the results of a passive cable simulation model with backward euler solver. According to the findings, the signal is predominately generated in the first 250 $\mu$ m of the  $\mu$ -channels, assisted by an agglomeration of cells and cell debris at the  $\mu$ -channel entrances that increases the extra-cellular resistivity and thereby also the signal amplitudes.

## Chapter 2

### Spike sorting of neuron signals in a $\mu$ -channel device

This chapter concentrates on my contribution (spike sorting) to a group project together with Ricardo Morales, Ling Wang, Rosalina Gavín, Jose Antonio Del Río, Ramon Alcubilla and Enric Claverol-Tinturé that also resulted in a publication (Morales, Riss, Wang, Gavin, Rio, Alcubilla, and Enric Claverol-Tinture, 2008). Beside the spike sorting aspect, this chapter will also cover parts of the common project that are necessary to understand the context of the spike sorting. For a more detailed description of the entire group project, please refer to the publication.

#### 2.1 Abstract

In-vitro  $\mu$ -channel devices are a promising approach to study neuron cultures for developmental research and drug screening.  $\mu$ -channel devices confine neuron growth to form several neuron populations connected by neurite bridges through  $\mu$ -channels. Electrophysiological recording takes place in the  $\mu$ -channels ensuring stable electrode-neuron association. In the context of the E2 dish device development - a low-cost  $\mu$ -channel technology - example recordings were taken, analyzed and spike sorting performed. Spike sorting was done with the newSpikeOMatic package using the k-means algorithm on either PCA-processed spike sweeps or directly on the raw sweeps. One recording with comparatively low S/N ratio of 7.7 yielded only 2 clusters based on PCA-processed spike sweep. Another recording with a S/N ratio of up to 34.1 yielded 9 clusters using raw sweeps, demonstrating that  $\mu$ -channel devices can discern several units per electrode.

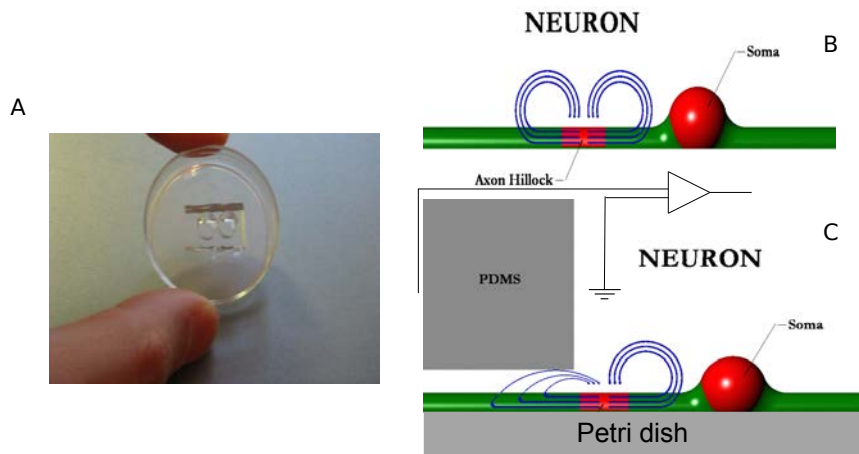


**Figure 2.1:** (A) 35 mm polystyrene dish with overlaid chamber–channel–chamber structure and cartoon sketch of hillock-produced extracellular currents in unconfined (B) and channel-confined neurons (C). - Reproduced and adapted by permission of The Royal Society of Chemistry

## 2.2 Introduction

In (Morales, Riss, Wang, Gavin, Rio, Alcubilla, and Enric Claverol-Tinture, 2008) we introduced a new electrophysiology platform based on recording from  $\mu$ -channels and using a low-cost PDMS-on-polystyrene (PoP) fabrication method. The platform is aimed at basic neuron research, e.g. for drug screening, and is complementing traditional electrophysiology methods such as patch clamp and multi electrode arrays (MEA), see chapter 1.

### 2.2.1 Rationale of the device

A propagating action potential (AP) creates an extra-cellular current in the surrounding medium. When directing the axon growth into a  $\mu$ -channel the current field of an AP propagating along the axon gets confined to the  $\mu$ -channel. Due to the small cross-section the extra-cellular medium inside the  $\mu$ -channel has a relatively high resistance. The extra-cellular current passing through this resistance causes an end-to-end voltage drop along the  $\mu$ -channel. This voltage drop can be recorded with electrodes in the extra-cellular medium on both sides of the  $\mu$ -channel. See also Fig. 2.1.



## 2.3 Materials and Methods

### 2.3.1 Microfabrication (Fig. 2.2)

#### *SU-8 soft-lithography master*

A soft-lithography master was fabricated consisting of a glass substrate and SU-8 stripes on the surface with dimensions:  $3.7 \mu\text{m}$  height  $\times$   $25 \mu\text{m}$  width  $\times$   $10 \text{mm}$  length. The SU-8 stripes were photolithographically patterned and represent the negative form of the  $\mu$ -channels.

#### *PDMS molding*

PDMS was poured 7 mm thick onto the SU-8 soft-lithography master and cured. After peeling off the PDMS slab the shape of the SU-8 stripes remained as  $\mu$ -channel profiles in the bottom surface of the PDMS.

#### *Hole opening*

A tissue puncher with 6 mm diameter was used to punch holes (wells) through the PDMS slab at the ends of the  $\mu$ -channel. Device 1 was fabricated with a  $\mu$ -channel length of  $60 \mu\text{m}$ , device 2 with a  $\mu$ -channel length of  $1600 \mu\text{m}$ .

#### *Device assembly*

The PDMS slab was then combined with a polystyrene petri dish. The  $\mu$ -channel profiles were oriented towards the polystyrene substrate in order to form the  $\mu$ -channels. A plexiglass frame with two Ag/AgCl electrodes was positioned above the device so that the electrodes enter the wells.

#### *Filling the device*

To fill the device (wells and  $\mu$ -channel) with water, the device was placed in a  $\text{CO}_2$  atmosphere. Once the  $\mu$ -channel was filled with  $\text{CO}_2$ , the wells were filled with water. The  $\text{CO}_2$  in the  $\mu$ -channel dissolved into the water; the missing  $\text{CO}_2$  volume caused a vacuum which pulled the water into the  $\mu$ -channel and completed the flooding of the device.

#### *Surface coating*

To coat the surfaces in the device for cell adhesion, the water was exchanged with 0.01% poly-D-lysine (PDL) solution. The PDL solution was kept in the device overnight before rinsing it.

### 2.3.2 Cell culture

E18 mice embryos were dissected and their hippocampus extracted. The hippocampus tissue blocks were dissociated at  $37^\circ\text{C}$  with papain (13 units/ml) and

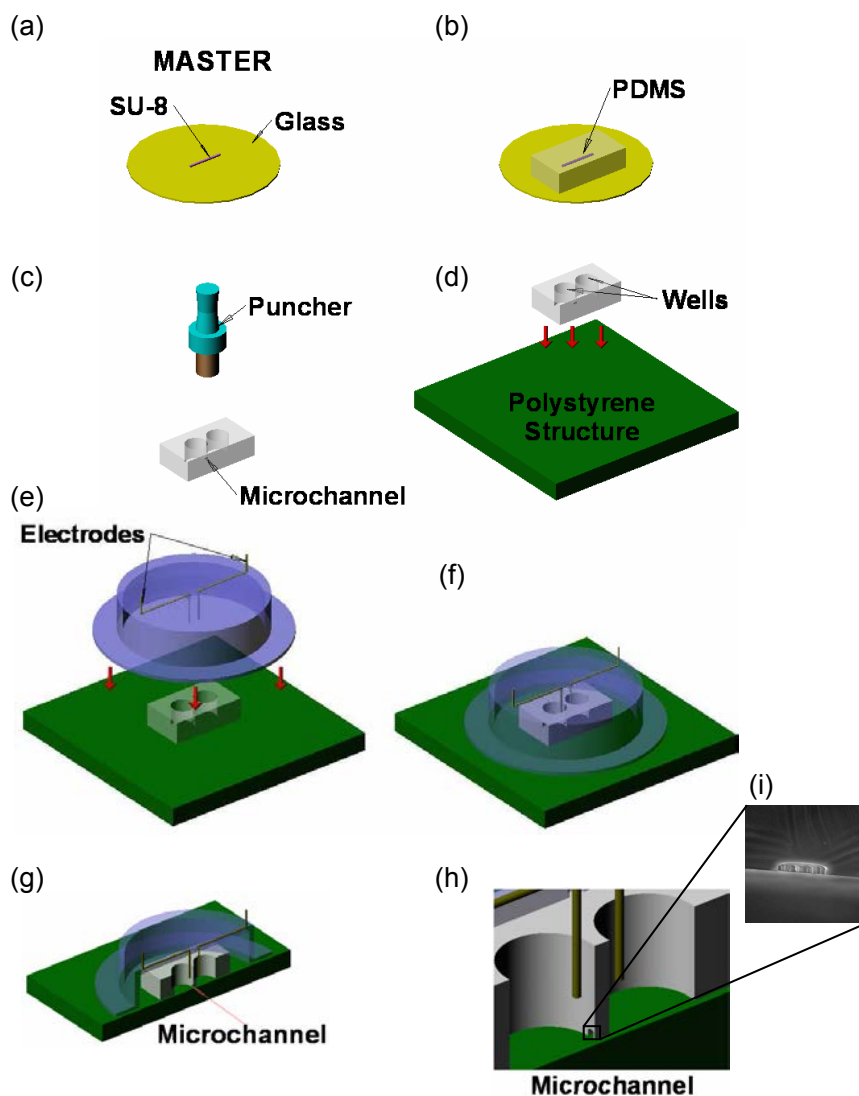


**Figure 2.2:** Fabrication steps. (a) An SU-8 master is produced by photolithographically defining a  $3.7 \mu\text{m} \times 25 \mu\text{m} \times 10 \text{mm}$  strip on a circular Pyrex substrate. PDMS is cast on the master (b) and 6 mm chambers are punched (c). The PDMS piece is overlaid on a polystyrene substrate (d). A plexiglass structure including two Ag/AgCl macroelectrodes is lowered into the chambers (e and f) to support recording and stimulation. (g) and (h) the position of the macroelectrodes inside the chambers with respect to the connecting microchannel. (i) A SEM picture of the microchannel entrance. - Reproduced and adapted by permission of The Royal Society of Chemistry

gentle pipetting. The dissociated cells were plated at  $3 \cdot 10^2$  to  $3.5 \cdot 10^3$  neurons/ $\text{mm}^2$  ( $10^4$  to  $10^5$  cells per well) into Neurobasal culture medium supplemented with 2% B27, 2 mM L-glutamine, 5% horse serum (all from Invitrogen) and 20 mg/ml gentamycin (Sigma). Every week 50% of the medium got exchanged and after the first week glial growth was inhibited by 1 mM Cytosine b-arabino furanoside (Sigma).

### 2.3.3 Cell imaging

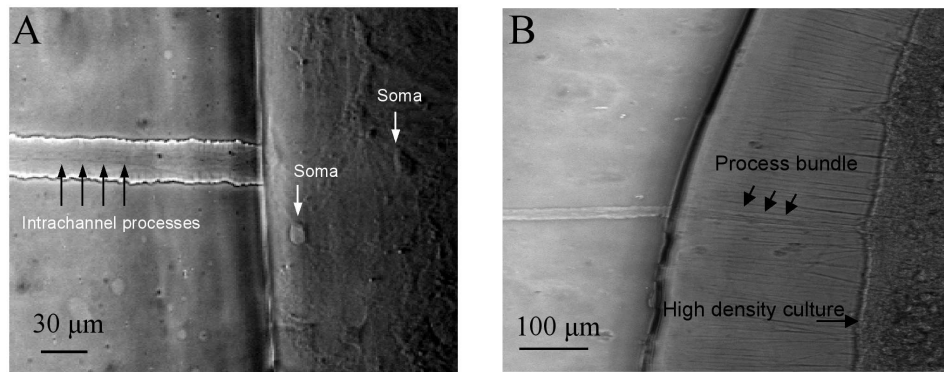
For illustration (not being part of my contribution), images of the grown cell culture are shown in figures 2.3 and 2.4. The description of the neuron preparation and images from the publication (Morales, Riss, Wang, Gavin, Rio, Alcubilla, and Enric Claverol-Tinture, 2008) follows:

To aid in visualizing intra-channel outgrowth, selected cultures were transfected with Green-Fluorescence-Protein (GFP) using the lentivirus vector. Lentiviral particles were produced by transient transfection of 293T cells with FuGENE6 (Roche) by use of the green fluorescent protein (GFP)-expressing vector pWPXL-GFP, the second-generation packaging construct psPAX2, and the envelope plasmid pMD2G. 293T cells were cultured in DMEM, supplemented with 10% fetal calf serum (FCS) and without antibiotics before transfection. The medium was changed and supplemented with antibiotics after 18 h. Vector supernatants, containing viral particles, were harvested approximately 24 and 48 h later and concentrated by ultracentrifugation (2 h, 26000 g at  $4^\circ\text{C}$ ).

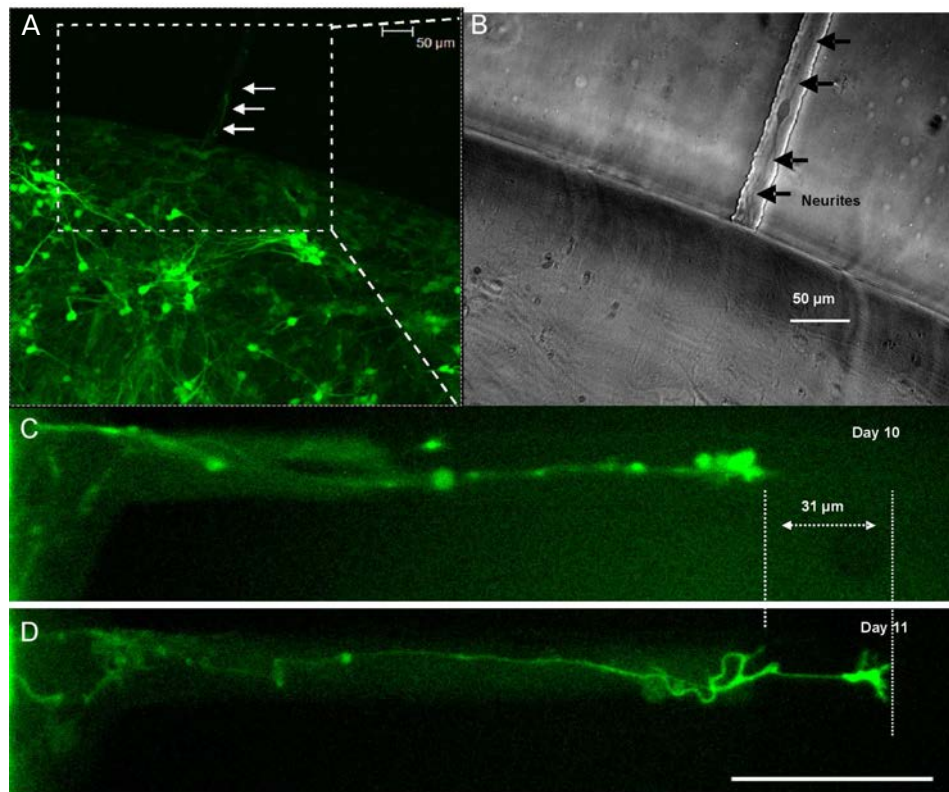
After 4 days *in vitro*, the neuronal cultures were incubated at  $33^\circ\text{C}$  and 5%  $\text{CO}_2$  with the lentivirus for 24 h. The cultures were then rinsed with lentivirus-free medium and further incubated ( $37^\circ\text{C}$ , 5%  $\text{CO}_2$ ) until use. Fluorescence imaging made use of an inverted Nikon Eclipse TE200 microscope.

Fig. 2.4 A and B show fluorescence and phase-contrast images, respectively, of a typical GFP-transfected culture after 7 days *in vitro*. Fig. 2.4 C and D show elongation of processes within a microchannel from a different culture.

Fig. 2.3 compares low *versus* high density cultures. Low density cultures resulted from plating densities of  $10^4$  fresh cells per well or, due to lower viability,  $4 \cdot 10^4$ – $10^5$  cryopreserved cells per well. Low density cultures (Fig. 2.3 A) usually show sparse growth of processes along the microchannels whereas high density populations ( $10^5$  fresh cells  $\text{well}^{-1}$ , Fig. 2.3 B) often form bundles of processes threading the channels.



**Figure 2.3:** Culture of cryopreserved cells plated at  $1.4 \cdot 10^3$  neurons  $\text{mm}^{-2}$  (A) and fresh cells at  $3.5 \cdot 10^3$  neurons  $\text{chamber}^{-1}$  (B) after 2 weeks *in vitro* showing multiple processes growing along the microchannel. - Reproduced by permission of The Royal Society of Chemistry



**Figure 2.4:** (A) Fluorescence and (B) phase contrast images of aGFP-transfected culture after 7 days *in vitro* illustrating sprouting within the microchannel. (C) and (D) show processes elongating in a microchannel from a different dish. - Reproduced by permission of The Royal Society of Chemistry

### 2.3.4 Recording

Recordings were conducted with an extra-cellular amplifier (MCS 1060-Inv-BC) that got manually connected to the electrodes. For device 1 a sampling frequency of 8 kHz and for device 2 a sampling frequency of 10 kHz was used.

### 2.3.5 Spike sorting

The recordings from the two devices were analyzed in the R statistics system with the new SpikeOMatic package (Pouzat, 2012). The used spike sorting protocol slightly differed between the devices: the preprocessing steps were the same, but sweep length and clustering step differed.

*Common preprocessing steps* Extracellular recordings were filtered (bandwidth 10 Hz – 3 kHz) and sections containing large-magnitude bursts, likely resulting from overlapping of field potentials and spikes from multiple cells, were blanked to avoid false spike detections. The data were then further filtered with a 3rd order butterworth zero-phase bandpass filter (60 Hz to 2 kHz). Spike detection with a threshold of  $5.5 \times \text{MAD}$  (median absolute deviation) was performed on the filtered data. The root mean square (RMS) noise level was determined by selecting a spike-free epoch of the recording and calculating the standard deviation (RMS).

*Device 1 - PCA based clustering* Around each spike a sweep with 16 ms length was cut out. Principal component analysis (PCA) was performed on the sweeps for dimensionality reduction, followed by K-means clustering on a 2-dimensional PCA space.

*Device 2 - direct k-means clustering* Sweeps with 20 ms length (200 samples) were cut out for each spike. K-means clustering was performed directly on the 200-dimensional vector space spanned by the sweeps. The results were manually refined either by re-applying the k-means algorithm to clusters that contain apparently different spike shapes or by merging clusters with very similar spike shapes.

## 2.4 Results

The results of the spike sorting are shown in figures 2.5 to 2.7. For the first device two clusters could be determined (Fig. 2.5). In this case the dimension-reduced data representation with the first two principal components was enough for the k-means algorithm to separate the clusters.

For the second device (Fig. 2.6) the first two principal components could not provide enough data to clearly separate the different clusters and therefore the alternative clustering step was chosen. E.g. in the 2-dimensional PCA space (Fig. 2.6b) cluster 9 lies nearly indistinguishable in between cluster 4 and cluster 6, yet in reality it clearly differs due to the second positive phase that is exhibited neither

Cluster	max. Amplitude	S/N ratio
Device 1		
1	131 $\mu$ V	7.7
2	101 $\mu$ V	5.9
Device 2		
1	461 $\mu$ V	17.1
2	499 $\mu$ V	18.5
3	179 $\mu$ V	6.6
4	313 $\mu$ V	11.6
5	175 $\mu$ V	6.5
6	183 $\mu$ V	6.8
7	354 $\mu$ V	13.1
8	921 $\mu$ V	34.1
9	279 $\mu$ V	10.3

**Table 2.1:** Maximum amplitude of the averaged spike shapes for each cluster and the corresponding signal to noise ratio.

by cluster 4 nor 6 (Fig. 2.6a).

Fig. 2.7 is a visualization of the 9 clusters in comparison to allow a manual judgment of uniqueness. E.g. cluster 3 and 6 could probably be joined whereas clusters 5 and 9 are clearly distinct.

RMS noise level was 17  $\mu$ V for the first device and 27  $\mu$ V for the second device. The maximum amplitudes for the averaged spike shape of each cluster are listed in table 2.1 together with the resulting signal to noise ratios.

## 2.5 Conclusion

Spike sorting was applied to recordings from  $\mu$ -channels. For the first device 2 different spike shapes were identified for the second device 9.

The different number of identified spike shapes can probably be attributed to different signal to noise ratios (Martinez, Pedreira, Ison, and Quian Quiroga, 2009). The recording that resulted in 9 spike shapes had relatively strong signals (S/N ratio from 6.5 to 34.1) the recording with only 2 spike shapes had weaker signals (S/N ratio from 5.9 to 7.7).

The basic spike shapes of the second dataset with 9 clusters were often quite similar (positive first phase and negative second phase); the spike shapes only differed by seemingly "piggy-packed" smaller positive or negative phases. E.g. the spike shape of cluster 9 looks similar to the spike shape of cluster 4 but has an additional smaller positive phase (Fig. 2.6a). The cause for this phenomenon is not known yet.

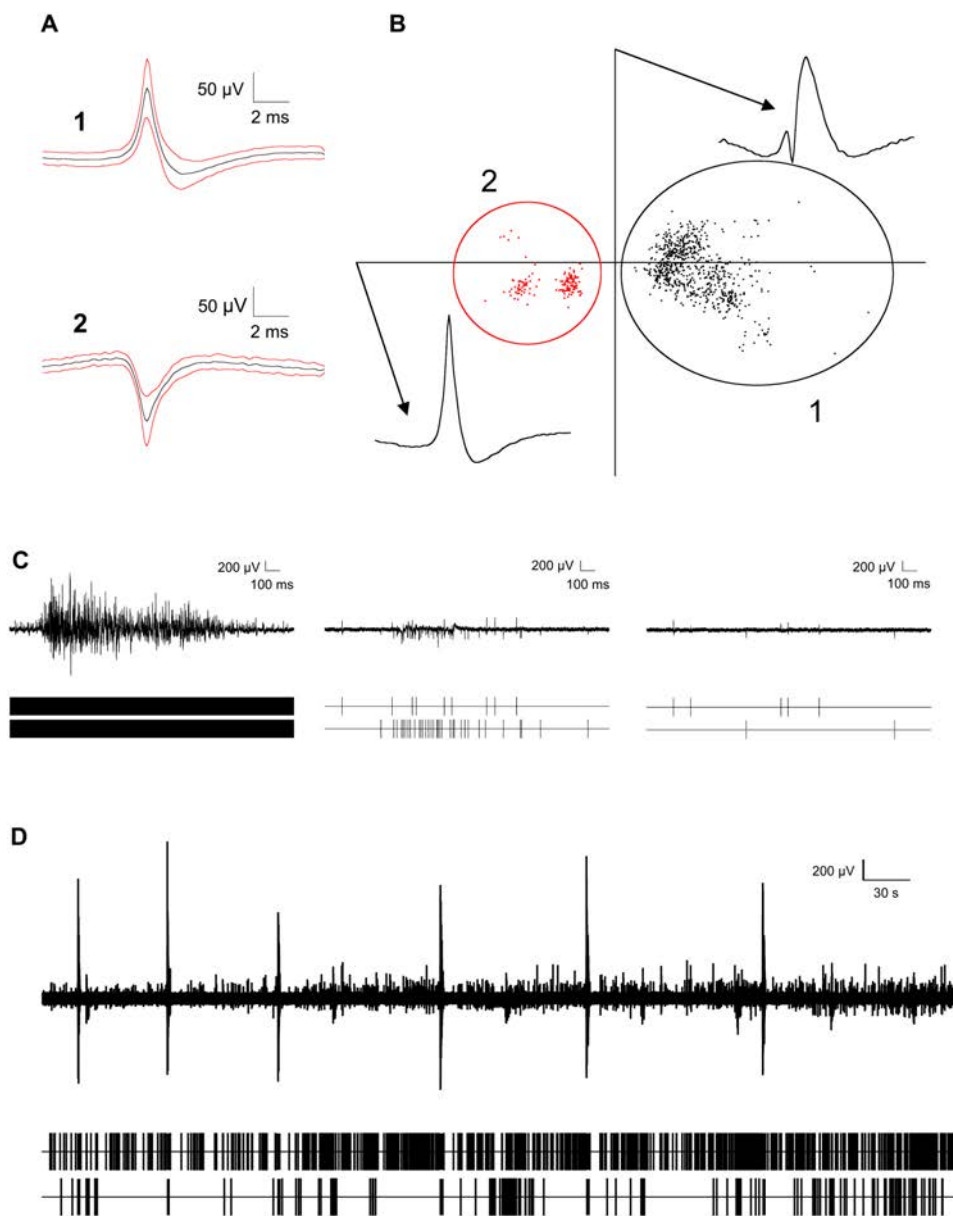


**Figure 2.5:** Spike sorting for the first device: (A) Two spike profiles recorded at a single  $\mu$ -channel and ascribed to different clusters by the spike sorting algorithm (middle and outer traces showing mean and mean-absolute-deviation respectively).  $n = 732$  and  $n = 147$  spikes were averaged to obtain traces 1 and 2, respectively. (B) Two-dimensional scatter plot in PCA space showing k-means clusters. (C) Short epochs of raw data and raster plots with various activity patterns. (D) Long epoch of raw data and raster plot including hippocampal bursting activity. - Reproduced by permission of The Royal Society of Chemistry

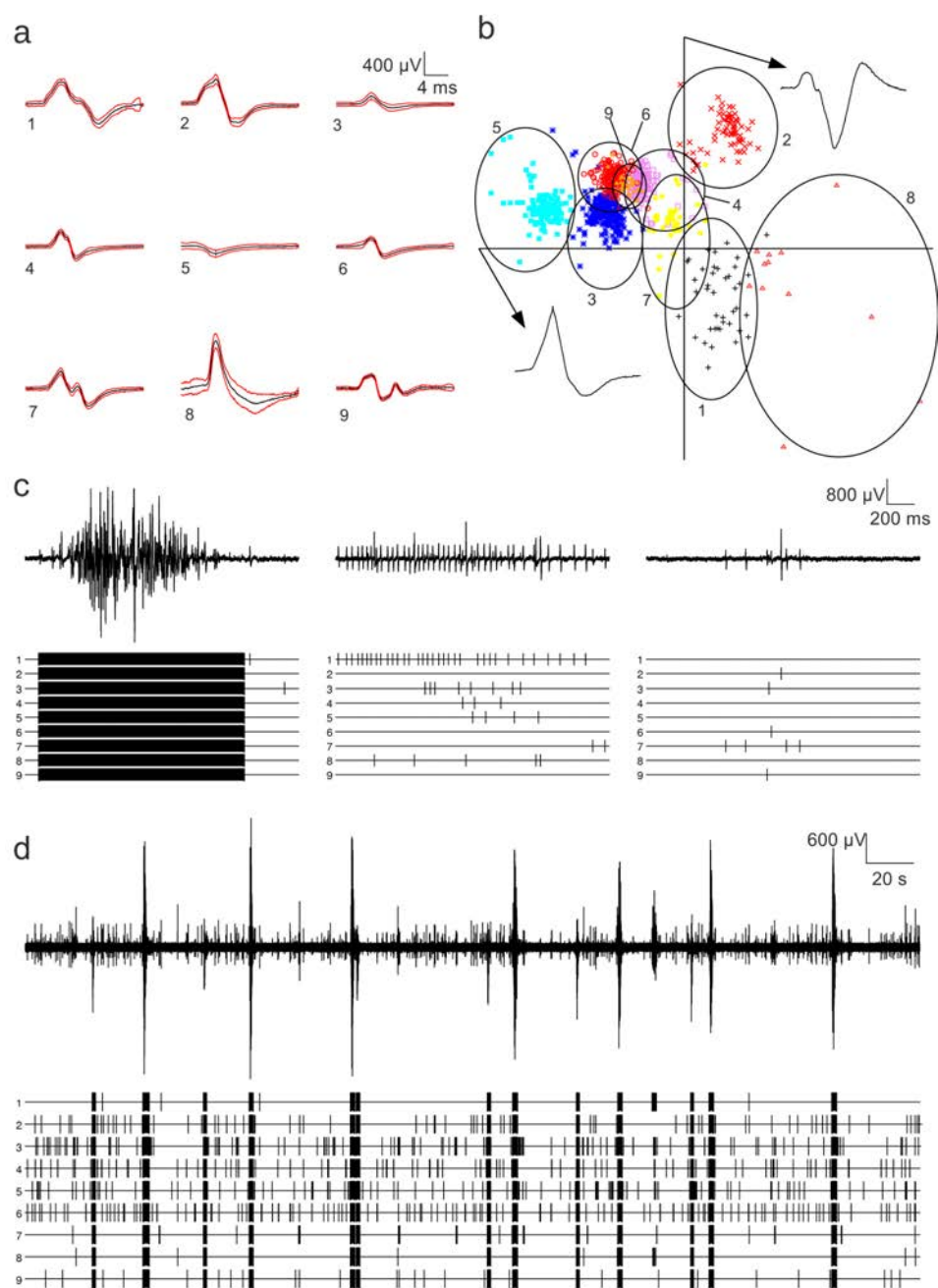


**Figure 2.6:** Spike sorting for the second device: (A) Nine spike profiles ascribed to different clusters by the spike sorting algorithm (black and red traces show mean and mean-absolute-deviation respectively). The number of spikes in each class was 41, 70, 197, 135, 135, 137, 45, 12 and 29 for classes 1 to 9 or a total of 801. (B) Two-dimensional scatter plot in PCA space showing the nine corresponding k-means clusters. (C) Short epochs of raw data (top traces) and raster plots (bottom) with bursting and sparse activity. (D) Longer epoch of raw data and raster plot including hippocampal bursts and inter-ictal periods. - Reproduced by permission of The Royal Society of Chemistry



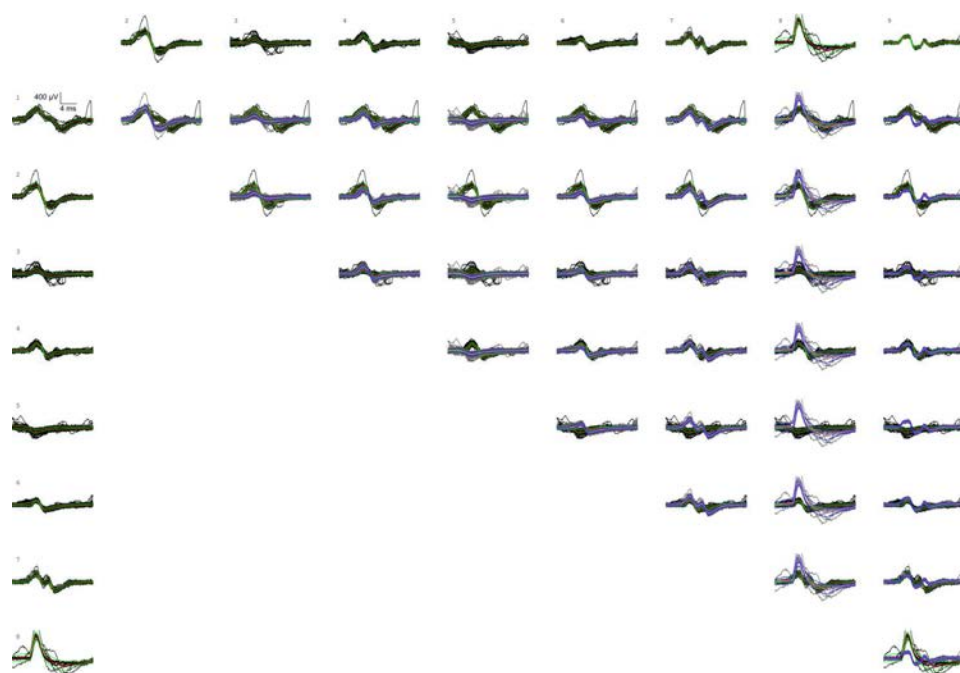


**Figure 2.7:** Pairwise matrix for the nine signal types shown in Fig. 2.6. Each entry in the matrix shows two overlapped profiles (mean and mean-absolute-deviation) for comparison. The numbered traces correspond to the individual profiles according to the clusters shown in Fig. 2.6 - Reproduced by permission of The Royal Society of Chemistry

*Remarks*

- In chapter 5 SEM images of  $\mu$ -channels were taken which show that indeed a high number of neurites can grow into  $\mu$ -channels. While determining the exact number of neurites was impeded due to bundled neurites and the blanket effect of carbon coating, the number of discernible neurites in Fig. 5.7, inset 1 can be estimated with  $> 7-9$ . In Fig. 5.6, inset 2 an even higher density is visible. These findings confirm the relatively high number of 9 identified spike shapes.
- In (Wang, Riss, Buitrago, and Claverol-Tinturé, 2012) we conclude that longer  $\mu$ -channels broaden the spike shape due to a low-pass filtering effect. This might contribute to the higher spike cluster count in the device with 1600  $\mu\text{m}$   $\mu$ -channel length compared to the 60  $\mu\text{m}$  device. Longer spike shapes contain more information that can be used by the k-means algorithm to separate the spike clusters.
- During the processing of the datasets, it became apparent that standard visualization methods (gnuplot, matlab, R plotting facility) are not suitable for plotting large amounts of time series data. Quick, interactive inspection of the recordings was not possible. This finding motivated the development of the `O1Plot` data viewer in chapter 3.

## Chapter 3

### O1Plot data viewer

This chapter focuses on rationale, implementation and performance test of the O1Plot data viewer. The necessity of this data viewer became obvious during the spike sorting project (chapter 2) as traditional plotting tools were struggling to display time series data beyond 10 or 20 mins fast enough to allow interactive data navigation. Before advancing to long-term monitoring of neuron activity this problem needed to be solved and fortunately it was possible to solve it.

#### 3.1 Abstract

Analysis of electrophysiological recordings often involves visual inspection of time series data to locate specific experiment epochs, mask artifacts and to verify the results of processing steps such as filtering or spike detection. Yet long-term experiments with continuous data acquisition generate large amounts of data and rapid browsing through these massive datasets poses a challenge to conventional data plotting software as with rising amounts of data plotting time increases. Here we present O1Plot, a visualization concept for large scale time series data using techniques from the field of high performance computer graphics such as hierarchic level of detail and out-of-core data handling. A demonstration prototype has been implemented and benchmarks show that the technology is capable of displaying arbitrary amounts of time series data, event and interval annotations in constant time -  $\mathcal{O}(1)$  - allowing interactive, lag-free ( $< 20\text{ms}$ ) navigation of long-term electrophysiological recordings. The current 64 bit implementation supports datasets with theoretically up to  $2^{63}$  samples, the benchmarks have been conducted up to  $2^{37}$  samples / 1 TiB dataset size. The presented software will be freely available

and can be included as a GUI component in further software projects, providing a standard visualization method for long-term electrophysiological experiments.

## 3.2 Introduction

For understanding long-term neuronal processes such as growth, plasticity/learning, de- and regeneration, it is necessary to monitor neuron activity over long periods of time. A plethora of single and multichannel extra-cellular electrophysiology techniques today offer long-term recording capability.

For in vivo experiments protruding electrode arrays are available to record extra-cellular potentials from cortical areas for over 2 years (Maynard, Nordhausen, and Normann, 1997; Leigh R. Hochberg, Serruya, Friebs, Mukand, Saleh, Caplan, Branner, D. Chen, Penn, and John P. Donoghue, 2006; O’Doherty, Lebedev, Ifft, Zhuang, Shokur, Bleuler, and Nicoletis, 2011; Simeral, S.-P. Kim, Black, J P Donoghue, and L R Hochberg, 2011), microwire bundles can be used to record from deeper areas within the brain for more than >1 year (Yamamoto and Wilson, 2008; Tseng, Yen, and M.-L. Tsai, 2011; Porada, Bondar, Spatz, and Krüger, 2000; Jackson and Fetz, 2007) and cuff/cone electrodes provide recordings from enclosed nerves and neural tissue with stable neuron-electrode connection for up to 3 years (Polasek, Hoyen, Keith, Kirsch, and Tyler, 2009; P. R. Kennedy, 1989; Bartels, Andreasen, Ehirim, Mao, Seibert, E. J. Wright, and P. Kennedy, 2008).

In vitro, plain culture dishes with integrated multi-electrode arrays (MEAs) are used for experiments on neuron cultures (Guenter Gross, 2011; G.W. Gross, Rieske, Kreuzberg, and Meyer, 1977; J Pine, 1980) and can keep the cultures alive for >9 months (Steve M. Potter and DeMarse, 2001). Optionally the cultures can be patterned chemically (Zhao, A. Chen, Revzin, and Pan, 2010) or physically (E. Claverol-Tinture, Cabestany, and Rosell, 2007; Morales, Riss, Wang, Gavin, Rio, Alcubilla, and Enric Claverol-Tinture, 2008; Dworak and Bruce C. Wheeler, 2008; Maher, J Pine, J. Wright, and Y. C. Tai, 1999) enabling circuit level observation of neuronal development and plasticity.

However, continuous long-term recording results in huge datasets which pose a challenge to storage and analysis of the data. E.g. when recording at 10 kHz and with 8 bytes per sample each recording channel generates  $\sim 6$  GiB (IEC nomenclature, IEC 2000) per day. In the past, high costs for data storage were prohibitive for saving the complete recording in raw data format. Algorithms were developed to conduct filtering, spike detection and classification during the experiment in real-time and only the time stamps and selected parameters of the classified spikes were saved to the hard disk (Asai, Aksenova, and A. E. P. Villa, 2005; Chan, T. Wu, S.-T. Lee, M.-A. Lin, S.-M. He, P.-K. Chao, and T. Tsai, 2010).

Recently, due to increasing hard disk capacity at low cost, raw data storage of long-term recordings has become feasible. Raw data storage offers the advantage that the data can be analyzed after the experiment with access to the complete

recording. This allows for iterative refinement of the analysis process, testing of alternative analysis algorithms, identification and processing of unexpected artifacts and it facilitates the study of neurons displaying time varying activity patterns.

During iterative data analysis, the visual inspection of time series data is a reoccurring work step. Initially artifacts and/or noise need to be identified and excluded from further analysis, e.g., incomplete power line shielding or manipulation of the experiment setup. At later stages of the analysis, results of processing steps such as filtering, spike detection and spike sorting need to be verified. Due to the interactive nature of such analysis, the user should be able to quickly navigate through the data and see it at different magnification levels.

This requirement poses a challenge to traditional plotting programs. The canonical approach to plot time series data is to project the samples one by one into the canvas and connect the resulting points with lines. The plotting time therefore depends on the amount of data; more data results in longer plotting time; the canonical algorithm has linear complexity, in  $O$ -notation (Knuth, 1976; Cook, 1983) expressed as  $\mathcal{O}(n)$ . Due to the large amounts of data produced by long-term recordings, the canonical plotting method cannot offer the necessary performance despite the impressive computational power of current computers and their graphics cards - a new algorithmic approach is needed.

In the field of 3D computer graphics similar problems have been solved in the past by combining various strategies.

Level-of-detail (LoD) methods use the fact that complex 3D models often have more detail than the monitor with its fixed resolution and pixel size can display (Tan Kim Heok and Daman, 2004; Luebke, 2001). This applies especially to scenes in which the object is far away and occupies only a small area on the monitor. The LoD method generates for each original, high-detail 3D model several additional 3D models with successively reduced geometric complexity. Depending on the size occupied by the object on the monitor, the algorithm chooses the 3D model which still provides the maximum amount of detail the monitor can display but avoids excess detail levels that go beyond the capabilities of the monitor.

This approach is further refined in newer surface splatting methods (Zwicker, Pfister, Baar, and M. Gross, 2001; Alexa, Behr, Cohen-Or, Fleishman, Levin, and T. Silva, 2003). They are aimed at high detail models which provide about one or more data points per pixel. This allows to abandon the polygon representation and just project the point cloud onto the pixel matrix of the monitor.

Handling the huge amount of data is an additional challenge. The size of high detail models usually exceeds the memory capacity of video cards and main memory; the bulk model data therefore needs to remain on the hard disk. However optimal performance can only be achieved by processing the data in the fast access memory levels (main and graphic card memory, caches) (Salasin, 1973). It is therefore necessary to load the used data segments on-demand into main

and graphics memory as the user navigates through the model (W. T. Correa, Klosowski, and Silva, 2003; Wald, Dietrich, and Slusallek, 2005).

With O1Plot we show how to apply such methods to allow fast, interactive display of electrophysiological time series data, event and interval annotations.

### 3.3 Materials and methods

#### 3.3.1 Overview

Fig. 3.1 shows an overview of the O1Plot concept. The original datasets are preprocessed to create static hierarchic data representations that are stored on the hard drive.

During visualization the main thread receives user input (panning/zooming) and quickly paints the current data section which is stored in a small OpenGL display list. Every time the user navigates towards the limits of the current display list the main thread requests a new data section at the required detail level (zoom level) from the background thread. The background thread reads data from the adequate static data reduction level, applies further data reduction (dynamic data reduction) to exactly match the needed detail level and stores the new data section as a new OpenGL display list in the graphics subsystem. Once completed, the main thread switches to the new display list and can now present the new data section to the user.

#### 3.3.2 Time series data

O1Plot works with electrophysiological datasets that store a single recording channel as a series of floating point values (IEEE 754, 64bit).

##### *Basic data reduction step*

The key technique underlying most hierarchical visualization techniques is the reduction of detail in the scene/model to accelerate plotting but without compromising the final visual result. This is possible because a computer display discretizes the image into pixels (Fig. 3.2a). When plotting large amounts of data onto a computer display the finite resolution of the display imposes a limit to the amount of details that can be displayed. If there are more data points than pixels, several data points get projected onto the same pixel (Fig. 3.2b). This allows the use of a replacement representation which has less detail but yields the same visual result, often also called proxy representations/models (Kruger and Westermann, 2003; Tikhonova, C. D. Correa, and Ma, 2010). For O1Plot vertical lines have been chosen as proxy representation for time series data (Fig. 3.2d). Each line represents an interval of the time series dataset. The minimum and maximum values in the interval define the vertical positions of the two ends of the vertical line and the average time-value define the horizontal position. As long as the intervals are smaller than the pixel columns on the monitor the visual results are indistinguishable from the normal, canonical visualization method.

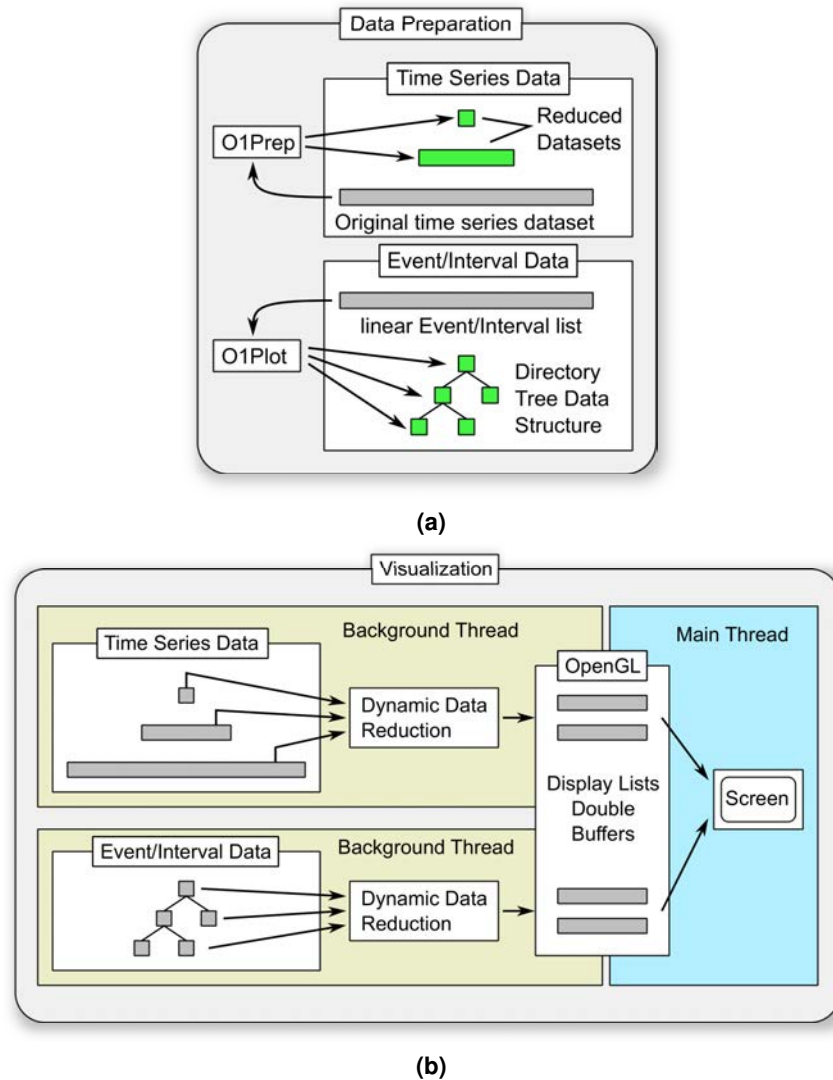


**Figure 3.1:** O1Plot overview. (a) Data is prepared in an offline processing step. Time series data is reduced with the batch tool O1Prep in several steps to form a static data reduction pyramid. Linear event/interval lists get converted to a hierarchical directory tree data structure directly in the O1Plot program. (b) During visualization each dataset gets read by a separate background thread from the hard disk, further reduced (dynamic reduction) to match the current zoom level of the visualization and stored in the graphics system as an OpenGL display list. The main thread then uses the prepared display lists to quickly draw the data to the screen. OpenGL display list double buffering allows simultaneous painting of the current display lists by the main thread while new display lists get prepared by the background threads.

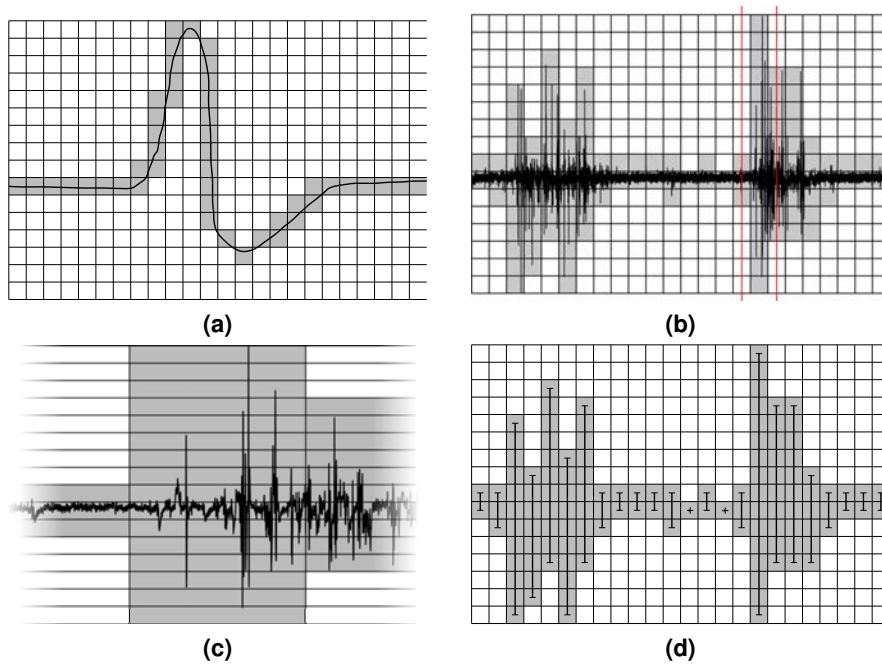


**Figure 3.2:** The basic principle of data reduction to accelerate time series plotting. (a) A computer display uses discrete pixels to display a graph. (b) Plotting large amounts of data results in overdraw; several data points get plotted into the same pixel column. A zoomed version of the marked area (red lines) in (b) is shown on (c) as an example for the amount of detail that can get collapsed into a single pixel column. (d) Replacing the original time series dataset with a reduced dataset consisting of minimum and maximum values for each pixel column gives the same visual result. The reduced dataset in this example consists only of 48 data points compared to the original time series with 38866 samples in (b) and can therefore be plotted considerably faster.



This basic data reduction by proxy representation is the central algorithmic technique used in O1PLOT to speed up data visualization. Instead of depending on the amount of data the plotting time now depends on the resolution of the computer display. As the display resolution is constant the algorithm also has constant complexity -  $\mathcal{O}(1)$ .

Before visualization however the reduced dataset needs to be computed, which is a task of linear complexity -  $\mathcal{O}(n)$  - as all the data points need to be processed to find the minimum and maximum values of the intervals. This step needs to be performed only once and it can be run unsupervised as a batch process before starting the visualization.

### ***Data reduction hierarchy***

The basic data reduction step described in the previous section solves the problem of quickly displaying time series data at a predefined magnification level. Scrolling/panning is possible but zooming is not. When zooming into the data, at a certain level the vertical lines would become visible - revealing the data reduction trick and destroying the impression of looking at proper time series data. When zooming out, more and more vertical lines would get projected onto single pixel columns which would linearly increase the plotting time and again result in a linear complexity -  $\mathcal{O}(n)$ .

To solve this problem the data gets reduced in several steps to create a static data reduction pyramid (Fig. 3.3) on the hard disk. The reduction factors of the pyramid levels are defined by  $(\text{THINNING FACTOR})^n$  with `THINNING FACTOR` being a user configurable parameter (needs to be a power of 2) and  $n$  being the pyramid level starting with 0 for the level of the original dataset.

### ***Time series display list generation***

During visualization the background thread (Fig. 3.1b) receives requests to prepare data sections for the main thread at specific reduction factors (depending on the current zoom level of the visualization). It chooses the closest static data reduction level in the pyramid “below” the requested reduction factor, i.e., the closest static data reduction level that still contains more detail than requested. With the dynamic data reduction step the data then gets further reduced by an additional reduction factor to match the reduction factor needed for visualization. Example: Assuming a `THINNING FACTOR` of 64, the first static reduction factor is 64, the second  $64 \times 64 = 4096$ , etc. If during visualization a reduction factor of 512 is requested, the algorithm would choose the first static reduction factor (64) and would then dynamically reduce the data with an additional reduction factor of 8 ( $64 \times 8 = 512$ ).

The computational cost for the dynamic data reduction depends on the additional reduction factor; the bigger the additional reduction factor the more data needs to be searched for minimum and maximum values. However, the additional reduction

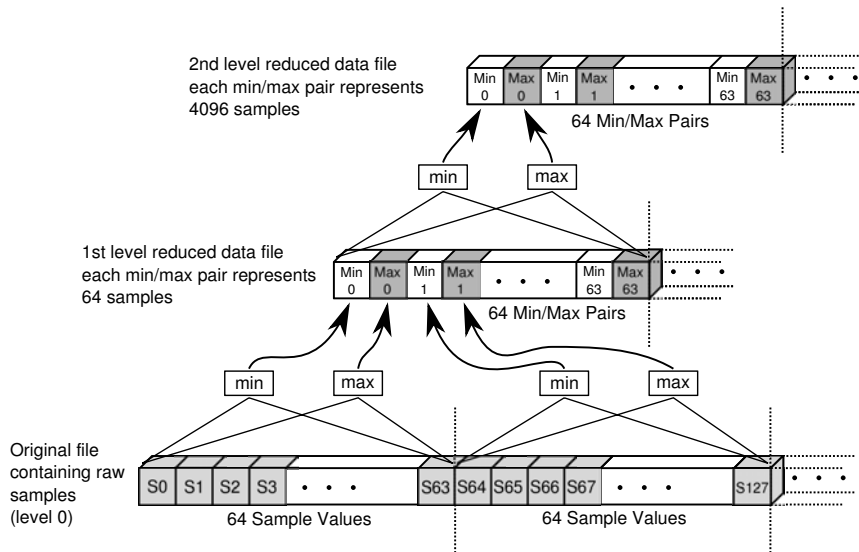


**Figure 3.3:** The data reduction pyramid for time series datasets and a THINNING FACTOR of 64. The original file with the samples is shown at the bottom. For each block of 64 samples the minimum and maximum value gets computed and stored in the file with the 1st level reduced dataset (middle). The computation of the 2nd level reduced dataset is similar, for each block of 64 min/max pairs on the 1st level the minimum and maximum value is computed and stored in the 2nd level. This process continues until the size of the highest level dataset drops below a predefined threshold value (currently 10 MiB).

factor cannot become bigger than THINNING FACTOR (the distance between two adjacent static reduction factors in the pyramid) because the algorithm always chooses the static reduction level of the pyramid that is closest to the requested reduction factor. As THINNING FACTOR is constant the computational cost for the dynamic data reduction is also constant -  $\mathcal{O}(1)$ .

In summary, both the basic data reduction step and the hierarchical data reduction have constant computational effort; combined they form the algorithmic framework that allows panning and zooming of time series data with constant complexity -  $\mathcal{O}(1)$ .

The initial calculation of the complete data reduction pyramid has a complexity of  $\mathcal{O}(n \cdot \log(n))$  - as  $\log(n)$  levels need to be computed, each with linear complexity.

### 3.3.3 Event data

When working with time series data, often events need to be marked. Events are points in time which can indicate the position of spikes, onsets of stimulation or other experiment and analysis parameters. In contrast to time series data, event data is sparse; an experiment can contain only few events (e.g. time points at which the cell culture medium got changed) or a very large amount of events (e.g. when marking all spikes). Events are also editable, the user may want to add or

remove events during visual inspection.

### Directory structure

In order to address these additional requirements, a new storage data structure has been designed. Instead of continuous files, a hierarchical hard disk data storage is used (Fig. 3.4). The events are stored as 64 bit sample positions in block

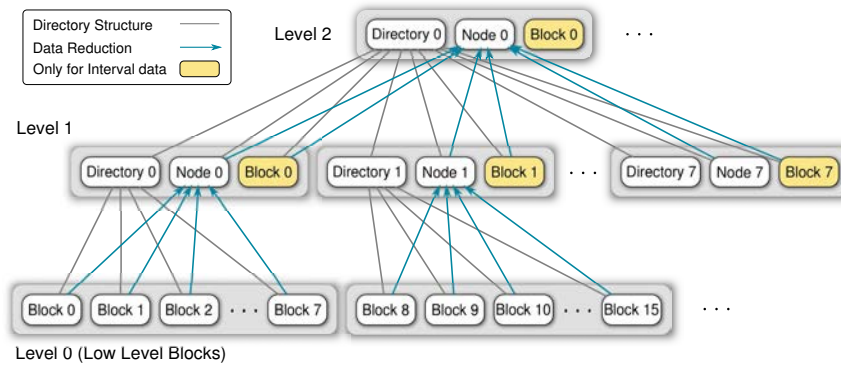


**Figure 3.4:** Directory structure for the storage of event or interval data. Events or intervals are stored in block files at the bottom in Layer 0. Each block file spans a predefined range of samples; all events or intervals within that range are stored in this block file. The events of all block files in a directory get combined into a node file on the directory level above; during this step data reduction takes place. When storing interval data (yellow boxes) additional block files on higher levels are used to store intervals with end points that do not fit into the sample range of a single block file at the bottom.

files on level 0. The storage location of the corresponding block file within the directory tree can be determined from the event value (Fig. 3.5a). The 64 bits of the event value are divided into a path section (high-level bits) and a block file section (low-level bits). The path section is divided into chunks with length `BRANCHFACTOR`, which is a tuning parameter set at compile time. Each chunk is converted into hexadecimal representation to form a component of the block file path. All events that share the same path and only differ in the block file section are stored in the same block file. The block file section consists of `BLOCKFACTOR` bits (`BLOCKFACTOR` is a tuning parameter set at compile time); a block file can therefore contain a maximum of  $2^{\text{BLOCKFACTOR}}$  different events.

The fixed association of event value and storage location within the directory tree facilitates searching the right block file for insert and delete operations. The depth of the directory tree is static and calculated from `BLOCKFACTOR` and `BRANCHFACTOR` (see also Fig. 3.5a):

$$treedepth = \frac{64 - \text{BLOCKFACTOR}}{\text{BRANCHFACTOR}} \quad (3.1)$$

The directory tree is sparse, directories and block files are created on demand when inserting a new event and they are deleted when deleting the last event in a block

file or subdirectory.

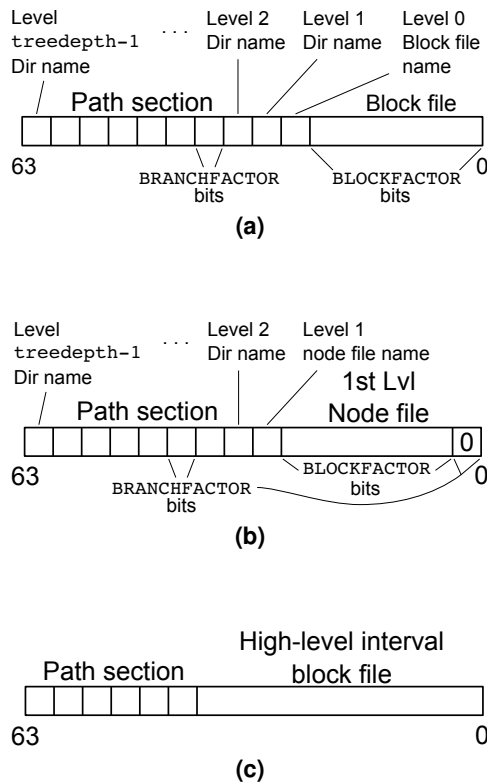
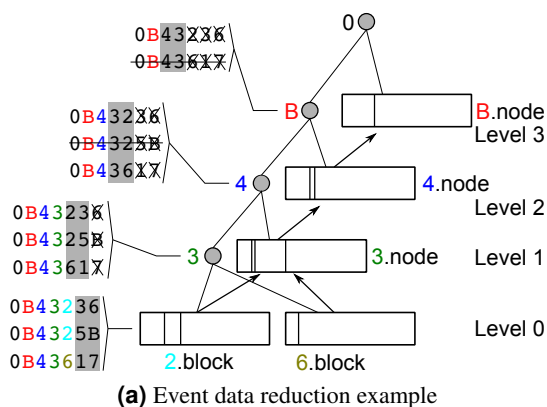


**Figure 3.5:** The 64 bit values of events and intervals define the storage location of the value within the directory tree. The high-level bits are divided into chunks of bits with length equal to tuning parameter `BRANCHFACTOR`. When converted to hexadecimal format they represent the path of the file in which the event or interval is stored. (a) The path of a normal block file consists of `treedepth-1` directories and the block file name. Each normal block file spans  $2^{\text{BLOCKFACTOR}}$  values. (b) Example of a node file on level 1. `BRANCHFACTOR` low-level bits are set to zero while the path section is shortened by `BRANCHFACTOR` bits (one directory level). Node files also span  $2^{\text{BLOCKFACTOR}}$  values. (c) [only applies to interval data] If an interval does not begin and end within the same block file on level 0, it gets stored in a high-level block file which offers - depending on its level - a larger value span.

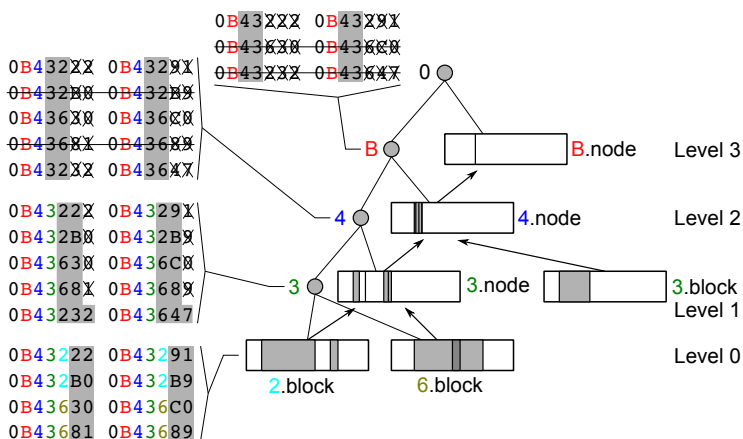
### Data reduction step

The visual representation of an event is a vertical line at its (sample) position. Several events projected to the same pixel position on the monitor are indistinguishable from a single plotted event. A large number of events can therefore be replaced by a single vertical line (proxy representation).

The reduced data representations are stored in node files throughout the directory tree, each node file represents its corresponding sub-directory tree (Fig. 3.4). For the calculation of a node file all events from the block and node files in the sub-



(a) Event data reduction example



(b) Interval data reduction example

**Figure 3.6:** (a) shows an example of three events on level 0 and their reduced representations in higher levels of the directory tree. The hexadecimal representation of the events (on the left) correspond to the path to the block file in the directory tree. The gray boxes mark the bits that are encoded within the files and not in the path. Each reduction step from level  $n$  to  $n + 1$  consists in chopping off the last bits (by the amount of `BRANCHFACTOR` bits, in this example 4 bits) and then eliminating duplicate values. (b) Interval data reduction is similar to event data reduction. The large interval (level 0, 2.block, left) gets reduced but still remains an interval on level 1. The smaller interval (level 0, 2.block, right) gets reduced and changes to a single line on level 1 because in the reduced representation interval begin and end collapse to the same value. Overlapping intervals are possible as shown in level 0, 6.block. The high-level block file 3.block on level 1 contains an interval that would, on level 0, start in 2.block and end in 6.block. High-level block files like 3.block get combined with the node files of their level (3.node) the form node files on the level above (level 2, 4.node).

directory are collected (Fig. 3.6a). Then for each event  $n \cdot \text{BRANCHFACTOR}$  low-level bits are zeroed (see also Fig. 3.5b);  $n$  is the level of the node file in the directory tree. Finally, duplicate events that result from the bit zeroing step are eliminated.

### *Event display list generation*

During visualization the background thread receives requests to prepare new display lists containing the events within a given sample range (defined by begin and end point) at a certain zoom factor (data reduction level). Due to the fixed assignment of event position to block/node file path the routine can directly calculate the path from where to start the search. It then traverses the directory tree at the level corresponding to the requested zoom factor, reading events and proxy representations from block/node files until the path of the end point is reached. The traversal level is chosen so that the static data reduction level of the events and proxy representations is just "below" the requested data reduction level. The events/proxy representations are further reduced (dynamic data reduction) to match the final reduction level (zoom factor) for the visualization; then they are added to the display list.

The directory tree can store a maximum of one event at each sample position and then has the same data density and topology as a time series dataset (compare Fig. 3.3 and 3.4). Therefore, analog to time series visualization, the combination of basic data reduction step (using a proxy representation to replace several events within one pixel column) and the data reduction hierarchy allow to generate display lists with constant complexity; panning and zooming of event annotations is possible with constant computational effort -  $\mathcal{O}(1)$ .

### **3.3.4 Interval data**

Besides marking single time points (events), time series analysis often also requires to mark intervals of the recording, e.g., spikes/bursts from their onset to their end, artifacts due to manipulation of the experiment setup or interesting periods of the recording. In O1Plot intervals are defined by the sample positions of interval begin and end. Visually, intervals are represented by semi-transparent colored rectangles that cover the interval range.

### *Directory structure*

Interval data is stored in a directory tree structure similar to the directory tree structure for event data (Fig. 3.4). Intervals are stored as two 64 bit values (begin and end) in block files with `begin` value  $\leq$  `end` value. Intervals can be overlapping. Intervals which begin and end in two different level 0 block files are stored in high-level block files (Fig. 3.5c) which have a larger range of sample positions.

### ***Data reduction step***

Projecting several intervals into the same pixel column is indistinguishable from plotting just a single vertical line into the pixel column. Therefore intervals are represented by a single vertical line as proxy representation.

The reduction process is analog to event data reduction, except that instead of one 64 bit value for an event, two 64 bit values are processed for an interval. Examples for the reduction process can be seen in figure 3.6b. Once begin and end value of an interval collapse to the same value, the interval is represented by a single proxy line. The additional high-level block files are used analog to normal block and node files for the creation of node files on the level above.

### ***Interval display list generation***

Interval data display list generation is similar to event data display list generation. Additionally, during the directory traversal a stack is maintained which contains all intervals from high-level block files along the path from the root node to the current block/node file. These intervals are combined with the intervals and proxy representations of the block/node files to form the final display list.

As the data structure allows overlapping intervals a block file spanning  $n$  bits can theoretically store a maximum of  $2^{2n-1} + 2^{n-1}$  intervals (both begin and end point can take on all  $2^n$  values under the condition that `begin value`  $\leq$  `end value`). Due to the large span of the high-level block files and the fact that their intervals are stored on a stack during display list generation, the worst case computational and memory complexity is exponential. However, during normal electrophysiology analysis such a maximally overlapped interval structure is not to be expected. It can rather be assumed that the intervals are mostly non-overlapping and sparse. In this case the data density and topology resembles time series and event data and the computational complexity for panning and zooming can be assumed constant -  $\mathcal{O}(1)$ .

### **3.3.5 Performance tuning parameters**

In order to achieve quick directory tree traversal during display list generation the tree structure parameters need to be tuned to match the performance characteristics of the used data storage device and file system.

- **Block file sample range (BLOCKFACTOR)**  
Controls the sample range covered by block and node files. Small ranges have the advantage that inserting and deleting events/intervals in small files is quick, but for visualization a lot of small files need to be traversed to create a new display list. This results in more time intensive directory and inode lookups, leading to poor visualization performance.  
Block files covering a large range on the other side have advantages due to quick visualization but are slow when inserting or deleting events/intervals.

- Branch width (BRANCHFACTOR)  
Controls the branching width of the directories. Small branch widths result in a deep directory tree that has only few sub-directories at each node, large branch widths result in a shallow directory tree and with many sub-directories at each node.  
The optimal value depends on the directory lookup characteristics of the used file system. For file systems that can quickly lookup large directories a large value is better, for file systems that are better at sequentially looking up several smaller directories a small value performs better.

### 3.3.6 Hiding the hard disk latency by double buffering

With the described methods above the amount of data that is needed to plot a single image is significantly reduced. These small chunks of data can now be loaded "on-demand" from the hard disk into main and graphic card memory. To avoid that the access latencies of the hard disk stall the real-time navigation, a display list double buffering system is used (Fig. 3.1b). While one display list is presented to the user by the main thread, a background thread is filling the other display list with new data from the hard disk. The display list contains more data than necessary to plot the current screen section, i.e., the display list is wider and has more resolution than necessary to plot the current screen. The extra data acts as a reserve which allows the user to continue navigating with the old display list while the background thread is preparing the new display list. As long as the new display list gets prepared in time before the user reaches the border of the current display list, the navigation appears to be seamless without noticeable display list switch. The current implementation works with display lists that are 3x the width and 4x the resolution of the current screen section. The size of the display list depends therefore on the screen width, and can contain up to  $screenwidth \cdot 3 \cdot 4$  elements (lines/rectangles).

### 3.3.7 Implementation

The software was implemented in C++ using the Qt 4.7.0 toolkit for platform independence; a 64-bit operating system is required for memory mapping files > 2 GiB. OIPlot has been built, tested and benchmarked on Linux (gcc 4.4.5); it also successfully builds and passes basic tests on Windows 7 (mingw64 or Microsoft Visual Studio 2010) and Mac OS X (Xcode 3), however, thorough tests and benchmarks were not conducted on these platforms.

#### *Standalone programs*

*OIPlot* OIPlot is the main program, the interactive data viewer. It can display multiple time series, event and interval datasets in a single graph window and provides intuitive navigation (panning and zooming) using the mouse. For each dataset it's possible to choose the plot color, temporarily exclude the dataset from



plotting and set the plot priority (datasets of high priority are plotted in front of lower priority datasets). The viewer can insert and delete events and intervals, traverse event and interval lists while optionally tracking the current event/interval in the graph window.

*O1Prep* Before time series datasets can be displayed in `O1Plot` they need to be preprocessed to generate the reduced data representations. Depending on the amount of data and hard disk speed this process can be quite time consuming. Therefore a separate program - *O1Prep* - has been developed for processing time series datasets in batch mode.

### *API and Qt widget*

To facilitate the adoption of the `O1Plot` visualization method it is possible to embed `O1Plot` as a component (Qt widget) into other software projects. In listing 1 a basic example of how to use the application programming interface (API) and library is shown.

```
#include <QApplication>

// Include the header file for the O1Plot Qt widget
#include <O1Plot.h>

// all definitions reside in the O1Plot namespace
using namespace O1Plot;

int main( int argc, char** argv )
{
    // Qt basic setup
    QApplication qapp( argc, argv );

    // create and show the O1Plot viewer widget
    SimpleViewWidget viewer( NULL );
    viewer.show();

    // add a time series dataset
    viewer.addTimeSeries ( "TestDataSet.cfg" );

    // zoom to view sample positions 7000-8000
    viewer.setXRange( 7000, 8000 );

    // at this point the GUI setup is complete
    // control goes to Qt for user input processing
    qapp.exec();
}
```

**Listing 1:** Example of how to use the `O1Plot` API to display a time series dataset

### 3.3.8 Benchmarks

The visualization performance of `O1Plot` has been evaluated with benchmarks. `O1Plot` was connected to a "remote-control" module which took control of view

navigation, allowing to reliably replay a sequence of display commands in different tests. The sequence used for the benchmarks visualized in each step  $n$  a sample range of length  $[0, 2^n]$  until covering the entire dataset. This way the sequence allowed to evaluate and compare the visualization performance at different magnification levels. The computation time was measured with `clock_gettime()` for both the preparation of the OpenGL display lists and for the actual painting of the display list. Several factors that can influence the performance have been examined:

- **Tuning parameters**  
The visualization modules for time series, event and interval data each have their performance tuning parameters (`THINNING_FACTOR` for time series, `BLOCKFACTOR` and `BRANCHFACTOR` for event and interval data). In order to find the optimal values for the tuning parameters several candidate values have been benchmarked and compared.
- **File system cache**  
Most modern operating system use free main memory to cache file system data. This speeds up further read access from cached data as main memory is much faster than raw hard disk access. `O1Plot` benefits from the file system cache as during normal navigation (panning and zooming) most data is already stored in the file system cache and only small portions of new data need to be read from the hard disk. In order to estimate the impact of the file system cache, benchmarks have been conducted both with file system cache and under a setting under which the file system cache got pruned before each test to simulate "cold-start" conditions. This was achieved by writing a "3" into `/proc/sys/vm/drop_caches`. Note that this did not prune the read cache of the hard disk itself, data cached there might still bias the results.
- **Directory and inode block fragmentation**  
Event and interval display list generation depends on quick directory traversal which is predominantly influenced by seek times between directory and inode blocks. Fragmented directories require more and longer seeks, increasing the total access time. To estimate the impact of directory and inode fragmentation, benchmarks were conducted with "fragmented" and "optimized" directories.  
For generating a "fragmented" directory the original directory tree was scanned to get a list of all files and sub-directories. After randomizing this list the original directory tree was copied to the new directory tree in the randomized order of the list. This ensured (on the tested XFS file system) that the directory and inode blocks in each directory were non-continuous. For generating "optimized" directories the original directory was copied to the new directory in a "depth first search" tree traversal order to achieve mostly continuous directory and inode block distribution.

The benchmarks were conducted on synthetic datasets. For time series data, a synthetic dataset was used, consisting of alternating values of  $-1$  and  $1$ .

For event and interval data the synthetic datasets have been designed to be densely filled with events/intervals in order to simulate "worst case performance". The event dataset contained events at every possible position (sample positions  $0, 1, 2, 3, \dots$ ).

The interval dataset consisted of overlapping intervals with variable lengths generated by the formula  $[n2^{k+1}, n2^{k+1} + (2^k - 1)]$  with  $k$  ranging from  $1$  to  $63$  and  $n$  ranging from  $0$  to  $\frac{2^{63} - 2^k + 1}{2^{k+1}}$ . The formula generates interval-gap stipple patterns (50% interval, 50% gap). The parameter  $k$  controls the length of the intervals and gaps ( $2^k - 1$ ). For a given  $k$  the parameter  $n$  then iterates through the individual intervals of the pattern.

Furthermore for event and interval data the directory tree got selectively pruned. The benchmark sequence only looks at the first samples in high detail, samples towards the end of the dataset are only displayed "zoomed out" and with significant data reduction applied. As the samples towards the end of the dataset are never displayed in high detail, their high detail representations can be omitted to save disk space. This way the benchmark datasets for event and interval data could virtually extend up to  $2^{63}$  samples.

For evaluating the storage overhead of event/interval directory structures additional test datasets have been created. They were designed to mimic the analysis situation of a recording from a neuron firing a spike train continuously for 14 days and with  $\sim 33$  Hz frequency. The test dataset for event data therefore contained events (detected spikes) every 300 samples (10 kHz sample frequency), the test dataset for interval data contained intervals every 300 samples and of 30 samples length.

The storage overhead of time series datasets was determined by measuring the file sizes with the command `ls -l`. For measuring the storage overhead of event/interval directories, the command `df -B 1` was used to determine the amount of used bytes on the hard disk before and after creating the directory tree; the final disk consumption was then calculated by subtracting the two values.

For comparing O1Plot time series display to common canonical plotting solutions (gnuplot, matlab and octave + octplot) benchmarks have been conducted with the alternative solutions also using increasing sample ranges analog to the O1Plot benchmarks. The canonical solutions load the complete dataset into main memory before visualization, the capacity of the main memory therefore limited the amount of data that could be benchmarked.

All benchmarks were run in a window with  $800 \times 600$  pixels resolution and on a freshly created file system to avoid bias due to unintentional fragmentation. Each benchmark was repeated several times and the results were averaged to even out external influences like CPU/Task-scheduling, interrupts, etc. The amount of repetitions was chosen depending on the duration of the specific benchmark; short benchmarks were repeated more often than long running benchmarks which

already even out sporadic external influences due to their long duration. Time series and cached event/interval benchmarks were repeated 1000 times, matlab and octave + octplot benchmarks 100 times, non-cached event/interval and gnuplot benchmarks 10 times.

- **gnuplot**  
Gnuplot benchmarks were controlled by a perl script stepping through the sample ranges and measuring the elapsed time with the `Time::HiRes::gettimeofday` function. Gnuplot was reading from binary files for improved performance (parsing ASCII files costs additional processing time).
- **matlab**  
Matlab offers several different plot modes: Hardware OpenGL, Software OpenGL and zBuffer plotting. For the comparison Hardware OpenGL was used which offered the best performance; results of the other matlab plot modes are not shown. Elapsed time has been measured with the `tic()-toc()` mechanism.
- **octave + octplot**  
The combination of octave and octplot has been included as it is a free open source solution using fast OpenGL plotting. Elapsed time has been measured with the `tic()-toc()` mechanism.

The specifications of the benchmark test machine:

PC with an Intel Core 2 Quad CPU Q9550 CPU @ 2.83GHz, 8 GiB memory, an ATI Radeon HD 4870 graphics card, running Linux with kernel 2.6 and proprietary ATI graphics driver. The data files were stored on a Western Digital WD20EARS hard drive (2 TB, 64 MB cache) using the XFS file system.

*O1Plot* has been compiled with gcc 4.4.5 and optimization option `-O3`. Other software package versions were gnuplot 4.2.6, matlab 2009b and octave 3.2.3 with adapted octplot extension.

### 3.4 Results

A functional prototype has been implemented and tested on the 64 bit Linux, Windows and Mac OS X platform. Benchmarks have been conducted only on Linux. The full user interface can be seen in Fig. 3.7 and Fig. 3.8 shows the program displaying an example 15h recording of embryonic mouse hippocampal neurons cultured in a substrate embedded  $\mu$ -channel device (Morales, Riss, Wang, Gavin, Rio, Alcubilla, and Enric Claverol-Tinture, 2008). At each level of magnification the data viewer offers a natural, artifact free visual impression of the recording.

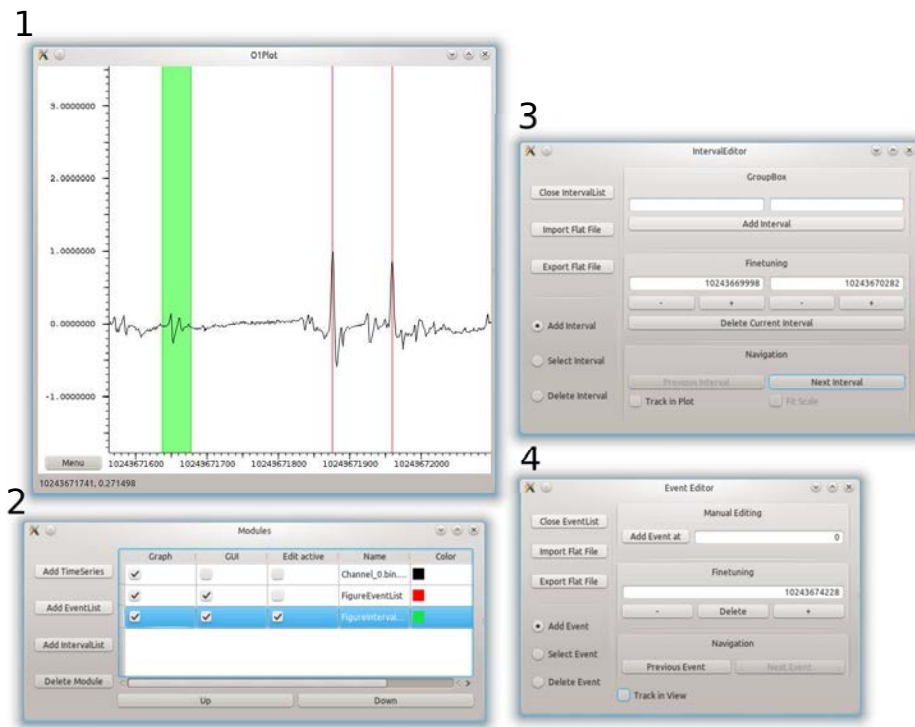


**Figure 3.7:** Screenshots of the O1Plot user interface during display of time series, event and interval data. The main O1Plot window (1) contains the displayed data and receives mouse and keyboard input for navigation and event/interval editing. In the "Modules" window (2) each data source is represented by a module. For each module various options are available, toggling its display in the main window (Graph), changing the display color (Color), redirecting mouse and keyboard input in the main window to a specific event/interval module for editing (Edit active) or opening/closing the option window for a specific event/interval module (GUI). These option windows (3), (4) contain functions for managing the datasets (top left section), selecting/manipulating data in the main window (lower left section), numeric data entry, manipulation, deletion (top right section) and functions to conveniently navigate event/interval lists (lower right section).

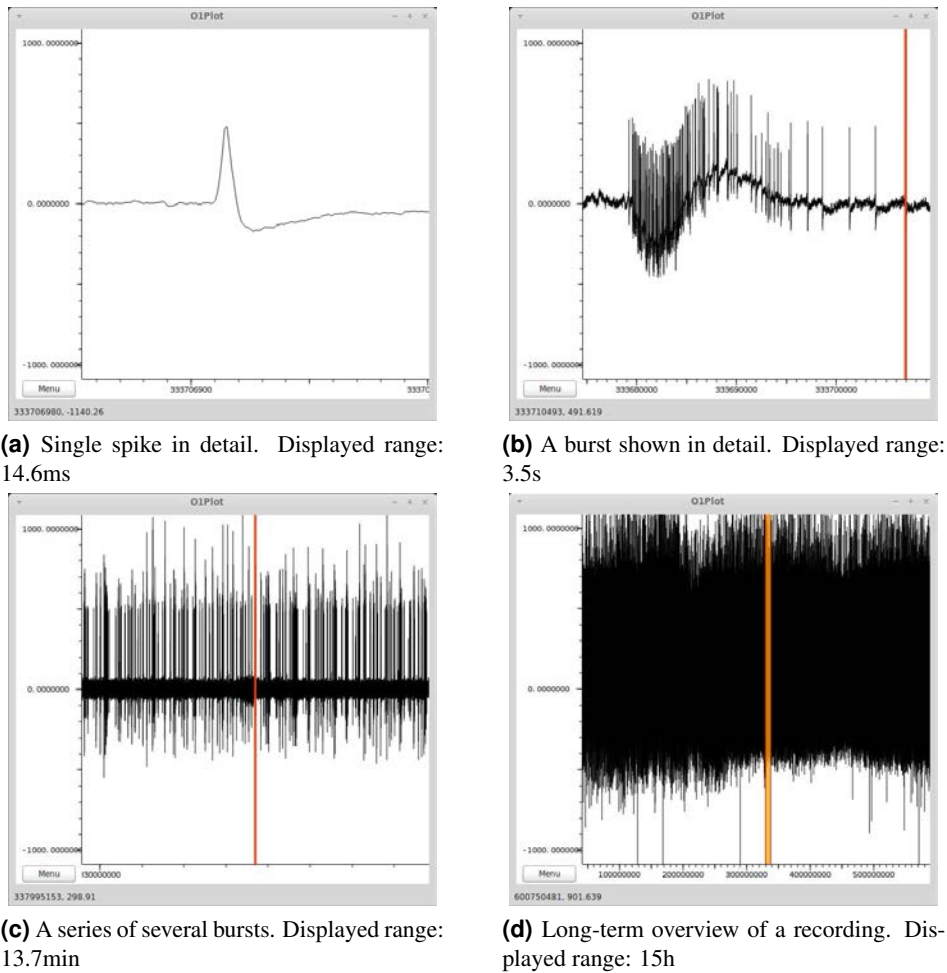


**Figure 3.8:** Example screenshots of the O1Plot prototype on Linux showing a real dataset (15h recording of hippocampal mice neurons in a device with embedded micro-channels (Morales, Riss, Wang, Gavin, Rio, Alcubilla, and Enric Claverol-Tinture, 2008)). The units on the x-axis are samples, the units on the y-axis micro-volts. The marked intervals each show the view range of the previous sub-figure. (d) Slight variations of maximum signal amplitude in long-term recordings allow orientation within the data even when low amplitude signals are too dense and blur together.

### 3.4.1 Benchmark results

The benchmark results are shown in figures 3.9 and 3.10. In each figure the x-axis corresponds to the amount of data that is displayed and the y-axis to the average processing time needed to plot one image or to generate one display list.

Fig. 3.9a shows the time series plotting performance of O1Plot compared to canonical solutions. The O1Plot display list painting and display list generation times remain with <10 ms considerably below the plotting time of the canonical solutions which rise linearly with the amount of data. The O1Plot data reduction can be seen to set in at 8192 samples, effectively cutting off the linear rise of display list generation and paint times.

Figures 3.9b and 3.10 show the influence of various parameters on the performance of O1Plot. In all the graphs, three performance phases can be seen. The first phase for displaying very small amounts of data shows little correlation between the amount of data and display list generation time (e.g. Fig. 3.10a, 0-250 samples). As the amount of processed data is very small the processing time is dominated by the static function call overhead and stays therefore constant.

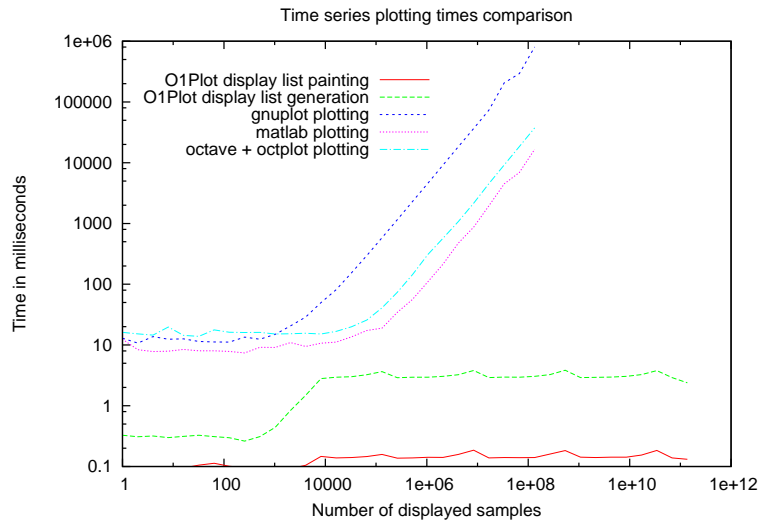
In the second phase the processing time is linearly correlated with the amount of displayed data (e.g. Fig. 3.10a, 250-8192 samples). In this phase the amount of data is still small, therefore the data reduction is not yet active and the processing time shows the typical linear correlation with the amount of data like canonical plotting solutions.

In the third phase (e.g. Fig. 3.10a, 8192+ samples) the data reduction is in effect, the processing time is not correlated to the amount of data anymore and shows artifacts that depend on the properties of the data reduction algorithm and underlying data structure.

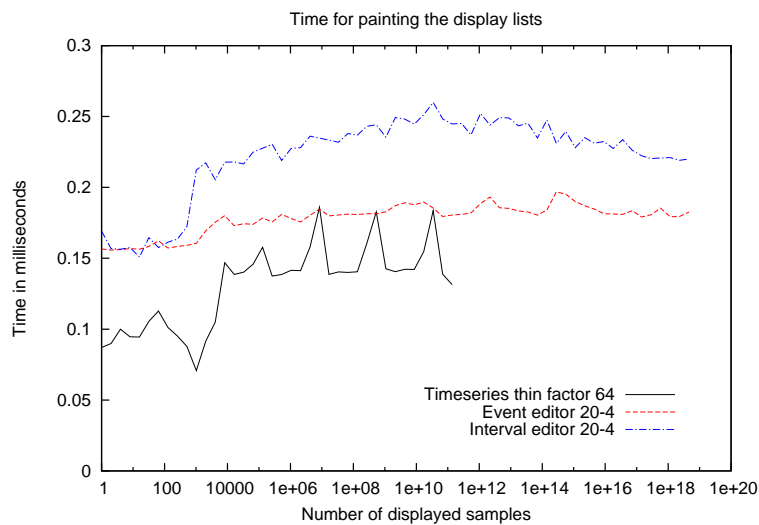
Fig. 3.9b shows the OpenGL painting times for time series, event and interval data. For each data type the optimal tuning parameters have been used (see below). The three phases - constant beginning, linear rise and plateau - are visible; overall painting times remain below 0.3 ms.

Fig. 3.10 contains a grid of benchmark results of OpenGL display list generation performance and how it is affected by various tuning parameters and external conditions. The different data types are arranged top down: times series data (Fig. 3.10a, 3.10b), event data (Fig. 3.10c, 3.10d) and interval data (3.10e, 3.10f). The results in the left column (Fig. 3.10a, 3.10c, 3.10e) were measured with activated file system cache which is the normal condition, the results in the right column (Fig. 3.10b, 3.10d, 3.10f) were measured with deactivated file system cache simulating "cold-start" behavior. In each sub-figure the results for different tuning parameter values are shown and for event and interval data benchmarks also if the file system was fragmented or not.

The results in detail:



(a)



(b)

**Figure 3.9:** In (a) the O1Plot time series plotting performance (THINNING FACTOR 64) is compared with canonical plotting solutions. Plotting times rise for canonical plotting solutions the more data is displayed while O1Plot can keep the plotting time stable. (b) shows the time needed to paint the display lists for time series data, events and intervals using optimal parameters.



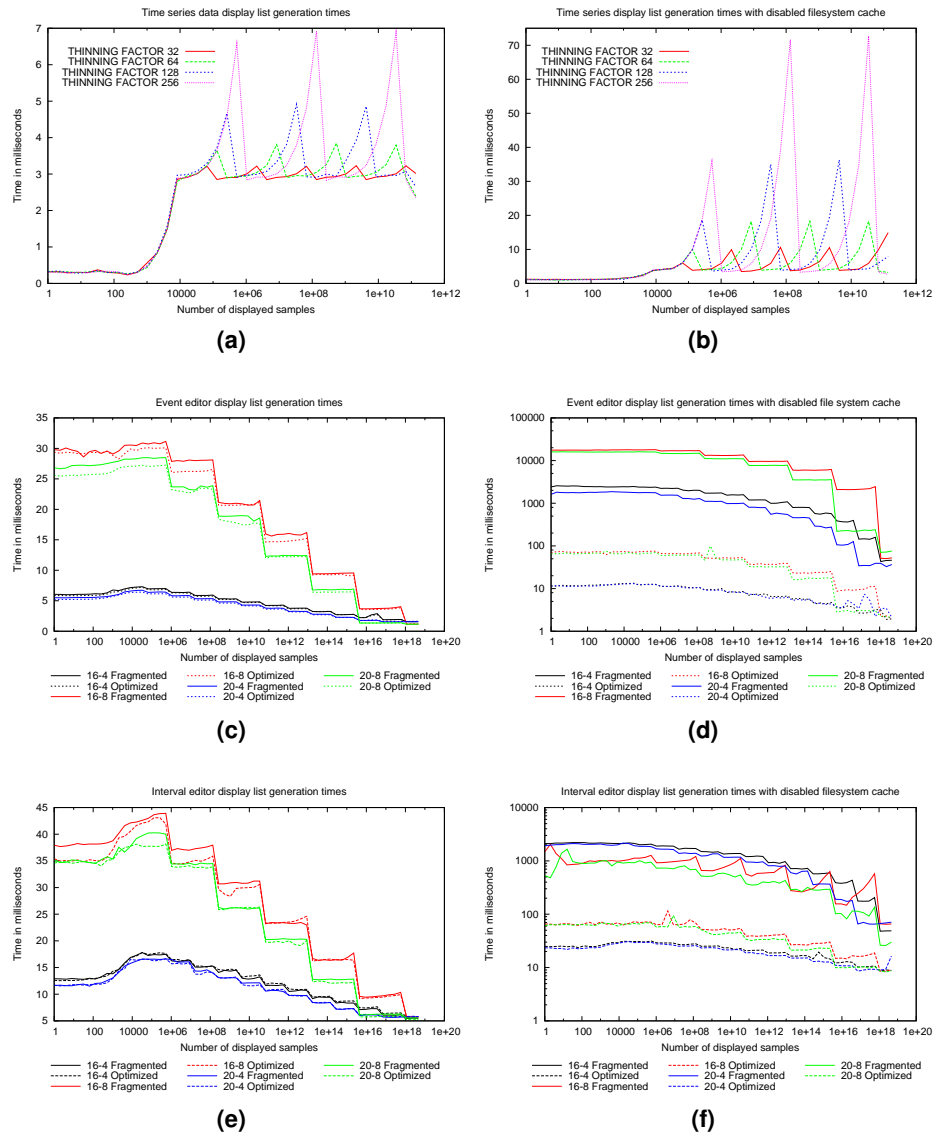


**Figure 3.10:** Results of OpenGL display list generation benchmarks for time series, event and interval data showing the influence of tuning parameters, file system cache and file system fragmentation. See main text for detailed discussion.

OpenGL display list generation performance for time series data (Fig. 3.10a, 3.10b) shows the typical three phase structure. From 0 to 256 samples the display list generation time is constant, from 256 to 8192 samples no data reduction takes place and the display list generation time is linearly correlated with the amount of data. Data reduction starts at 8192 samples and processing time then shows a characteristic saw-tooth profile which results from the algorithm switching through several levels of statically reduced datasets. In the rising phases the dynamic data reduction works with the same static reduction level and has to process more data the more samples are displayed, resulting in rising processing time. When switching from one static reduction level to the next the processing time drops again. Setting the tuning parameter `THINNING_FACTOR` to low values limits the processing time for display list generation but increases the number of reduced datasets (in this example 4 saw-tooth) and the extra storage space (Table 3.1). High values for `THINNING_FACTOR` increase display list generation time but reduce the number of reduced datasets (here 3 saw-tooth) and extra storage space. When conducting the benchmarks with deactivated file system cache, display list generation time rises in general (Fig. 3.10b). Also the first "saw-tooth" is now smaller than the following ones. This is because the first dynamic data reduction phase uses the original dataset with one 8 byte floating point value per sample compared to 2x8 bytes floating point values per sample in the reduced (min/max) datasets for the following dynamic data reduction phases. As the display list generation speed without file system cache depends mainly on the reading speed of the hard disk this difference is now reflected in the display list generation time.

Figures 3.10c, 3.10d, 3.10e and 3.10f show the OpenGL display list generation times for event and interval data. The third phase (>8192 samples) shows a characteristic step wise decrease in processing time. The node files with reduced data are stored closer to the root node than the block files. Therefore when displaying more data, the directory traversal from the tree root to the node files gets shorter and the display list generation time becomes stepwise faster whenever the traversal switches to the next higher directory level. With file system cache, the fragmentation level of the directory and inode blocks has only little influence on the processing times, showing that the data gets predominantly served from the file system cache (Fig. 3.10c, 3.10e). Without file system cache, directory fragmentation now has a strong influence on processing time, as data gets read directly from the hard disk and access times depend on the directory and inode block layout. "Optimized" directory and inode block layouts can be read faster than "fragmented" block layouts.

### 3.4.2 Storage overhead

The statically reduced datasets that are needed for speeding up visualization (proxies) are stored on hard disk and consume extra space. Table 3.1 contains the relative storage overhead for time series data depending on the used THINNING FACTOR.

**Table 3.1:** Time series data overhead

Thinning factor	Relative overhead
32	6.5%
64	3.2%
128	1.6%
256	0.8%

Determining the storage overhead for event and interval data is more difficult as storage requirements for directories largely depend on the used file system and how it is organizing its internal data structures. Also events and intervals are often sparsely distributed which leads to

- small files, which are often too small to fill up a complete physical block on the hard disk, resulting in poor disk usage and effectively higher disk space consumption.
- a multiplication of data; from each block file a chain of node files extends towards the root of the directory tree, consuming extra disk space.

Two types of datasets were used to evaluate the storage overhead: "regular" datasets simulating a spike train analysis (see methods section) and the "sparse", pruned directory datasets used for the benchmarks. The results are shown in table 3.2. While the regular datasets showed a noticeable storage overhead of up to 4

**Table 3.2:** Event and Interval data overhead

Type, Block/Branch parameters	Regular dataset overhead	Sparse dataset overhead
Event, 16-4	378%	217481%
Event, 16-8	253%	118621%
Event, 20-4	212%	176257%
Event, 20-8	117%	96915%
Interval, 16-4	253%	8696%
Interval, 16-8	128%	4032%
Interval, 20-4	213%	8064%
Interval, 20-8	104%	3780%

times the original dataset size, the sparse datasets raised the disk space consumption drastically up to 2175 times the original dataset size. Here the artificially sparse nature of the pruned directory tree leads to very small and distributed file and directory entries. Together with a relatively large disk block size of 4096 bytes (compared to 8 or 16 bytes for a single event/interval entry) this results in such huge storage overhead.

In the more realistic, non-sparse dataset events/intervals can group more closely together and start sharing the same resources (using the same disk blocks if they are in the same block file or sharing the same directory and node file blocks when they are in the same sub directory tree).

### 3.4.3 Optimal tuning parameters

From the benchmarking results optimal parameters can be chosen for the fine tuning parameters.

For time series data, the optimal value for tuning parameter `THINNING_FACTOR` is 64. It has been chosen as the best compromise between speed (paint time  $< 0.3$  ms, OpenGL display list generation time  $< 4$  ms with file system cache and  $< 20$  ms without file system cache) and storage overhead (3.2%).

For event and interval data the storage overhead did not influence the decision of the optimal tuning parameters as the amount of event and interval data is assumed to be small and therefore negligible compared to the storage requirements for time series data. Therefore only visualization speed and event/interval insertion/deletion speed (results not shown) were considered for choosing the optimal tuning parameters resulting in `BLOCKFACTOR` = 20 (max. 1.048.576 samples) and `BRANCHFACTOR` = 4 (max. 16 directories) for both event and interval data.

## 3.5 Discussion

With the `O1Plot` project we have shown that time series data, event and interval annotations can be visualized in constant time -  $\mathcal{O}(1)$  - and therefore independent of the amount of data, allowing fast, interactive navigation of long-term electrophysiological recordings.

In comparison with canonical plotting solutions, which slow down the more data is plotted, this represents a qualitative improvement of the algorithmic complexity from  $\mathcal{O}(n)$  to  $\mathcal{O}(1)$ .

*Further performance considerations* The computational effort to prepare the reduced datasets with `O1Prep` is very small, therefore the limiting factor for the static data reduction is the sequential reading speed of the hard disk. E.g., preparing a single channel recording of 1 day length (6.4 GiB) takes  $\sim 1.3$ min assuming a hard disk throughput of 85 MiB/sec. In further versions of the software

the data reduction may even be included into the recording and analysis software so that the reduction can occur "on the fly" during recording/analysis.

The storage overhead for reduced time series datasets remains (using the optimal THINNING FACTOR of 64) below 4% of the original data size. In contrast the storage overhead for event and interval datasets cannot be bounded by an upper limit as it depends on the sparseness of the data and on the used file system. In extreme cases with very sparse data the storage overhead can grow drastically (Table 3.2), but for practical applications the storage overhead should remain below 4x the size of the original dataset. While in most cases this overhead is acceptable considering today's hard disk capacities and prices, the increased disk space consumption should be considered when planning experiment and analysis steps that generate a lot of event or interval data.

Care needs to be taken that the data hard disks are used exclusively during visualization. Multi-user/multi-program access to the data hard disk can lead to increased access times that the double buffering strategy of O1Plot may not be able to compensate. While time series visualization is quite well adapted to the sequential access characteristics of hard disks, event and interval visualization with its random access pattern may further benefit from Solid State Disks (SSDs) that offer faster random access.

A requirement of the current implementation is the use of a 64 bit operating system as by memory mapping the data files, private memory consumption of the O1Plot process can be reduced while the file system cache of the operating system can provide an optimal caching strategy on system level. This way O1Plot can use all available main memory for caching when it is exclusively used on the system while its effective memory consumption is reduced if O1Plot is idle and other programs are active and filling the file system cache.

We plan to offer O1Plot as a free standalone software for evaluating its capabilities and as software component (Qt widget) for inclusion in further projects. Together with high performance data analysis components O1Plot can form a software infrastructure for analyzing large scale time series data. This should allow continuous monitoring of electrophysiological experiments towards understanding long-term neural processes of growth, plasticity, degeneration and regeneration.

*Remarks*

- The O1Plot data viewer underwent its first practical test in the StarPoM project (chapter 4). There it proved to meet the expectations and successfully helped with rapid visual inspection of raw data and output of filtering operations.
- The current O1Plot demonstration prototype concentrates mainly on the display of one or few data channels. A potential further development direction therefore is to search for visualization techniques to display several parallel time series channels at once.
- Another extension option is a print export function. Currently, large sections of time series data can be included in publications either as bitmaps, which leads to blocky graphics, or in a vector format, which has the disadvantage of very long plotting times. Using a similar data reduction method as for plotting time series data on the monitor could help to achieve high-quality figures at fast plotting speeds.

## Chapter 4

### The StarPoM device

This exploratory project was an effort to both improve on the PoM (Polymer-on-MEA) fabrication technique, as well as pioneer continuous long-term neuron monitoring in  $\mu$ -channel devices. Technical detail problems were to be identified and - if possible - resolved. The `OlPlot` data viewer of chapter 3 turned out to be a very useful tool for data analysis.

#### 4.1 Abstract

A refined fabrication method for PoM (Polymer-on-MEA) devices is presented. Employing a substrate integrated chrome mask, backside exposure and a custom aligner allows the step from 1D  $\mu$ -channel geometries to 2D geometries. The StarPoM device has been built as a first prototype using the new fabrication method. It contains several chambers for confined neuron populations. The populations can connect with neurites through  $\mu$ -channels; the  $\mu$ -channels are also the recording sites for electrophysiological signals.

The StarPoM device has then been used to record electrophysiological signals continuously in the 14 days after plating. The data was later analyzed offline with the aim of studying the development of spike parameters during neuron growth. Finally, `ISI viewer`, a new software for inter spike interval (ISI) visualization has been developed and tested with the 14 day dataset.

#### 4.2 Introduction

In-vitro experiments with dissociated neuron cultures are commonly used in neuroscience for drug testing (Novellino, Scelfo, Palosaari, Price, Sobanski, Shafer,

Johnstone, G. W. Gross, Gramowski, Schroeder, et al., 2011; Rijal and Guenter W Gross, 2008; Morales, Riss, Wang, Gavin, Rio, Alcubilla, and Enric Claverol-Tinture, 2008) and research of neural development and plasticity (Ferrández, Lorente, delaPaz, Cuadra, Álvarez-Sánchez, and Fernández, 2011; Erickson, Tooker, Y.-C. Tai, and Jerome Pine, 2008; Bakkum, Z. C. Chao, and Steve M. Potter, 2008). Studying a small amount of neurons in an artificial device offers the advantage that the environment parameters of the neurons throughout experiment can be tightly controlled. This allows for automated control and monitoring of long-term neuron process, such as the formation of neural networks (Chiappalone, Bove, Vato, Tedesco, and Martinoia, 2006; Wagenaar, Jerome Pine, and Steve M Potter, 2006), learning (Chiappalone, Massobrio, and Martinoia, 2008), degeneration - by aging or pathology (Chong, Benilova, Shaban, De Strooper, Devijver, Moechars, Eberle, Bartic, Van Leuven, and Callewaert, 2011) - and regeneration (H. J. Kim, Jeong Won Park, Jae Woo Park, Byun, Vahidi, Rhee, and Jeon, 2012). In (E. Claverol-Tinture, Cabestany, and Rosell 2007; Morales, Riss, Wang, Gavin, Rio, Alcubilla, and Enric Claverol-Tinture 2008, chapter 2) we proposed  $\mu$ -channels for amplifying and recording electrophysiological signals while confining neurite growth.

This project focused on further development of our  $\mu$ -channel fabrication technology and on its application on long-term neuron monitoring.

#### 4.2.1 Methods that were developed in this project

A device design was chosen that offers 8 small culture wells that are connected with  $\mu$ -channels to a bigger central culture chamber (Fig. 4.1). One electrode per  $\mu$ -channel monitors the neural activity of each connection. The idea of this design is to study the communication between the neuron populations in the separated neuron chambers.

The device was build using the Polymer-on-MEA (PoM) technology (E. Claverol-Tinture, Cabestany, and Rosell, 2007) (see Fig. 4.2 for its application in the context of the StarPoM device). During the fabrication of the device a backside exposure method for improved alignment between thick SU-8 layers of the soft-lithography master was tested.

Neural activity was recorded continuously for 14 days starting with the day of plating. Beside the technical challenge of such a long-term recording, the recording also offered the opportunity to study how spike amplitudes and frequencies develop over time in a  $\mu$ -channel device.

The analysis of the long-term recording had to deal with a huge amount of data. Both performance optimization of existing tools as well as the development of new tools was required to make the data processing practicable.

One of the new tools is `ISI viewer`, a software that can generate fast inter-spike



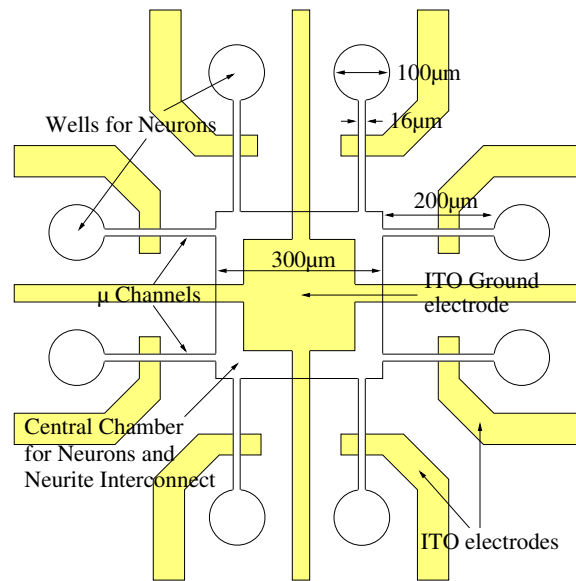


**Figure 4.1:** The StarPoM Design: 8 small wells are connected to a big central chamber by  $\mu$ -channels. Neurons are plated in the wells and the central chamber and grow their neurites through the  $\mu$ -channels. Electrodes (yellow) in the  $\mu$ -channels record the extra-cellular component of action potentials propagating along the axons through the  $\mu$ -channels. The electrode in the central chamber can be used as ground electrode.

interval visualizations of large spike lists. Its purpose is to quickly find temporal correlations between spike clusters in a device.

### 4.3 Materials and methods

Due to the complexity of the fabrication process the detailed fabrication protocol is listed here for reference. Note that the absolute numbers like exposure time, hold time, etc. are specific to each equipment. They are provided as a lead but the final process parameters need to be fine-tuned for each clean room setup.

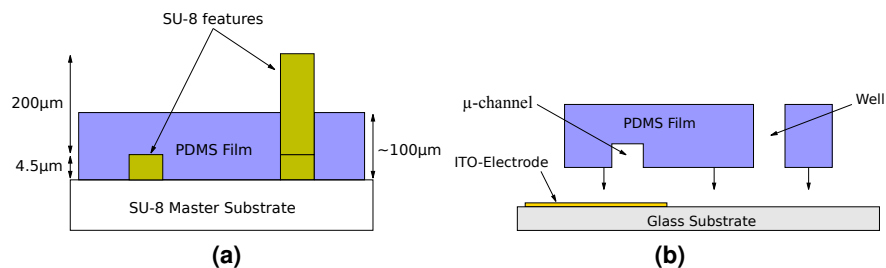


**Figure 4.2:** The StarPoM device composition: In (a) a PDMS film is cured on a SU-8 soft-lithography master with features for  $\mu$ -channels and wells. In (b) the PDMS film gets combined with the MEA to form the final device.

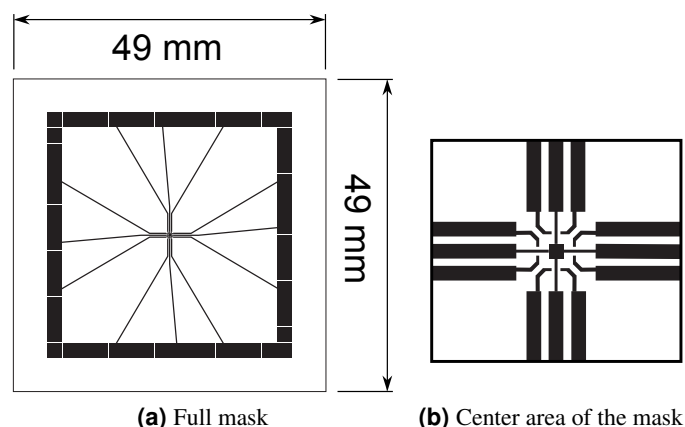


**Figure 4.3:** StarPoM Electrode Mask, suitable for the Multi Channel System MEA 1060 Inv amplifier. The contact pads have 2x2 mm. The electrode in the central chamber is connected to contact pads 15, 42, 84, 57, so that it is grounded regardless of the orientation of the MEA.

#### 4.3.1 MEA fabrication

The mask design for the MEA is shown in Fig. 4.3. The size of the MEA substrate and the layout of the contact pads were configured to match the Multi Channel Systems MEA 1060 Inv amplifier system. The masks were printed onto transparent foils (Leicrom, Barcelona). As substrates ITO-coated glass slides in the dimension 49x49x1.1mm and with resistivity  $\leq 20 \frac{\Omega}{\square}$  were used (PGO, präzisions glas & optik). The substrates were cleaned with acetone and polymer paper and rinsed with isopropanol. After drybaking them in an oven at 180 °C for 30 mins Megaposit SPR-220-7.0 was spun onto the substrates at 3000 rpm. The substrates were returned to an oven to softbake the photo resist at 115 °C for 20 mins. The substrates were exposed through the mask (Fig. 4.3) for 70 seconds in a Karl Suss MA4 mask aligner. After a hold time of 30 mins post exposure bake was conducted at 115 °C for 20 mins. Development took place for 10 - 20 mins in MF-24A developer.

For etching the ITO the following solution was prepared and heated up to 50 °C.

- 200 ml H<sub>2</sub>O
- 200 ml 32% HCl
- 40 ml 69% HNO<sub>3</sub>

The substrates were lowered into the etch solution on a Teflon substrate holder for 1 min intervals. After each interval the substrates were removed from the etch solution, rinsed and the conductivity of the ITO layer was tested with a voltmeter. Until the conductivity of the etched sections dropped to 0 the etching process was

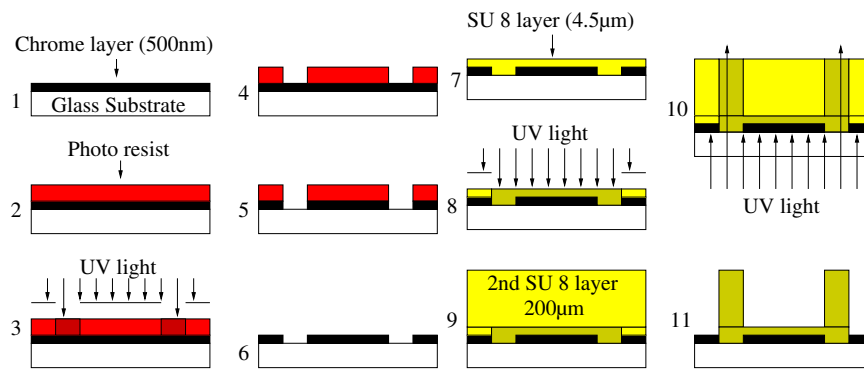


**Figure 4.4:** Microfabrication of the SU-8 StarPoM soft-lithography master: 1. Evaporate chrome onto a glass substrate. 2. Spin SPR-220 photo resist. 3. Expose with the column mask. 4. Develop the SPR-220 photo resist. 5. Etch the chrome layer. 6. Remove the SPR-220 photo resist. 7. Spin-coat a thin SU-8 layer. 8. Expose with the channel mask. 9. Spin-coat a second, thick layer. 10. Backside exposure to expose the columns. 11. Develop the SU-8.

repeated. After finishing the etching process the SPR photo resist was removed from the substrate with acetone and the substrates were rinsed with isopropanol.

### 4.3.2 SU-8 soft-lithography master fabrication

For the fabrication of the SU-8 soft-lithography master a method using an integrated chrome mask and backside exposure was used (Peterman, Huie, Bloom, and Fishman, 2003). This approach solved the problem of missing contrast during the alignment of the well mask to the already exposed SU-8 layer for the  $\mu$ -channels. The conventional approach depends on aligning the well mask through a thick (200 $\mu\text{m}$ ) SU-8 layer to the thin (4.5 $\mu\text{m}$ ), exposed SU-8 layer which is embedded within non-developed SU-8. This alignment method proved unsuitable, as the exposed SU-8 is not visible in the green light used by the aligner (Karl Suss MA 4).

With the new approach first a chrome mask got embedded into the substrate and then the  $\mu$ -channel mask got aligned through only a thin (4.5 $\mu\text{m}$ ) SU-8 layer to the features of the chrome mask (Fig. 4.4). This method provided very good contrast during the alignment process.

- Glass substrates
  - A circular Schott Borofloat 33 glass substrate with 4" diameter was cleaned with polymer paper (clean room paper), acetone and isopropanol
- Chrome coating
  - Dry-bake the glass substrate in an oven at 180 °C for >15 mins

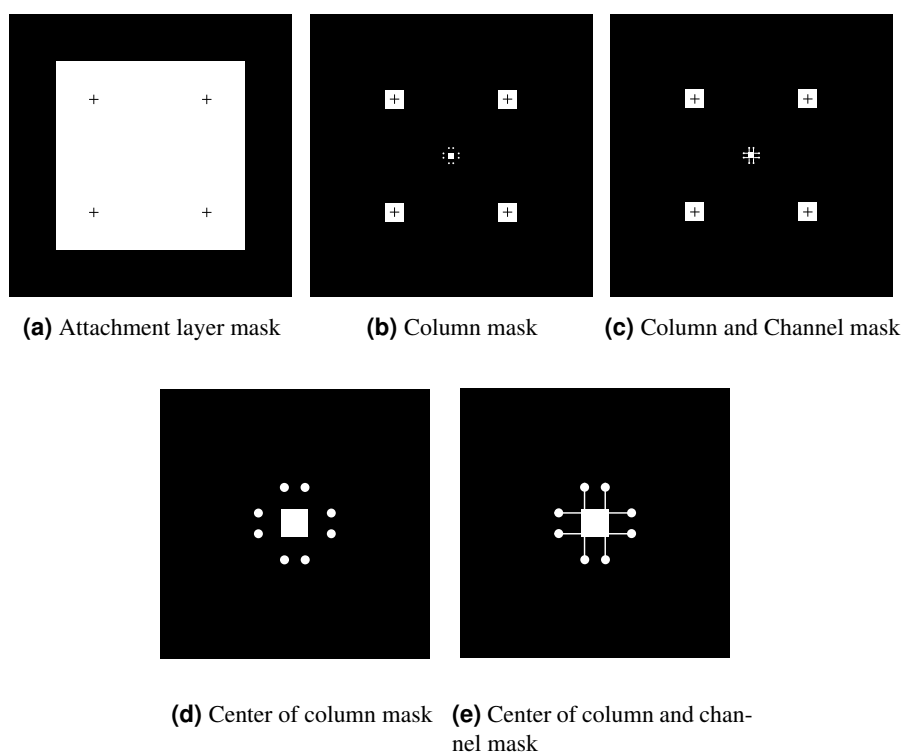


**Figure 4.5:** Masks used for the SU-8 soft lithography master

- E-beam evaporate chrome with 500 nm thickness onto substrate (25-45mA @ 3kV)
- Chrome masking with SPR-220
  - Dry-bake substrate in oven at 180 °C for 30 mins
  - Spin-coat Microposit SPR-220-7.0 photo resist onto the chrome layer with 3000 rpm
  - Soft-bake on a hotplate at 115 °C for 25 mins
  - Expose through column mask for 80 sec
  - Hold time, keep substrate under wet petri dish for 35 mins
  - Post-exposure bake for 2 mins in oven at 95 °C and then on hotplate for 5 mins at 115 °C
  - Develop for 4 min in MF-24A developer
  - Rinse with H<sub>2</sub>O
- Chrome etching
  - Immerse substrate into chrome etch solution for 2 mins
  - Rinse with water
- Remove photo resist from chrome layer
  - Remove SPR-220-7.0 photo resist with acetone
  - Rinse with isopropanol
- SU-8 attachment layer
  - Dry-bake substrate in oven at 180 °C for 30 mins
  - Spin-coat SU-8 2002 at 1000 rpm onto the chrome side of the substrate
  - Soft-bake SU-8 on hotplate at 95 °C for 10 mins
  - Align the attachment layer mask to the substrate in the mask aligner (Karl Suss MA4), use alignment crosses on mask and chrome layer
  - Expose 65 sec
  - Post-exposure bake on hotplate at 95 °C for 5 mins
- SU-8 channel layer
  - Spin-coat SU-8 2002 at 1000 rpm onto the attachment layer
  - Soft-bake the SU-8 on a hotplate at 95 °C for 10 mins
  - Align the column & channel mask to the substrate in the mask aligner, use alignment marks on mask and chrome layer.

- Expose the SU-8 through the column & channel mask for 65 sec
- Post-exposure bake the substrate on a hotplate at 95 °C for 5 mins
- SU-8 column layer
  - Spin-coat SU-8 2050 at 750 rpm
  - Soft-bake on hotplate at 95 °C for 45 min
  - Spin-coat SU-8 2050 a second time at 750 rpm
  - Soft-bake on hotplate at 95 °C for 17h
  - Expose the SU-8 from the backside through the embedded chrome mask (with the column pattern) for 99 sec
  - Post-exposure bake on hotplate at 95 °C for 5 mins
  - Develop SU-8 until there are no more white streaks when rinsing with isopropanol

### 4.3.3 PDMS film fabrication

PDMS (Sylgard 184) has been prepared by mixing elastomer base and curing agent in volume relation 10:1, followed by degassing with vacuum. The PDMS was spin-coated onto the SU-8 soft-lithography master with 400 rpm for spreading the PDMS and then with 750 rpm for obtaining the correct thickness. The PDMS was cured at 60 °C for 1h. The PDMS was cut on the master to form tiles, each with a StarPoM structure at its center. The tiles were then peeled off with tweezers and remaining PDMS skins over the well and central chamber orifices were removed by sweeping over them with a tweezers end.

### 4.3.4 The aligner

*Note: This section contains a general description of the aligner, its application in the fabrication protocol follows in the next section 4.3.5.*

When combining the PDMS film with the MEA it is important to properly align the features of the PDMS film ( $\mu$ -channels and wells) with the electrodes of the MEA. The electrodes need to be in the correct position within the  $\mu$ -channels for recording and the leads of the electrodes have to be completely covered with PDMS for isolation.

For this reason a custom-built aligner has been fabricated. At its core it consists of two acrylic blocks; one is mounted to a XYZ Stage (Standa 7T38XYZ), the other to a rotation stage (Standa 7R170-2). Together the two stages offer the necessary degrees of freedom for alignment (XY + rotation) and making contact (Z). The aligner is mounted onto a stereo microscope (Nikon SMZ645). The acrylic blocks and the 2" hole in the rotation stage offer the necessary optical transparency to observe the alignment process in the microscope.

PDMS is naturally sticky and the PDMS film will spontaneously stick to the MEA

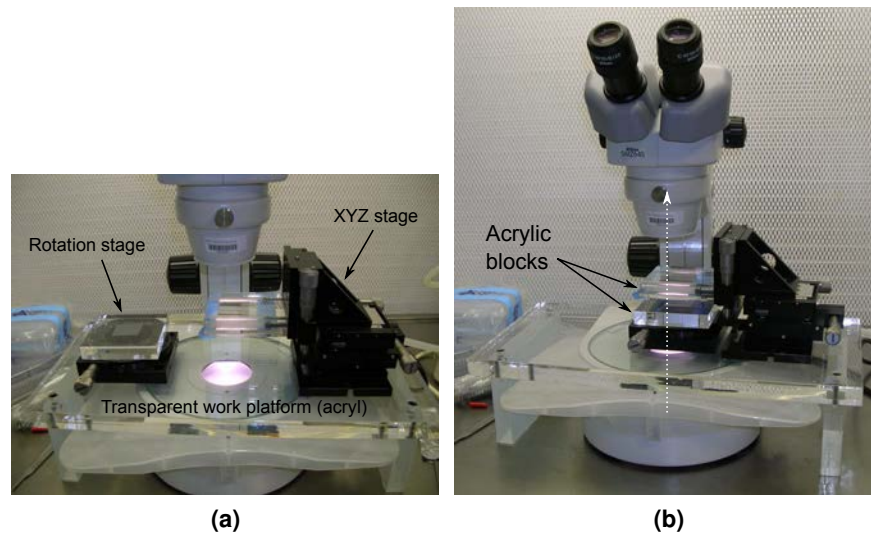


**Figure 4.6:** Aligner setup - parts separated (a), combined (b): A XYZ stage and a rotation stage each hold an acrylic block. Both are placed on top of transparent work platform (acryl) over a stereoscopic microscope. Due to the transparency of the acryl glass and the hole in the center of the rotation stage the alignment process can be optically monitored (dashed white line in (b) shows the optical path).

substrate without the need for further bonding. To facilitate the release process of the PDMS film from its original carrier a method using a piece of transparent foil as intermediate carrier was developed (Fig. 4.7). In this case 125  $\mu\text{m}$  thick Melinex 505/506 foil (Pütz Folien) was used for the carrier film.

Note: Care needs to be taken to avoid static charges on the small piece of plastic foil; else it's difficult to keep it from attaching to a random surface.

#### 4.3.5 Device assembly

The MEA substrate was cleaned 1 h in a UV/ozone cleaner (Bioforce ProCleaner). Then the StarPoM PDMS film was aligned and attached to the MEA using the custom aligner (4.3.4). The PDMS film got extended to also cover the electrode leads (Fig. 4.8). To avoid that fresh PDMS enters the open features (wells and central chamber), they were covered with a thin piece of plastic foil (Melinex 400/401 CW, Pütz Folien). Then the MEA was pressed into a petri dish with a drop of uncured PDMS. The process was monitored under a microscope that was focused on the central features of the StarPoM PDMS film. The pressure was increased until the first air bubbles were about to escape from the wells. At that moment it is necessary to stop the pressure, else air bubbles will leave which will then later be missing to fill the hollow features of the StarPoM => liquid uncured PDMS gets sucked into them and blocks them. The PDMS then got cured 1h at 60 °C. After curing, the petri dish was carefully twisted to detach the PDMS film

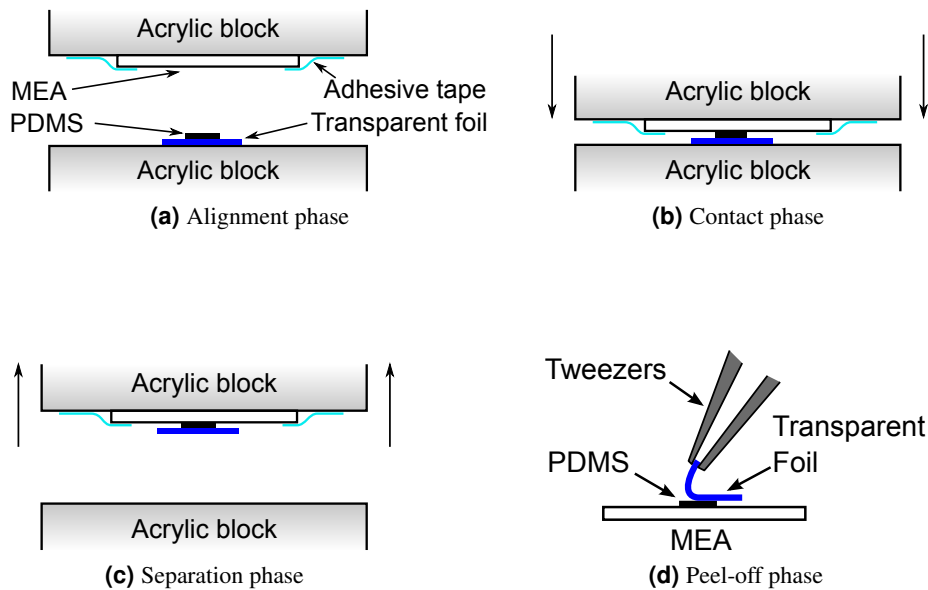


**Figure 4.7:** PDMS film attachment: Due to its stickiness PDMS is difficult to detach from its original carrier during alignment. Here this is solved by placing the PDMS on top of a small piece of transparent foil (a). The foil sticks to the PDMS during contact (b) and separation (c) phase and can later be removed by carefully bending it with tweezers and then peeling it off. As the detachment during peel-off happens only at a limited area the generated force remains below the adhesion force between PDMS and the MEA substrate below => the PDMS film sticks to the MEA. (d).

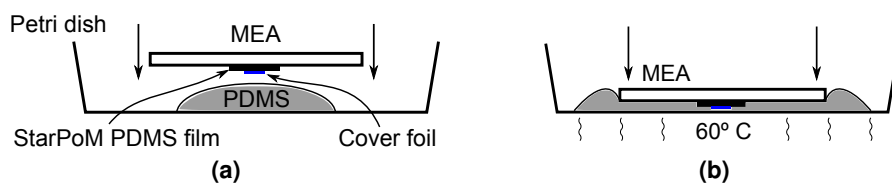


**Figure 4.8:** To extend the PDMS film to also cover the electrode leads on the MEA, the open features of the StarPoM film (wells and central chamber) are covered with a thin foil (a) before pressing the MEA into a petri dish with an uncured PDMS drop. The drop gets squeezed between the petri dish and the MEA and forms a thin film (b). After curing, old and new PDMS form a single film on top of the MEA.



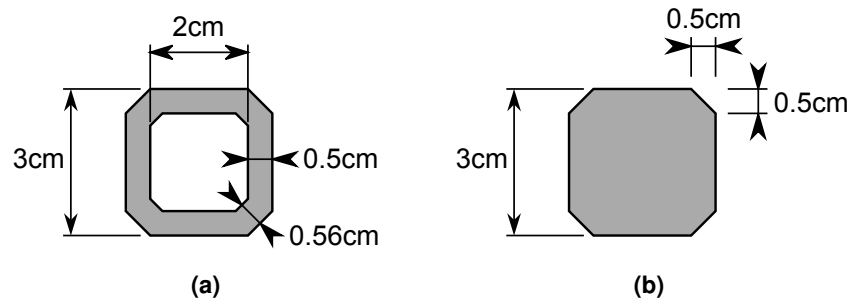


**Figure 4.9:** Dimensions of the PDMS fence (a) and lid (b) used for the StarPoM device. Height of the fence was 7-8mm, thickness of the lid 4mm.

from the bottom of the PDMS dish without detaching it from the MEA substrate. With tweezers the Melinex foil got removed. Two PDMS slabs with 4 mm and 7 mm thickness got cured for 60 min at 65 °C. The 7 mm thick slab was used to cut out the fence of the StarPoM device (Fig. 4.9a) and the 4 mm thick layer was used to cut out the lid of the StarPoM device (Fig. 4.9b). A platinum electrode was punched through the PDMS lid which later acted as ground electrode. The features of the StarPoM PDMS film on the MEA substrate were filled with water (Fig. 4.10). MEA substrates with PDMS film and PDMS ring were then autoclaved to improve biocompatibility (Wang, 2011, Section 6.4.3). After drying all PDMS pieces the fence piece was attached to the PDMS film on the MEA with a drop of uncured PDMS and the "uncured PDMS glue" was cured at 60 °C for 1h. The PDMS film on top of the MEA was then cut to provide co-culture areas (Fig. 4.11) within the fence and to open the contact pads to the amplifier. The StarPoM features were again filled with water using the CO<sub>2</sub> method (Fig. 4.10). The water was exchanged with a 0.1% Poly-L-lysine (PLL) solution. After 13 h the device was rinsed with water.

#### 4.3.6 Cell Culture

Previously, E18 embryonic mice hippocami were dissected and cryopreserved in DMEM (Dulbecco modified Eagle medium) with 10% DMSO as cryoprotectant and with 100 mg/ml streptomycin, 100 units/ml penicillin and 10% horse serum as supplements. At the day of plating the tissue blocks were quickly thawed in a 37 °C water bath and dissociated by gentle pipetting. A drop of 200 µL cell suspension (~ 280,000 cells) was plated into each of the co-culture areas and the cells were given 45 mins to settle. Then additional Neurobasal (supplemented by 2% B27, 1% Glutamate, 10% horse serum and 20 µg/ml gentamicin) was added to connect the co-culture areas with the central StarPoM structure. 200,000 additional cells were plated and stirred in the common cell culture medium to achieve homogeneous distribution. After a short settle time the wells contained from 1 to 3 cells. Finally the device was sealed with the PDMS lid.

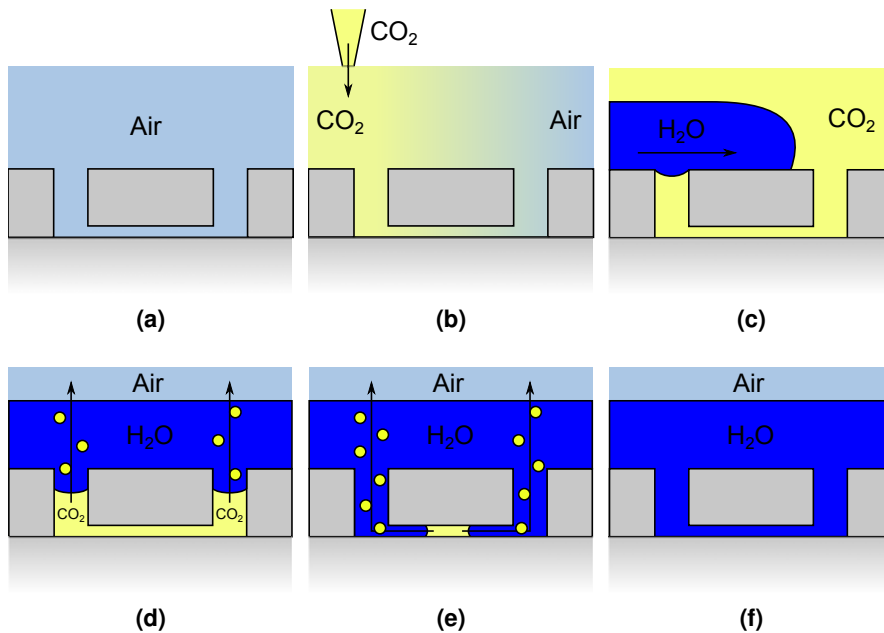


**Figure 4.10:** Method using  $\text{CO}_2$  to fill micro cavities with water: Filling micro cavities is often impeded by the surface tension of water. To overcome this problem the atmosphere in the device is first changed from air (a) to  $\text{CO}_2$  (b). Then the device is submerged into water (c). The  $\text{CO}_2$  in the cavities dissolves into the water and from there back into the surrounding air (d), (e). The shrinking  $\text{CO}_2$  volume creates a vacuum that pulls the water into the cavities (f) in typically < 10 mins.

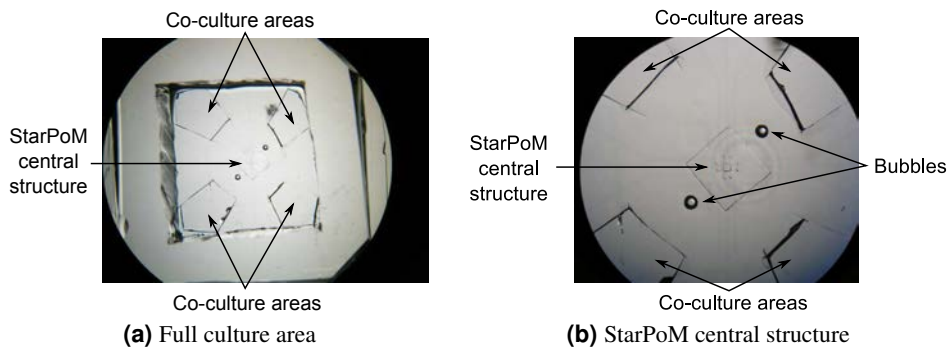


**Figure 4.11:** Co-culture areas of the StarPoM device. Displayed is an early model of the device which was used for fabrication testing and which had a different fence shape. The visible bubbles developed during PDMS film extension and were completely enclosed in the PDMS. Therefore they did not connect the MEA leads with the cell culture chamber.

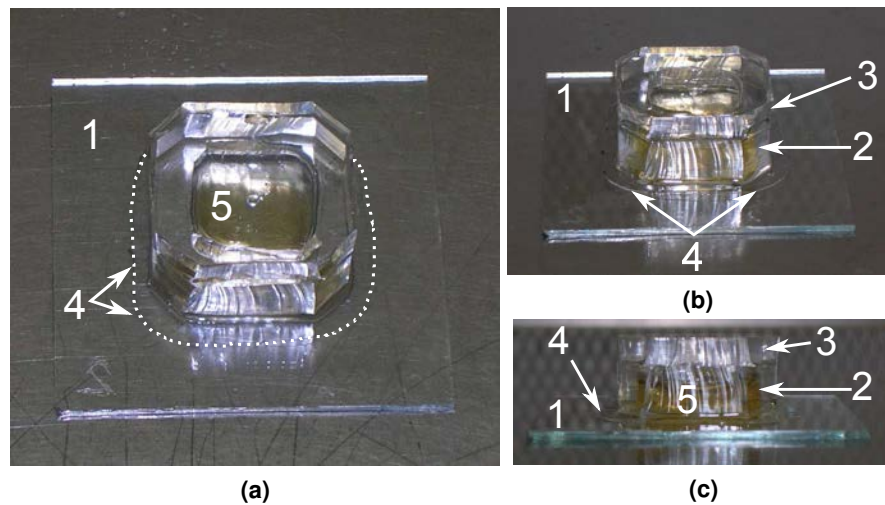


**Figure 4.12:** Final assembly of the StarPoM device. Visible are the 1. MEA, 2. the PDMS fence, 3. PDMS lid, 4. the extended PDMS film that got cut (dotted line) to open the contact pads and 5. in yellow the cell culture medium.

#### 4.3.7 Recording Setup

The recording system consisted of a Multi Channel System MEA 1060-Inv-BC amplifier connected to a Windows-XP PC with a National Instruments NI PCI-6255 data acquisition card. The amplifier was built into an incubator (Heraeus HeraCell 150i), running dry with 5% CO<sub>2</sub> and at 31.5 °C. The additional heat of the amplifying circuit raised the temperature within the culture medium to the required 37 °C. A custom Labview program (developed by Ling Wang) was used to record the signals. The data was stored onto an external 2 TiB hard disk connected via USB. As only 8 channels were recorded the bandwidth of  $8 \times 8 \times 10,000$  bytes/s (channels  $\times$  bytes per sample  $\times$  sampling rate) = 625 KiB/s are well below the effectively available USB bandwidth of  $\sim 28$  MiB/s. The data was stored block wise; each block (367 MiB size) got saved to a separate file in order to limit data loss in case of a power outage.

#### 4.3.8 Recording

Recording was fully unattended. After 4 days and 1 hour it got interrupted by a power outage of 5 hours, 15 minutes. 34 minutes after the power outage a maintenance break of 10 minutes for connecting the recording setup to the secured power grid interrupted the recording a second time. After that the recording continued without further interruptions until the end after 14 days 13 hours. Before and after the recording the osmolarity of the cell culture medium was measured with a Wescor Vapro Osmometer 5520.

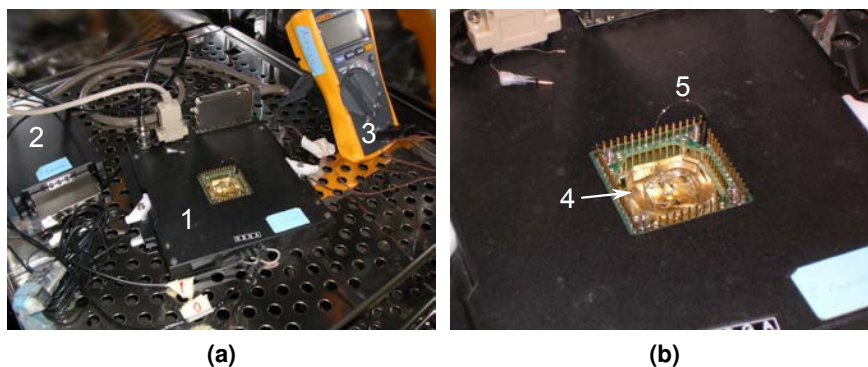


**Figure 4.13:** StarPoM amplifier setup in the incubator during recording: 1. MEA mount and pre-amplifier (MCS MEA 1060-Inv-BC), 2. 2nd amplifier stage (MCS FA60S-BC), 3. Multimeter equipped with temperature sensor, 4. StarPoM device, 5. Platinum electrode protruding the PDMS cover lid, connecting the cell culture medium to the amplifier ground. (b) On the inside of the PDMS lid condensation is visible.

#### 4.3.9 Phase Contrast Images

After recording, phase contrast images have been taken, covering the whole Star-PoM structure. The images were fused to a single image with the panoramic stitching software Hugin.

#### 4.3.10 Data Analysis

Due to the large amount of recorded data, computation performance during analysis is important. Especially the treatment of the time series datasets requires efficient programming tools and algorithms. Therefore the time series analysis has predominantly been implemented in C++, while the handling of smaller and more condensed data, such as spike lists, was done either in python/numpy when the algorithm required to solve vector oriented problems or C++ for element-wise problems.

The following principles outline the general philosophy of software development for the time series analysis:

- Unix philosophy of using small programs operating on files and each solving just a single problem (Raymond, 2003).

As the analysis tool chain for long term continuous recordings is still new and in the prototyping stage, a modular approach has the advantage that various approaches can easily be tested by exchanging the modules. Also as each module (each program) just solves a single task it's easier to reuse the algorithms/implementations in future programs. A downside however, is that saving intermediate results after each processing step requires more storage space on the hard disk than a monolithic analysis program that keeps intermediate results just in main memory.

- Avoid processing data block-wise and use memory mapping and process data out-of-core (Wald, Dietrich, and Slusallek, 2005; W. T. Correa, Klosowski, and Silva, 2003).

The out-of-core approach has been chosen as it simplifies the main loop of the program and because 64 bit operating systems and memory mapping are now common even for standard PCs. While the main section of a block oriented program contains two loops - one iterating over all the blocks and one iterating over the data points in each block - a memory mapped out-of-core program only contains one loop iterating over all data points from the beginning of the dataset to the end. Error prone lead-in/lead-out code to transfer state information from one block to the next - for example for filters - can be avoided, likewise special treatment for the last, possibly partially filled block. Finally, most operating systems automatically optimize performance for linear memory mapped I/O by issuing asynchronous read-ahead commands to preload new data parallel to processing. This way the processing thread receives new data with minimal latency and the practical throughput gets close to the maximum throughput of the hard disk.

- Use low-level C++ algorithms instead of high-level vector oriented programming paradigms.

Vector oriented programming environments such as matlab or numpy/python exhibit several problems when combined with a out-of-core memory mapped approach. While they provide functions to access memory mapped files as vectors or matrices, many of their vector operations are not yet prepared to work with objects larger than main memory (usually because they try to create internal working copies of the data objects in main memory). To avoid these problems, data can either be processed blockwise which leads again to the aforementioned problems with block setup (lead-in/lead-out code), or algorithms are used that access the data element-wise. But element-wise access in matlab or python/numpy is very slow.

Therefore, low-level C++ algorithms are a better match for the out-of-core principle, as they do not impose design limits on the algorithm and allow iterating element-wise over data without performance penalty. This freedom of algorithm design can be used to

- ensure that the data is accessed in a linear fashion to match the optimal hard disk access pattern
- consume less memory in comparison to vector oriented algorithms that often have to store intermediate results in temporary vectors/matrices
- reduce instruction count in situations of inter-data if-then-else cases (execute instructions on data points depending on a if-then-else condition of neighboring data points)

For illustration the base C++ code frame that has been commonly used for the analysis tools is shown in listing 2.

In the following section a chronological protocol of the data analysis is given with a description of the individual analysis steps.

#### 4.3.11 De-Interleaving and concatenation

During recording, data was saved in blocks of 367 MiB size. Each of these blocks contained interleaved data from the 8 channels. To simplify analysis, the data was de-interleaved and concatenated, so that in the end 8 files remained, each containing just one channel and spanning the entire duration of the recording.

#### 4.3.12 Visual Inspection with O1Plot

Throughout the analysis the time series data was visually inspected with `O1Plot` (Chapter 3) to obtain an overview of the data, to decide further analysis steps and to verify the results of previous data processing steps (especially for filtering), e.g. in figures 4.14, 4.15, 4.16, 4.27, 4.33.

#### 4.3.13 Common Signal Elimination

To eliminate distortions in the data that are common to all channels (probably because they originated from the ground electrode) a common signal elimination was performed. The common signal was obtained by calculating for each time point the mean sample value of the 8 channels, but excluding the two channels with the biggest deviation from the mean value. Excluding the two channels ensures that regular spike shapes do not get included into the mean value and only signals that are present in at least 6 channels contribute to the common signal. The common signal was then subtracted from the original signal (see Fig. 4.14).

#### 4.3.14 Channel 6 Artifact Elimination

Channel 6 showed artifacts of sudden positive pulses followed by exponential decay. To exclude them from further processing they were identified with a "sign streak filter" and then wiped clean.

The sign streak filter works by identifying streaks of samples with the same sign. The sample values of each streak are summed up and the sum is tested against a threshold (here the threshold was set to 10). If it surpasses the threshold, the streak is added to the result interval list.

The resulting interval list is then used to "wipe" the intervals - the intervals are replaced by an interpolated line between the data points at the begin and end of the interval. In this case, as the intervals are sign streaks, the begin and end points will have values close to zero and the interpolated interval will be a flat line almost at zero value.

```

#include <iostream>
#include <fstream>
#include <boost/iostreams/device/mapped_file.hpp>
#include <boost/program_options.hpp>

using namespace std;
namespace po = boost::program_options;
namespace bio = boost::iostreams;

int main( int argc, char** argv )
{
    // parse program options for example with boost::program_options
    ...

    // open files and memory map them
    ...
    // example for an input file
    bio::mapped_file inMap( inFile, ios_base::in | ios_base::binary );
    // memory map file
    double* inPtr = (double*) inMap.const_data();

    // example for an output file
    bio::mapped_file_params outParams;
    outParams.path = outFile;
    outParams.mode = ios_base::in | ios_base::out | ios_base::binary;
    // set the output file size to the input file size
    outParams.new_file_size = inMap.size();
    bio::mapped_file outMap( outParams );
    // memory map file
    double* outPtr = (double*) outMap.data();

    // main loop
    size_t maxIdx = inMap.size() / sizeof(double);
    for( size_t idx = 0; idx < maxIdx; idx++ )
    {
        ... // specific algorithm of the analysis tool
        // identity example
        outPtr[idx] = inPtr[idx];
    }

    // close files
    outPtr = NULL;
    inPtr = NULL;
    outMap.close();
    inMap.close();

    return 0;
}

```

**Listing 2:** C++ code frame for the out-of-core processing tools used during the data analysis. After the setup phase (program option parsing, opening and mapping files) the algorithm can access in and output files as simple C++ arrays and with high performance. The actual analysis algorithm would replace the copy statement `outPtr[idx] = inPtr[idx];` in the main loop of the code frame.

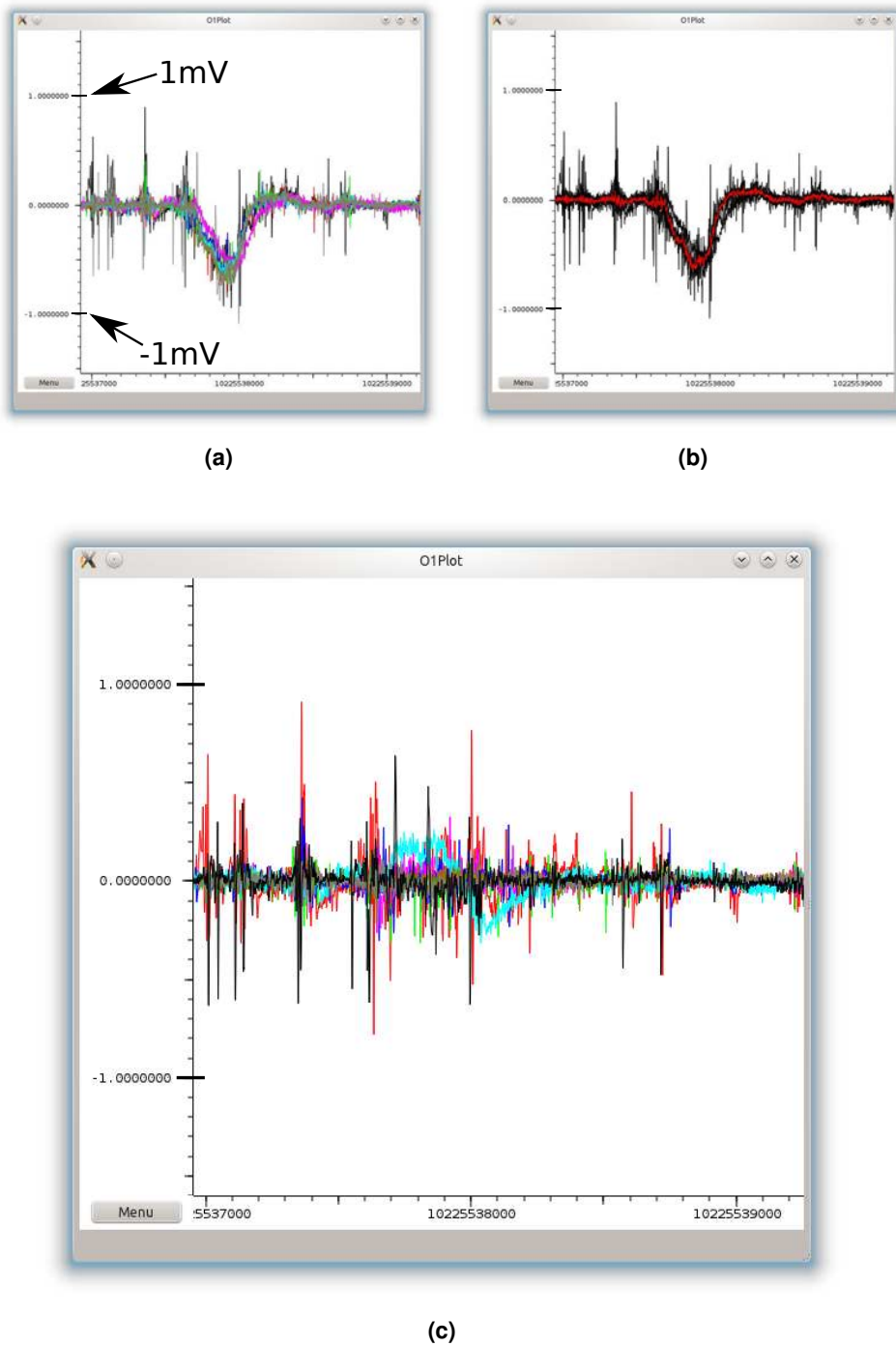


**Figure 4.14:** Elimination of artifacts common to all channels (a): A mean signal is calculated for the artifact cancellation, shown red in (b). The exclusion of the two channels with the most extreme values (see main text) assures that no spikes are included into the mean signal. After subtracting the mean signal from the original channels the common artifact is largely suppressed while the superimposed spikes remain intact (c). Channel 4 (light blue) still shows its own, individual base line drift. The longer tick marks on the y-axis each mark +1mV or -1mV.



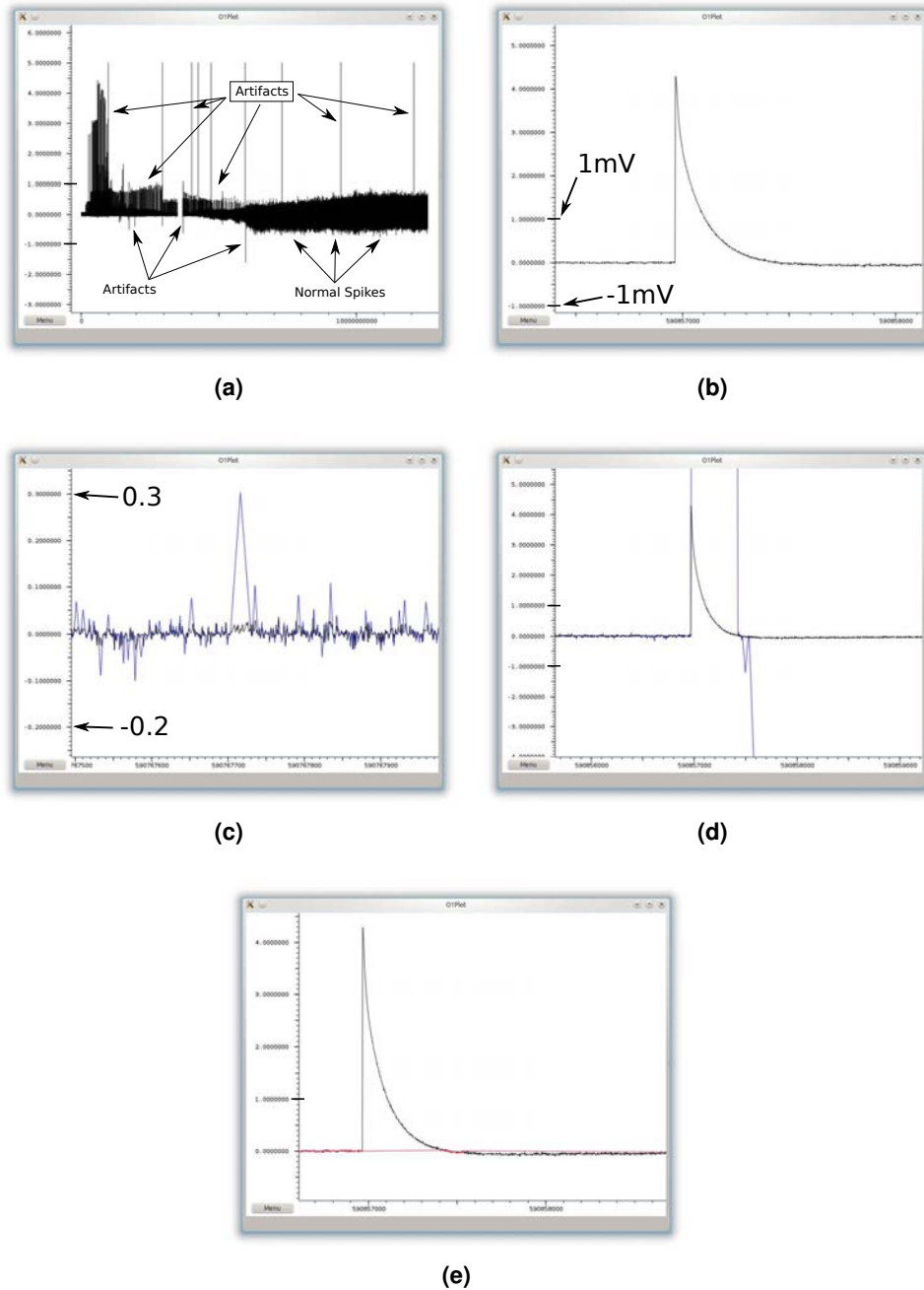


**Figure 4.15:** Elimination of Channel 6 Exponential Artifacts. The neuronal signals in channel 6 are superimposed with artifacts (a). The artifacts have exponential decaying shape (b). The effect of the sign streak filter is shown in (c); y-values are a score value without units. Each triangular edge of the blue line represents a streak of values without zero crossing. The maximum amplitude of the triangles corresponds to the sum of all values in the streak. When applied to the exponential artifacts the sign streak filter generates huge values (d). This allows to identify and blank the artifacts for further processing (red line in (e)). The elongated ticks on the y-axis correspond to the +1mV and -1mV values.

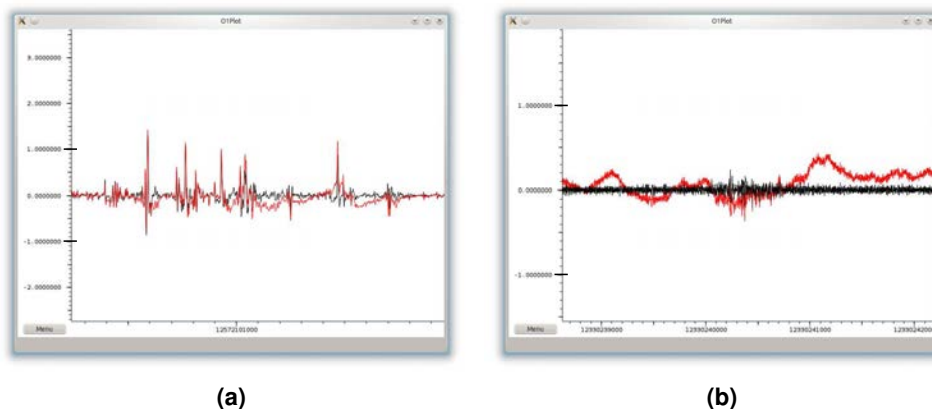


**Figure 4.16:** Examples for Wavelet Filtering of time series data. The original time series data (red) shows base line drift in between the spikes (a), channel 4 showed a non spike related base line drift throughout the recording (b). In the filtered time series data (black, in both figures) the base line drift is eliminated while maintaining to a large extend the shape and amplitude of the main spikes. The enlarged y-axis ticks represent +1mV or -1mV.

#### 4.3.15 Base line drift Elimination (Wavelet Filter)

Most channels showed base line drifts in the vicinity of large spikes or bursts. channel 4 furthermore showed large base line drifts over long periods of time (probably related to the bubbles on the electrodes, Fig. 4.26). To eliminate these base line drifts a wavelet filter was used with the Daubechies 4 wavelet, level 5. The used filter is based on a previous implementation (Wiltchko, Gage, and Berke, 2008) but extended to make use of multi-threading for performance enhancement.

#### 4.3.16 Spike Detection

Spike detection has been performed with a heuristic algorithm which performs a number of tests at each sample position of the recording to determine if the sample position is accepted as the position of a spike. In principle it is a threshold spike detection method that has been extended to avoid spike detection in bursts. It does so by ensuring that in front and back of the main spike (shoulder sections) there are no further signals with large amplitudes.

For performance reasons the algorithm was implemented in C++. Also, if one of the tests in the chain fails, the algorithm immediately continues with the next sample position, bypassing the rest of the tests.

The tests are (see also Fig 4.17):

- The sample value is tested against a user provided threshold. If the absolute value of the sample is bigger than the threshold, the test is passed.
- The sample has to be a local maximum, i.e. the sample before and the sample

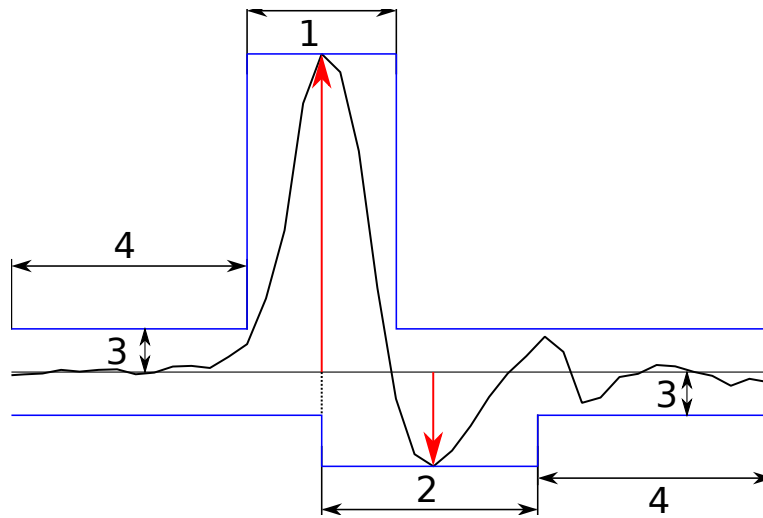


**Figure 4.17:** Spike detection heuristics: Several conditions have to be met to accept a spike: 1. The sample under test must surpass a given threshold and be a local maximum. 2. In a window of given length starting with the sample under test, the maximum of the second spike phase is searched. 3. The bigger maximum of first and second phase is chosen and multiplied with a given ratio to get the height of the shoulder sections. 4. If the waveform remains within the shoulder section envelope (length of the shoulder sections is given by the user) the waveform is accepted as a valid spike.

after need to have a smaller amplitude than the sample under test.

- The waveform has to fit into the boundaries of the shoulder envelopes. To calculate the shoulder envelopes:
  - The maximum amplitude of the second phase of the spike is determined. For this the section starting with the sample position of the sample under test and with user provided length is searched for the maximum value of opposing sign to the first phase maximum.
  - The maximum amplitude of first and second phase is determined and user provided shoulder ratio parameter determines the height of the shoulder sections in relation to the maximum spike amplitude.
  - The length of the shoulder sections is user provided.

The waveform within the shoulder area is tested sample by sample whether it stays in the envelope boundaries. If this final test is passed the current sample position is marked as the position of a valid spike.

The used parameters for spike detection were:

The detection threshold parameter was set manually depending on the noise level of the individual channels to values ranging from 0.055 to 0.19V (Table 4.1). The rest of the parameters were the same for all channels:

- The window width for the first spike phase was set to 8 samples ( $\cong 0.8$  ms).

Channel	0	1	2	3	4	5	6	7
Threshold in Volt	0.07	0.06	0.06	0.06	0.19	0.055	0.07	0.08

**Table 4.1:** Threshold values used for the spike detection

- The window width for the second spike phase was set to 12 samples ( $\cong 1.2$  ms).
- The shoulder lengths were set to 8 samples each ( $\cong 0.8$  ms).
- The shoulder ratios were set to 0.5, meaning that the waveform within the shoulder sections can only have half the amplitude of the main spike section.
- For each detected spike an interval with a width of 20 samples ( $\cong 2.0$  ms), from spike position -7 to spike position + 13, is generated and appended to the result interval list.

#### 4.3.17 Elimination of Overlapping Spikes

Despite the shoulder envelope tests that should eliminate triple phase signals, the spike detection can still generate overlapping spikes, for example when the first spike is superimposed with noise that creates a double peak.

For these cases the spike detection is followed by an overlapped spike filter. It searches for overlapping intervals, and then chooses the "bigger" spike. The "size" of the spike is determined by adding the amplitudes at position 7 and 16 in the spike interval, the positions where the maxima of the two spike phases are expected.

#### 4.3.18 Fine-tuning Spike Position

Due to construction, the spike intervals are initially centered on the first phase maximum at position 7. The fine-tuning step refines this position by using the half-height criteria. The positions on the flanks of the spike are searched that have half the height of the spike maximum. Then the spike gets re-centered between these two points. This fine-tuning improves in some cases spike sweep alignment because it's less susceptible to superimposed noise.

#### 4.3.19 Sweep Cutting

All spike intervals (sweeps, with a length of 20 samples  $\cong 2.0$  ms) are extracted from the time series file and stored into a new file. This supports the next step, the spike sorting, by compacting the necessary data, thereby speeding up access times and also reducing memory consumption.

#### 4.3.20 K-Means Spike Sorting

Spikes were sorted with the k-means algorithm which was chosen for its low memory requirements and quick performance. The compacted file with the sweeps

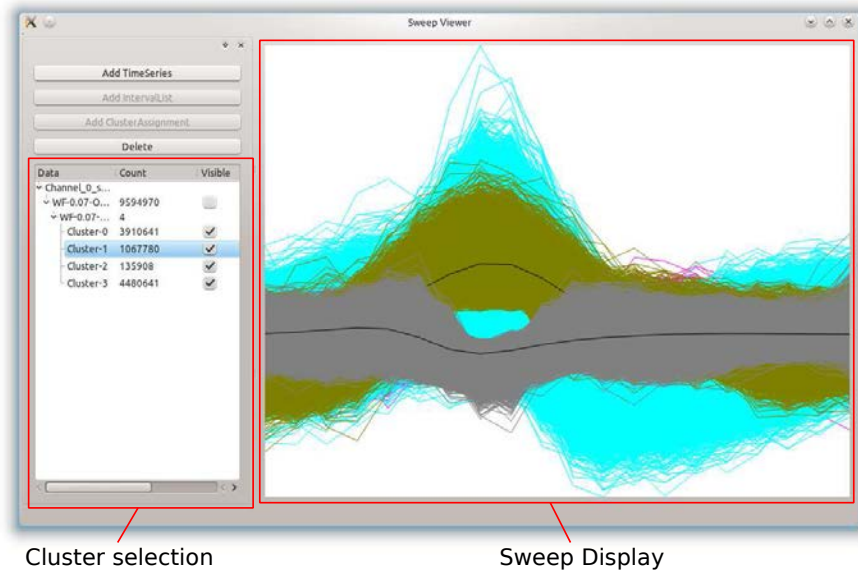


**Figure 4.18:** Screenshot of the Sweep Viewer program. In the left section the user can select the time series dataset, the corresponding spike list and clustering, in the right section the sweeps are superimposed with different colors and average line.

helped to maintain all sweeps in main memory (8 GiB) to avoid paging. Each sweep was fed directly into the k-means algorithm as a 20 element vector observation. The chosen mlpy implementation (Albanese, Visintainer, Merler, Riccadonna, Jurman, and Furlanello, 2012) can set the seed of the random number generator. This allows to deterministically repeated the clustering which helps to compare the results when testing various parameters and methods.

The number of clusters was always set to 10. After k-means clustering the clusters were visualized in a custom cluster viewer and were manually joined where necessary. Manual joining was performed

- when the two clusters were visually similar enough to be considered identical.
- when the two clusters were identical but shifted due to misalignment. Misaligned clusters are caused by the spike detection in combination with spikes that have a small first phase and a bigger second phase. If the first phase surpasses the detection threshold (see section 4.3.16, first test), the spike interval will be centered around the first spike phase. If the first phase remains below the detection threshold the spike interval will be centered around the second spike phase. If a cluster contains spikes with first phases above and below the threshold, the cluster will get separated by misalignment.

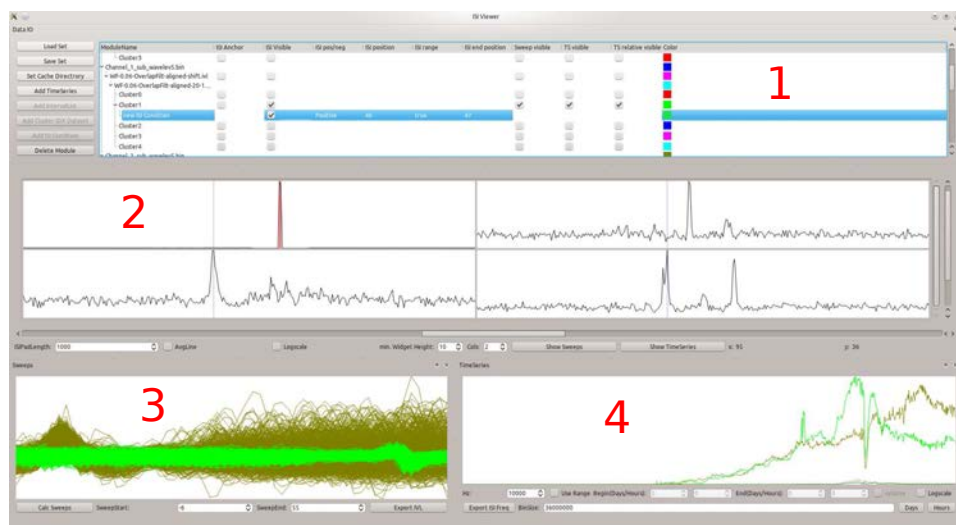


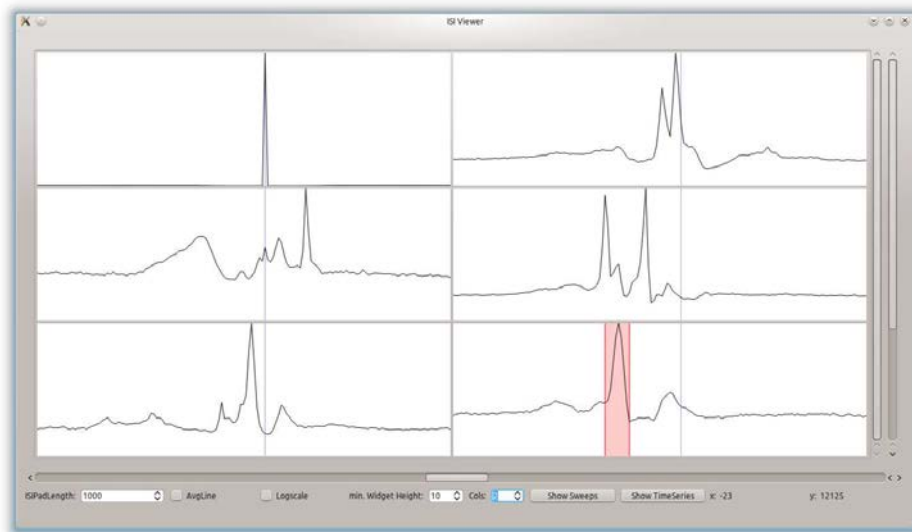
**Figure 4.19:** Screenshot of the ISI Viewer program. In section 1 data sources are managed: time series datasets, spike lists, cluster groups, spike lists of individual clusters and ISI conditions. Data sources can be added, removed, related (e.g. clustering of a spike list which **corresponds** to a time series dataset) and data sources can be selected for the different visualization options below. In section 2 multiple ISI histograms can be displayed. The histograms can be zoomed, scrolled and arranged in multi-column layout (two column format is shown in the example). Section 3 is for displaying sweeps to verify ISI relations in the time series domain. Section 4 shows the development of spike frequency over time.

#### 4.3.21 ISI Analysis

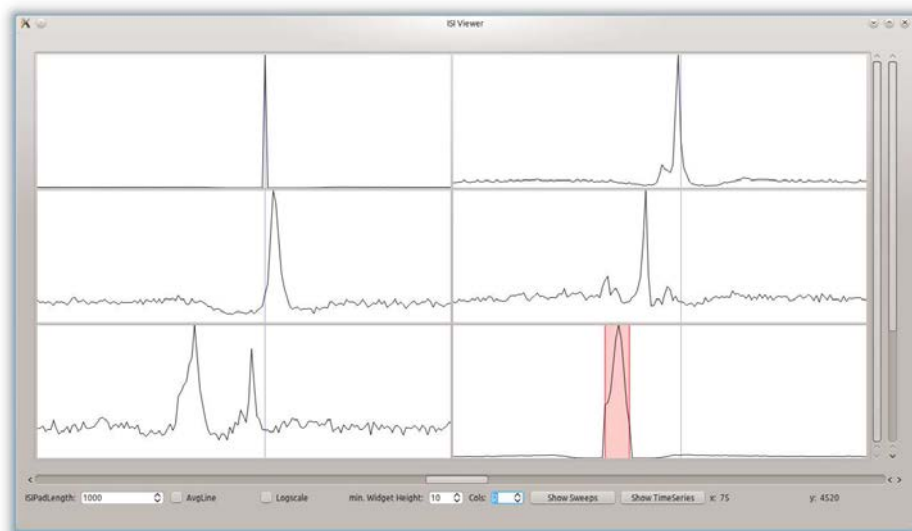
For the ISI (Inter Spike Interval) analysis a GUI-based visualization program has been developed. It can operate on several spike lists simultaneously. One spike list is selected as the anchor list. All ISIs are relative to the spikes of the anchor list. The ISI histograms are calculated both into the past and into the future. Multiple ISI histograms can be displayed at once. Extra conditions can be defined, which either ensure or disallow spikes in a defined spike list range (Fig. 4.20). Further functions are:

- display of sweeps for ISI constellations
- a time course display of ISI frequency
- the possibility to limit the ISI calculation to a time range

The program was realized in C++, using Qt for the GUI. The used algorithms are canonical, but have been performance optimized by efficient programming in the main loop (inlining function calls and avoiding pointer dereferentiations) and by caching ISI and sweep results on disk.



(a)



(b)

**Figure 4.20:** ISI condition example: Both figures (a) and (b) show the same spike clusters. Top left is the anchor cluster C0C3 (channel 0, cluster 3) with its steep auto-correlation spike at 0. Cluster C7C3 on the bottom right contains a red ISI condition section. In (a) the condition is *not* active and all ISI histograms show the normal correlation of their spike clusters to the anchor cluster. In (b) the condition is active, which means that spikes only contribute to the ISI histograms if there also is a spike in C7C3 within the red section. The displayed histograms C2C4 (top right), C2C5, C3C0, C5C2 (bottom left) show noticeable differences under the influence of the conditions, which could be used to analyze the connectivity between the neurons in the device.

## 4.4 Results

### 4.4.1 Fabrication results

Fabrication results for the SU-8 soft-lithography master are shown in Fig. 4.21 and results for the fabricated PDMS film (using the SU-8 master) are shown in Fig. 4.22. The features of the masks (Fig. 4.1) are all present. The  $\mu$ -channels however are wider than specified by the mask ( $\sim 23 \mu\text{m}$  instead of  $16 \mu\text{m}$ ) and the side walls are suffering from an uneven surface. Both can be attributed to the use of low resolution foil masks. Still, the fabricated PDMS films are functional.

Thanks to the tweezers wipe trick all wells were reliably freed from the PDMS skin (Fig. 4.22e).

### 4.4.2 Phase contrast image of the device with cells

In Fig. 4.23 a stitched phase contrast image of the StarPoM device after the recording is shown. A dense layer of neurons, neurites and glial cells has developed in the main chamber (see also Fig. 4.24 for a magnification).

The quality of the phase contrast microscopy in the small wells was affected by the proximity of the vertical walls of the wells, therefore judging the cell density is difficult.

In the magnification of the center chamber a neurite bridge can be seen connecting the neuron population in the chamber with the neuron population on top of the PDMS film (Fig. 4.24, 4.25).

An apparent defect of the device is shown magnified in Fig. 4.26, bubbles formed between the ITO electrodes and the PDMS film. They didn't extend visibly into the  $\mu$ -channels but are close enough for potential interaction, e.g. gas exchange between bubbles and medium in the channels. Interestingly, the two affected recording channels, 4 and 6, were superimposed with artifacts and noise (see section 4.5.2).

### 4.4.3 Osmolarity measurements results

The osmolarity in the cell culture medium increased during the 14 days from 223 mmol/kg to 291 mmol/kg, which indicates that  $\sim 25\%$  of the water in the medium evaporated through the PDMS walls.

### 4.4.4 Data analysis results

#### *Recorded data*

Recording lasted 14 days, 13 hours, 24 minutes and 3 seconds or 12,578,436,014 samples (10kHz sampling rate). Each of the 8 channels was finally saved to a separate file with 94GiB (samples were saved in 8 byte double format).



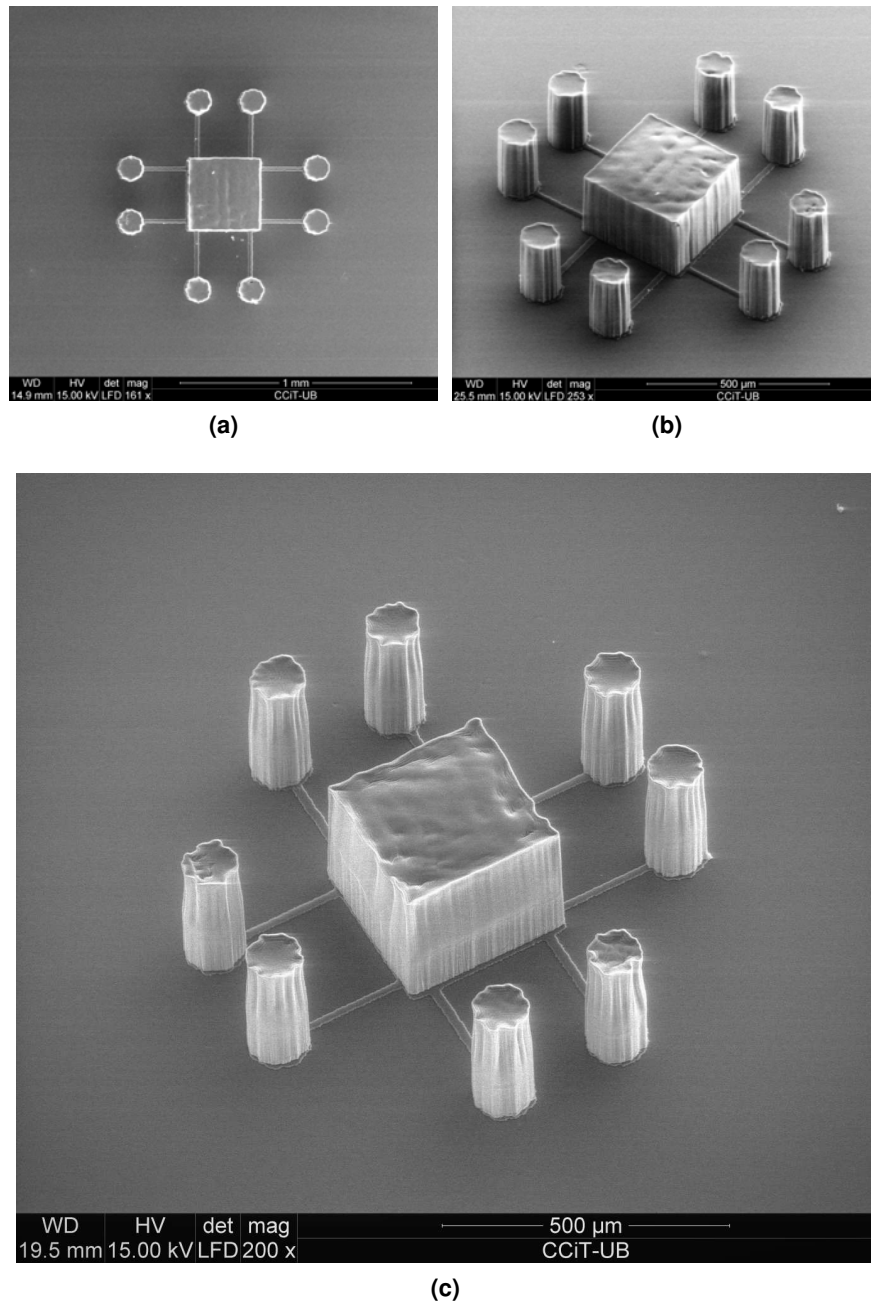


**Figure 4.21:** SEM images of the StarPoM SU-8 soft-lithography master. (a) view from top, (b) perspective view, (c) high dynamic range (HDR) composition of two SEM images for better contrast. The channel layer and the column layer have a slight offset and imperfections (rough side walls) due to low-resolution masks are visible.

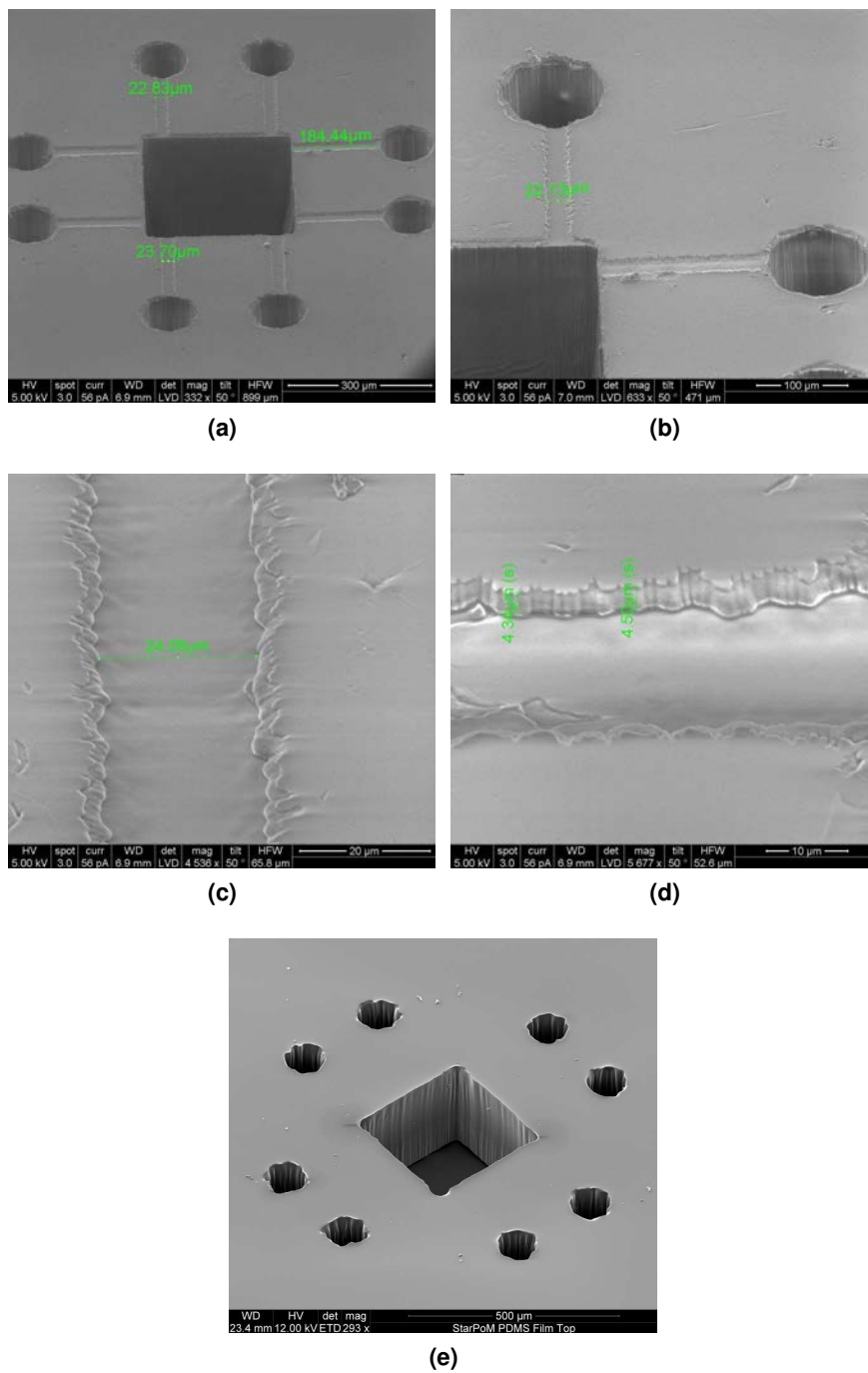


**Figure 4.22:** SEM images of the StarPoM PDMS film. (a) - (d) Images of the bottom side of the PDMS film with the  $\mu$ -channels. (e) Top side of the PDMS film.

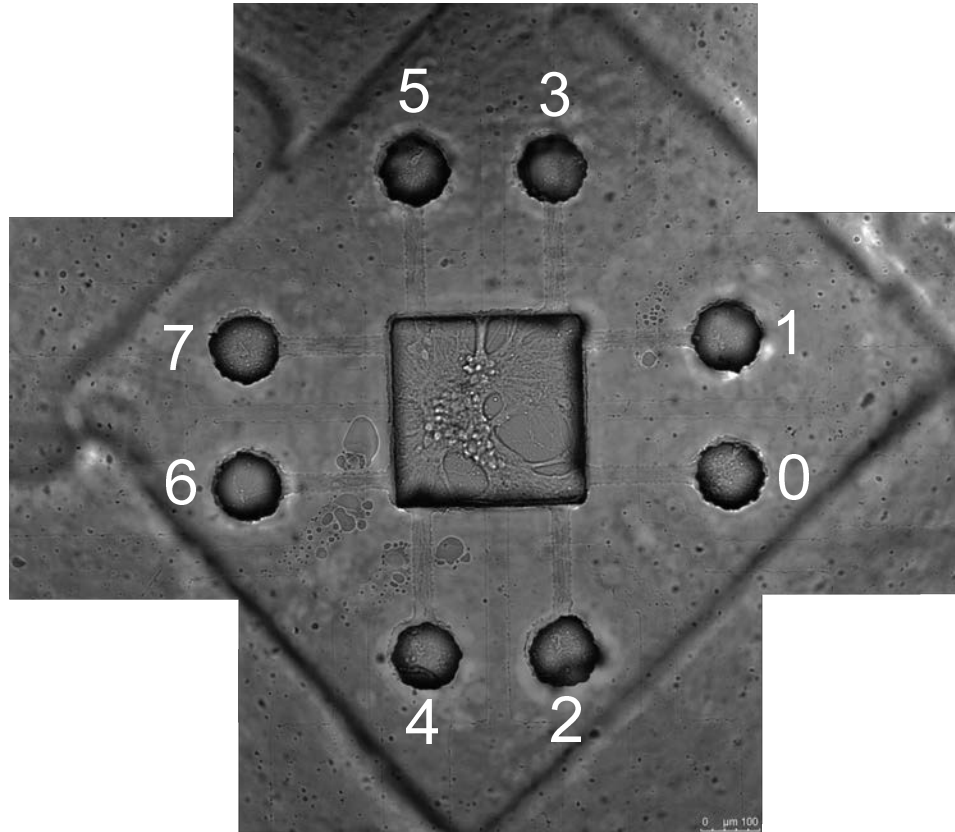


**Figure 4.23:** Phase contrast image of the StarPoM device after the long term recording. The numbers in white indicate the recording channel number. On channels 1, 4 and 6 apparently bubbles developed between the ITO-electrodes and the PDMS isolation, that may explain the observed artifacts on these channels.

The diagonal features are artifacts of the fabrication described in Fig. 4.8. A thin piece of foil was used to cover the central chamber and wells during the extension of the PDMS film, the artifacts are the negative imprint of the foil shape. The attached round shape to the top left is the remnant of a bubble that formed at the same time during PDMS curing; to the best knowledge it had no influence on the functioning of the device.

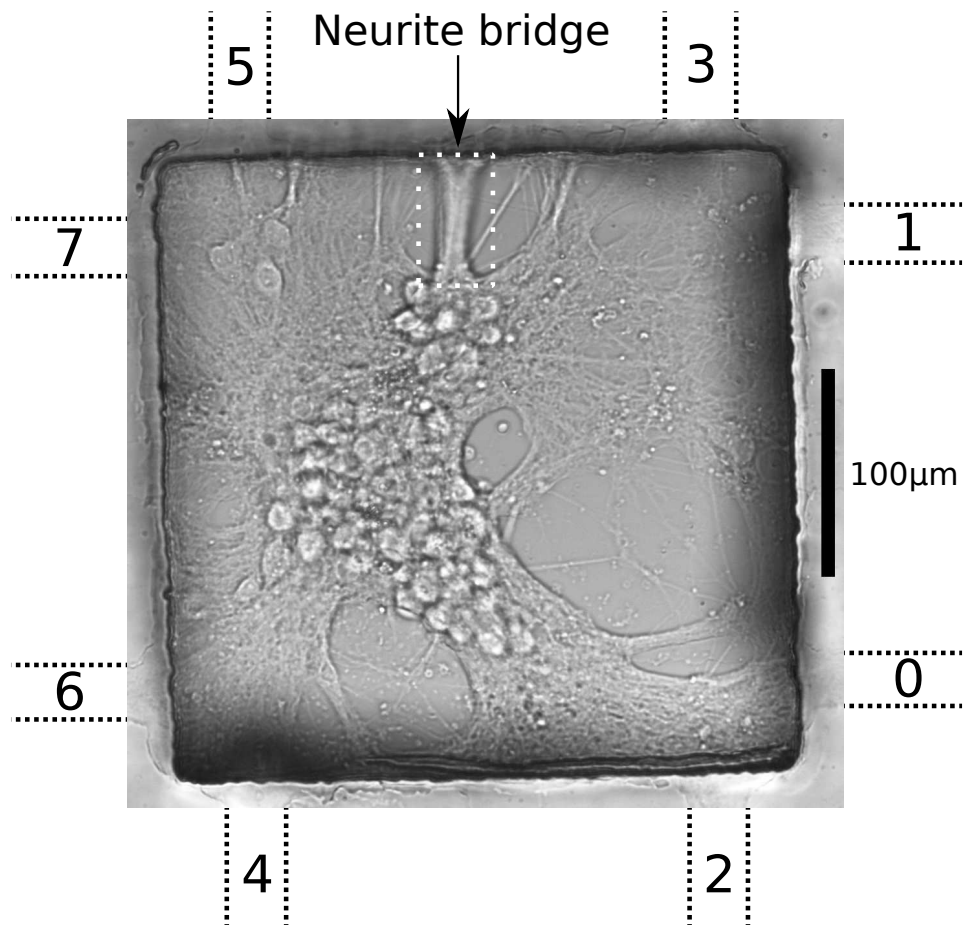


**Figure 4.24:** Phase contrast image of the center section of the StarPoM device after the long term recording. Several somas are visible and a dense layer of neurites and glial cells. The position of the  $\mu$ -channels are indicated by the dotted lines on the border with the corresponding number. A neurite bridge from the neurons in the central chamber to the neurons on top of the PDMS film is marked within the dotted area.

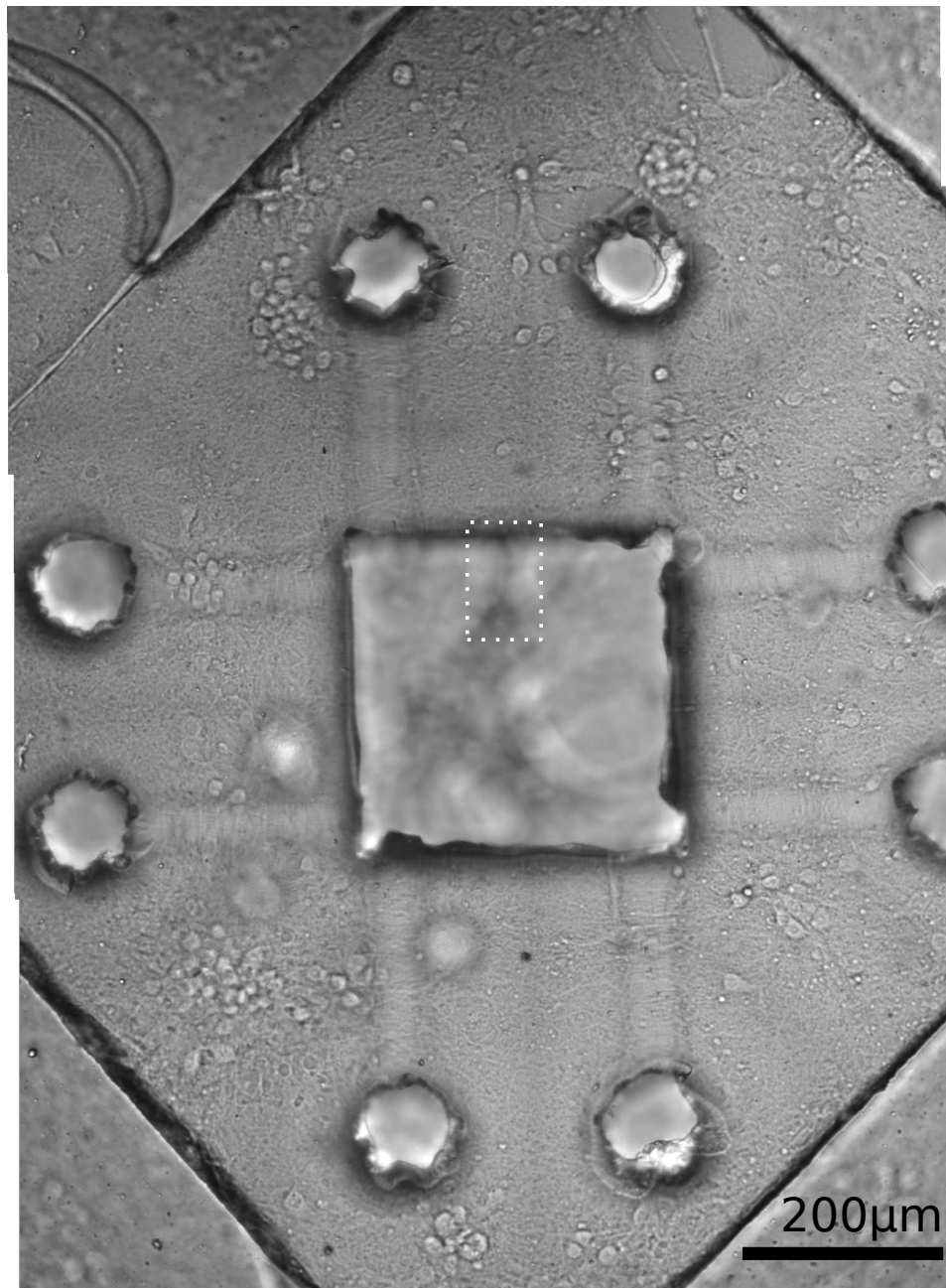


**Figure 4.25:** Phase contrast image of the PDMS surface of the StarPoM device after the long term recording. A dense layer of neurites and several somas are visible. In the dotted area a neurite bridge leads into the central chamber.

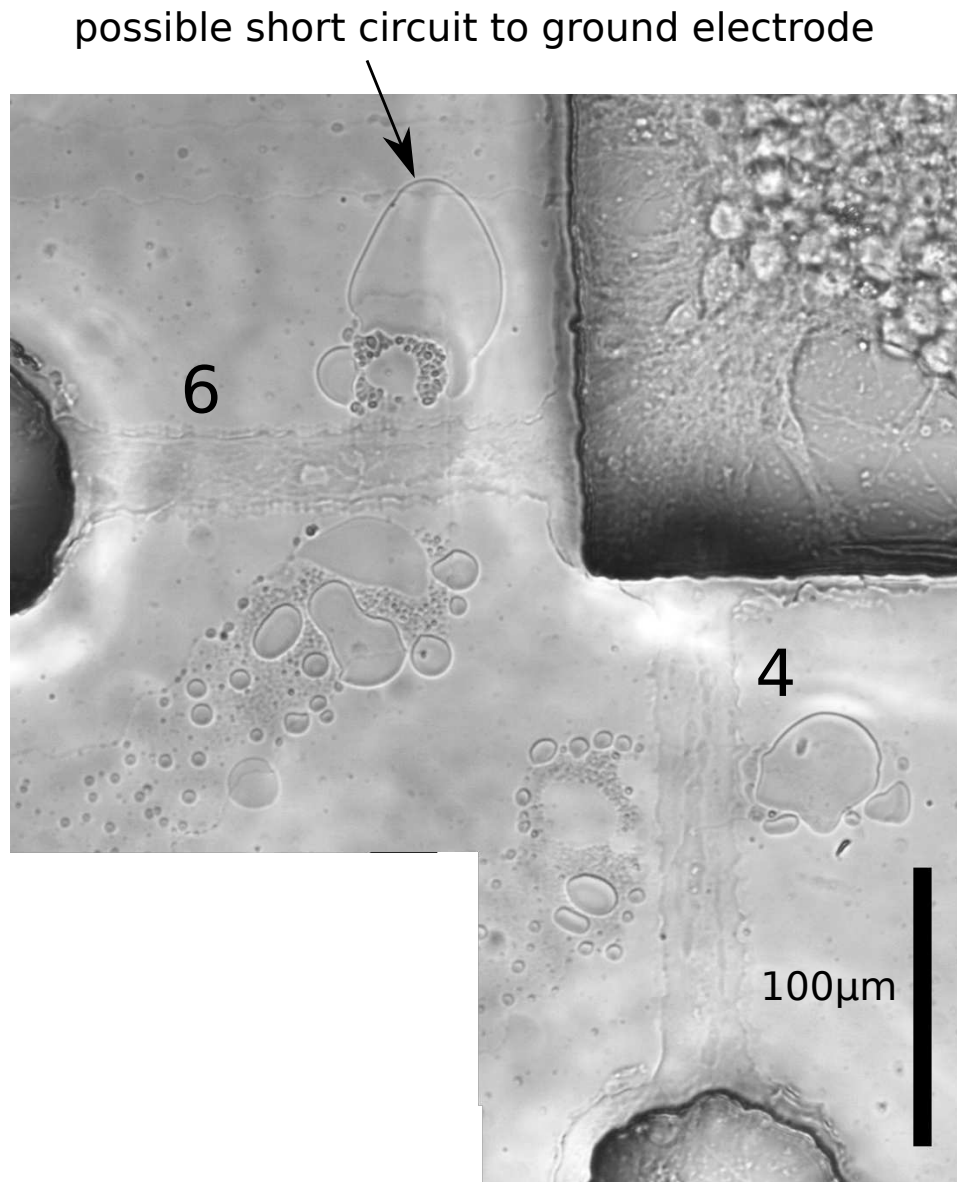


**Figure 4.26:** Phase contrast image of the bubbles in the StarPoM device after the long term recording. The bubbles develop on top of the recording electrodes of  $\mu$ -channels 4 and 6 under the PDMS but don't seem to extend into the medium of the  $\mu$ -channels.

### *Noise*

The noise levels were determined as average absolute deviation and standard deviation (see Tables 4.2). Where the noise level has been measured over time it remained mostly stable. The filtering operations always reduced the noise, which is to be expected. Channel 4 exhibits exceptionally high noise levels due to its base line drift.

### *Time series visualization*

Long-term time series visualization with `OlPlot` allowed to inspect the entire 14 days (Fig. 4.27). Starting on day 4 and 5 the first signals become visible and then gradually increase in amplitude. While the increase seems to slow down in the last days, the amplitude development on several channels still goes on until day 14.

channel	full recording		signal free sections			
	raw	filtered	raw		filtered	
			begin	end	begin	end
0	0.0144 V	0.0108 V	0.0089 V	0.0105 V	0.0075 V	0.0082 V
1	0.0091 V	0.0068 V	0.0094 V	0.0080 V	0.0070 V	0.0060 V
2	0.0117 V	0.0083 V	0.0107 V	0.0116 V	0.0071 V	0.0085 V
3	0.0116 V	0.0080 V	0.0107 V	0.0111 V	0.0063 V	0.0082 V
4	0.0319 V	0.0166 V	0.0174 V	0.0701 V	0.0129 V	0.0177 V
5	0.0095 V	0.0083 V	0.0093 V	0.0090 V	0.0064 V	0.0081 V
6	0.0090 V	0.0081 V	0.0083 V	0.0078 V	0.0073 V	0.0071 V
7	0.0117 V	0.0110 V	0.0088 V	0.0094 V	0.0079 V	0.0086 V

(a) Noise estimation using Average Absolute Deviation

channel	full recording		signal free sections			
	raw	filtered	raw		filtered	
			begin	end	begin	end
0	0.0339 V	0.0276 V	0.0111 V	0.0134 V	0.0099 V	0.0107 V
1	0.0130 V	0.0108 V	0.0118 V	0.0100 V	0.0092 V	0.0078 V
2	0.0175 V	0.0139 V	0.0134 V	0.0147 V	0.0094 V	0.0112 V
3	0.0162 V	0.0124 V	0.0134 V	0.0140 V	0.0083 V	0.0107 V
4	0.0507 V	0.0218 V	0.0224 V	0.0968 V	0.0171 V	0.0223 V
5	0.0128 V	0.0118 V	0.0116 V	0.0113 V	0.0084 V	0.0106 V
6	0.0134 V	0.0124 V	0.0104 V	0.0098 V	0.0096 V	0.0093 V
7	0.0248 V	0.0246 V	0.0110 V	0.0119 V	0.0106 V	0.0114 V

(b) Standard Deviation Noise Estimation

**Table 4.2:** Noise values using average absolute deviation (a) and standard deviation (b): In **full recording** the average absolute deviation is calculated for the entire recording including spikes and bursts. In **signal free sections** without spikes or bursts have been manually selected for the average absolute deviation calculation. The **raw** columns contain the data from the original recordings, the **filtered** columns contain the data after filtering and artifact elimination. The signal free sections are split between sections that have been selected in the beginning (**begin**) and at the **end** of the 14 recording days.



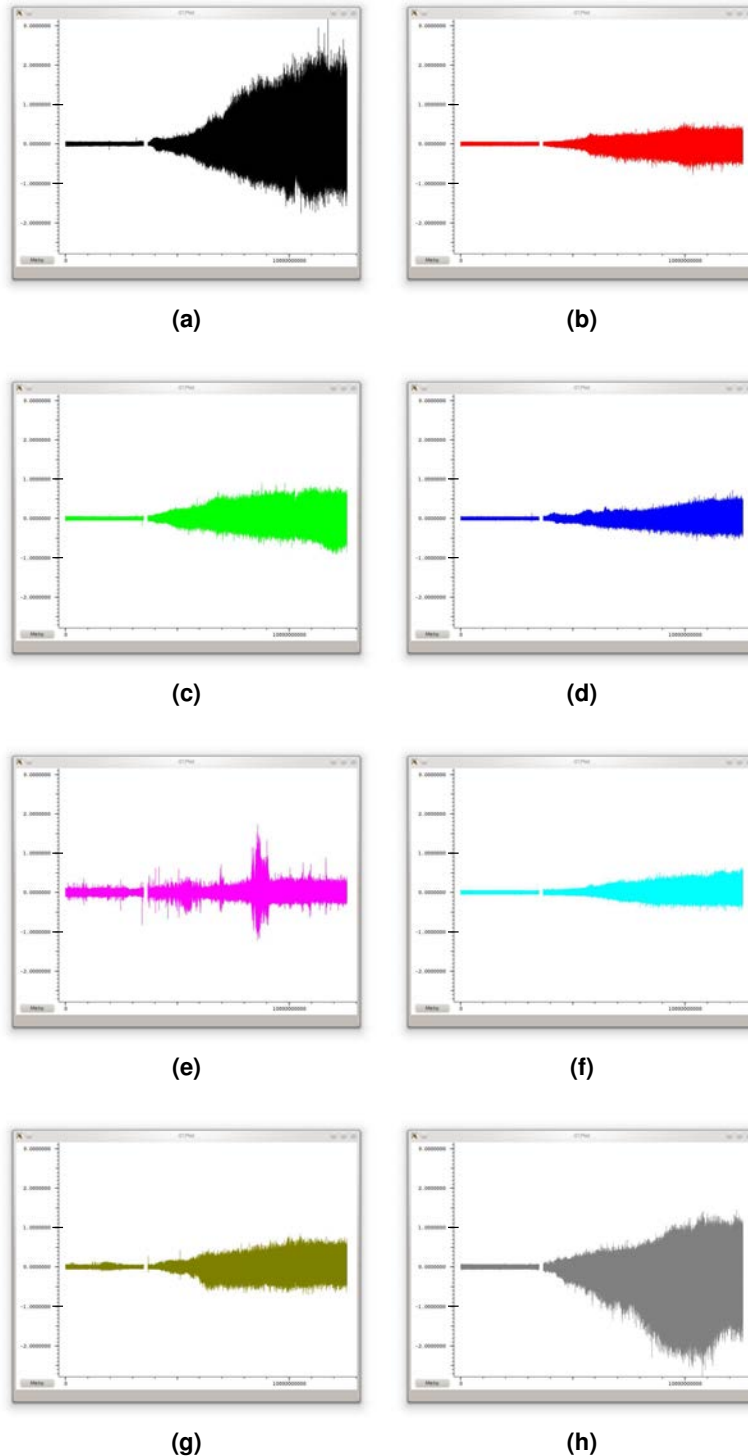


**Figure 4.27:** 14 days of time series data shown in O1Plot for channels 0 (a) to 7 (h). The units on the x-axis are samples and the unit on the y-axis are mV. The small gap in the time series data was caused by power outage on day 4. At about the same time between day 4 and 5 the first signals become visible and grow in amplitude. X-axis shows samples, y-axis shows mV, elongated y-axis ticks mark the position of +1mV or -1mV.

### *Spike detection and clustering*

Spike detection with the heuristic algorithm worked well and allowed to reliably detect spikes above the threshold while avoiding spike detection within bursts. The exact numbers of detected spikes per channel is listed in table 4.3.

The clustering process included two manual steps, determining the number of clusters and then manually merging clusters. These steps have turned out to be difficult as the cluster shapes are blurred/spread out and overlap with the shapes of the neighboring clusters (see the cluster of channel 0 in Fig. 4.29 as example). Therefore, proper spike shape distinction by detecting sweep free "white spaces" between the cluster sweeps was not possible (for comparison, see Fig. 2.7 as example of spike shape distinction with proper "white spaces"). Clusters had to be distinguished by differences in the base line shape (single-phasic spikes, bi-phasic spikes, positive leading spikes, negative leading spikes). If spikes had the same base line shape but different scales (different amplitudes), they were usually merged, but there were also exceptions (e.g. clusters 0 and 1 of channel 7, Fig. 4.28h) where the visual inspection of the spikes in the time series data gave confidence to keep spike clusters separate.

In summary, the problems of distinguishing spike clusters led most probably to sub-optimal spike sorting, where several clusters were collapsed into one. Nevertheless, the following analysis steps are based on these results.

### *Development of spike parameters over time*

The long recording period allowed to study the development of spike amplitude and spike frequency over time. In Fig. 4.30 the development of spike amplitudes during the 14 days is displayed. For each spike sweep of a channel the maximum amplitude was determined. The maximum amplitudes were sorted into two groups: positive and negative amplitudes. The values in each group were then binned into 1h blocks and minimum, maximum and mean value of each block were calculated.

The first regular spikes were detected from day 4 or 5 onwards. While the mean amplitudes stabilized quickly (day 6-8) in the range of 0.1 - 0.3 mV and then remained constant until the end of the recording, the maximum amplitudes kept rising (up to 3.16 mV on channel 0) and on several channels they did not reach a stable level until the end of the 14 days.

Channel 4 shows a non-typical amplitude profile with large spike amplitudes around day 10 with 1.72 mV and in the rest of the time comparatively small amplitudes of mostly < 0.5 mV.

For figures with the amplitude development for each cluster see appendix A.

For the visualization of the spike frequency development the spike times were binned in blocks of 1h length and for each block the spike frequency was calculated. In Fig. 4.31 the development of spike frequencies per channel is displayed (without clustering) and in Fig. 4.32 the development of spike frequency for each

Channel	Total Number of spikes	Number of clusters	Number of spikes per Cluster
0	9,594,970	4	3,910,641 1,067,780 135,908 4,480,641
1	6,998,179	5	1,261,005 3,620,693 661,934 328,113 1,126,434
2	6,895,282	7	2,042,973 461,540 70,398 322,843 2,167,640 1,704,944 124,944
3	5,022,802	4	2,718,687 503,468 1,247,899 552,748
4	70,739	3	39,435 19,261 12,043
5	4,345,638	4	1,250,202 330,771 1,538,769 1,225,896
6	4,033,366	3	1,755,017 1,792,997 485,352
7	6,428,650	4	2,884,034 493,910 1,696,978 1,353,728

**Table 4.3:** Overview of the spike detection and spike sorting step. The total numbers spikes that have been detected are listed as well as the results of the spike sorting, the number of clusters per channel and they amount of spikes per cluster. Apart from channel 4 all channels exhibit spikes in the range of  $10^9$ .

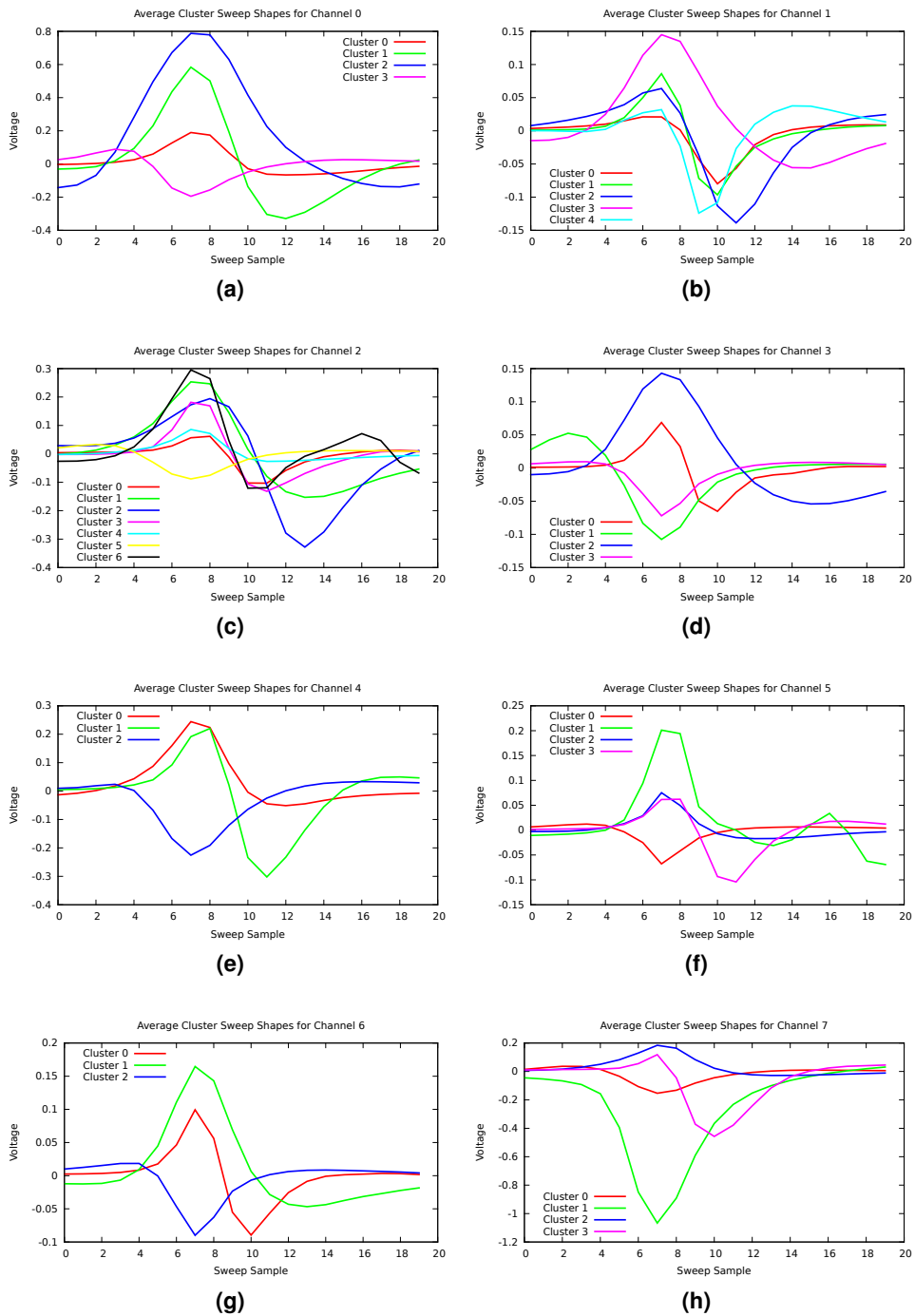
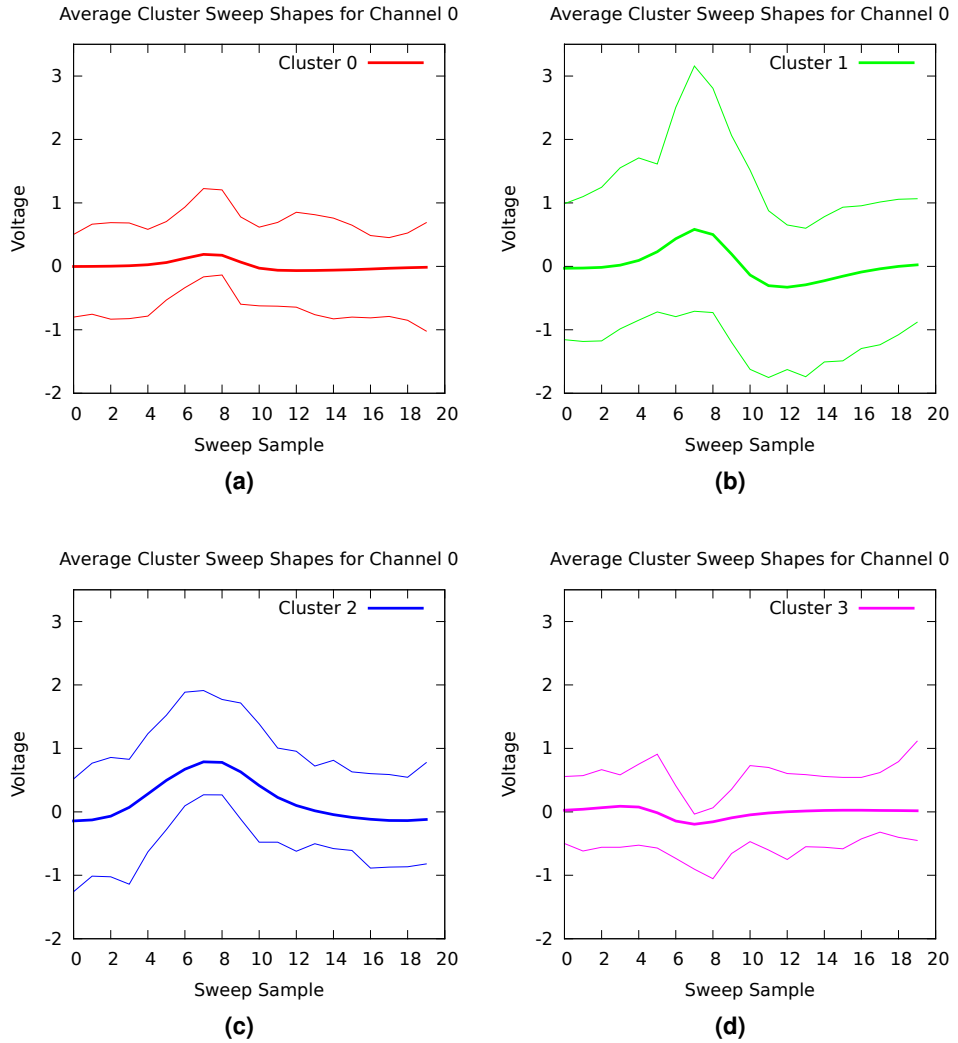
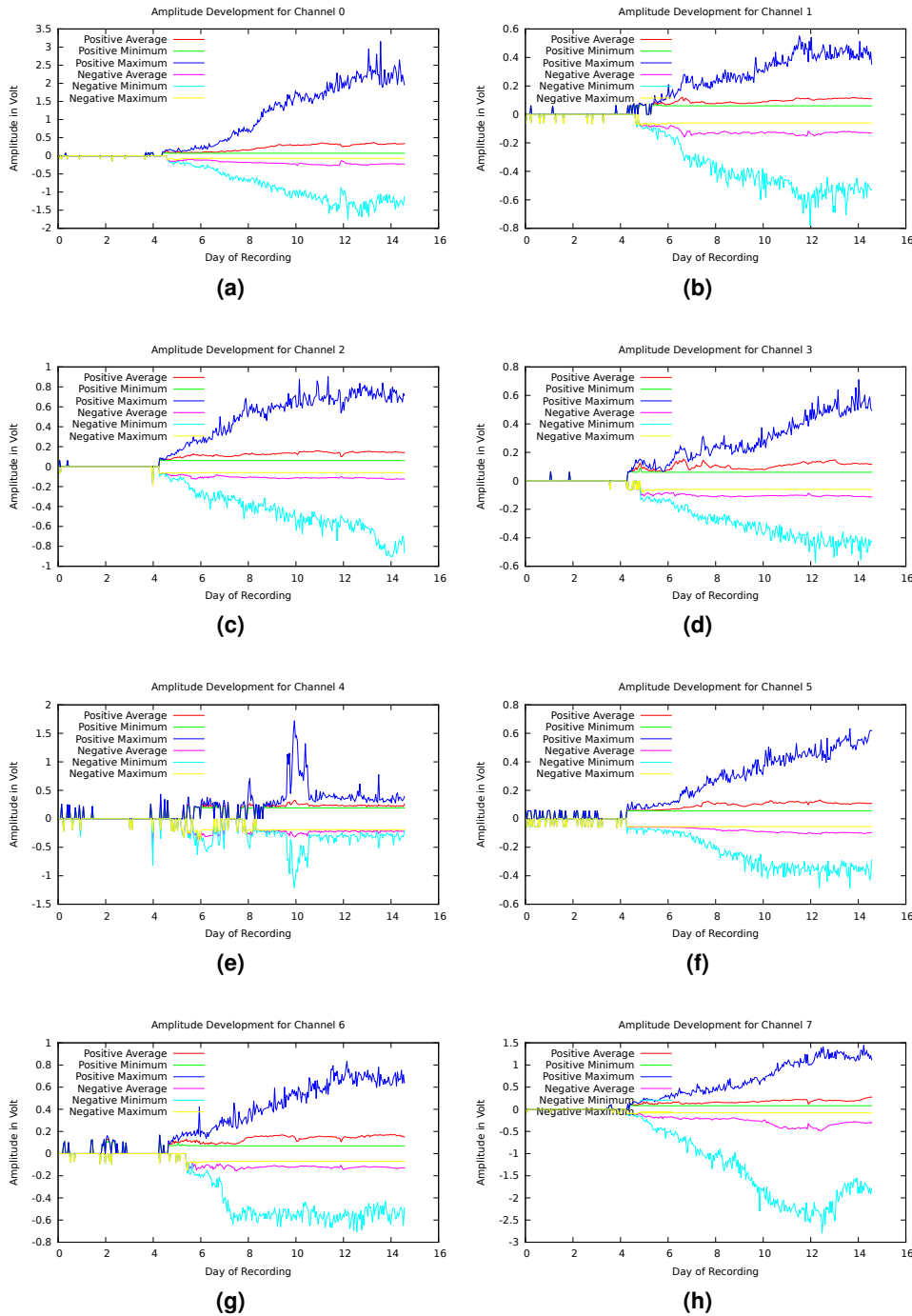


Figure 4.28: Average sweep shapes for all clusters from channel 0 (a) to channel 7 (h).



**Figure 4.29:** The cluster sweeps of channel 0 in detail. The bold line represents the average sweep shape while the thin lines mark the minimum/maximum amplitude of the sweeps in this cluster. It can be seen that the clusters overlap to a large extent.



**Figure 4.30:** Development of the spike amplitudes during the 14 days of recording. For each spike the maximum amplitude was determined. The amplitudes were then binned in blocks of 1 h and minimum, maximum and mean values computed. While the maximum spike amplitudes resemble the plots in Fig. 4.27 by growing and evolving until day 14, the average spike amplitudes reach their maximum quite early (day 6 - day 8) and then remain surprisingly constant.

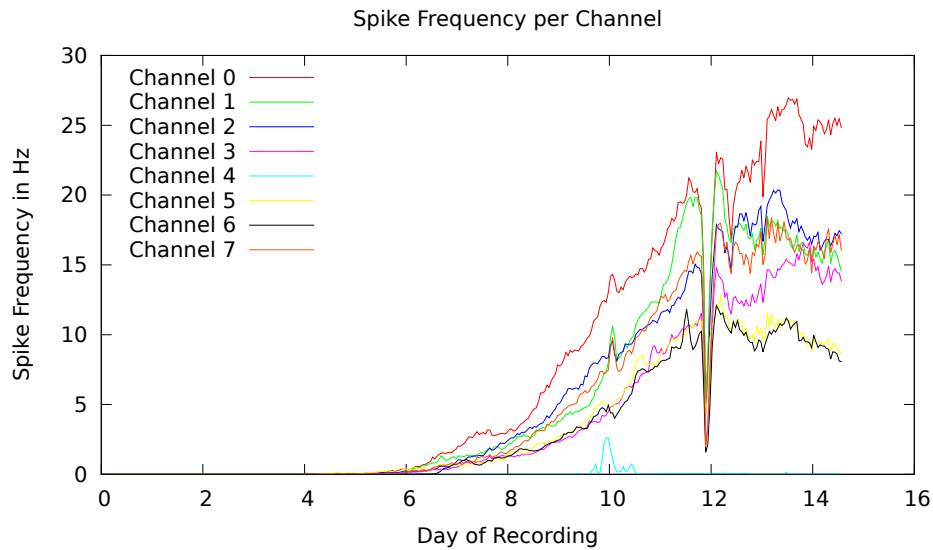


**Figure 4.31:** Development of spike frequency over time on each channel during the 14 days of recording. In general the spike frequencies rise from day 6 onward. Notable events are the drastic drop in spike frequency on day 12 and the slight increase of spike frequency on day 10 on a few channels.

cluster is shown.

In general, spike frequencies rise between day 5 and day 12; from day 12 to day 14 in some channels/clusters the spike frequency keeps rising, in others it's stagnating or going moderately down.

Two obvious events happened at day 12 and day 10. On day 12 the spike frequencies dropped drastically on all channels and clusters for a short time. E.g. on channel 0 the spike rate dropped from 21 to 5 spikes/sec and then quickly recovered to 23 spikes/sec.

The event on day 10 was less drastic with a couple of clusters temporarily increasing their spike rate. At the same time other channels temporarily decreased their spike rate. In one case (channel 5, cluster 2, Fig. 4.32f) the phase of depressed spiking activity was followed by a short period of over-proportionally increased spiking frequency. At the same time on day 10 channel 4 showed its short active phase, while exhibiting very low activity during the rest of the time.

### ***Day 12 incident***

To better understand the event that happened on day 12 the corresponding section in the time series data was visually inspected (Fig. 4.33) which confirmed the drop in spike rate, the spike shapes and amplitudes seem unaffected.

Using the start time of the recording and a manual approximation of the sample positions where the spike rates changed allowed to reconstruct the time course of the day 12 "incident" (see table 4.4).

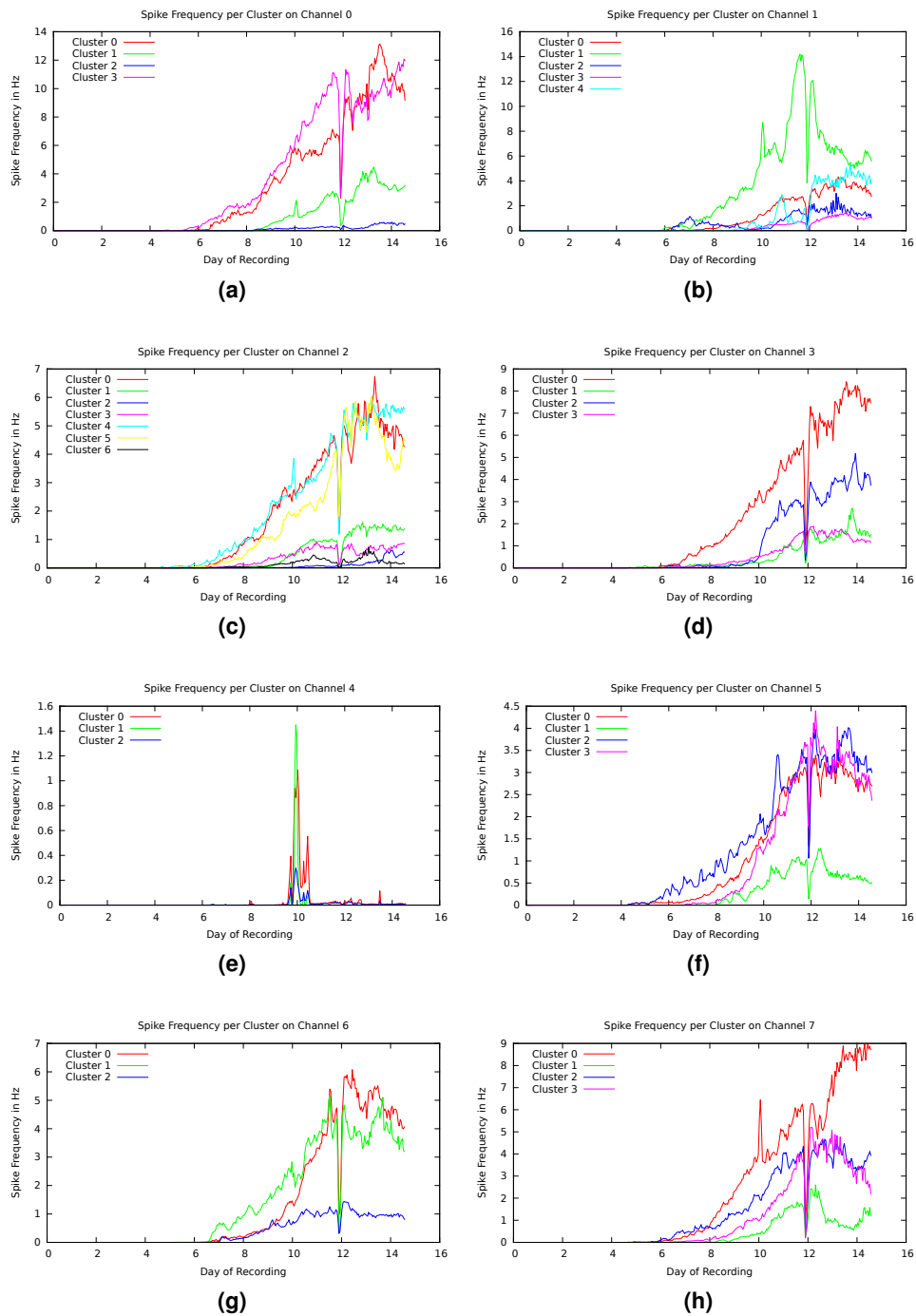


**Figure 4.32:** Development of spike frequency over time for all clusters on all channels during the 14 days of recording. On day 14 the spike frequency dropped drastically for a short period independent of the cluster. On day 10 the spike frequency rose on several channels for a short period, other channels showed a small depression at the same time which in one case channel 5, cluster 2 was followed by a temporary increase in spike frequency.



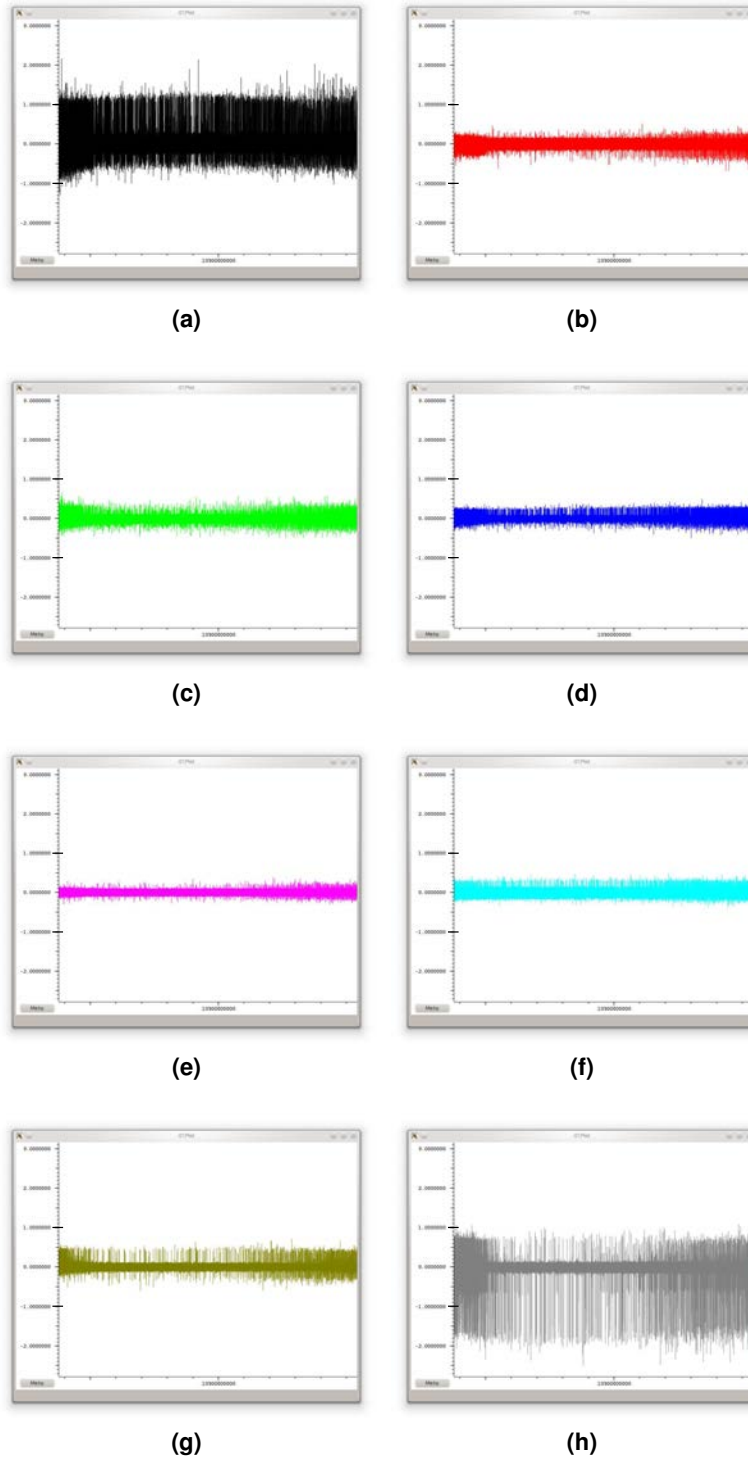


**Figure 4.33:** Day 12 incident: Due to unknown reason the neuronal activity diminished on day 12 on all 8 channels simultaneously and started to recover 1h 30min later. After 6h the activity had mostly returned to its previous level. In (a) (channel 0) to (h) (channel 7) the incident is shown. X-axis shows samples, y-axis shows mV, elongated y-axis ticks mark the position of +1mV or -1mV.

Event	Sample Position	Reconstructed Time
Soft Begin	10239049365	Saturday, 3. April, 00:00
Hard Begin	10251102474	Saturday, 3. April, 00:20
Recovery Begin 1st Spike	10294731528	Saturday, 3. April, 01:32
Recovery Begin 2nd Spike	10309336804	Saturday, 3. April, 01:57
Intermediate Spike Density	10360216444	Saturday, 3. April, 03:22
Full Recovery	10470657566	Saturday, 3. April, 06:26

**Table 4.4:** Reconstruction of the day 12 incident time course. The decline of spike rate started to show at midnight, but it was not until 00:20 when the drastic drop occurred. The recovery also took place in several steps, the first spikes came back at 01:32 and at 01:57. Over the following hours the spike density/rate increased (a notable step occurred at 03:22) until at 06:26 the spike frequency reached normal level again.

### *Day 10 incident*

On day 10 several clusters temporarily changed their spike rate (Fig. 4.32). Clusters C0C0 (channel 0, cluster 0), C0C1, C1C1, C2C4, C7C0 increased their spike rate for a short duration (3h in the case of C1C1 and C7C0). Other clusters slightly depressed their spike frequency: C2C0, C3C0, C5C2, C6C1 (6h in the case of C5C2, followed by a 9h spike frequency peak).

At the same time channel 4 exhibited its period of increased activity.

### *Example raster plots*

For illustration, raster plots of the spike activity have been made (Fig. 4.34). They show both single cluster activity as well as correlated inter-cluster, inter-channel activity.

### *Inter spike interval (ISI) analysis*

ISI analysis was done with the custom-developed `ISI Viewer` which allowed to efficiently visualize multiple ISI histograms at once. Figures 4.35, 4.36, 4.37 show an example with channel 0, cluster 3 (with blue background) being used as anchor spike list. All other subplots show the ISI histograms of the remaining 33 clusters relative to the anchor list. Each histogram spans from the past (left) to the future (right). The vertical blue line in the middle marks the position of the anchor spike with  $ISI = 0$ . The three figures differ in the width of the ISI histograms. While on the first the histogram width was chosen for best visualization of the central ISI spikes, the second and third figure expand the histogram width to 10,000 and 100,000 samples both into the past and into the future, corresponding to 1 and 10 seconds.

*ISI histogram patterns* The different magnifications highlight the three patterns of the ISI histogram data. The biggest histogram width of 10 seconds shows that

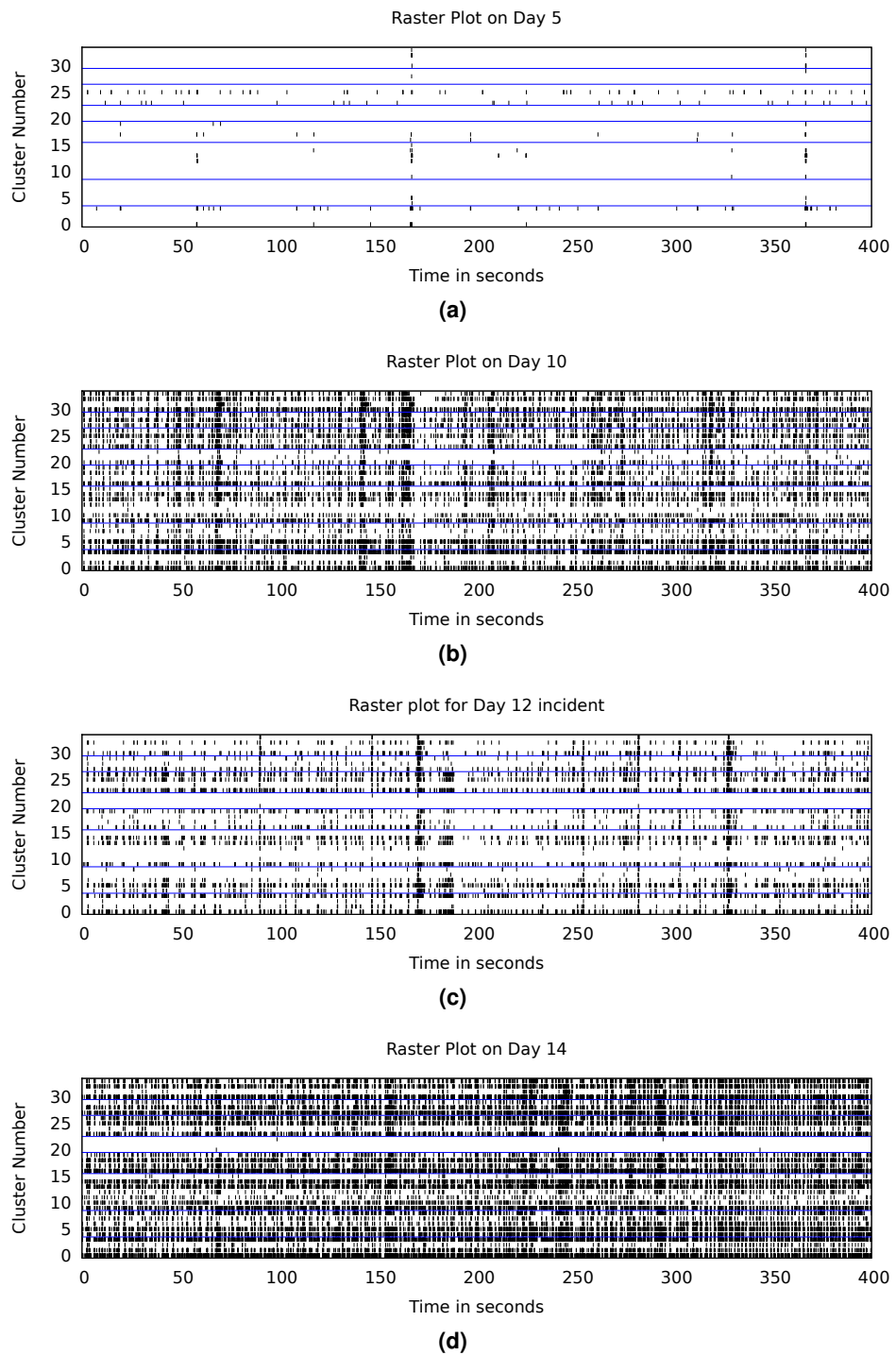


**Figure 4.34:** Example Raster Plots. The blue lines separate the channels, all clusters within two blue lines belong to the same channel. On day 5 (a) the activity was still low. On day 10 (b) the activity increased and there was also activity on channel 4 (clusters 20-22). For day 12 (c) the episode with reduced activity has been chosen and the raster plot for day 14 (d) shows full activity on all channels, except channel 4.

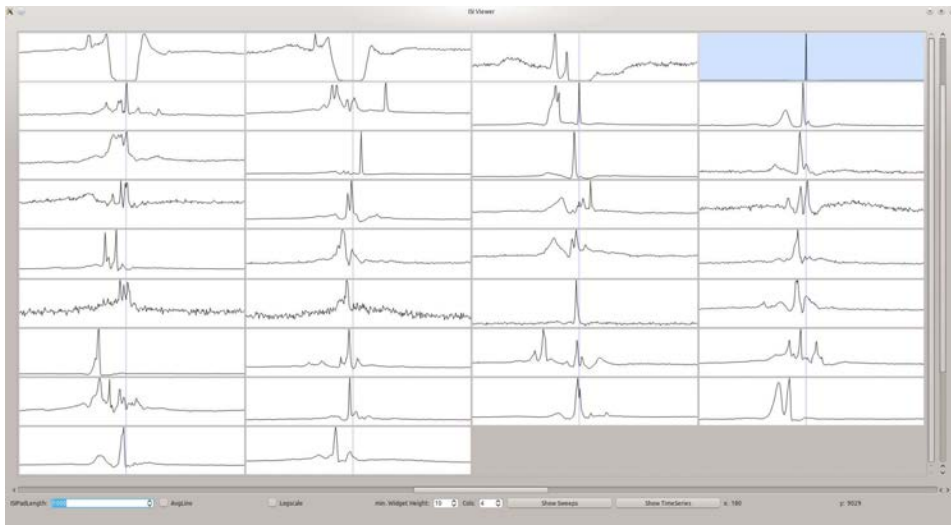


**Figure 4.35:** Screenshot of the multi histogram area of the ISI viewer displaying ISI "spikes" for all channels and clusters relative to C1C3 (blue background). The vertical blue lines indicate the ISI = 0 position. ISI values to its left range into the past, ISI values to the right range into the future.

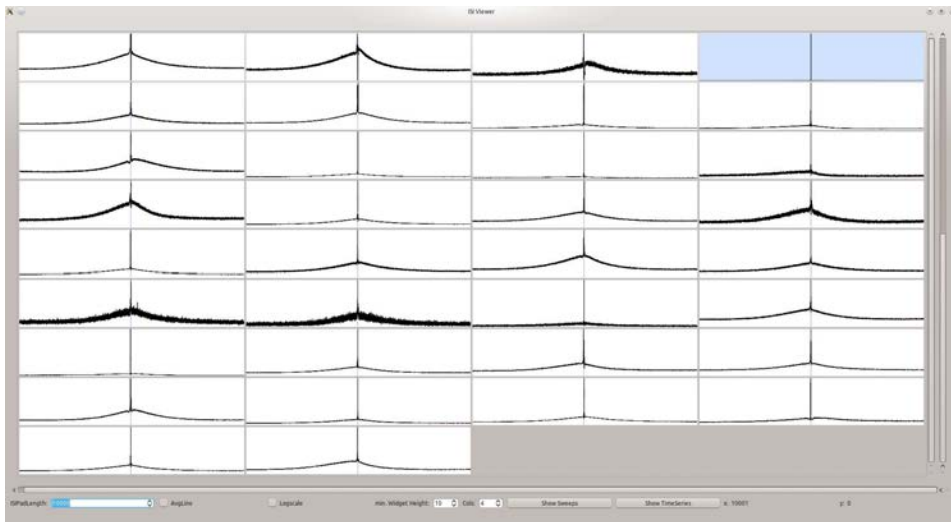


**Figure 4.36:** Screenshot of the multi histogram area of the ISI viewer displaying the same ISI histograms as in Fig. 4.35 but with larger histogram width (max ISI = 10000 samples  $\approx$  1 sec). The larger histogram width reveals the ISI "hat" shape which resembles roughly a two-sided exponential decay function.

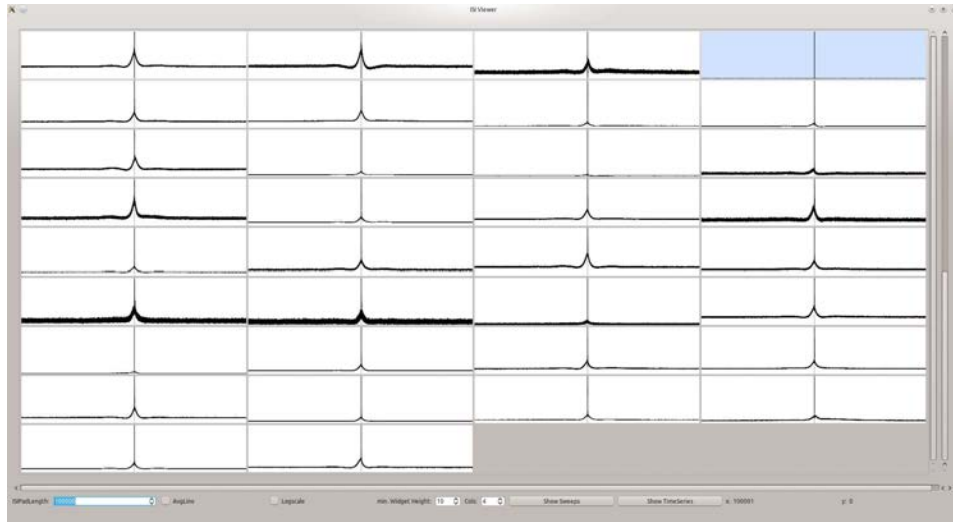


**Figure 4.37:** Screenshot of the multi histogram area of the ISI viewer displaying the same ISI histograms as in Fig. 4.35 and 4.36 but with even larger histogram width (max ISI = 100000 samples  $\hat{=}$  10 sec). The 10 sec histogram width reveals the ISI "noise" level of each cluster/cluster combination.

for large ISI values the histogram bin values become constant, in the following it is called the "ISI noise level" (Fig. 4.37).

Closer to ISI = 0 the histogram bin values increase to form an "ISI hat", which in most cases resembles a two sided exponential decay function (Fig. 4.36). However, there are also exceptions, see figure 4.38 for an example of ISI histogram with asymmetric "hat" shape. The "hat" usually has a width of around 6000-7000 samples (manually estimated) which correspond to 600-700ms ISI.

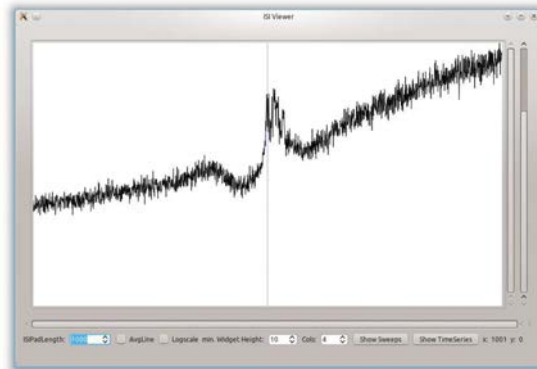
Finally, on top of the "hat", close to ISI = 0, narrow and steep "ISI spikes" can be found (Fig. 4.35).

*ISI spike histogram* In total 421 ISI spikes have been counted, figure 4.40 shows a histogram of the ISI distribution. It resembles roughly an exponential decay function with a maximal correlation range of up to 4 or 5 ms.

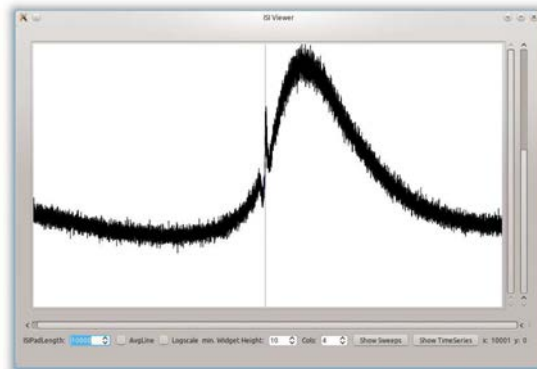
*Sub-noise ISI values* Usually when ISI noise, "ISI hat" and ISI spikes get superimposed, they add up, but there are also examples of "ISI hats" and spikes that actually subtract from the ISI noise level (Fig. 4.39).

## 4.5 Discussion and conclusion

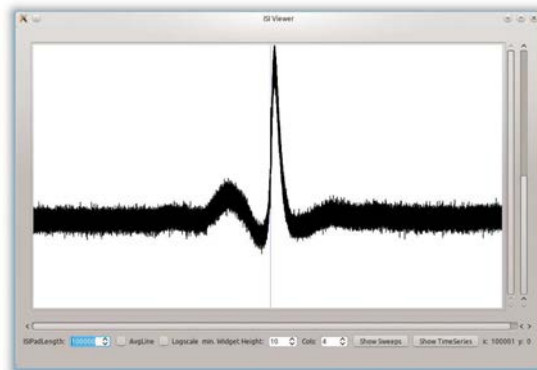
The StarPoM device has been built to culture neurons confined to 9 chambers connected by  $\mu$ -channels. E18 embryonic mice hippocampus neurons were plated in the device and their electrical activity in the  $\mu$ -channels was monitored and recorded continuously for 14 days. The recorded data was analyzed using a perfor-



(a)

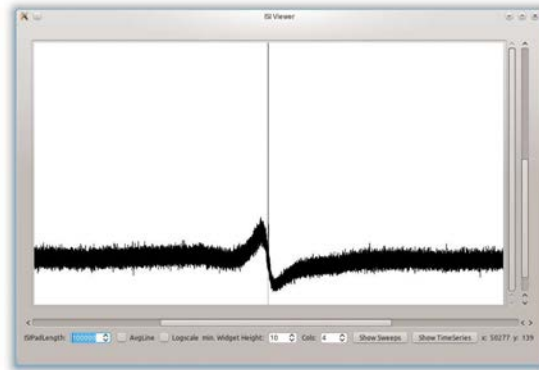


(b)

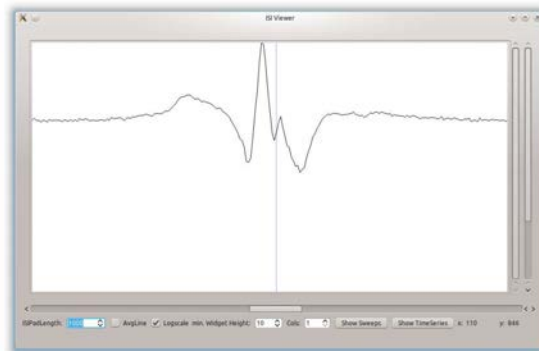


(c)

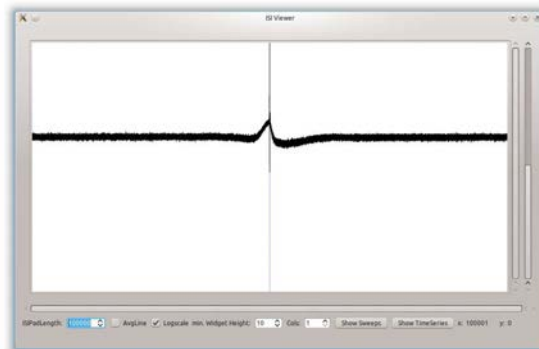
**Figure 4.38:** ISI asymmetric "hat" shape of channel 1, cluster 4 relative to channel 7, cluster 3 as anchor spike list. Normally the "hat" shape is symmetric and the ISI spikes sit on top of the "hat". Here the "hat" shape is asymmetric, so that the spikes are actually smaller than the "hat" bulge on the right (b). Further away on the left side (past) another bulge emerges from the ISI noise level (c).



(a)



(b)



(c)

**Figure 4.39:** Examples of sub-noise ISI values. The ISI histogram of C2C1 anchored to C1C4 is shown in (a). The ISI "hat" shape on the right of ISI = 0 drops below the ISI noise level, meaning that there are less ISIs than statistically expected. The ISI histogram of C2C1 with COC3 as anchor in (b) and (c) shows narrow sub-noise ISI regions (negative ISI spikes) close to ISI = 0 beside regular positive ISI spikes. The narrow, vertical black line in (c) represents the spikes in (b), it ends below the noise level. The values in the noise level range from 300-360 the minimum value in the negative spikes are 156 on the left and 105 to the right. Both figures use log scale on the y axis to improve the visualization. Sub-noise ISI regions could be starting points to search for inhibition between anchor spike cluster and other spike clusters.

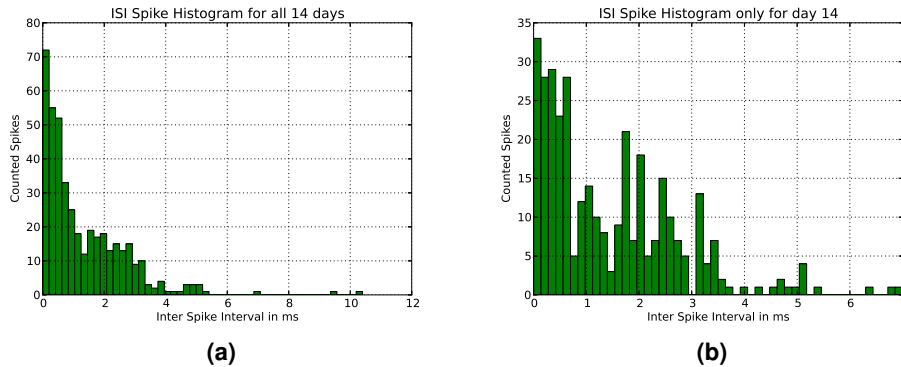


**Figure 4.40:** Histograms showing the distribution of ISI spikes for all 14 days (a) with 421 ISI spikes and for day 14 only (b) consisting of 339 ISI spikes. In general the number of ISI spikes is declining with larger ISI values up to  $\sim 5$ ms, stray outliers can be found up to 10ms.

mance enhanced tool-chain. Finally, the `ISI viewer` software was introduced which can help to quickly identify temporal correlations between spike clusters.

#### 4.5.1 Notes on the methods

For the microfabrication of the StarPoM device a SU-8 soft-lithography master was built using a substrate-integrated chrome mask and backside exposure. This approach solved the contrast problem during the alignment of  $\mu$ -channel and well features. Furthermore, the exposure from the backside leads to a more favorable taper of the SU-8 columns, with a bigger diameter at the bottom and a thinner diameter at the top. This later aids with PDMS film release and provides a more stable adhesion between SU-8 columns and substrate.

For the analysis of the large dataset a performance enhanced tool-chain was developed. The tools were mostly written in C++ which offered enough performance to keep up with the bandwidth of a single hard disk (60-120MiB/sec). One major exception was the wavelet filter tool which was written in python/numpy/pywavelets because it provided better filter quality than the C++ based alternatives. Despite optimization to use 4-core multi-processing for better performance it was not able to keep up with the bandwidth of a single hard disk and provided a throughput of  $\sim 27$  MiB/sec.

The `ISI viewer` proved to be a useful tool to search for temporal correlation between spike clusters. It benefited from the large dataset which leads to high sample numbers in the histogram bins, resulting in smooth plots and easy identifiable spikes/features.



### 4.5.2 Caveats

This project extended in-vitro neuro culture techniques in several aspects - with new fabrication methods, long-term monitoring and large scale data processing. The first iteration of this new approach revealed the following problems:

At the end of the 14 days bubbles have formed on the ITO electrodes below the PDMS film (Fig. 4.26). These could be the result of a partial detachment of the PDMS film from the MEA substrate due to thermal expansion. Glass and PDMS have different thermal expansion coefficients -  $8 \cdot 10^{-6} K^{-1}$  (glass) vs.  $3.1 \cdot 10^{-4} K^{-1}$  (PDMS) (Kunnavakkam, Houlihan, Schlaw, Liddle, Kolodner, Nalamasu, and Rogers, 2003) - and a  $10^\circ C$  temperature difference between device assembly and incubator can already result in a length difference of  $\sim 1\mu m$  for the 3cm StarPoM device length.

The artifacts on channel 6 (Fig. 4.15) and the baseline drift on channel 4 (Fig. 4.16b) could be a consequence of the bubbles or the formation of the bubbles. To avoid detachment, a better bonding may be necessary in the future. The current device relied only on the natural adhesion between PDMS and the MEA. Oxygen plasma bonding, for example, provides improved adhesion and should avoid detachment.

The fabrication of the culture chamber from PDMS blocks represented a simple and rapid solution. It succeeded in avoiding infection, providing sufficient  $CO_2$  circulation while slowing evaporation to keep the neuron culture alive. However, during the 14 days,  $\sim 25\%$  of the culture medium evaporated. For longer recordings, either medium changes would be necessary or a more elaborate culture chamber design (Steve M. Potter and DeMarse, 2001).

The ground electrode was punched through the PDMS lid covering the culture chamber and was hanging then into the culture medium. During the 14 days condensation was observed on the cover lid with varying drop formations. This indicates that there was a circulation within the culture chamber, warmer culture medium ( $37^\circ C$ ) evaporated and condensed on the cover lid which is cooled by the lower temperature of the incubator ( $31.5^\circ C$ ). It can be assumed that the drops formed by condensation, at some point detach from the lid and fall back into the culture medium (rain). In this process the ground electrode could act as a drop guide and the drops wetting its surface might temporarily change the electrode potential - a possible explanation for the common base line fluctuations on all channels (chapter 4.3.13). A solution to this problem would be to isolate the ground electrode above the culture medium liquid level.

Spike sorting of the large dataset was hindered by lack of discernability of the spike clusters. The clusters identified by the k-means method tended to be blurred, overlapped and manual judgment was necessary to decide on the final clustering. Possible causes that contributed to this problem:

- The  $\mu$ -channels contained a large number of neurites generating too many similar and also overlapping spike shapes, especially in bursts.
- Spike sweeps contained too little information; they consisted of 20 samples of which often only 4 or 5 samples actually described the spike.

In section 4.5.6 several ideas for improvement are discussed.

### 4.5.3 Findings

This project had on one side the purpose to further develop the PoM (Polymer-on-MEA) technology. The used methods were based on previous work in our group (E. Claverol-Tinture, Cabestany, and Rosell, 2007); improvements were done on the alignment accuracy between  $\mu$ -channel and well features. This was achieved by integrating the well features into the SU-8 soft-lithography master using the embedded chrome mask and backside exposure. Together with the custom built aligner, which can accurately combine the PDMS film to the MEA substrate, this allowed the step from 1D structures (a single  $\mu$ -channel crossing an electrode array - E. Claverol-Tinture, Cabestany, and Rosell 2007) to 2D geometries - with the StarPoM device as first prototype design.

On the other side the StarPoM device served as a test platform for continuous long-term recordings and to get a first impression of spike parameter development in  $\mu$ -channel devices over time. Spikes could be detected from day 5 onwards. They grew in maximum amplitude and frequency; in some channels they reached their maximum amplitude around day 10, in other channels they continued to grow/evolve until day 14. For comparison, spiking frequency on MEAs grows up to day 21 before declining again (Chiappalone, Bove, Vato, Tedesco, and Martinoia, 2006), so the spike frequency development during the first 14 days in  $\mu$ -channel devices is consistent with neuron behavior on MEAs.

The average spike amplitude, however, reached its maximum already between day 6 and day 8; from then on, they remained almost constant. This surprising finding indicates that while maximum spike amplitudes are growing on one side, the amount of small amplitude signals that gets recorded by the  $\mu$ -channels seems to proportionally increase on the other side. This can be partially seen when comparing figures 4.28 and 4.32. E.g. clusters 1 and 2 of channel 0 with large amplitudes (Fig. 4.28a) have relatively low spiking frequencies compared to the small amplitude clusters 0 and 3 which show a steep growth of spiking frequency over the 14 days (Fig. 4.32a). This means that either neurons generating small signals have higher spiking rate, or that due to the aforementioned problems with spike sorting, several spike clusters with small amplitude signals are collapsed into one spike cluster, so that the spike counts add up. The last interpretation would correspond to a similar consideration for general extra-cellular recordings (Martinez, Pedreira, Ison, and Quiñan Quiroga, 2009). Extra-cellular electrodes usually record only few neuron units that are close by with large amplitudes.

Several more neuron units at medium distances are recorded with smaller amplitudes that collapse into single clusters during spike sorting and many more, very distant neuron units contribute to general recording noise. However, currently it is not clear where the neurons with mid-sized amplitudes could be situated in a  $\mu$ -channel device. Are these units deep in the culture wells and the  $\mu$ -channel entrances act as general extra-cellular electrodes? Or are these neurons that just manage to grow their neurites partially into the  $\mu$ -channels?

The rasterplot in figure 4.34 shows neural activity that is largely synchronized across all channels. This means that the neuron populations are functionally connected, either directly by neurite connections or indirectly by being stimulated within the same bursting activity.

The `ISI viewer` has proven to be useful for searching correlated activity between the spike clusters: Two types of ISI correlations were observed: ISI "spikes" and ISI "hats".

*ISI spikes* These are short term correlations with a temporal delay of 0 to  $\sim 5$  ms (Fig. 4.35 and 4.40). Neuron processes in this time range are fast synaptic transmissions and action potential propagation delays.

Fast synaptic transmissions in the central nervous system have latencies from  $<1$  ms in the cerebellum (Sabatini and Regehr, 1996) to 3-4ms for CA3 synapses (Sayer, Friedlander, and Redman, 1990; Jonas, Major, and B Sakmann, 1993) and fit therefore directly into the ISI spike range.

The longest electrode to electrode distance in the StarPoM device is  $\sim 570$   $\mu\text{m}$  ( $2 \times 100\mu\text{m}$   $\mu$ -channel + diagonal shortcut across the central chamber). In order to travel this distance in 5 ms an action potential would need a propagation velocity of 0.11 m/s which is below the range of reported axon conduction speeds in the central nervous system (Kress and Mennerick, 2009). An action potential traveling at 0.3 m/s (fast for hippocampus neurons) would need for the same distance 1.9 ms.

ISI "spikes" could therefore have several explanations. They could correspond to direct neuron connections; a neurite that has grown through two  $\mu$ -channels generating signals in both. Another possibility could be that an axon enters the central chamber through a  $\mu$ -channel in which its action potential generates a signal. In the central chamber the axon connects with a synapse to a second neuron which has its axon passing through another  $\mu$ -channel where the second signal is generated. As there is a neurite bridge connecting the central chamber to the neuron population on top of the PDMS film (Fig. 4.24 and 4.25), a likely explanation is that the spontaneous (and bursty) activity originates in the larger neuron population on top of the PDMS film, propagates down the neurite bridge into the central chamber and from there along several axons into different  $\mu$ -channels. The temporal offset would then be a result of different delays in the signal transmission from neurite bridge to the final axons entering the  $\mu$ -channels. This interpretation would also

explain ISI spikes at 0, a common originating signal gets split up into two action potentials running down two different axons into two separate  $\mu$ -channels and generating signals simultaneously.

The high number of ISI spikes per histogram can be explained with the suboptimal spike sorting (see 4.4.4). Each detected spike cluster may in fact contain several real units and the obtained ISI histograms are then superpositions of the ISI histograms of the individual units.

*ISI hats* ISI hats are wide spans of increased probability for a correlated spike (Fig. 4.36 and 4.38). The ISI hats are broader than the ISI spikes, meaning that their ISI delay has larger jitter. The width of ISI hats is 600-700 ms, which puts it into the range of burst durations (Wagenaar, Jerome Pine, and Steve M Potter, 2006) or slow synaptic transmissions (Greengard, 2001). Both could be valid explanations for the observed ISI hats. Bursts have a chaotic structure that would explain the large jitter. Slow synaptic transmissions can have a modulating effect, they raise the probability for signal propagation through a neuron. So while slow synaptic transmissions do not stimulate spikes on their own, they create a time window in which random background noise (with high jitter) can more easily elicit action potentials.

*Sub-noise sections* The ISI noise level represents the un-correlated neural background activity - random spikes. ISI histogram sections have been observed with histogram values below the noise level. These sub-noise sections may provide useful information related to inhibition between neurons, but more detailed analysis has to be developed. Sub-noise sections are mostly wide range sections - similar to ISI hats - but also narrow ISI spike-like sub-noise sections have been observed (Fig. 4.39).

#### 4.5.4 Unexpected observations

Unexpected events were observed on day 10 and 12.

On day 10 the spiking frequency in several clusters increased for about 3h, other clusters lowered their spiking rate at about the same time, but for about 6h. In one case the depression was followed by a 9h period of increased spiking frequency. At the same time channel 4 exhibited its short phase of intense activity. The interpretation is unclear; one possibility could be that during day 10 the conditions in  $\mu$ -channel 4 allowed signal transmission from the small well into the central chamber for a short time. The extra input from  $\mu$ -channel 4 then changed the spike dynamics in the rest of the device until the signal transmission through  $\mu$ -channel 4 stopped.

On day 12 the spiking frequency on all channels dropped dramatically for  $\sim$ 6h. The cause for this is unknown. As the spike amplitudes during this period showed only little change, obvious problems on the amplifying equipment (e.g. power

failure, short circuit) can be excluded. One possible explanation could be a temperature shock. In the past we observed diminishing spike activity when bringing neurons in  $\mu$ -channel devices from an incubator at 37 °C to room temperature (not published). Unfortunately it was not possible to verify in hindsight whether the incubator was plugged into the secured power supply together with the recording setup (which continued to work) or if it was connected to the standard power grid that might have had a power outage at that time (Friday to Saturday around midnight).

An alternative theory could be that the signal transmission over the neurite bridge collapsed for this period and that the missing stimulation from the PDMS film surface resulted in the activity decrease in the device.

Other noteworthy observations:

Excluding channel 4, the spike counts per channel remained within the range of one magnitude from  $4.0 \cdot 10^6$  to  $9.6 \cdot 10^6$  spikes (Table 4.3). This could be explained by the predominantly synchronized activity in the device. Most spikes were parts of bursts and bursts affected all channels simultaneously.

#### **4.5.5 Contribution to the field**

In the described project a number of previously available technologies were combined and extended - to our knowledge for the first time - to prototype long-term in-vitro electrophysiology experiments with continuous data acquisition. This research direction resulted from the technological advancement that led to low cost data storage, maturing long-term cell culturing techniques and the necessity to study long-term neuron processes to understand important aspects of human mental health: How does the brain develop? What happens during neuronal diseases and aging? How can neuronal structures regenerate? And what can be done to help patients?

Once the technological infrastructure (long-term recording equipment and data analysis software for large scale data) is in place, continuous recordings from neurons should not cause any more extra effort. The advantages of this technology are:

- Changes of neuronal activity can be tracked continuously over time.
- Unforeseen events - such as the events on day 10 or day 12 - are detected and can highlight problems with the experiment setup or the experiment itself and also reveal new, unexpected opportunities that otherwise would go unnoticed.

#### **4.5.6 Outlook**

Further developments of this technology should address the currently most pressing flaw - the suboptimal spike sorting and tracking. The problem could be ap-

proached by improving the signal quality of the device. In (Wang, Riss, Buitrago, and Claverol-Tinturé, 2012) we described that narrower channels can improve signal quality. Also, narrower channels would limit the amount of units per channel which should facilitate spike sorting.

Comparing the signals that were used for the spike sorting in chapter 2 / (Morales, Riss, Wang, Gavin, Rio, Alcubilla, and Enric Claverol-Tinture, 2008) - an end-to-end recording from a 1.6 mm long  $\mu$ -channel - with the signals recorded in the StarPoM device with its 200 $\mu$ m long  $\mu$ -channels, shows that the longer  $\mu$ -channel also produces longer spike shapes. While the spike sweeps for the 1.6 mm  $\mu$ -channel had 200 samples, the sweeps for the StarPoM spikes had only 20 samples (both signals were recorded at 10 kHz). The signal broadening can be explained by the low-pass filtering effect of long  $\mu$ -channels (Wang, Riss, Buitrago, and Claverol-Tinturé, 2012). Longer  $\mu$ -channels could therefore represent an opportunity improve spike sorting by providing more information in longer spike sweeps.

Apart from changes to the device to improve signal quality, improvements are also needed on the spike sorting algorithm to accommodate the new needs of long-term recordings. Two keys aspects will be

- the ability to automatically determine the correct number of spike clusters
- track spike units over time.

While  $\mu$ -channel devices and long-term monitoring are a good combination, the long-term monitoring technology could also be combined with other device types, such MEAs, given that a stable association between neuron units and electrodes can be ensured or that the experiment does not require individual neuron tracking.

## Chapter 5

### Biophysics of the $\mu$ -channel

This chapter covers my contribution to the group effort to understand the biophysics of signal generation in  $\mu$ -channel devices. Here, our first attempt to correlate  $\mu$ -channel length and signal amplitudes, both experimentally and theoretically, is documented. This work got later extended and led to a publication (Wang, Riss, Buitrago, and Claverol-Tintur , 2012).

#### 5.1 Abstract

Conventional micropipette-based electrophysiology on cultured neurons is a widely used labor intensive, technically complex and low throughput experimental approach in neuroscience. We previously demonstrated that substrate-embedded  $\mu$ -channels afford automated, low-complexity and potentially high throughput loose-patch electrophysiology on developing cells in vitro in a lab-on-a-chip format. Here we study, theoretically and experimentally, the influence of  $\mu$ -channel length on signal magnitude towards optimizing the device geometry in terms of signal-to-noise ratio. In 60 experiments dissociated neurons were grown in PDMS chambers to spontaneously sprout and thread  $\mu$ -channels with lengths ranging from 40 $\mu$ m to 3050 $\mu$ m. Interestingly spike amplitudes up to 2mV were recorded over a wide range of channel lengths from 3mm down to 120 $\mu$ m. Our data suggest that the loose-patch signal is primarily generated at the  $\mu$ -channel entrance due to partial blockage by sprouting axons within 150 $\mu$ m of the entrance, so that a short (< 150 $\mu$ m)  $\mu$ -channel suffices to generate large magnitude signals.

## 5.2 Introduction

Substrates including microstructures such as microwells (Dworak and Bruce C. Wheeler, 2008), trenches (Merz and Fromherz, 2005) or chemical micropatterns (Chang, Brewer, and Bruce C Wheeler, 2003) can confine somas and guide axons to shape the geometry of cultured neuronal networks for basic neuroscience studies. We have previously demonstrated that  $\mu$ -channels can afford automated low-complexity loose-patch electrophysiological recordings (Morales, Riss, Wang, Gavin, Rio, Alcubilla, and Enric Claverol-Tinture, 2008) acting as substrate-integrated micropipettes. Here we investigated the influence of the channel length on the spike amplitudes in-vitro and addressed the question if an optimal length exists.

A series of 60 experiments has been conducted on  $\mu$ -channel devices with varying channel lengths (40 $\mu$ m - 3050 $\mu$ m). For each device the amplitude of the neural signals and the end-to-end resistance of the channel was measured. A compartment model of the confined axon based on the passive cable theory (Segev, 1998) including non-zero extracellular axial resistance associated with  $\mu$ -channel lumen was developed and compared to the experimental results. Additionally the axial  $\mu$ -channel resistivity profile in the model has been developed assuming that the resistivity at the channel entrance is higher than in the middle of the channel. This approach has been inspired by both observation that in microscopy images typically a clog of cells and debris could be seen at the entrances of the channels and the measurement of end-to-end resistance of the  $\mu$ -channels showing a steep rise for short channels (< 300 $\mu$ m) and then a slower rise for longer channels consistent with a channel clog causing increased resistivity. SEM images have been taken to confirm the channel clog theory.

## 5.3 Materials and Methods

### 5.3.1 Device Fabrication

The fabrication of the devices has been described elsewhere (Morales, Riss, Wang, Gavin, Rio, Alcubilla, and Enric Claverol-Tinture, 2008). Briefly, a soft-lithography master with SU-8 stripes (height 3.7 $\mu$ m, width 25 $\mu$ m) was produced. PDMS was poured at a thickness of 6mm on top of the master and cured at 60°C. A tissue puncher was used to punch wells of 6mm diameter at the ends of the  $\mu$ -channels. The distance between the wells was varied between 40 $\mu$ m and 3050 $\mu$ m.

Polystyrene dishes were coated overnight with 0.01% poly-L-lysine. After rinsing and drying the dishes they were sandwiched with the PDMS structure to form the final device.



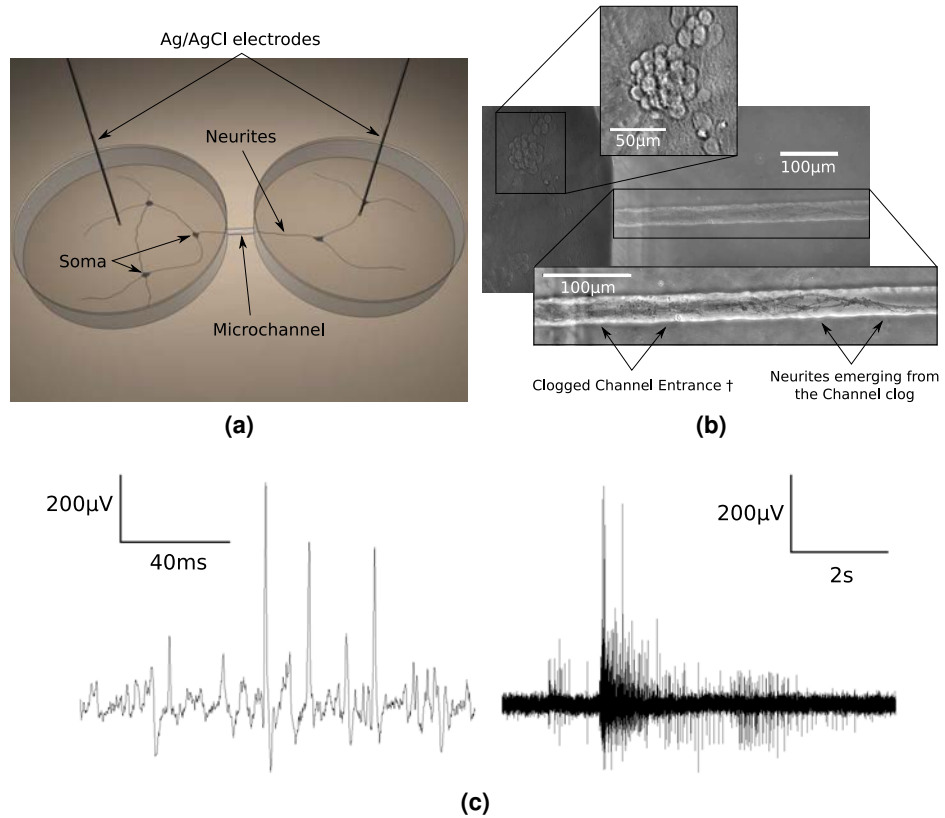


**Figure 5.1:** (a) Two culture chambers are connected by a  $\mu$ -channel. Neurons growing in the chambers extend their neurites through the channel. Their electrical activity causes a transient potential drop along the channel that can be recorded by electrodes in the chambers. (b) The entrance of a  $\mu$ -channel: At the beginning of the channel a “clog” of cells and debris is visible (†). Deeper in the channel a neurite bundle emerges from the clog. (c) Recordings from the  $\mu$ -channels, left: several spikes in high magnification, right: a larger recording with typical bursting behavior.

### 5.3.2 Neuron Culture

Dissociated cultures of mouse hippocampus neurons were prepared as described previously (Morales, Riss, Wang, Gavin, Rio, Alcubilla, and Enric Claverol-Tinture, 2008). Briefly, E18 embryonic mice hippocampi blocks were dissected and cryopreserved in DMEM (Dulbecco modified Eagle medium) with 10% DMSO as cryoprotectant and with 100 mg ml<sup>-1</sup> streptomycin, 100 units ml<sup>-1</sup> penicillin and 10% horse serum as supplements. After maintaining the tissue blocks in liquid nitrogen for up to 6 months they were quickly thawed in a 37° C water bath, dissociated by gentle pipetting and plated at  $5 \cdot 10^4$  neurons chamber<sup>-1</sup> ( $1.7 \cdot 10^3$  neurons mm<sup>-2</sup>) in Neurobasal cell culture medium supplemented by 2% B27, 1% Glutamate, 10% horse serum and 20  $\mu$ g ml<sup>-1</sup> gentamicin. The neurons were kept in the incubator for 14 days, 50% of the medium volume was exchanged twice a week with fresh medium.

### 5.3.3 SEM Imaging

For the SEM images cells have been cultured in devices similar to the ones described in section 5.3.1, but with glass substrates (coated with 0.1% poly-L-lysine) instead of polystyrene dishes.

The following cell fixation steps were done on a lab shaker at 50rpm. The culture medium was removed from the wells and the PDMS structure carefully detached from the glass substrates. The 1st fixation step was done by submerging the samples in Glutaraldehyde 2.5% in 0.1M phosphate buffer (PB) solution for 90 min. The samples were then washed 4 times at 4°C in 0.1M PB solution for 10 min. each. Dehydration was done at 4°C in several steps: In 50% ethanol for 1×10 min., in 70% ethanol for 2×10 min., in 90% ethanol for 3×10 min., in 96% ethanol for 3×10 min. and in 100% ethanol for 3×10 min. For the 2nd fixation step the substrates were submerged in hexamethyldisilazane (HDMS) for 5 min. After HDMS treatment, excess HDMS was blotted away with filter paper. The samples were transferred to a desiccator for 25 min. to avoid water contamination. After drying, the samples were mounted on stubs and were carbon coated.

Images were taken in a FEI Quanta 200 SEM microscope and stitched together with the software Hugin.

### 5.3.4 Recording and Data Analysis

Recordings were conducted with an Aleria 600 A prototype amplifier (Aleria Biodevices, Spain) for at least 10 minutes per dish.

The resistance of each channel was measured with a Model 2400 patch clamp amplifier (A-M Systems, USA).

Images of the  $\mu$ -channel entrances were taken with a DM IRBE inverted phase-contrast microscope (Leica, Germany) and a CoolSNAP<sub>fx</sub> camera (Photometrics, USA) directly after conducting the electrical recordings. For Fig. 5.1b three images have been combined with the panoramic stitcher software Hugin, the

Base resistivity	1.021 $\Omega m$
Clog resistivity	3.96 $\Omega m$
Clog depth	154 $\mu m$

**Table 5.1:** Parameters used by the clogged channel model

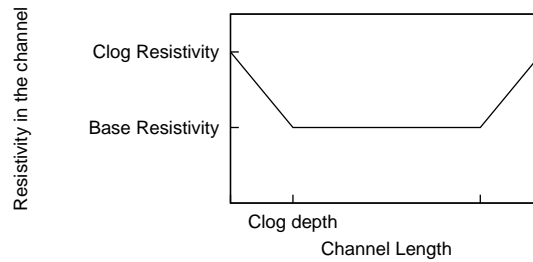


**Figure 5.2:** Postulated resistivity profile in the  $\mu$ -channel, cells and debris at the entrances clog the channel and rise the resistivity. Values after fitting the parameters to the experimental data: Base resistivity: 1.021 $\Omega m$ , Clog resistivity: 3.96 $\Omega m$ , Clog depth 154 $\mu m$ .

insets have been contrast enhanced with Gimp.

The conductivity of the Neurobasal cell culture medium has been measured with a BASIC 30+ EC-Meter (Crison, Spain).

### 5.3.5 Theoretical models

#### *Clogged Channel Entrance Model*

On microscopy images of the devices it was common to see a high density of cells, processes and debris (clog) at the entrances of the channels (Fig. 5.1b). Further, measurement of end-to-end channel resistance showed a non-linear correlation to the channel length (Fig. 5.4). For short channels ( $< 300\mu m$ ) the resistance grows fast with length, for longer channels the increase is slower, implying that the resistivity at the channel entrance is higher than in the middle of the channel (the linear, non-clogged model for comparison:  $R = \frac{l \cdot \rho}{A}$ ,  $l$  = length of the  $\mu$ -channel,  $\rho$  = resistivity of the Neurobasal medium = 1.021 $\Omega m$ ,  $A$  = cross section of the  $\mu$ -channel = 3.7  $\mu m \cdot 25 \mu m$ ).

Therefore a resistivity model for clogged channels has been proposed (Fig. 5.2). While the resistivity in the middle of the channel rests at the base level it starts to rise linearly towards the ends of the channels. The starting point of the linear raising phase is defined by the “clog depth” parameter.

The resistivity in the middle of the channel has been set to the experimentally determined value of 1.021 $\Omega m$  (measured Neurobasal resistivity), the “clog resistivity” and the “clog depth” parameters have been least-squares fitted to the measured data.

Soma diameter	30 $\mu\text{m}$
Axon diameter	0.4 $\mu\text{m}$ - 1.2 $\mu\text{m}$
Axon length	3000 $\mu\text{m}$
Axon Hillock diameter	4 $\mu\text{m}$ - Axon diameter
Axon Hillock length	20 $\mu\text{m}$
Extracellular Resistivity	1.02 $\Omega\text{m}$ - 3.96 $\Omega\text{m}$
Intracellular Resistivity	1.0 $\Omega\text{m}$
Membrane Capacitance	$1.0 \cdot 10^{-2} \text{ Fm}^{-2}$
Membrane Resistivity	$1.5 \Omega\text{m}^{-2}$
Time step	50 $\mu\text{s}$
No. Soma compartments	1
No. AH compartments	4
No. Axon Compartments	300
No. compartments in first well outside the channel	15 (incl. soma and AH) $\cong 150 \mu\text{m}$
Current injection into the soma	25 % (19 parts Kole, Ilschner, Kampa, Williams, Ruben, and Stuart, 2008)
Current injection into the axon hillock	75 % (57 parts Kole, Ilschner, Kampa, Williams, Ruben, and Stuart, 2008)

**Table 5.2:** Parameters used by the compartment model

### ***Compartment Model***

A compartment model based on the passive cable theory of axons (Segev, 1998) has been implemented in Octave and Matlab to simulate the propagation of action potentials through the  $\mu$ -channel (Fig. 5.3). The intracellular medium of the neuron and the extracellular medium in the channel are divided into several compartments, the medium in each well is represented by a single lumped compartment. The extra-cellular resistivity in the channel was modeled according to the clogged channel entrance model.

Action potentials were simulated by injecting a physiologically shaped biphasic current spike at the soma and axon hillock with current density values according to the literature (Kole, Ilschner, Kampa, Williams, Ruben, and Stuart, 2008). The injection current was scaled until a potential drop of 95mV was seen across the soma membrane.

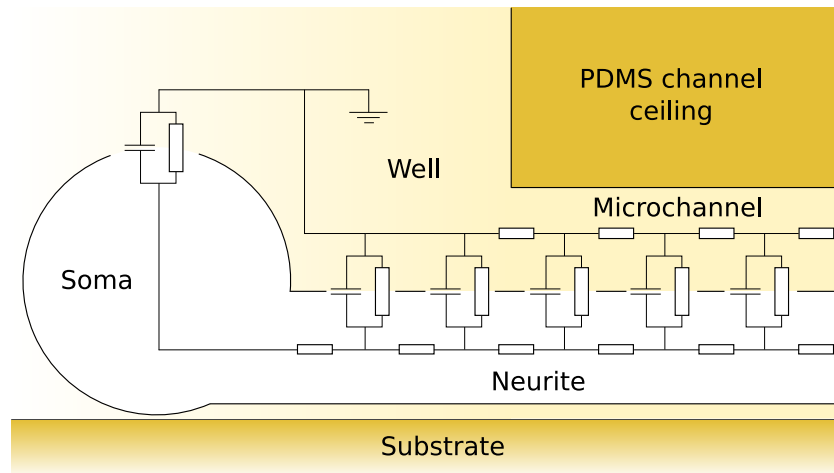


**Figure 5.3:** Compartment Model with passive cable dynamics: the intracellular space of the neurite and the extracellular medium in the  $\mu$ -channel are divided into compartments. The medium in the wells is assumed isopotential.

## 5.4 Results

Neuronal activity was recorded in 59 experiments. The measurements of resistance vs.  $\mu$ -channel length are shown in Fig. 5.4 (crosses). The end-to-end resistance increases steeply with length for short channels ( $< 300\mu\text{m}$ ) and then slower for longer channels, which led to the development of the clogged channel resistivity model (solid line). The dashed line shows the theoretical resistance without the channel clog.

In Fig. 5.5 the peak-to-peak spike amplitude is plotted against the  $\mu$ -channel length (crosses). Large spikes are measured both for long but also for short  $\mu$ -channels.

The compartment model generates a family of curves relating to various axon diameters (Fig. 5.5, solid lines). Up to a  $\mu$ -channel length of  $250\mu\text{m}$  the amplitudes are rising with length to a maximum, then they drop about 16% and stabilize on a lower plateau level. Experimental data shows a similar structure (Fig. 5.5, dashed line).

The characteristic behavior of the model results from three main aspects:

1. Action potentials (AP) entering the  $\mu$ -channels get attenuated quickly and only reach to a depth of  $300\mu\text{m} - 500\mu\text{m}$ .  $\mu$ -channels longer than  $500\mu\text{m}$  therefore do not yield larger spike amplitudes.
2. For a channel length between  $250\mu\text{m} - 500\mu\text{m}$  the second (repolarization) phase of the AP enters the  $\mu$ -channel before the first (depolarization) phase has left it. A partial cancellation between the two AP phases occurs which attenuates the spike amplitude and causes the decline to the lower plateau level.
3. When combining the compartment model with the model for clogged channel entrances the resistivity at the entrance of the  $\mu$ -channel is increased which causes

a larger voltage drop for the first section of the  $\mu$ -channel. Therefore we see already large spikes for channels  $< 250\mu\text{m}$ .

SEM images were taken (Fig. 5.6, 5.7). The increased neurite/cell density at the  $\mu$ -channel entrances confirm the clogged channel resistivity model.

## 5.5 Discussion and Conclusion

Our experimental data suggest that  $\mu$ -channel clogging has a major influence on the spike amplitudes whereas the channel length has only little effect. Even short  $\mu$ -channels ( $< 250\mu\text{m}$ ) yield large spike amplitudes (up to 2mV, leading to amplifier saturation).

The proposed combination of a compartment model with a model of clogged channel entrances explains the large spike amplitudes for short channels ( $< 250\mu\text{m}$ ) with increased resistivity at the channel entrances due to clogging with cells and debris. Optimal fitting of the clogged channel model to the experimental data results in an increase of effective resistivity from  $1.021\Omega\text{m}$  to  $3.96\Omega\text{m}$  ( $\sim$ factor 4), consistent with previously published data (Dworak and Bruce C. Wheeler, 2008). The increased resistivity causes a larger voltage drop in the first section of the  $\mu$ -channel and therefore raises the spike amplitudes for short channels.

The compartment model can also explain the stabilization of spike amplitudes for channels  $> 250\mu\text{m}$  by AP phase cancellation and rapid attenuation of the APs in the  $\mu$ -channel.

Further experimentation will be necessary to understand the large variation in spike amplitudes for the same channel length and to investigate whether the channel cross-section has an influence on the spike amplitude.

*Remarks* In continuation of this project an improved experiment was designed. Instead of the PoP (PDMS on Polystyrene) device a PoM (PDMS on MEA) device was planned that provides multiple electrodes along the  $\mu$ -channel to monitor the development of the signal.

MEAs were fabricated analog to the fabrication to the StarPoM device (chapter 4). Briefly, ITO-coated glass substrates were spin-coated with SPR-220-7.0 photoresist and exposed through a photomask with the electrode pattern. After developing, the patterned photoresist was used as a wet etch mask to selectively etch the ITO to obtain the desired electrode pattern. In Fig. 5.8 images are shown that were taken of the MEAs in an Olympus BX61 microscope to check for short circuits between the electrodes.

At this stage the project was continued by Ling Wang. Our combined results can be found in Wang, Riss, Buitrago, and Claverol-Tintur , 2012.

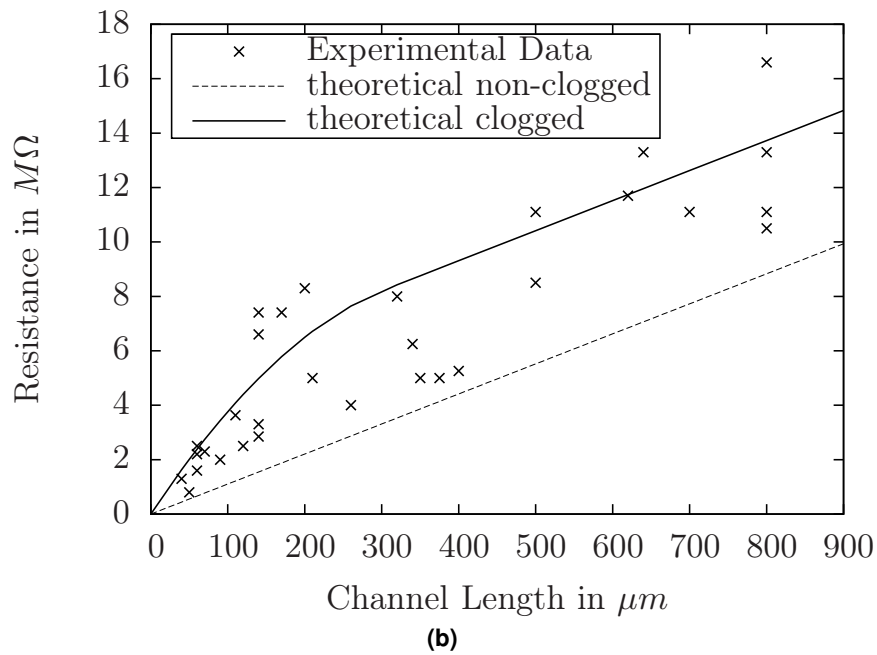
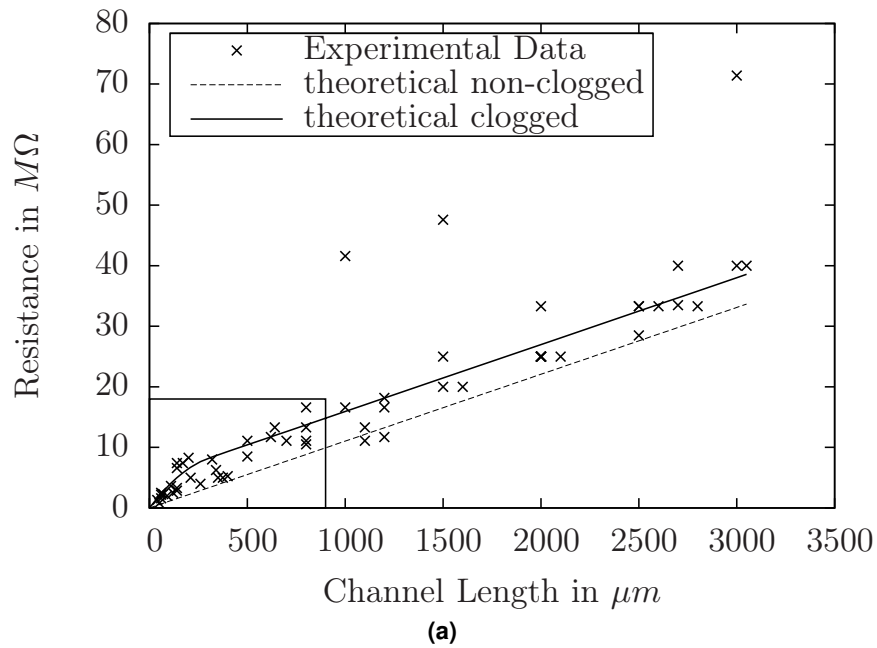


**Figure 5.4:** The resistance relative to the channel length: The simple (non-clogged) model based only on the homogeneous resistivity of Neurobasal underestimates the real resistivity for short channels (mean squared error,  $MSE: 73.204M\Omega^2$ ). The proposed resistivity model that incorporates clogging of the channel entrances offers a better approximation of the real data ( $MSE: 47.269M\Omega^2$ ). (a) Full range plot: the outliers with very high resistances are probably a result of further channel clogging due to e.g. micro-fabrication defects. (b) Detail plot for the short channel lengths, corresponding to the box in (a).

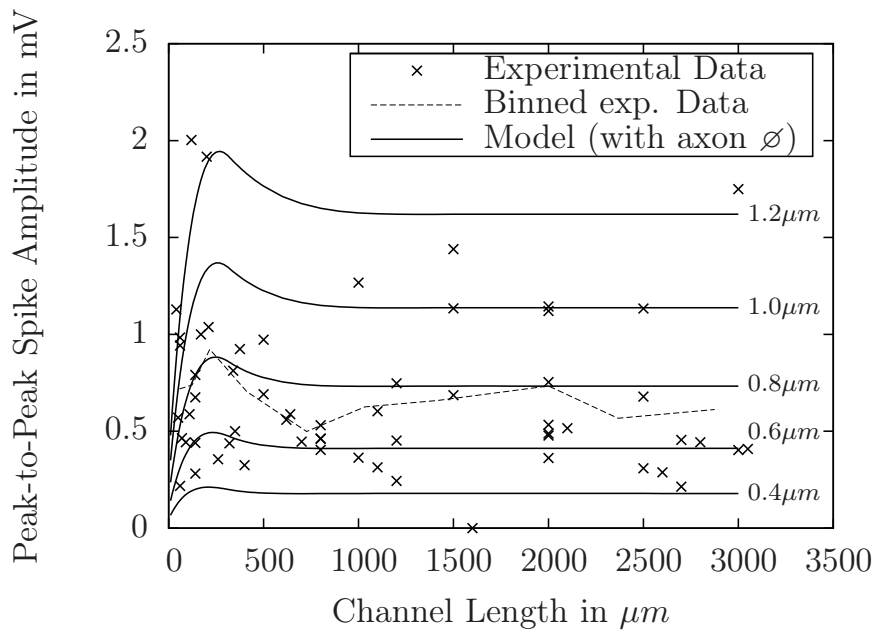


**Figure 5.5:** Maximum spike amplitude relative to the channel length: The experimental data show little or no correlation to the channel length. When binning the experimental data (6 data points each were averaged in x and y value) a rise-maximum-plateau structure becomes visible. The compartment model shows the same structure. Neurite diameters used in the model: 0.4 $\mu m$ , 0.6 $\mu m$ , 0.8 $\mu m$ , 1.0 $\mu m$ , 1.2 $\mu m$  (from bottom to top)



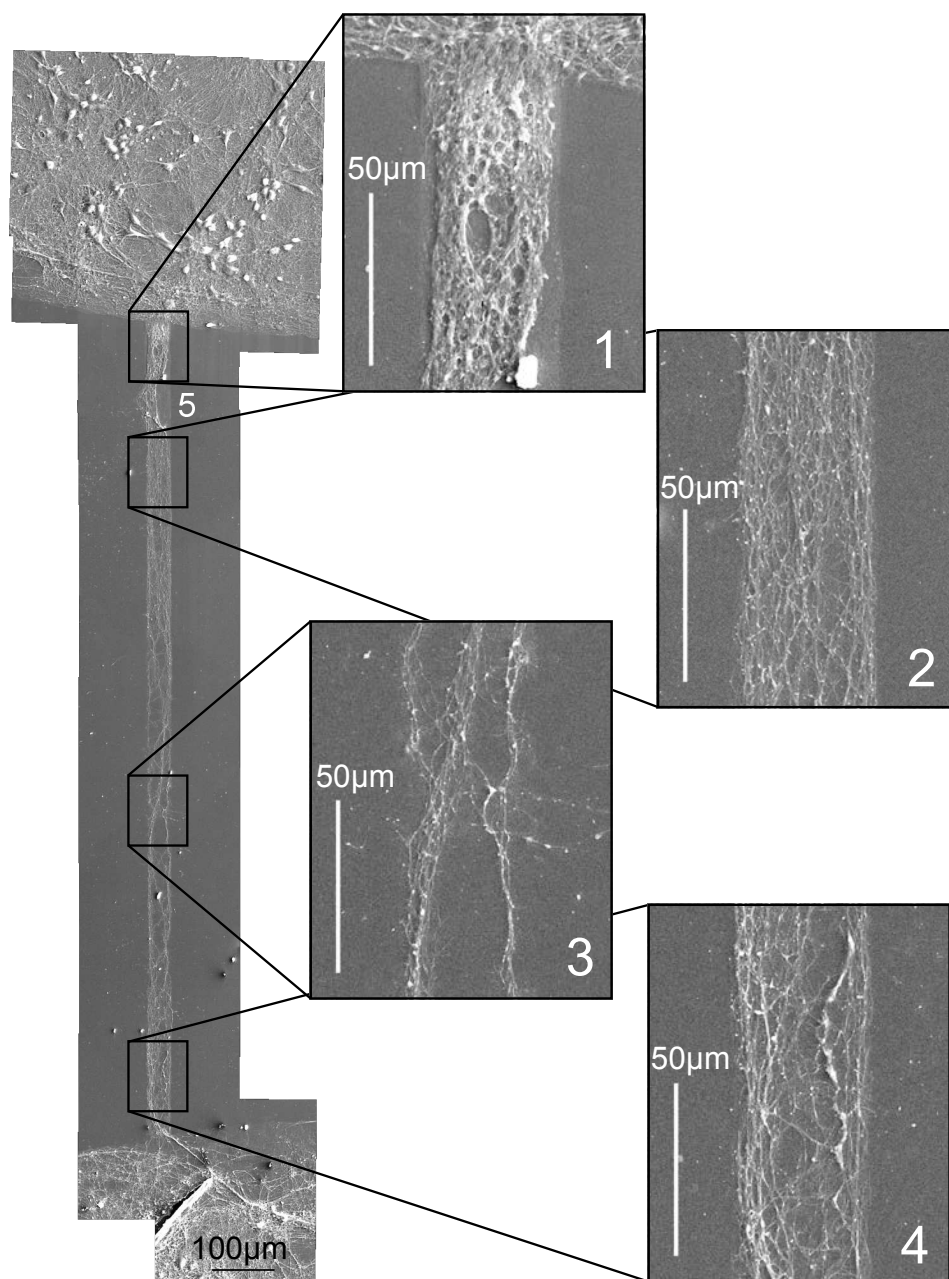


**Figure 5.6:** On the left is the stitched SEM image of the first device, showing the complete  $\mu$ -channel between the two culture wells. The zoom boxes highlight the different neurite/cell densities in the  $\mu$ -channel. Close to the culture wells (boxes 1 and 4) the neurite/cell density is high, consistent with the postulated channel clog. In the middle section of the  $\mu$ -channel (boxes 2 and 3) the neurite density is lower. At 5 the preparation got damaged, most likely during the detachment of the PDMS overlay.

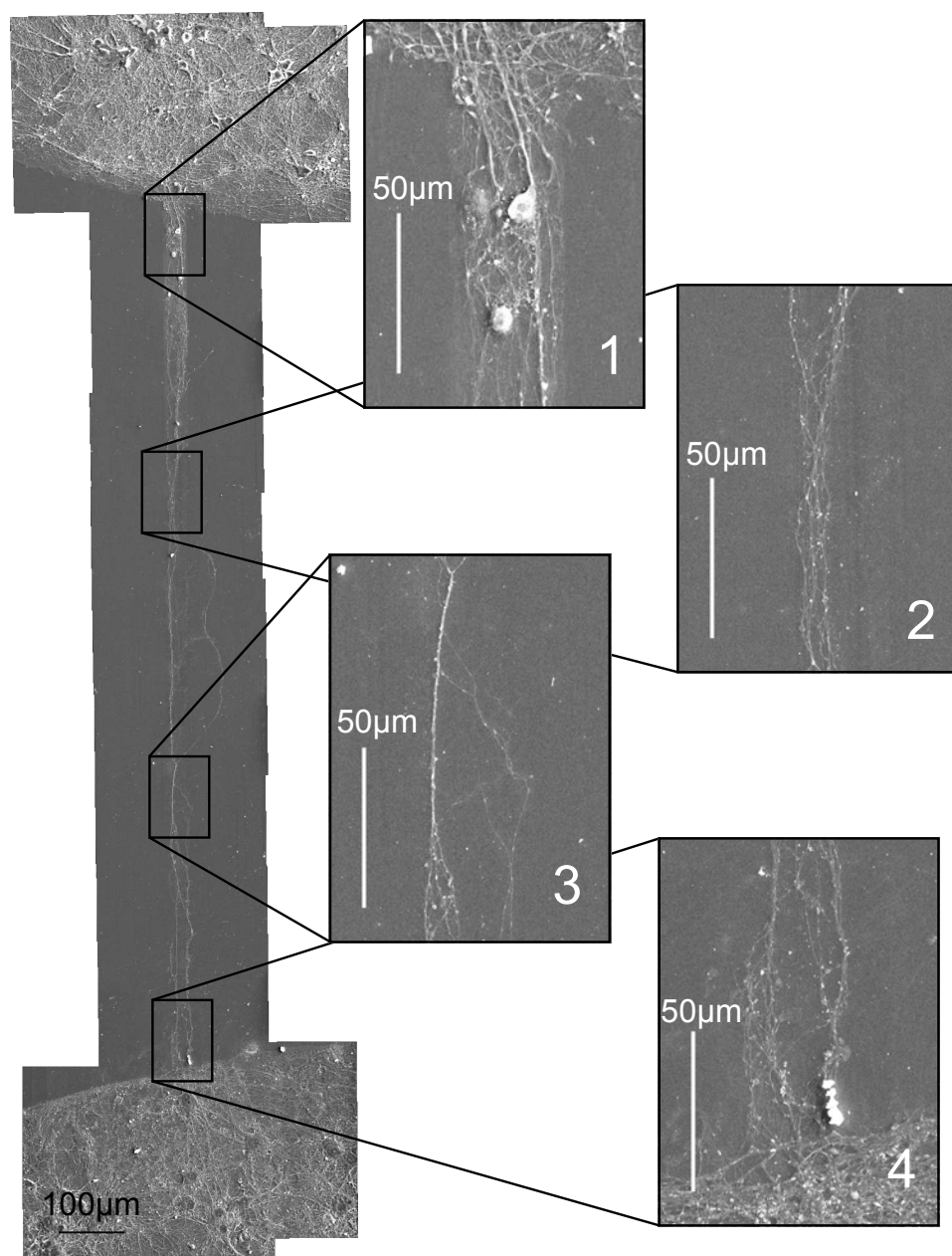


**Figure 5.7:** SEM image of the second device. Analog to Fig. 5.6 the full  $\mu$ -channel is shown to the left and the zoom boxes on the right show higher neurite density at the  $\mu$ -channel entrances (boxes 1 and 4) than in the middle section of the  $\mu$ -channel (boxes 2 and 3). In contrast to the first device the overall neurite/cell density in the  $\mu$ -channel is lower.

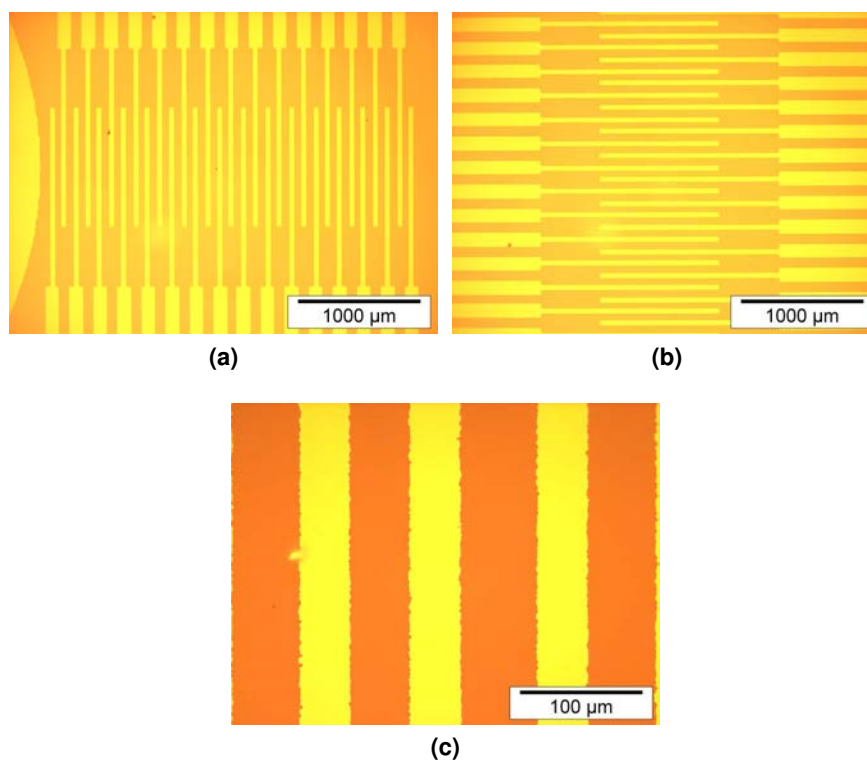


**Figure 5.8:** Light microscopy images (Olympus BX61) of the multi electrode array (MEA) substrates fabricated for the improved experiment. The images were taken to ensure that there are no short circuits between the electrodes. On the left side of (a) the ground electrode (for setting the potential of the left well to zero) can be seen. The width of the electrodes in (c) (bright yellow) is  $41\mu\text{m}$ , the gap widths (dark, orange) range from  $48\mu\text{m}$  to  $63\mu\text{m}$ . The gap width variation and the jagged edges result from the use of low resolution photomasks.



## Chapter 6

### Conclusions

This thesis focused on several engineering aspects of in-vitro  $\mu$ -channel devices.

#### 6.1 Summary of results

Spike sorting has been evaluated with signals from two  $\mu$ -channel devices (chapter 2). The signals of the device with the lower signal/noise ratio of 7.7 yielded 2 spike units, the signals of the second device with the higher signal/noise ratio of up to 34.1 yielded 9 spike units.

For the analysis a standard spike sorting software package (SpikeOMatic, Pouzat, 2012) was used. While for the signal with two spike units the standard approach of 2D-PCA followed by k-means clustering was sufficient, the 2D-PCA representation of the 9 spike units could not properly separate the 9 spike units. Therefore, a different approach was used: the k-means algorithm was applied directly on the spike sweeps. Using this 200-dimensional vector space (the sweeps had a length of 200 samples) the k-means algorithm could successfully separate all spike units. Observation: Several of the 9 units had a quite similar spike shape, a positive first phase followed by a negative second phase. The spike shapes differed only by small extra phases seemingly "piggy-packed" onto the basic two phase shape. The cause for this effect is still unknown.

One of the most important results of the thesis is the `OlPlot` data viewer in chapter 3. It is capable of visualizing time series datasets, event and interval annotations independent of the actual amount of data. As its paint time usually remains between 4 and 20ms, data navigation is possible interactively in real-time allowing

quick and intuitive inspection of datasets. This represents an important qualitative improvement over previous visualization techniques that were practically limited to a maximum of 10-20 minutes of recording time. The performance improvement was possible due to a combination of algorithms for hierarchic data reduction, Level of Detail (LoD) visualization and Out-of-Core processing. `OlPlot` could become a versatile tool for all kinds of experiments that produce large time series datasets, even beyond electrophysiology.

Chapter 4 documents several methods that were developed towards continuous electrophysiology long-term monitoring of neuron development. The StarPoM device improved the PoM (Polymer-on-MEA) fabrication technology by integrating both  $\mu$ -channel and well features into a multi-level SU-8 soft-lithography master using a substrate-integrated chrome mask and backside exposure. Together with a custom aligner the new fabrication method sufficiently augmented alignment accuracy to move from 1D PoM designs to the 2D StarPoM design. The 2D design allowed to connect 8 small culture wells with  $\mu$ -channels to a large central culture chamber. Electrodes were placed in the  $\mu$ -channels to record action potentials from the neurite connections between the confined neuron populations.

The StarPoM device was then used for one of the first reported continuous long-term monitoring of electrophysiological activity during neuron development in the first 14 days of growth in the device. Visible neuron signals appeared between day 4 and 5. Maximum spike amplitudes kept then rising over the 14 days up to 3.16mV. Average spike amplitudes however, soon stabilized between day 6 and 8 around 0.1 - 0.3mV. Spiking frequency in general kept rising until day 12 and then - depending on channel and spike cluster - either stagnated or slightly increased/decreased towards the end of the 14 days.

For the analysis of the data, a performance optimized tool-chain has been created to cope with the large datasets. Where possible, the tool-chain used an out-of-core processing design pattern; file I/O was implemented via 64 bit memory mapping which simplified the main loop as only array-to-array operations were needed. Such modules implemented in C++ usually achieved processing speeds matching (or exceeding) the hard disk throughput of 60-120 MiB/s.

The newly developed `ISI viewer` software was used to discover correlations between spike clusters of the 14 day recording. It revealed short-term ISI "spikes" which seem to correspond to direct neuron-neuron connections, wider ISI "hats" which fall into the temporal range of bursts and slow synaptic transmissions and ISI "sub-noise" sections which could be used to detect inhibition between neurons.

The analysis of how  $\mu$ -channel length influences the signal amplitude contributed to a better understanding of the signal generation biophysics in  $\mu$ -channels (chapter 5 and Wang, Riss, Buitrago, and Claverol-Tintur , 2012). Recordings from 59 devices with varying  $\mu$ -channel lengths have been analyzed; large spike amplitudes were measured for both long but also for short  $\mu$ -channels.

A passive cable simulation model with backward euler solver has been developed. It showed that for  $\mu$ -channels with length  $< 250\mu\text{m}$  the signal amplitude rises rapidly with length up to 2mV, beyond 250 $\mu\text{m}$  the signal amplitude stabilizes on a lower level due to a phase cancellation effect.

One of the contributing factors to the steep increase of amplitudes for short channels is channel clogging. Cells and debris enter the  $\mu$ -channel from the culture well and block the  $\mu$ -channel at the entrance. This channel clog increases the extra-cellular resistivity and causes a larger voltage drop during action potentials leading to larger spike amplitudes. Experimental end-to-end resistance measurements of the  $\mu$ -channels confirm the clog model and indicate a 4-fold increase in clog resistivity which is consistent with previously published data (Dworak and Bruce C. Wheeler, 2008).

## 6.2 Outlook

The  $\mu$ -channel technology in general shows a large potential for future applications in in-vitro neuron development research, drug testing and probably also for in-vivo applications. Its strengths are: ease of use, a signal amplification effect, fixed neuron-electrode association and the integration of neuron/neurite growth confinement/patterning.

A near-term research focus could be to improve spike sorting and spike cluster tracking over time. In this project we saw datasets that were very differently suited to spike sorting. The dataset from chapter 2 - an end-to-end recording from a 1600 $\mu\text{m}$  long  $\mu$ -channel - offered very long spikes resulting in sweeps of 200 samples. These long sweeps also showed very characteristic spike forms that further facilitated spike sorting so that spike clusters could clearly be differentiated due to the "white space" between the cluster sweeps (Fig. 2.7). The dataset in chapter 4 - a mid-channel recording from a 200 $\mu\text{m}$   $\mu$ -channel - in contrast offered only very short spikes resulting in sweeps of 20 samples. Here, spike sorting yielded only suboptimal results and without any margin between the clusters sweeps.

Therefore, the first objective towards improving spike sorting and cluster tracking should be to find the  $\mu$ -channel geometry that is best suited for optimal spike clustering efficiency. Once a good spike shape separability has been achieved, algorithms will need to be developed that can handle both spike sorting without prior knowledge about the number of spike clusters and the tracking of spike cluster development over time.





### 6.3 Publications and Presentations

#### Publications

Ricardo Morales, Michael Riss, Ling Wang, Rosalina Gavin, Jose Antonio Del Rio, Ramon Alcubilla, and Enric Claverol-Tinture (2008). “Integrating multi-unit electrophysiology and plastic culture dishes for network neuroscience”. In: *Lab on a Chip* 8 (11), pp. 1896–1905. URL: <http://dx.doi.org/10.1039/b802165a>

Ling Wang, Michael Riss, Jennifer Olmos Buitrago, and Enric Claverol-Tinturé (Feb. 15, 2012). “Biophysics of microchannel-enabled neuron-electrode interfaces”. In: *Journal of Neural Engineering* 9 (2). PMID: 22333069, p. 026010. ISSN: 1741-2552. DOI: 10.1088/1741-2560/9/2/026010. URL: <http://www.ncbi.nlm.nih.gov/pubmed/22333069>

#### Presentations

Michael Riss and Enric Claverol-Tinturé (Sept. 2006). “Star-shaped Polymer-on-Multielectrode (PoM) arrays for interfacing with neurons”. In: 32nd International Conference on Micro- and Nano- Engineering 2006. Barcelona, Spain, Fig. 6.1

Michael Riss and Enric Claverol-Tinturé (Nov. 2007). “Star-shaped Polymer-on-Multielectrode (PoM) arrays for interfacing with neurons”. In: 1st IBEC Symposium. Barcelona, Spain, Fig. 6.2

Michael Riss and Enric Claverol-Tinturé (Apr. 2009). “Characterizing the signal pickup of neuron signals in microchannels: Influence of channel length on signal amplitude”. In: 2nd IBEC Symposium. Barcelona, Spain, Fig. 6.3

Michael Riss, Jennifer Olmos Buitrago, and Enric Claverol-Tinturé (June 2010). “SEM-imaging of Neuron growth in Microchannel devices”. In: 3rd IBEC Symposium on Bioengineering and Nanomedicine. Barcelona, Spain, Fig. 6.4

Michael Riss and Enric Claverol-Tinturé (June 2010). “Axon-threaded  $\mu$ -tunnels as neural interface: In vitro model evaluation”. In: 39th Neural Interfaces Conference. Long Beach, California, USA, Fig. 6.5

Introduction

In this project we develop PoM (Polymer-on-Multielectrode) devices to culture neurons in confined spaces, guide the growth of their neurites and to record and stimulate their signals. We are specially interested in recording from small groups of neurons or even single neurons. Our current PoM device with a star-shaped geometry offers 8 wells, in which the neurons can grow in and a central chamber where their neurites can meet and interconnect.

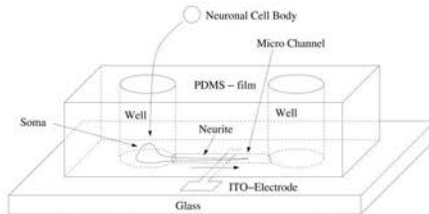


FIGURE 1: A PDMS film with wells and  $\mu$ -channels is placed on top of a glass substrate with open ITO-electrodes on its surface. Neurons are dropped into the wells and attach to the poly-L-lysine coated glass substrate at the bottom. The neurite growth is guided into the  $\mu$ -channels and across the ITO electrodes where the recording takes place.

Polymer-on-Multielectrode (PoM)

Neurons are confined between a glass substrate and a film of PDMS (Polydimethylsiloxane). They attach to the glass substrate on the bottom of wells in the PDMS film. They sprout dendrites and axons which grow on the glass substrate into  $\mu$ -channels in the PDMS film (Figure 1). The recording takes place in the channels. Spikes running down a neurite change the potential of the medium around the neurite. In enclosures as small as our  $\mu$ -channels (16 $\mu$ m) this potential change can be recorded by extracellular electrodes.

MEMS-fabrication

- a ITO-coated glass substrate is treated with a standard one-pass photolithography process for etching the electrodes
- a SU-8 soft-lithography master is fabricated with a negative image of the  $\mu$ -channels and wells (Figure 2)
- a PDMS film is cured over the SU-8 master inheriting the  $\mu$ -channels and wells from the master as a positive (Figure 2)
- the PDMS film and the glass substrate with ITO electrodes are aligned and attached resulting in the final PoM device core (Figure 2.5)
- a PDMS ring and a 35mm petri dish with hole in the ground are placed on top of the core to provide a container for the cell culture medium (Figure 3)

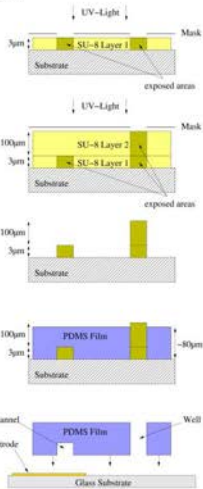


FIGURE 2: Soft-lithography process for the production of PDMS films with wells and  $\mu$ -channels (in development). For the  $\mu$ -channels and the wells we need SU-8 structures of different height. The  $\mu$ -channels have a height of 3  $\mu$ m and the wells a height of 100  $\mu$ m. Therefore the SU-8 masters are done in a two step process. The first SU-8 layer is coated and exposed but before developing it the second layer is coated, exposed and then both layers are developed simultaneously. PDMS is spun in a thin (60-100 $\mu$ m) layer and cured on the SU-8 master. After curing the PDMS film is peeled off and mounted on the glass substrate with ITO electrodes.



FIGURE 3: Assembly for a PoM device: The glass substrate with the ITO electrodes makes up the base. Mounted on top is a 35mm petri dish to hold the culture medium. A PDMS ring between glass substrate and petri dish seals the construct.

Star-shaped PoM device

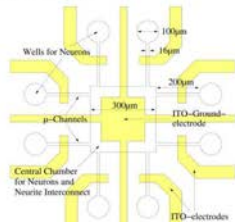


FIGURE 4: The star-shaped design offers 8 wells and one central chamber for neurons to grow and 8  $\mu$ -channels for recording. It is suited for one central and 8 satellite neuron populations. The electrical signals between the central and the satellite populations can be recorded.

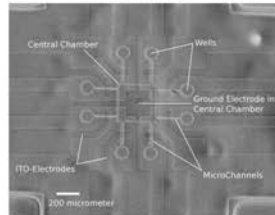


FIGURE 5: A top-view phase-contrast image of star-device prototype displaying the schedule alignment accuracy with our custom made aligner. The alignment error is below 30  $\mu$ m.

Cell Culture and Plating

The devices are pretreated with poly-L-lysine to ensure adhesion. Neurons from the hippocampus of embryonic mice (16 days old) are chemically and mechanically dissociated and plated on the devices. The neurons are kept alive in Neurobasal culture medium (Neurobasal Base, 2% B27 supplement, 2mM L-Glutamine, 20  $\mu$ g/ml Gentamicin).

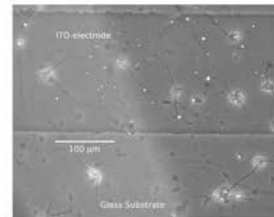


FIGURE 6: Preliminary biocompatibility test showing a group of unpatterned neurons on a glass substrate with ITO electrodes on day 4 after plating.

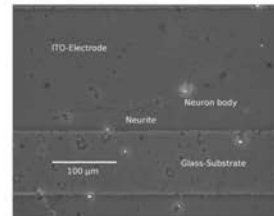


FIGURE 7: A single neuron on a ITO electrode in a culture with very low density on day 6 after plating.

References

- Claverol-Tinturé E, Ghazizadeh M, Fumara F, Rowell X, Calabrony J: Multielectrode arrays with elastomeric microstructures for neuronal patterning towards interfacing with uni-dimensional neuronal networks. *Journal of Neural Engineering* 2:L1-L7 (2005)
- E. Claverol-Tinturé, J. Calabrony, X. Rowell: Multisite recording of extracellular potentials produced by microchannel-confined neurons in-vitro. *IEEE Transactions on Biomedical Engineering*, available online

Acknowledgements:

This work was funded by the Generalitat de Catalunya, the Ministerio de Educación y Ciencia and by the EU.

Figure 6.1: MNE 2006 Poster

Introduction

In this project we develop PoM (Polymer-on-Multielectrode) devices to culture neurons in confined spaces, guide the growth of their neurites and to record and stimulate their signals. We are especially interested in recording from small groups of neurons or even single neurons. Our current PoM device with a star-shaped geometry offers 8 wells, in which the neurons can grow in and a central chamber where their neurites can meet and interconnect.

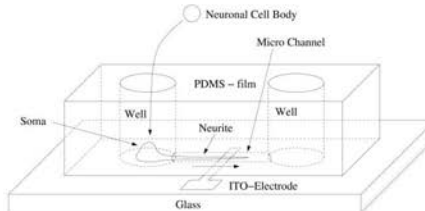


FIGURE 1: A PDMS film with wells and  $\mu$ -channels is placed on top of a glass substrate with open ITO electrodes on its surface. Neurons are dropped into the wells and attach to the poly-L-lysine coated glass substrate at the bottom. The neurite growth is guided into the  $\mu$ -channels and across the ITO electrodes where the recording takes place.

Polymer-on-Multielectrode (PoM)

Neurons are confined between a glass substrate and a film of PDMS (Polydimethylsiloxane). They attach to the glass substrate on the bottom of wells in the PDMS film. They sprout dendrites and axons which grow on the glass substrate into  $\mu$ -channels in the PDMS film (Figure 1). The recording takes place in the channels. Spikes running down a neurite change the potential of the medium around the neurite. In enclosures as small as our  $\mu$ -channels (16x4.5  $\mu$ m) this potential change can be recorded by extracellular electrodes.

MEMS-fabrication

- an ITO-coated glass substrate is treated with a standard one-pass photolithography process for etching the electrodes
- a SU-8 soft-lithography master is fabricated with a negative image of the  $\mu$ -channels and wells (Figure 3)
- a PDMS film is cured over the SU-8 master inheriting the  $\mu$ -channels and wells from the master as a positive (Figure 2)
- the PDMS film and the glass substrate with ITO electrodes are aligned and attached resulting in the final PoM device core (Figure 2.6)

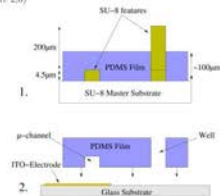


FIGURE 2: 1. Soft lithography of the polymer film: PDMS is spun onto a master with SU-8 features for  $\mu$ -channels and wells. The PDMS cures on the master and can be peeled off as a film. 2. Assembly of the device: The PDMS film is aligned to the glass substrate with the ITO-electrodes and then lowered to attach to it.

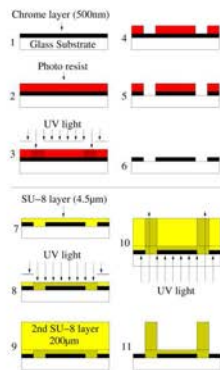


FIGURE 3: Fabrication of the soft lithography SU-8 master. The challenge is the mask alignment for two SU-8 layers on a glass substrate as all these materials are transparent and cannot be seen in the aligner. Therefore first a chrome layer is evaporated onto the glass substrate and one mask image is transferred to this chrome layer (steps 1-6). Then the first SU-8 layer can be deposited. The alignment of the second mask to the "embedded" chrome mask in step 8 is possible due to the good contrast of the chrome mask. After the exposure of the first, thin SU-8 layer a second, thick SU-8 layer is deposited (step 9). The thick layer is exposed from the back-side<sup>1</sup> of the glass substrate through the embedded chrome mask (step 10).

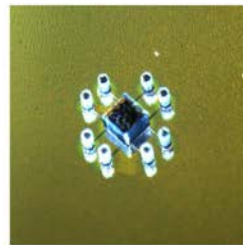


FIGURE 4: Closeup picture of the finished SU-8 soft lithography master with an optical microscope. The chrome layer is illuminated with a distant fluorescent light and the SU-8 structures were illuminated with a strong light source from the sides.

Star-shaped PoM device

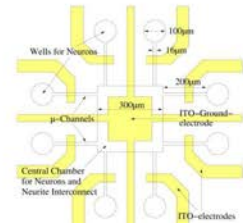


FIGURE 5: The star-shaped design offers 8 wells and one central chamber for neurons to grow and 8  $\mu$ -channels for recording. It is suited for one central and 8 satellite neuron populations. The electrical signals between the central and the satellite populations can be recorded.

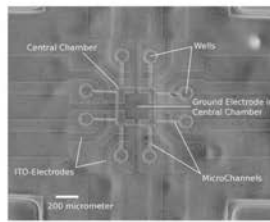


FIGURE 6: A top-view phase-contrast image of star-device prototype displaying the achievable alignment accuracy with our custom made aligner. The alignment error is below 30  $\mu$ m.

Cell Culture and Plating

The devices are pretreated with poly-L-lysine to ensure adhesion. Neurons from the hippocampus of embryonic mice (16 days old) are chemically and mechanically dissociated and plated on the devices. The neurons are kept alive in Neurobasal culture medium (Neurobasal Base, 2% B27 supplement, 20nM L-Glutamine, 20  $\mu$ g/ml Gentamicin).

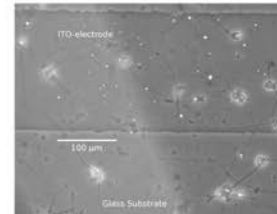


FIGURE 7: Preliminary biocompatibility test showing a group of un-patterned neurons on a glass substrate with ITO electrodes on day 4 after plating.

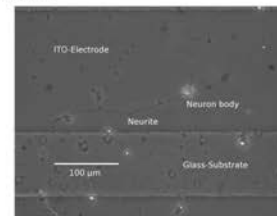


FIGURE 8: A single neuron on a ITO electrode in a culture with very low density on day 6 after plating.

References

Claverol-Tinturé E., Ghitadi M., Fimasa F., Rosell X., Cabestany J.: *Multielectrode arrays with elastomeric microstructures for neuronal patterning towards interfacing with uni-dimensional neuronal networks*. Journal of Neural Engineering 2:L1-L7 (2005)

E. Claverol-Tinturé, J. Cabestany, X. Rosell: *Multisite recording of extracellular potentials produced by microchannel-confined neurons in-vitro*. IEEE Transactions on Biomedical Engineering, available online

<sup>1</sup> Mark C Peterman, Philip Haic, D M Bloom and Harvey A Felmans: *Building thick photoresist structures from the bottom up*. J. Microscop. Microeng. 13 (2003) 380-382.

Acknowledgements

This work was funded by the Generalitat de Catalunya, the Ministerio de Educación y Ciencia and by the EU.

Figure 6.2: IBEC Symposium 2007 Poster



Characterizing the signal pickup of neuron signals in microchannels:  
Influence of of channel length on signal amplitude

Michael Riss (mrisss@eel.upc.edu), Enric Claverol-Tintur  (claverol@eel.upc.edu)  
Neuroengineering, Institut de Bioenginyeria de Catalunya (IBEC), Barcelona, Spain

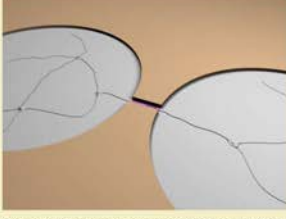


**Technology**

The development of a reliable Neuron-Machine Interface is an important key aspect of Neuroengineering. A promising approach is to culture neurons in devices with embedded microchannels. During the growth neurons extend neurites through the channels. Action potentials propagating along the neurites through the channels cause an electrical potential difference between the channel entrances which can be recorded by electrodes.

This technology offers several advantages:

- Easy handling and a very high success rate
- Very stable neuron-electrode assignment
- Good signal/noise ratio



**Project**

In order to better understand the signal pickup dynamics of the microchannel and to optimize its geometry we investigate the influence of the microchannel length on the amplitude of the recorded signals.

In this project an experiment series with 60 microchannel devices has been conducted. The channel lengths varied from 60  $\mu\text{m}$  to 3000  $\mu\text{m}$ . Neurons were cultured in the devices, their signals recorded and the signal amplitudes were correlated with the channel lengths. Additionally models were developed to explain the experimental data.

FIGURE 1: Two culture chambers are connected with a microchannel. The neurons grow neurites through the channel. Action potentials propagating along the neurite across the channel cause a potential drop between the culture chambers which is picked up by electrodes in the culture chambers (not shown)

---

**Device Fabrication**




FIGURE 2: The device in the right proportions: The wells are 6 mm high and 6 mm in diameter. The microchannel has a height of 3  $\mu\text{m}$  and a width of 25  $\mu\text{m}$ . The length of the channel here is 1000  $\mu\text{m}$  but has been varied in the experiment series between 60  $\mu\text{m}$  and 3000  $\mu\text{m}$ .

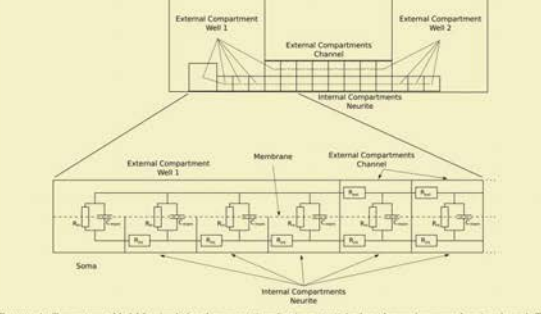


FIGURE 4: Compartment Model for simulating the propagation of action potentials along the neurite across the microchannel. The neurite is modeled as a passive cable, the action potential is simulated as a current injection at the axon hillock between soma and channel entrance.

---

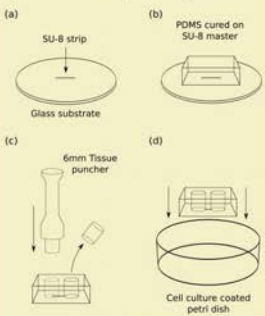


FIGURE 3: Device Fabrication: (a) a softlithography master with a 1 cm long, 25  $\mu\text{m}$  wide and 3  $\mu\text{m}$  high SU-8 strip on a glass substrate is fabricated (b) PDMS is poured and cured 6 mm thick on the softlithography master. After peeling off the PDMS from the softlithography master the SU-8 strip has left an embossed microstructure in the PDMS. (c) two holes of 6 mm diameter are punched at the end of the channels, the distance between the holes was varied from 60  $\mu\text{m}$  to 3000  $\mu\text{m}$  in this experiment series (d) the PDMS blocks are joined with cell culture coated petri dishes to form the final microchannel device




FIGURE 5: The recording setup in an Aleria Biodevices prototype amplifier. The petri dish with the PDMS block contains six microchannel devices in parallel. Visible are the 12 culture wells (pink) and the electrodes descending into the wells.

---

**Acknowledgements**

This work was funded by the Generalitat de Catalunya.

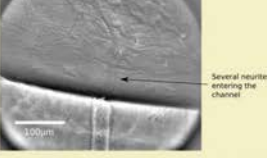


FIGURE 7: Phase contrast microscopy picture of the channel entrance. Several neurites originating from a cell cluster enter the channel.

---

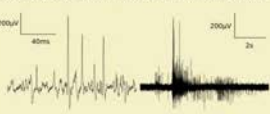


FIGURE 6: Example recordings from the devices, on the left a short epoch with single spikes, on the right a larger epoch showing a burst.

**References**

- 1: Ricardo Morales, Michael Riss, Ling Wang, Rosalina Govia, Jose Antonio Del Rio, Ramon Alcubilla, Enric Claverol-Tintur . *Integrating multi-unit electrophysiology and plastic culture dishes for network neuroscience*. *Lab on a Chip*, 8(11): 1896-1905, 2008.
- 2: Claverol-Tintur , E. and Cabestany, J. Rosell, X. *Multisite Recording of Extracellular Potentials Produced by Microchannel-Confined Neurons In-Vitro*. *IEEE Trans Biomed Eng*, 54(2): 331-335, 2007.
- 3: E. Claverol-Tintur , M. Ghanbari, F. Fumasa, X. Rosell, J. Cabestany. *Multielectrode arrays with elastomeric microstructured overlays for extracellular recordings from patterned neurons*. *J Neural Eng*, 2(2): L1-L7, 2005.

Figure 6.3: IBEC Symposium 2009 Poster



SEM-imaging of Neuron growth in Microchannel devices

Michael Riss<sup>1</sup>, Jennifer Olmos Buitrago<sup>2,3</sup>, Enric Claverol-Tinturé<sup>2,3</sup>

1. Universitat Politècnica de Catalunya, C/ Jordi Girona, 31. 08034 Barcelona – Spain, mrriss@eel.upc.edu

2. Institut de Bioenginyeria de Catalunya, Baldiri Reixac, 15-21, 08028 Barcelona – Spain

3. Aleria Biodevices, Baldiri Reixac, 15-21, 08028 Barcelona – Spain

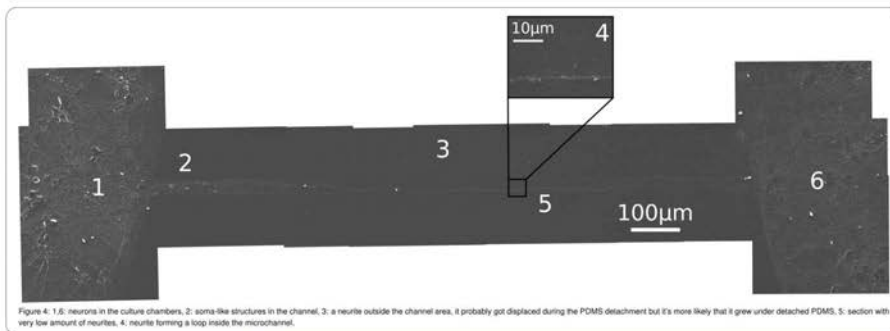
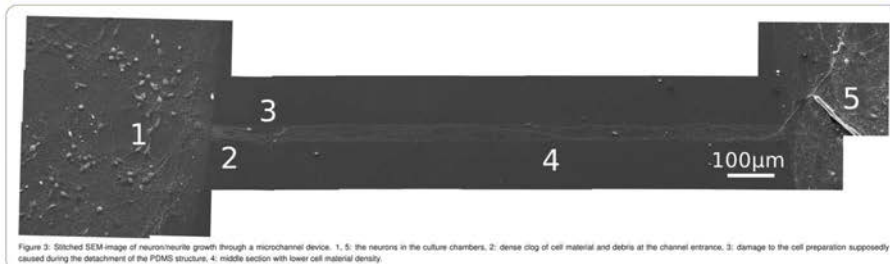
Neuroengineering

**Introduction:**  
Microchannel enabled devices are a promising technique to interface with neurons. Neurons grow in culture chambers that are connected by microchannels. Neurites (axons and dendrites) sprout through the microchannels connecting the neuron populations. Action potentials propagating along the axons in the microchannel cause an electrical potential which can be picked up by electrodes in the channel (Fig. 2). The confined area in the microchannels ensures good signal strength and stable long-term recording from the same neurons.

In previous work we investigated the influence of microchannel geometry on spike size (Fig. 1). While we could explain some aspects by numerical models (channel length has only little influence on spike size) other aspects like the large variance of spike sizes in general are still poorly understood. For this reason a series of Scanning Electron Microscopy (SEM) images of neurons in our devices has been taken to better understand neuron and neurite growth in our devices.

**Results and Conclusions:**  
The images (Fig. 3, 4) show that the neurites are small in comparison to the microchannels. The neurites have a lot of space and freedom to grow. We see channel sections with high neurite and cell material density (mostly at the channel entrances) and sections with low neurite density. Even soma-like structures can grow directly inside the channel (Fig. 4(2)). The large variability of neurite growth could explain the range in spike amplitudes and shapes we have been recording. Narrowing down the microchannels in future devices might help to better confine neurite growth and limit the variation in spike amplitudes and shapes.

Figure 1: In previous experiments the measured spike sizes were constant. The culture chambers are connected by with the length of the microchannels, a microchannel. Neurons were plated in the chambers and cultured for 14 days. After peeling off the PDMS neurite growth in microchannel devices, structure the cells were fixed for SEM imaging.



**Acknowledgements**  
This work was funded by the Generalitat de Catalunya and the Institut de Bioenginyeria de Catalunya (IBEC).

**References**  
1: Ricardo Morales, Michael Riss, Ling Wang, Rosalina Gavin, Jose Antonio Del Rio, Ramon Alcubilla, Enric Claverol-Tinturé. Integrating multi-unit electrophysiology and plastic culture dishes for network neuroscience. Lab on a Chip, 8(11): 1896-1905, 2008.  
2: Claverol-Tinturé, E. and Cabestany, J. Rosell, X. Multisite Recording of Extracellular Potentials Produced by Microchannel-Confined Neurons In-Vitro. IEEE Trans Biomed Eng. 54(2): 331-335, 2007.  
3: E. Claverol-Tinturé, M. Ghirardi, F. Fumara, X. Rosell, J. Cabestany. Multielectrode arrays with elastomeric microstructured overlays for extracellular recordings from patterned neurons. J Neural Eng. 2(2): L1-L7, 2005.

Figure 6.4: IBEC Symposium 2010 Poster

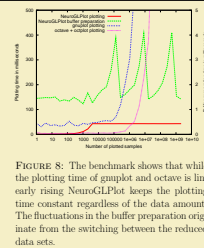
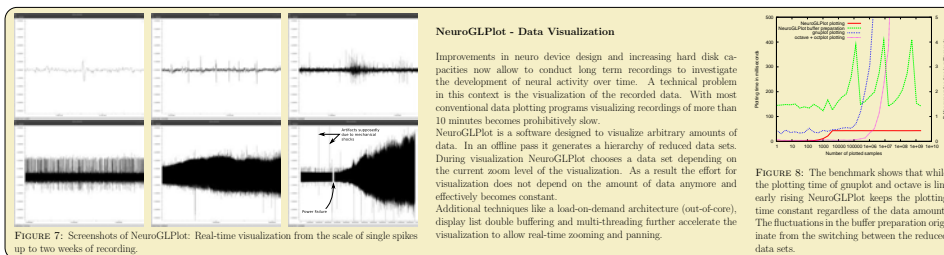
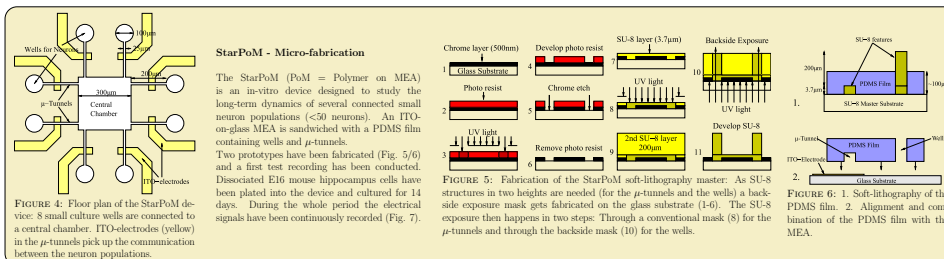
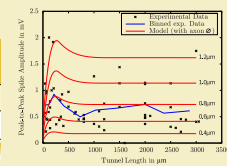
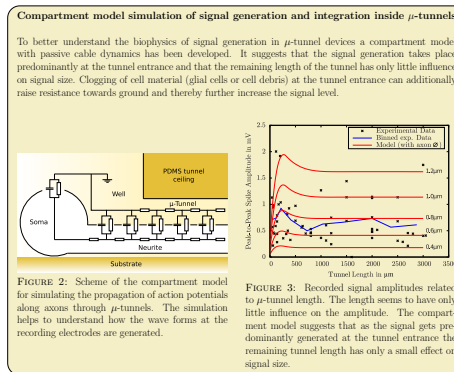
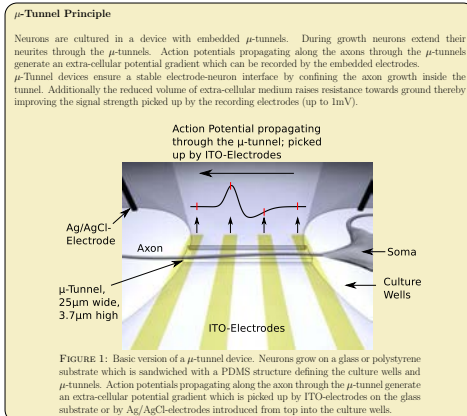


Axon-threaded  $\mu$ -tunnels as neural interface: In vitro model evaluation



Michael Riss<sup>1</sup>, Eric Claverol-Tintur<sup>2,3</sup>

1. Universitat Politècnica de Catalunya, C/ Jordi Girona, 31, 08034 Barcelona – Spain, mris@eel.upc.edu
2. Institut de Bioenginyeria de Catalunya, Baldric Reixac, 15-21, 08028 Barcelona – Spain
3. Aleria Biodevices, Baldric Reixac, 15-21, 08028 Barcelona – Spain



**Acknowledgments**  
This work was funded by the Generalitat de Catalunya, the Institut de Bioenginyeria de Catalunya (IBEC), the European Union (Project VSN) and the Ministerio de Ciencia e Innovación (Project RMEA).

**References**  
1: Ricardo Morales, Michael Riss, Ling Wang, Rosalina Gavin, Jose Antonio Del Rio, Ramon Aleualla, Eric Claverol-Tintur. *Integrating multi-unit electrophysiology and plastic culture dishes for network neuroscience*. Lab on a Chip, 8(11): 1896-1905, 2008.  
2: Claverol-Tintur, E. and Cabestany, J. Rosell, X. *Multisite Recording of Extracellular Potentials Produced by Microchannel-Confined Neurons In-Vitro*. IEEE Trans Biomed Eng, 54(2): 331-335, 2007.  
3: E. Claverol-Tintur, M. Ghirardi, F. Finamara, X. Rosell, J. Cabestany. *Multielectrode arrays with elastomeric microstructured overlays for extracellular recordings from patterned neurons*. J Neural Eng, 2(2): L1-L7, 2005.

Figure 6.5: Neural Interfaces 2010 Poster

## Chapter 7

### Bibliography

- Acikgoz, Canet, Mark A. Hempenius, Jurriaan Huskens, and G. Julius Vancso (Nov. 2011). “Polymers in conventional and alternative lithography for the fabrication of nanostructures”.  
In: *European Polymer Journal* 47 (11), pp. 2033–2052. ISSN: 0014-3057.  
DOI: 10.1016/j.eurpolymj.2011.07.025.  
URL: <http://www.sciencedirect.com/science/article/pii/S0014305711002916> (cit. on p. 18).
- Agay, Nirit, Eldad Yechiam, Ziv Carmel, and Yechiel Levkovitz (July 2010).  
“Non-specific effects of methylphenidate (Ritalin) on cognitive ability and decision-making of ADHD and healthy adults”.  
In: *Psychopharmacology* 210 (4). PMID: 20424828, pp. 511–519.  
ISSN: 1432-2072. DOI: 10.1007/s00213-010-1853-4.  
URL: <http://www.ncbi.nlm.nih.gov/pubmed/20424828>  
(cit. on p. 13).
- Albanese, Davide, Roberto Visintainer, Stefano Merler, Samantha Riccadonna, Giuseppe Jurman, and Cesare Furlanello (Feb. 29, 2012).  
“mlpy: Machine Learning Python”. In: *arXiv:1202.6548*.  
URL: <http://arxiv.org/abs/1202.6548> (cit. on p. 85).
- Alexa, Marc, Johannes Behr, Daniel Cohen-Or, Shachar Fleishman, David Levin, and Claudio T. Silva (Jan. 2003).  
“Computing and Rendering Point Set Surfaces”.  
In: *IEEE Transactions on Visualization and Computer Graphics* 9 (1), 3–15.  
ISSN: 1077-2626. DOI: 10.1109/TVCG.2003.1175093.

- URL: <http://dl.acm.org/citation.cfm?id=614289.614541>  
(cit. on p. 37).
- Alt, K W, C Jeunesse, C H Buitrago-Téllez, R Wächter, E Boës, and S L Pichler (May 22, 1997). “Evidence for stone age cranial surgery”.  
In: *Nature* 387 (6631). PMID: 9163419, p. 360. ISSN: 0028-0836.  
DOI: 10.1038/387360a0.  
URL: <http://www.ncbi.nlm.nih.gov/pubmed/9163419>  
(cit. on pp. 4, 14).
- Asai, Yoshiyuki, Tetyana I. Aksenova, and Alessandro E. P. Villa (2005).  
“On-Line Real-Time Oriented Application for Neuronal Spike Sorting with  
Unsupervised Learning”. In:  
*Artificial Neural Networks: Biological Inspirations – ICANN 2005*. Ed. by  
Włodzisław Duch, Janusz Kacprzyk, Erkki Oja, and Sławomir Zadrozny.  
Vol. 3696. Berlin, Heidelberg: Springer Berlin Heidelberg, pp. 109–114.  
ISBN: 978-3-540-28752-0. URL: [http://www.springerlink.com/  
content/c81ghpe555yk54ff/](http://www.springerlink.com/content/c81ghpe555yk54ff/) (cit. on p. 36).
- Bakkum, Douglas J., Zenas C. Chao, and Steve M. Potter (May 7, 2008).  
“Long-Term Activity-Dependent Plasticity of Action Potential Propagation  
Delay and Amplitude in Cortical Networks”.  
In: *PLoS ONE* 3 (5). PMID: 18461127 PMCID: PMC2324202.  
ISSN: 1932-6203. DOI: 10.1371/journal.pone.0002088.  
URL: [http://www.ncbi.nlm.nih.gov/pmc/articles/  
PMC2324202/](http://www.ncbi.nlm.nih.gov/pmc/articles/PMC2324202/) (cit. on p. 64).
- Bartels, Jess, Dinal Andreasen, Princewill Ehirim, Hui Mao, Steven Seibert,  
E. Joe Wright, and Philip Kennedy (Sept. 30, 2008). “Neurotrophic electrode:  
Method of assembly and implantation into human motor speech cortex”.  
In: *Journal of Neuroscience Methods* 174 (2), pp. 168–176. ISSN: 0165-0270.  
DOI: 10.1016/j.jneumeth.2008.06.030.  
URL: [http://www.sciencedirect.com/science/article/  
pii/S0165027008003865](http://www.sciencedirect.com/science/article/pii/S0165027008003865) (cit. on pp. 18, 36).
- Bean, Bruce P (June 2007). “The action potential in mammalian central neurons”.  
In: *Nature Reviews. Neuroscience* 8 (6). PMID: 17514198, pp. 451–465.  
ISSN: 1471-003X. DOI: 10.1038/nrn2148.  
URL: <http://www.ncbi.nlm.nih.gov/pubmed/17514198>  
(cit. on p. 15).
- Benveniste, Helene and Stephen J Blackband (June 2006).  
“Translational neuroscience and magnetic-resonance microscopy”.  
In: *Lancet neurology* 5 (6). PMID: 16713925, pp. 536–544. ISSN: 1474-4422.  
DOI: 10.1016/S1474-4422(06)70472-0.  
URL: <http://www.ncbi.nlm.nih.gov/pubmed/16713925>  
(cit. on p. 14).
- Berdichevsky, Yevgeny, Kevin J. Staley, and M. L. Yarmush (Apr. 21, 2010).  
“Building and manipulating neural pathways with microfluidics”.



- In: *Lab on a chip* 10 (8). PMID: 20358106 PMCID: 3137909, pp. 999–1004. ISSN: 1473-0197. DOI: 10.1039/b922365g (cit. on p. 18).
- Berdondini, Luca, Kilian Imfeld, Alessandro Maccione, Mariateresa Tedesco, Simon Neukom, Milena Koudelka-Hep, and Sergio Martinoia (Sept. 21, 2009). “Active pixel sensor array for high spatio-temporal resolution electrophysiological recordings from single cell to large scale neuronal networks”. In: *Lab on a Chip* 9 (18). PMID: 19704979, pp. 2644–2651. ISSN: 1473-0197. DOI: 10.1039/b907394a. URL: <http://www.ncbi.nlm.nih.gov/pubmed/19704979> (cit. on p. 17).
- Bezannila, Francisco (2006). “The action potential: from voltage-gated conductances to molecular structures”. In: *Biological Research* 39 (3). PMID: 17106575, pp. 425–435. ISSN: 0716-9760. DOI: /S0716-97602006000300005. URL: <http://www.ncbi.nlm.nih.gov/pubmed/17106575> (cit. on p. 15).
- Brecht, Michael, Michale S Fee, Olga Garaschuk, Fritjof Helmchen, Troy W Margrie, Karel Svoboda, and Pavel Osten (Oct. 20, 2004). “Novel approaches to monitor and manipulate single neurons in vivo”. In: *The Journal of Neuroscience: The Official Journal of the Society for Neuroscience* 24 (42). PMID: 15496655, pp. 9223–9227. ISSN: 1529-2401. DOI: 10.1523/JNEUROSCI.3344-04.2004. URL: <http://www.ncbi.nlm.nih.gov/pubmed/15496655> (cit. on p. 14).
- Bridge, Holly and Stuart Clare (Jan. 29, 2006). “High-resolution MRI: in vivo histology?”. In: *Philosophical Transactions of the Royal Society B: Biological Sciences* 361 (1465). PMID: 16553313 PMCID: 1626544, pp. 137–146. ISSN: 0962-8436. DOI: 10.1098/rstb.2005.1777 (cit. on p. 14).
- Burns, Kelly and Antoine Bechara (2007). “Decision making and free will: a neuroscience perspective”. In: *Behavioral Sciences & the Law* 25 (2). PMID: 17393405, pp. 263–280. ISSN: 0735-3936. DOI: 10.1002/bsl.751. URL: <http://www.ncbi.nlm.nih.gov/pubmed/17393405> (cit. on p. 13).
- Calhoun, V D and G D Pearlson (Jan. 2, 2012). “A selective review of simulated driving studies: Combining naturalistic and hybrid paradigms, analysis approaches, and future directions”. In: *NeuroImage* 59 (1). PMID: 21718791, pp. 25–35. ISSN: 1095-9572. DOI: 10.1016/j.neuroimage.2011.06.037. URL: <http://www.ncbi.nlm.nih.gov/pubmed/21718791> (cit. on p. 14).

Campenot, Robert B (Oct. 1, 1977).

“Local control of neurite development by nerve growth factor”.

In: *Proceedings of the National Academy of Sciences* 74 (10), pp. 4516–4519.  
ISSN: 0027-8424, 1091-6490.

URL: <http://www.pnas.org/content/74/10/4516> (cit. on p. 18).

Campo, A del and C Greiner (June 1, 2007).

“SU-8: a photoresist for high-aspect-ratio and 3D submicron lithography”.

In: *Journal of Micromechanics and Microengineering* 17 (6), R81–R95.  
ISSN: 0960-1317, 1361-6439. DOI: 10.1088/0960-1317/17/6/R01.

URL: <http://iopscience.iop.org/0960-1317/17/6/R01>  
(cit. on p. 19).

Chang, John C, Gregory J Brewer, and Bruce C Wheeler (Aug. 2003).

“A modified microstamping technique enhances polylysine transfer and neuronal cell patterning”.

In: *Biomaterials* 24 (17). PMID: 12742724, pp. 2863–2870. ISSN: 0142-9612.  
URL: <http://www.ncbi.nlm.nih.gov/pubmed/12742724>

(cit. on p. 120).

Chan, Hsiao-Lung, Tony Wu, Shih-Tseng Lee, Ming-An Lin, Shau-Ming He, Pei-Kuang Chao, and Yu-Tai Tsai (Mar. 2010). “Unsupervised wavelet-based spike sorting with dynamic codebook searching and replenishment”.

In: *Neurocomput.* 73 (7-9), 1513–1527. ISSN: 0925-2312.

DOI: 10.1016/j.neucom.2009.11.006.

URL: <http://dx.doi.org/10.1016/j.neucom.2009.11.006>  
(cit. on p. 36).

Chiappalone, Michela, Marco Bove, Alessandro Vato, Mariateresa Tedesco, and Sergio Martinoia (June 6, 2006). “Dissociated cortical networks show spontaneously correlated activity patterns during in vitro development”.

In: *Brain research* 1093 (1). PMID: 16712817, pp. 41–53. ISSN: 0006-8993.  
DOI: 10.1016/j.brainres.2006.03.049.

URL: <http://www.ncbi.nlm.nih.gov/pubmed/16712817>  
(cit. on pp. 64, 114).

Chiappalone, Michela, Paolo Massobrio, and Sergio Martinoia (July 2008).

“Network plasticity in cortical assemblies”. In: *The European journal of neuroscience* 28 (1). PMID: 18662344, pp. 221–237. ISSN: 1460-9568.

DOI: 10.1111/j.1460-9568.2008.06259.x.

URL: <http://www.ncbi.nlm.nih.gov/pubmed/18662344>  
(cit. on p. 64).

Chong, Seon-Ah, Iryna Benilova, Hamdy Shaban, Bart De Strooper, Herman Devijver, Dieder Moechars, Wolfgang Eberle, Carmen Bartic, Fred Van Leuven, and Geert Callewaert (Dec. 2011).

“Synaptic dysfunction in hippocampus of transgenic mouse models of Alzheimer’s disease: a multi-electrode array study”.

In: *Neurobiology of disease* 44 (3). PMID: 21807097, pp. 284–291.

- ISSN: 1095-953X. DOI: 10.1016/j.nbd.2011.07.006.  
 URL: <http://www.ncbi.nlm.nih.gov/pubmed/21807097>  
 (cit. on p. 64).
- Claverol-Tinture, E., J. Cabestany, and X. Rosell (Feb. 2007).  
 “Multisite Recording of Extracellular Potentials Produced by  
 Microchannel-Confined Neurons In-Vitro”.  
 In: *IEEE Transactions on Biomedical Engineering* 54 (2), pp. 331–335.  
 ISSN: 0018-9294. DOI: 10.1109/TBME.2006.880903.  
 URL: <http://ieeexplore.ieee.org/xpl/downloadCitations>  
 (cit. on pp. 22, 36, 64, 114).
- Claverol-Tinture, Enric and Jerome Pine (May 30, 2002).  
 “Extracellular potentials in low-density dissociated neuronal cultures”.  
 In: *Journal of Neuroscience Methods* 117 (1). PMID: 12084560, pp. 13–21.  
 ISSN: 0165-0270.  
 URL: <http://www.ncbi.nlm.nih.gov/pubmed/12084560>  
 (cit. on p. 19).
- Cook, Stephen A. (June 1983). “An overview of computational complexity”.  
 In: *Communications of the ACM* 26 (6), pp. 400–408. ISSN: 00010782.  
 DOI: 10.1145/358141.358144.  
 URL: <http://dl.acm.org/citation.cfm?id=358144>  
 (cit. on p. 37).
- Correa, Wagner T., James T. Klosowski, and Claudio T. Silva (2003).  
 “Visibility-Based Prefetching for Interactive Out-Of-Core Rendering”.  
 In: *Proceedings of the 2003 IEEE Symposium on Parallel and Large-Data  
 Visualization and Graphics*. PVG ’03.  
 Washington, DC, USA: IEEE Computer Society, 2–. ISBN: 0-7695-2091-X.  
 DOI: 10.1109/PVG.2003.10002.  
 URL: <http://dx.doi.org/10.1109/PVG.2003.10002>  
 (cit. on pp. 38, 77).
- Decker, Michael and Torsten Fleischer (Dec. 2008). “Contacting the  
 brain—aspects of a technology assessment of neural implants”.  
 In: *Biotechnology Journal* 3 (12). PMID: 19072906, pp. 1502–1510.  
 ISSN: 1860-7314. DOI: 10.1002/biot.200800225.  
 URL: <http://www.ncbi.nlm.nih.gov/pubmed/19072906>  
 (cit. on p. 13).
- Dittrich, Petra S and Andreas Manz (Mar. 2006).  
 “Lab-on-a-chip: microfluidics in drug discovery”.  
 In: *Nature Reviews. Drug Discovery* 5 (3). PMID: 16518374, pp. 210–218.  
 ISSN: 1474-1776. DOI: 10.1038/nrd1985.  
 URL: <http://www.ncbi.nlm.nih.gov/pubmed/16518374>  
 (cit. on p. 14).
- Dworak, Bradley J. and Bruce C. Wheeler (Nov. 18, 2008).  
 “Novel MEA platform with PDMS microtunnels enables the detection of

- action potential propagation from isolated axons in culture”. en.  
In: *Lab Chip* 9 (3), pp. 404–410. DOI: 10.1039/B806689B.  
URL: <http://pubs.rsc.org/en/Content/ArticleLanding/2009/LC/b806689b> (cit. on pp. 18, 36, 120, 126, 135).
- Erdal, Y. S and Ö. D Erdal (Sept. 1, 2011).  
“A review of trepanations in Anatolia with new cases”. en.  
In: *International Journal of Osteoarchaeology* 21 (5), pp. 505–534.  
ISSN: 1099-1212. DOI: 10.1002/oa.1154.  
URL: <http://onlinelibrary.wiley.com/doi/10.1002/oa.1154/abstract> (cit. on pp. 4, 14).
- Erickson, Jonathan, Angela Tooker, Y-C Tai, and Jerome Pine (Oct. 30, 2008).  
“Caged neuron MEA: a system for long-term investigation of cultured neural network connectivity”.  
In: *Journal of Neuroscience Methods* 175 (1). PMID: 18775453, pp. 1–16.  
ISSN: 0165-0270. DOI: 10.1016/j.jneumeth.2008.07.023.  
URL: <http://www.ncbi.nlm.nih.gov/pubmed/18775453>  
(cit. on pp. 17, 64).
- Eversmann, B., M. Jenkner, F. Hofmann, C. Paulus, R. Brederlow, B. Holzapfl, P. Fromherz, M. Merz, M. Brenner, M. Schreiter, et al. (Dec. 2003).  
“A 128 × 128 CMOS biosensor array for extracellular recording of neural activity”. English.  
In: *IEEE Journal of Solid-State Circuits* 38 (12), pp. 2306–2317.  
ISSN: 0018-9200. DOI: 10.1109/JSSC.2003.819174 (cit. on p. 17).
- Ferrández, J.M., V. Lorente, F. delaPaz, J.M. Cuadra, José Ramón Álvarez-Sánchez, and E. Fernández (Mar. 15, 2011).  
“A biological neuroprocessor for robotic guidance using a center of area method”. In: *Neurocomputing* 74 (8), pp. 1229–1236. ISSN: 0925-2312.  
DOI: 10.1016/j.neucom.2010.07.018.  
URL: <http://www.sciencedirect.com/science/article/pii/S0925231210003772> (cit. on p. 64).
- Fertig, Niels, Robert H Blick, and Jan C Behrends (June 2002).  
“Whole cell patch clamp recording performed on a planar glass chip.”  
In: *Biophysical Journal* 82 (6). PMID: 12023228 PMCID: 1302093,  
pp. 3056–3062. ISSN: 0006-3495 (cit. on p. 16).
- Fitzgerald, James J, Stéphanie P Lacour, Stephen B McMahon, and James W Fawcett (Mar. 2008). “Microchannels as axonal amplifiers”.  
In: *IEEE Transactions on Bio-Medical Engineering* 55 (3). PMID: 18334406,  
pp. 1136–1146. ISSN: 0018-9294. DOI: 10.1109/TBME.2007.909533.  
URL: <http://www.ncbi.nlm.nih.gov/pubmed/18334406>  
(cit. on p. 18).
- Forti, L, M Bossi, A Bergamaschi, A Villa, and A Malgaroli (Aug. 28, 1997).  
“Loose-patch recordings of single quanta at individual hippocampal synapses”. In: *Nature* 388 (6645). PMID: 9278048, pp. 874–878.

- ISSN: 0028-0836. DOI: 10.1038/42251.  
URL: <http://www.ncbi.nlm.nih.gov/pubmed/9278048>  
(cit. on p. 15).
- Franke, Felix, Michal Natora, Clemens Bousein, Matthias H. J. Munk, and Klaus Obermayer (Aug. 2010).  
“An online spike detection and spike classification algorithm capable of instantaneous resolution of overlapping spikes”.  
In: 29 (1-2). PMID: 19499318 PMCID: 2950077, pp. 127–148.  
ISSN: 0929-5313. DOI: 10.1007/s10827-009-0163-5 (cit. on p. 21).
- Gold, Carl, Darrell A Henze, Christof Koch, and György Buzsáki (May 2006).  
“On the origin of the extracellular action potential waveform: A modeling study”.  
In: *Journal of Neurophysiology* 95 (5). PMID: 16467426, pp. 3113–3128.  
ISSN: 0022-3077. DOI: 10.1152/jn.00979.2005.  
URL: <http://www.ncbi.nlm.nih.gov/pubmed/16467426>  
(cit. on p. 19).
- Gong, Gaolang, Yong He, Luis Concha, Catherine Lebel, Donald W Gross, Alan C Evans, and Christian Beaulieu (Mar. 2009).  
“Mapping anatomical connectivity patterns of human cerebral cortex using in vivo diffusion tensor imaging tractography”. In: *Cerebral Cortex (New York, N.Y.: 1991)* 19 (3). PMID: 18567609, pp. 524–536. ISSN: 1460-2199.  
DOI: 10.1093/cercor/bhn102.  
URL: <http://www.ncbi.nlm.nih.gov/pubmed/18567609>  
(cit. on p. 14).
- Greengard, P (Nov. 2, 2001). “The neurobiology of slow synaptic transmission”.  
In: *Science (New York, N.Y.)* 294 (5544). PMID: 11691979, pp. 1024–1030.  
ISSN: 0036-8075. DOI: 10.1126/science.294.5544.1024.  
URL: <http://www.ncbi.nlm.nih.gov/pubmed/11691979>  
(cit. on p. 116).
- Gross, Charles G. (July 16, 1999).  
*Brain, vision, memory: tales in the history of neuroscience*. en. MIT Press.  
284 pp. ISBN: 9780262571357 (cit. on p. 14).
- Gross, Guenter (2011). “Multielectrode arrays”. In: *Scholarpedia* 6 (3), p. 5749.  
ISSN: 1941-6016. DOI: 10.4249/scholarpedia.5749.  
URL: [http://www.scholarpedia.org/article/Multielectrode\\_arrays](http://www.scholarpedia.org/article/Multielectrode_arrays) (cit. on p. 36).
- Gross, G.W., E. Rieske, G.W. Kreutzberg, and A. Meyer (Nov. 1977).  
“A new fixed-array multi-microelectrode system designed for long-term monitoring of extracellular single unit neuronal activity in vitro”.  
In: *Neuroscience Letters* 6 (2-3), pp. 101–105. ISSN: 0304-3940.  
DOI: 10.1016/0304-3940(77)90003-9.  
URL: <http://www.sciencedirect.com/science/article/pii/0304394077900039> (cit. on pp. 16, 36).

- Gross, G W, W Y Wen, and J W Lin (Dec. 1985). “Transparent indium-tin oxide electrode patterns for extracellular, multisite recording in neuronal cultures”. In: *Journal of Neuroscience Methods* 15 (3). PMID: 4094480, pp. 243–252. ISSN: 0165-0270.  
URL: <http://www.ncbi.nlm.nih.gov/pubmed/4094480> (cit. on p. 16).
- Hagmann, Patric, Maciej Kurant, Xavier Gigandet, Patrick Thiran, Van J Wedeen, Reto Meuli, and Jean-Philippe Thiran (2007). “Mapping human whole-brain structural networks with diffusion MRI”. In: *PloS One* 2 (7). PMID: 17611629, e597. ISSN: 1932-6203.  
DOI: 10.1371/journal.pone.0000597.  
URL: <http://www.ncbi.nlm.nih.gov/pubmed/17611629> (cit. on p. 14).
- Hamill, O P, A Marty, E Neher, B Sakmann, and F J Sigworth (Aug. 1981). “Improved patch-clamp techniques for high-resolution current recording from cells and cell-free membrane patches”. In: *Pflügers Archiv: European Journal of Physiology* 391 (2). PMID: 6270629, pp. 85–100. ISSN: 0031-6768.  
URL: <http://www.ncbi.nlm.nih.gov/pubmed/6270629> (cit. on p. 15).
- Hochberg, Leigh R., Mijail D. Serruya, Gerhard M. Friehs, Jon A. Mukand, Maryam Saleh, Abraham H. Caplan, Almut Branner, David Chen, Richard D. Penn, and John P. Donoghue (July 13, 2006). “Neuronal ensemble control of prosthetic devices by a human with tetraplegia”. In: *Nature* 442 (7099), pp. 164–171. ISSN: 0028-0836.  
DOI: 10.1038/nature04970.  
URL: <http://dx.doi.org/10.1038/nature04970> (cit. on p. 36).
- Hodgkin, A. L and A. F Huxley (Aug. 28, 1952). “A quantitative description of membrane current and its application to conduction and excitation in nerve”. In: *The Journal of Physiology* 117 (4), pp. 500–544. ISSN: 0022-3751, 1469-7793.  
URL: <http://jp.physoc.org/content/117/4/500> (cit. on p. 19).
- IEC (Nov. 2000). *IEC 60027-2, Second edition, 2000-11, Letter symbols to be used in electrical technology - Part 2: Telecommunications and electronics*. International Electrotechnical Commission (cit. on pp. 12, 36).
- Jackson, Andrew and Eberhard E Fetz (Nov. 2007). “Compact movable microwire array for long-term chronic unit recording in cerebral cortex of primates”. In: *Journal of Neurophysiology* 98 (5). PMID: 17855584, pp. 3109–3118. ISSN: 0022-3077. DOI: 10.1152/jn.00569.2007.  
URL: <http://www.ncbi.nlm.nih.gov/pubmed/17855584> (cit. on p. 36).
- James, Conrad D, Andrew J H Spence, Natalie M Dowell-Mesfin, Rifat J Hussain, Karen L Smith, Harold G Craighead, Michael S Isaacson,

- William Shain, and James N Turner (Sept. 2004). “Extracellular recordings from patterned neuronal networks using planar microelectrode arrays”. In: *IEEE Transactions on Bio-Medical Engineering* 51 (9). PMID: 15376512, pp. 1640–1648. ISSN: 0018-9294. DOI: 10.1109/TBME.2004.827252. URL: <http://www.ncbi.nlm.nih.gov/pubmed/15376512> (cit. on p. 17).
- Jonas, P, G Major, and B Sakmann (Dec. 1993). “Quantal components of unitary EPSCs at the mossy fibre synapse on CA3 pyramidal cells of rat hippocampus.” In: *The Journal of Physiology* 472. PMID: 7908327 PMCID: PMC1160505, pp. 615–663. ISSN: 0022-3751 (cit. on p. 115).
- Kennedy, P R (Sept. 1989). “The cone electrode: a long-term electrode that records from neurites grown onto its recording surface”. In: *Journal of Neuroscience Methods* 29 (3). PMID: 2796391, pp. 181–193. ISSN: 0165-0270. URL: <http://www.ncbi.nlm.nih.gov/pubmed/2796391> (cit. on pp. 18, 36).
- Kim, Hyung Joon, Jeong Won Park, Jae Woo Park, Jae Hwan Byun, Behrad Vahidi, Seog Woo Rhee, and Noo Li Jeon (Feb. 1, 2012). “Integrated Microfluidics Platforms for Investigating Injury and Regeneration of CNS Axons”. In: *Annals of biomedical engineering*. PMID: 22302320. ISSN: 1521-6047. DOI: 10.1007/s10439-012-0515-6. URL: <http://www.ncbi.nlm.nih.gov/pubmed/22302320> (cit. on p. 64).
- Knuth, Donald E. (Apr. 1976). “Big Omicron and big Omega and big Theta”. In: *ACM SIGACT News* 8 (2), pp. 18–24. ISSN: 01635700. DOI: 10.1145/1008328.1008329. URL: <http://dl.acm.org/citation.cfm?id=1008329> (cit. on p. 37).
- Kole, Maarten H P, Susanne U Ilschner, Björn M Kampa, Stephen R Williams, Peter C Ruben, and Greg J Stuart (Feb. 2008). “Action potential generation requires a high sodium channel density in the axon initial segment”. In: *Nature Neuroscience* 11 (2). PMID: 18204443, pp. 178–186. ISSN: 1097-6256. DOI: 10.1038/nn2040. URL: <http://www.ncbi.nlm.nih.gov/pubmed/18204443> (cit. on p. 124).
- Kress, Geraldine J. and Steven Mennerick (Jan. 12, 2009). “Action potential initiation and propagation: upstream influences on neurotransmission”. In: *Neuroscience* 158 (1). PMID: 18472347 PMCID: PMC2661755, pp. 211–222. ISSN: 0306-4522. DOI: 10.1016/j.neuroscience.2008.03.021. URL: <http://www.ncbi.nlm.nih.gov/pmc/articles/PMC2661755/> (cit. on p. 115).

Kruger, J. and R. Westermann (2003).

“Acceleration Techniques for GPU-based Volume Rendering”.

In: *Proceedings of the 14th IEEE Visualization 2003 (VIS'03)*. VIS '03.

Washington, DC, USA: IEEE Computer Society, 38–. ISBN: 0-7695-2030-8.

DOI: 10.1109/VIS.2003.10001.

URL: <http://dx.doi.org/10.1109/VIS.2003.10001>

(cit. on p. 38).

Kunnavakkam, Madanagopal V., F. M. Houlihan, M. Schlax, J. A. Liddle,

P. Kolodner, O. Nalamasu, and J. A. Rogers (Feb. 2003). “Low-cost, low-loss microlens arrays fabricated by soft-lithography replication process”.

In: *Applied Physics Letters* 82 (8), pp. 1152–1154. ISSN: 0003-6951.

DOI: 10.1063/1.1555694 (cit. on p. 113).

Lau, Adrian Y, Paul J Hung, Angela R Wu, and Luke P Lee (Dec. 2006).

“Open-access microfluidic patch-clamp array with raised lateral cell trapping sites”. In: *Lab on a Chip* 6 (12). PMID: 17203154, pp. 1510–1515.

ISSN: 1473-0197. DOI: 10.1039/b608439g.

URL: <http://www.ncbi.nlm.nih.gov/pubmed/17203154>

(cit. on p. 16).

Le Bihan, D, J F Mangin, C Poupon, C A Clark, S Pappata, N Molko, and H Chabriat (Apr. 2001).

“Diffusion tensor imaging: concepts and applications”. In: *Journal of*

*Magnetic Resonance Imaging: JMRI* 13 (4). PMID: 11276097, pp. 534–546.

ISSN: 1053-1807.

URL: <http://www.ncbi.nlm.nih.gov/pubmed/11276097>

(cit. on p. 14).

Lent, Roberto, Frederico A C Azevedo, Carlos H Andrade-Moraes, and

Ana V O Pinto (Jan. 2012). “How many neurons do you have? Some dogmas of quantitative neuroscience under revision”.

In: *The European Journal of Neuroscience* 35 (1). PMID: 22151227, pp. 1–9.

ISSN: 1460-9568. DOI: 10.1111/j.1460-9568.2011.07923.x.

URL: <http://www.ncbi.nlm.nih.gov/pubmed/22151227>

(cit. on p. 13).

Lewicki, M S (Nov. 1998). “A review of methods for spike sorting: the detection and classification of neural action potentials”.

In: *Network (Bristol, England)* 9 (4). PMID: 10221571, R53–78.

ISSN: 0954-898X.

URL: <http://www.ncbi.nlm.nih.gov/pubmed/10221571>

(cit. on p. 21).

Lichtman, Jeff W, Jean Livet, and Joshua R Sanes (June 2008).

“A technical approach to the connectome”.

In: *Nature reviews. Neuroscience* 9 (6). PMID: 18446160, pp. 417–422.

ISSN: 1471-0048. DOI: 10.1038/nrn2391.



- URL: <http://www.ncbi.nlm.nih.gov/pubmed/18446160>  
(cit. on p. 14).
- Luebke, David P (May 2001).  
“A Developer’s Survey of Polygonal Simplification Algorithms”.  
In: *IEEE Comput. Graph. Appl.* 21 (3), 24–35. ISSN: 0272-1716.  
URL: <http://dl.acm.org/citation.cfm?id=616070.618821>  
(cit. on p. 37).
- Lynch, Gary, Linda C Palmer, and Christine M Gall (Aug. 2011).  
“The likelihood of cognitive enhancement”. In: *Pharmacology, Biochemistry,  
and Behavior* 99 (2). PMID: 21215768, pp. 116–129. ISSN: 1873-5177.  
DOI: 10.1016/j.pbb.2010.12.024.  
URL: <http://www.ncbi.nlm.nih.gov/pubmed/21215768>  
(cit. on p. 13).
- Maher, M P, J Pine, J Wright, and Y C Tai (Feb. 1, 1999). “The neurochip: a new  
multielectrode device for stimulating and recording from cultured neurons”.  
In: *Journal of Neuroscience Methods* 87 (1). PMID: 10065993, pp. 45–56.  
ISSN: 0165-0270.  
URL: <http://www.ncbi.nlm.nih.gov/pubmed/10065993>  
(cit. on p. 36).
- Mahoney, Melissa J, Ruth R Chen, Jian Tan, and W Mark Saltzman (Mar. 2005).  
“The influence of microchannels on neurite growth and architecture”.  
In: *Biomaterials* 26 (7). PMID: 15350782, pp. 771–778. ISSN: 0142-9612.  
DOI: 10.1016/j.biomaterials.2004.03.015.  
URL: <http://www.ncbi.nlm.nih.gov/pubmed/15350782>  
(cit. on p. 17).
- Margrie, Troy W, Michael Brecht, and Bert Sakmann (July 2002).  
“In vivo, low-resistance, whole-cell recordings from neurons in the  
anaesthetized and awake mammalian brain”. In: *Pflügers Archiv: European  
Journal of Physiology* 444 (4). PMID: 12136268, pp. 491–498.  
ISSN: 0031-6768. DOI: 10.1007/s00424-002-0831-z.  
URL: <http://www.ncbi.nlm.nih.gov/pubmed/12136268>  
(cit. on p. 16).
- Martinez, Juan, Carlos Pedreira, Matias J Ison, and Rodrigo Quian Quiroga  
(Nov. 15, 2009). “Realistic simulation of extracellular recordings”.  
In: *Journal of Neuroscience Methods* 184 (2). PMID: 19703490, pp. 285–293.  
ISSN: 1872-678X. DOI: 10.1016/j.jneumeth.2009.08.017.  
URL: <http://www.ncbi.nlm.nih.gov/pubmed/19703490>  
(cit. on pp. 30, 114).
- Maynard, Edwin M., Craig T. Nordhausen, and Richard A. Normann (Mar. 1997).  
“The Utah Intracortical Electrode Array: A recording structure for potential  
brain-computer interfaces”. In: *Electroencephalography and Clinical  
Neurophysiology* 102 (3), pp. 228–239. ISSN: 0013-4694.  
DOI: 10.1016/S0013-4694(96)95176-0.

- URL: <http://www.sciencedirect.com/science/article/pii/S0013469496951760> (cit. on p. 36).
- Merz, M. and P. Fromherz (May 1, 2005). “Silicon Chip Interfaced with a Geometrically Defined Net of Snail Neurons”. en.  
In: *Advanced Functional Materials* 15 (5), pp. 739–744. ISSN: 1616-3028.  
DOI: 10.1002/adfm.200400316. URL: <http://onlinelibrary.wiley.com/doi/10.1002/adfm.200400316/abstract>  
(cit. on pp. 17, 120).
- Morales, Ricardo, Michael Riss, Ling Wang, Rosalina Gavin, Jose Antonio Del Rio, Ramon Alcubilla, and Enric Claverol-Tinture (2008). “Integrating multi-unit electrophysiology and plastic culture dishes for network neuroscience”. In: *Lab on a Chip* 8 (11), pp. 1896–1905.  
URL: <http://dx.doi.org/10.1039/b802165a>  
(cit. on pp. 18, 21, 23, 24, 27, 36, 52, 54, 64, 118, 120, 122, 137).
- Moulin, Céline, Alain Glière, Daniel Barbier, Sebastien Joucla, Blaise Yvert, Pascal Mailley, and Régis Guillemaud (Feb. 2008). “A new 3-D finite-element model based on thin-film approximation for microelectrode array recording of extracellular action potential”.  
In: *IEEE Transactions on Bio-Medical Engineering* 55 (2 Pt 1). PMID: 18270005, pp. 683–692. ISSN: 1558-2531.  
DOI: 10.1109/TBME.2007.903522.  
URL: <http://www.ncbi.nlm.nih.gov/pubmed/18270005>  
(cit. on p. 20).
- Nam, Yoonkey, John C Chang, Bruce C Wheeler, and Gregory J Brewer (Jan. 2004). “Gold-coated microelectrode array with thiol linked self-assembled monolayers for engineering neuronal cultures”. In: *IEEE Transactions on Bio-Medical Engineering* 51 (1). PMID: 14723505, pp. 158–165.  
ISSN: 0018-9294. DOI: 10.1109/TBME.2003.820336.  
URL: <http://www.ncbi.nlm.nih.gov/pubmed/14723505>  
(cit. on p. 17).
- Neher, E (May 1992). “Nobel lecture. Ion channels for communication between and within cells.”  
In: *The EMBO Journal* 11 (5). PMID: 1374709 PMCID: 556623,  
pp. 1672–1679. ISSN: 0261-4189 (cit. on p. 15).
- Novellino, A., Bibiana Scelfo, T. Palosaari, A. Price, Tomasz Sobanski, T. J. Shafer, A. F. M. Johnstone, G. W. Gross, A. Gramowski, O. Schroeder, et al. (Apr. 27, 2011). “Development of Micro-Electrode Array Based Tests for Neurotoxicity: Assessment of Interlaboratory Reproducibility with Neuroactive Chemicals”.  
In: *Frontiers in Neuroengineering* 4. PMID: 21562604 PMCID: PMC3087164. ISSN: 1662-6443. DOI: 10.3389/fneng.2011.00004.  
URL: <http://www.ncbi.nlm.nih.gov/pmc/articles/PMC3087164/> (cit. on p. 63).

- O'Doherty, Joseph E., Mikhail A. Lebedev, Peter J. Ifft, Katie Z. Zhuang, Solaiman Shokur, Hannes Bleuler, and Miguel A. L. Nicolelis (Nov. 10, 2011). "Active tactile exploration using a brain-machine-brain interface". In: *Nature* 479 (7372), pp. 228–231. ISSN: 0028-0836. DOI: 10.1038/nature10489. URL: <http://dx.doi.org/10.1038/nature10489> (cit. on p. 36).
- Ong, Wee-Liat, Kum-Cheong Tang, Ajay Agarwal, Ranganathan Nagarajan, Lian-Wee Luo, and Levent Yobas (Oct. 2007). "Microfluidic integration of substantially round glass capillaries for lateral patch clamping on chip". In: *Lab on a Chip* 7 (10). PMID: 17896022, pp. 1357–1366. ISSN: 1473-0197. DOI: 10.1039/b707439e. URL: <http://www.ncbi.nlm.nih.gov/pubmed/17896022> (cit. on p. 16).
- Pakkenberg, Bente, Dorte Pelvig, Lisbeth Marner, Mads J Bundgaard, Hans Jørgen G Gundersen, Jens R Nyengaard, and Lisbeth Regeur (Feb. 2003). "Aging and the human neocortex". In: *Experimental Gerontology* 38 (1-2). PMID: 12543266, pp. 95–99. ISSN: 0531-5565. URL: <http://www.ncbi.nlm.nih.gov/pubmed/12543266> (cit. on p. 13).
- Perkins, Katherine L (June 30, 2006). "Cell-attached voltage-clamp and current-clamp recording and stimulation techniques in brain slices". In: *Journal of Neuroscience Methods* 154 (1-2). PMID: 16554092, pp. 1–18. ISSN: 0165-0270. DOI: 10.1016/j.jneumeth.2006.02.010. URL: <http://www.ncbi.nlm.nih.gov/pubmed/16554092> (cit. on p. 15).
- Peterman, Mark C, Philip Huie, D M Bloom, and Harvey A Fishman (May 1, 2003). "Building thick photoresist structures from the bottom up". In: *Journal of Micromechanics and Microengineering* 13 (3), pp. 380–382. ISSN: 0960-1317. DOI: 10.1088/0960-1317/13/3/305. URL: <http://iopscience.iop.org/0960-1317/13/3/305> (cit. on p. 67).
- Phan, K Luan, Tor Wager, Stephan F Taylor, and Israel Liberzon (June 2002). "Functional neuroanatomy of emotion: a meta-analysis of emotion activation studies in PET and fMRI". In: *NeuroImage* 16 (2). PMID: 12030820, pp. 331–348. ISSN: 1053-8119. DOI: 10.1006/nimg.2002.1087. URL: <http://www.ncbi.nlm.nih.gov/pubmed/12030820> (cit. on p. 14).
- Pine, J (Feb. 1980). "Recording action potentials from cultured neurons with extracellular microcircuit electrodes". In: *Journal of Neuroscience Methods* 2 (1). PMID: 7329089, pp. 19–31. ISSN: 0165-0270.

- URL: <http://www.ncbi.nlm.nih.gov/pubmed/7329089>  
(cit. on p. 36).
- Polasek, Katharine H., Harry A. Hoyen, Michael W. Keith, Robert F. Kirsch, and Dustin J. Tyler (Oct. 2009).  
“Stimulation Stability and Selectivity of Chronically Implanted Multicontact Nerve Cuff Electrodes in the Human Upper Extremity”.  
In: *IEEE transactions on neural systems and rehabilitation engineering : a publication of the IEEE Engineering in Medicine and Biology Society* 17 (5).  
PMID: 19775987 PMID: 2927980, pp. 428–437. ISSN: 1534-4320.  
DOI: 10.1109/TNSRE.2009.2032603 (cit. on p. 36).
- Porada, I, I Bondar, W B Spatz, and J Krüger (Jan. 31, 2000).  
“Rabbit and monkey visual cortex: more than a year of recording with up to 64 microelectrodes”.  
In: *Journal of Neuroscience Methods* 95 (1). PMID: 10776811, pp. 13–28.  
ISSN: 0165-0270.  
URL: <http://www.ncbi.nlm.nih.gov/pubmed/10776811>  
(cit. on p. 36).
- Potter, Steve M. and Thomas B. DeMarse (Sept. 30, 2001).  
“A new approach to neural cell culture for long-term studies”.  
In: *Journal of Neuroscience Methods* 110 (1-2), pp. 17–24. ISSN: 0165-0270.  
DOI: 10.1016/S0165-0270(01)00412-5.  
URL: <http://www.sciencedirect.com/science/article/B6T04-43YR2C9-3/2/aeade8a968d0a645c7befba49990e653>  
(cit. on pp. 16, 36, 113).
- Pouzat, Christophe (2012). *The new version (in progress) of SpikeOMatic. A free software for spike sorting*.  
URL: [http://www.biomedicale.univ-paris5.fr/phycserv/C\\_Pouzat/newSOM/newSOMtutorial/newSOMtutorial.html](http://www.biomedicale.univ-paris5.fr/phycserv/C_Pouzat/newSOM/newSOMtutorial/newSOMtutorial.html)  
(cit. on pp. 29, 133).
- Quiroga, Rodrigo (2007). “Spike sorting”. In: *Scholarpedia* 2 (12), p. 3583.  
ISSN: 1941-6016. DOI: 10.4249/scholarpedia.3583. URL:  
[http://www.scholarpedia.org/article/Spike\\_sorting](http://www.scholarpedia.org/article/Spike_sorting)  
(cit. on p. 21).
- Rall, Wilfrid (2009). “Rall model”. In: *Scholarpedia* 4 (4), p. 1369.  
ISSN: 1941-6016. DOI: 10.4249/scholarpedia.1369.  
URL: [http://www.scholarpedia.org/article/Rall\\_model](http://www.scholarpedia.org/article/Rall_model)  
(cit. on p. 19).
- Raymond, Eric S. (Oct. 3, 2003). *The Art of UNIX Programming*. 1st ed.  
Addison-Wesley Professional. 560 pp. ISBN: 0131429019 (cit. on p. 76).
- Rijal, Sabnam O and Guenter W Gross (Aug. 30, 2008).  
“Dissociation constants for GABA(A) receptor antagonists determined with neuronal networks on microelectrode arrays”.  
In: *Journal of neuroscience methods* 173 (2). PMID: 18590768, pp. 183–192.

- ISSN: 0165-0270. DOI: 10.1016/j.jneumeth.2008.05.025.  
 URL: <http://www.ncbi.nlm.nih.gov/pubmed/18590768>  
 (cit. on p. 64).
- Riss, Michael and Enric Claverol-Tinturé (Sept. 2006). “Star-shaped Polymer-on-Multielectrode (PoM) arrays for interfacing with neurons”. In: 32nd International Conference on Micro- and Nano- Engineering 2006. Barcelona, Spain (cit. on p. 137).
- (Nov. 2007). “Star-shaped Polymer-on-Multielectrode (PoM) arrays for interfacing with neurons”. In: 1st IBEC Symposium. Barcelona, Spain (cit. on p. 137).
- (Apr. 2009). “Characterizing the signal pickup of neuron signals in microchannels: Influence of channel length on signal amplitude”. In: 2nd IBEC Symposium. Barcelona, Spain (cit. on p. 137).
- (June 2010). “Axon-threaded  $\mu$ -tunnels as neural interface: In vitro model evaluation”. In: 39th Neural Interfaces Conference. Long Beach, California, USA (cit. on p. 137).
- Riss, Michael, Jennifer Olmos Buitrago, and Enric Claverol-Tinturé (June 2010). “SEM-imaging of Neuron growth in Microchannel devices”. In: 3rd IBEC Symposium on Bioengineering and Nanomedicine. Barcelona, Spain (cit. on p. 137).
- Sabatini, B L and W G Regehr (Nov. 14, 1996). “Timing of neurotransmission at fast synapses in the mammalian brain”. In: *Nature* 384 (6605). PMID: 8906792, pp. 170–172. ISSN: 0028-0836. DOI: 10.1038/384170a0. URL: <http://www.ncbi.nlm.nih.gov/pubmed/8906792> (cit. on p. 115).
- Sah, P, S Hestrin, and R A Nicoll (Nov. 1990). “Properties of excitatory postsynaptic currents recorded in vitro from rat hippocampal interneurons.” In: *The Journal of Physiology* 430. PMID: 1982315 PMCID: 1181756, pp. 605–616. ISSN: 0022-3751 (cit. on p. 16).
- Salasin, John (May 1973). “Hierarchical storage in information retrieval”. In: *Communications of the ACM* 16 (5), pp. 291–295. ISSN: 00010782. DOI: 10.1145/362041.362196. URL: <http://dl.acm.org/citation.cfm?id=362196> (cit. on p. 37).
- Saniotis, Arthur and Maciej Henneberg (Sept. 2011). “Future Evolution of the Human Brain”. English. In: *Journal of Future Studies* 16 (1), pp. 1–18. URL: <http://www.jfs.tku.edu.tw/16-1/A01.pdf> (cit. on p. 13).
- Sayer, R J, M J Friedlander, and S J Redman (Mar. 1990). “The time course and amplitude of EPSPs evoked at synapses between pairs of CA3/CA1 neurons in the hippocampal slice”.

- In: *The Journal of neuroscience: the official journal of the Society for Neuroscience* 10 (3). PMID: 2319304, pp. 826–836. ISSN: 0270-6474.  
URL: <http://www.ncbi.nlm.nih.gov/pubmed/2319304>  
(cit. on p. 115).
- Segev, Idan, ed. (June 4, 1998).  
*Methods in Neuronal Modeling - 2nd Edition: From Ions to Networks*.  
second edition. A Bradford Book. 844 pp. ISBN: 0262112310  
(cit. on pp. 120, 124).
- Seo, J., C. Ionescu-Zanetti, J. Diamond, R. Lal, and L. P Lee (Mar. 2004).  
“Integrated multiple patch-clamp array chip via lateral cell trapping  
junctions”. English. In: *Applied Physics Letters* 84 (11), pp. 1973–1975.  
ISSN: 0003-6951. DOI: 10.1063/1.1650035 (cit. on p. 16).
- Shi, Peng, Stephane Nedelec, Hynek Wichterle, and Lance Kam (Apr. 21, 2010).  
“Combined Microfluidics / Protein Patterning Platform for Pharmacological  
Interrogation of Axon Pathfinding”.  
In: *Lab on a chip* 10 (8). PMID: 20358107 PMCID: 2867106, pp. 1005–1010.  
ISSN: 1473-0197. DOI: 10.1039/b922143c (cit. on p. 18).
- Shtark, M. B., A. S. Ratushnyak, L. V. Voskresenskaya, and S. N. Olenev (Sept.  
1974). “A multielectrode perfusion chamber for tissue culture research”.  
In: *Bulletin of Experimental Biology and Medicine* 78 (3), pp. 1090–1092.  
ISSN: 0007-4888, 1573-8221. DOI: 10.1007/BF00796678.  
URL: [http://www.springerlink.com/content/  
x212878213600742/](http://www.springerlink.com/content/x212878213600742/) (cit. on p. 16).
- Simeral, J D, S-P Kim, M J Black, J P Donoghue, and L R Hochberg (Apr. 2011).  
“Neural control of cursor trajectory and click by a human with tetraplegia  
1000 days after implant of an intracortical microelectrode array”.  
In: *Journal of Neural Engineering* 8 (2). PMID: 21436513, p. 025027.  
ISSN: 1741-2552. DOI: 10.1088/1741-2560/8/2/025027.  
URL: <http://www.ncbi.nlm.nih.gov/pubmed/21436513>  
(cit. on p. 36).
- Sporns, Olaf (Apr. 2011). “The human connectome: a complex network”.  
In: *Annals of the New York Academy of Sciences* 1224. PMID: 21251014,  
pp. 109–125. ISSN: 1749-6632.  
DOI: 10.1111/j.1749-6632.2010.05888.x.  
URL: <http://www.ncbi.nlm.nih.gov/pubmed/21251014>  
(cit. on p. 14).
- Steller, L, M Kreir, and R Salzer (Jan. 2012).  
“Natural and artificial ion channels for biosensing platforms”. In: *Analytical  
and Bioanalytical Chemistry* 402 (1). PMID: 22080413, pp. 209–230.  
ISSN: 1618-2650. DOI: 10.1007/s00216-011-5517-y.  
URL: <http://www.ncbi.nlm.nih.gov/pubmed/22080413>  
(cit. on p. 14).

- Stewart, Donald A, T R Gowrishankar, and James C Weaver (Sept. 2006).  
“Three dimensional transport lattice model for describing action potentials in axons stimulated by external electrodes”. In: *Bioelectrochemistry (Amsterdam, Netherlands)* 69 (1). PMID: 16443399, pp. 88–93.  
ISSN: 1567-5394. DOI: 10.1016/j.bioelechem.2005.11.004.  
URL: <http://www.ncbi.nlm.nih.gov/pubmed/16443399>  
(cit. on p. 20).
- Stieglitz, T. (July 29, 2010). “Neuroprothetik und Neuromodulation”.  
In: *Bundesgesundheitsblatt - Gesundheitsforschung - Gesundheitsschutz* 53 (8), pp. 783–790. ISSN: 1436-9990, 1437-1588.  
DOI: 10.1007/s00103-010-1093-0.  
URL: <http://www.springermedizin.de/neuroprothetik-und-neuromodulation/267014.html>  
(cit. on p. 18).
- Strickholm, A (July 1, 1961).  
“Impedance of a Small Electrically Isolated Area of the Muscle Cell Surface”.  
In: *The Journal of General Physiology* 44 (6). PMID: 19873540,  
pp. 1073–1088. ISSN: 0022-1295.  
URL: <http://www.ncbi.nlm.nih.gov/pubmed/19873540>  
(cit. on p. 15).
- Stühmer, W. and W. Almers (Feb. 1, 1982).  
“Photobleaching through glass micropipettes: sodium channels without lateral mobility in the sarcolemma of frog skeletal muscle”. en.  
In: *Proceedings of the National Academy of Sciences* 79 (3), pp. 946–950.  
ISSN: 0027-8424, 1091-6490.  
URL: <http://www.pnas.org/content/79/3/946> (cit. on p. 15).
- Sujith, O K (May 2008).  
“Functional electrical stimulation in neurological disorders”.  
In: *European journal of neurology: the official journal of the European Federation of Neurological Societies* 15 (5). PMID: 18394046, pp. 437–444.  
ISSN: 1468-1331. DOI: 10.1111/j.1468-1331.2008.02127.x.  
URL: <http://www.ncbi.nlm.nih.gov/pubmed/18394046>  
(cit. on p. 18).
- Suzuki, Ikurou, Yoshihiro Sugio, Yasuhiko Jimbo, and Kenji Yasuda (Mar. 2005).  
“Stepwise pattern modification of neuronal network in photo-thermally-etched agarose architecture on multi-electrode array chip for individual-cell-based electrophysiological measurement”.  
In: *Lab on a Chip* 5 (3). PMID: 15726199, pp. 241–247. ISSN: 1473-0197.  
DOI: 10.1039/b406885h.  
URL: <http://www.ncbi.nlm.nih.gov/pubmed/15726199>  
(cit. on p. 17).
- Tang, Y, J R Nyengaard, D M De Groot, and H J Gundersen (Sept. 1, 2001).  
“Total regional and global number of synapses in the human brain neocortex”.

- In: *Synapse (New York, N.Y.)* 41 (3). PMID: 11418939, pp. 258–273.  
ISSN: 0887-4476. DOI: 10.1002/syn.1083.  
URL: <http://www.ncbi.nlm.nih.gov/pubmed/11418939>  
(cit. on p. 13).
- Tan Kim Heok and D. Daman (July 26, 2004).  
“A review on level of detail”. English.  
In: *International Conference on Computer Graphics, Imaging and Visualization, 2004. CGIV 2004. Proceedings.*  
International Conference on Computer Graphics, Imaging and Visualization,  
2004. CGIV 2004. Proceedings. IEEE, pp. 70–75. ISBN: 0-7695-2178-9.  
DOI: 10.1109/CGIV.2004.1323963 (cit. on p. 37).
- Taylor, Anne M, Mathew Blurton-Jones, Seog Woo Rhee, David H Cribbs,  
Carl W Cotman, and Noo Li Jeon (Aug. 2005). “A microfluidic culture  
platform for CNS axonal injury, regeneration and transport”.  
In: *Nature Methods* 2 (8). PMID: 16094385, pp. 599–605. ISSN: 1548-7091.  
DOI: 10.1038/nmeth777.  
URL: <http://www.ncbi.nlm.nih.gov/pubmed/16094385>  
(cit. on p. 17).
- Thomas C A, Jr, P A Springer, G E Loeb, Y Berwald-Netter, and L M Okun  
(Sept. 1972). “A miniature microelectrode array to monitor the bioelectric  
activity of cultured cells”.  
In: *Experimental Cell Research* 74 (1). PMID: 4672477, pp. 61–66.  
ISSN: 0014-4827.  
URL: <http://www.ncbi.nlm.nih.gov/pubmed/4672477>  
(cit. on p. 16).
- Tikhonova, Anna, Carlos D. Correa, and Kwan-Liu Ma (2010). “Visualization by  
Proxy: A Novel Framework for Deferred Interaction with Volume Data”.  
In: *IEEE Transactions on Visualization and Computer Graphics* 16 (6),  
pp. 1551–1559. ISSN: 1077-2626. DOI:  
<http://doi.ieeecomputersociety.org/10.1109/TVCG.2010.215>  
(cit. on p. 38).
- Triaud, Frederique, Diane-Helene Clenet, Yves Cariou, Tanguy Le Neel,  
Delphine Morin, and Alain Truchaud (Dec. 1, 2003).  
“Evaluation of Automated Cell Culture Incubators”. en.  
In: *Journal of the Association for Laboratory Automation* 8 (6), pp. 82–86.  
ISSN: 2211-0682, 1540-0245.  
DOI: 10.1016/S1535-5535(03)00018-2.  
URL: <http://jla.sagepub.com/content/8/6/82> (cit. on p. 14).
- Tseng, Wan-Ting, Chen-Tung Yen, and Meng-Li Tsai (Oct. 15, 2011).  
“A bundled microwire array for long-term chronic single-unit recording in  
deep brain regions of behaving rats”.  
In: *Journal of Neuroscience Methods* 201 (2). PMID: 21889539, pp. 368–376.  
ISSN: 1872-678X. DOI: 10.1016/j.jneumeth.2011.08.028.



- URL: <http://www.ncbi.nlm.nih.gov/pubmed/21889539>  
(cit. on p. 36).
- Van Geit, W, E De Schutter, and P Achard (Nov. 2008).  
“Automated neuron model optimization techniques: a review”.  
In: *Biological Cybernetics* 99 (4-5). PMID: 19011918, pp. 241–251.  
ISSN: 1432-0770. DOI: 10.1007/s00422-008-0257-6.  
URL: <http://www.ncbi.nlm.nih.gov/pubmed/19011918>  
(cit. on p. 20).
- Wagenaar, Daniel A, Jerome Pine, and Steve M Potter (Sept. 30, 2004).  
“Effective parameters for stimulation of dissociated cultures using  
multi-electrode arrays”.  
In: *Journal of Neuroscience Methods* 138 (1-2). PMID: 15325108, pp. 27–37.  
ISSN: 0165-0270. DOI: 10.1016/j.jneumeth.2004.03.005.  
URL: <http://www.ncbi.nlm.nih.gov/pubmed/15325108>  
(cit. on p. 16).
- (2006). “An extremely rich repertoire of bursting patterns during the  
development of cortical cultures”.  
In: *BMC neuroscience* 7. PMID: 16464257, p. 11. ISSN: 1471-2202.  
DOI: 10.1186/1471-2202-7-11.  
URL: <http://www.ncbi.nlm.nih.gov/pubmed/16464257>  
(cit. on pp. 64, 116).
- Wald, Ingo, Andreas Dietrich, and Philipp Slusallek (2005). “An interactive  
out-of-core rendering framework for visualizing massively complex models”.  
In: *ACM SIGGRAPH 2005 Courses on - SIGGRAPH '05*.  
ACM SIGGRAPH 2005 Courses. Los Angeles, California, p. 17.  
DOI: 10.1145/1198555.1198756.  
URL: <http://dl.acm.org/citation.cfm?id=1198756>  
(cit. on pp. 38, 77).
- Wang, Ling (Dec. 15, 2011). “Microchannel enhanced neuron-computer  
interface: design, fabrication, biophysics of signal generation, signal strength  
optimization, and its applications to ion-channel screening and basic  
neuroscience research”. English. Universitat Politècnica de Catalunya.  
Departament d’Enginyeria de Sistemes, Automàtica i Informàtica Industrial.  
183 pp. URL: <http://hdl.handle.net/10803/52810> (cit. on p. 73).
- Wang, Ling, Michael Riss, Jennifer Olmos Buitrago, and Enric Claverol-Tinturé  
(Feb. 15, 2012).  
“Biophysics of microchannel-enabled neuron-electrode interfaces”.  
In: *Journal of Neural Engineering* 9 (2). PMID: 22333069, p. 026010.  
ISSN: 1741-2552. DOI: 10.1088/1741-2560/9/2/026010.  
URL: <http://www.ncbi.nlm.nih.gov/pubmed/22333069>  
(cit. on pp. 22, 34, 118, 119, 126, 134, 137).
- Wiltschko, Alexander B., Gregory J. Gage, and Joshua D. Berke (Aug. 15, 2008).  
“Wavelet Filtering before Spike Detection Preserves Waveform Shape and

Enhances Single-Unit Discrimination”. In: *Journal of neuroscience methods* 173 (1). PMID: 18597853 PMCID: PMC2602872, pp. 34–40.

ISSN: 0165-0270. DOI: 10.1016/j.jneumeth.2008.05.016

(cit. on p. 82).

Yamamoto, Jun and Matthew A Wilson (Oct. 2008).

“Large-scale chronically implantable precision motorized microdrive array for freely behaving animals”.

In: *Journal of Neurophysiology* 100 (4). PMID: 18667539, pp. 2430–2440.

ISSN: 0022-3077. DOI: 10.1152/jn.90687.2008.

URL: <http://www.ncbi.nlm.nih.gov/pubmed/18667539>

(cit. on p. 36).

Zhao, Siwei, Arnold Chen, Alexander Revzin, and Tingrui Pan (Nov. 26, 2010).

“Stereomask lithography (SML): a universal multi-object micro-patterning technique for biological applications”. en. In: *Lab Chip* 11 (2), pp. 224–230.

DOI: 10.1039/C0LC00275E. URL: <http://pubs.rsc.org/en/Content/ArticleLanding/2011/LC/c0lc00275e> (cit. on p. 36).

Zwicker, Matthias, Hanspeter Pfister, Jeroen van Baar, and Markus Gross (2001).

“Surface splatting”. In: *Proceedings of the 28th annual conference on Computer graphics and interactive techniques - SIGGRAPH '01*.

the 28th annual conference. Not Known, pp. 371–378.

DOI: 10.1145/383259.383300.

URL: <http://dl.acm.org/citation.cfm?id=383300>

(cit. on p. 37).

## **Chapter A**

### **Cluster Spike Amplitudes**

The figures with the amplitude development for each cluster have been moved into the appendix section as their value is unclear due to the kmeans spike clustering method. The kmeans spike clustering method sorts clusters by spike sweep shape which includes the amplitude. Thus it should group spike sweeps with similar amplitude and therefore amplitude development within a cluster will be limited. However, for completeness and to give an impression of the current state of cluster spike amplitude tracking these plots have been included as appendix chapter.

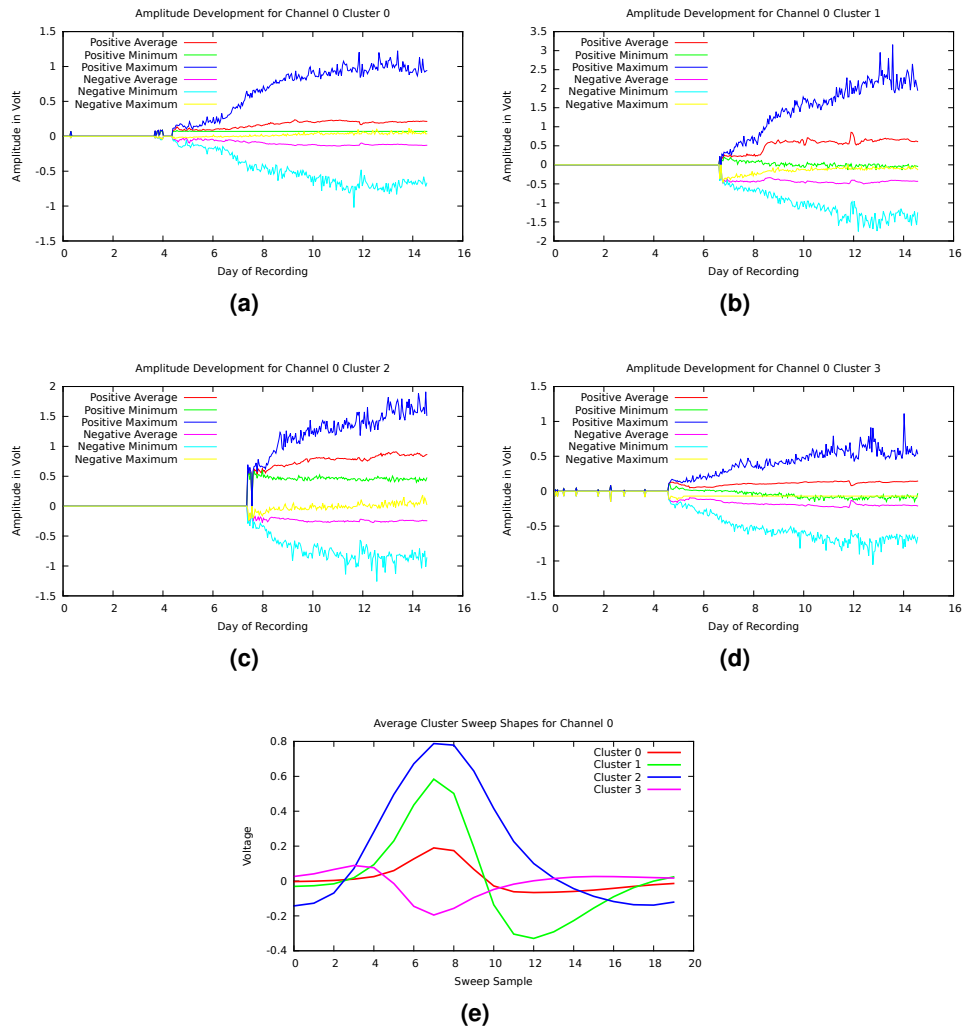


**Figure A.1:** Development of spike amplitudes over time for each cluster in channel 0. (a) to (d) show the amplitudes for the individual clusters. (e) contains the average spike sweeps of the clusters for reference. Cluster 1 (b) contains a noteworthy step in average spike amplitude between day 8 and 9.

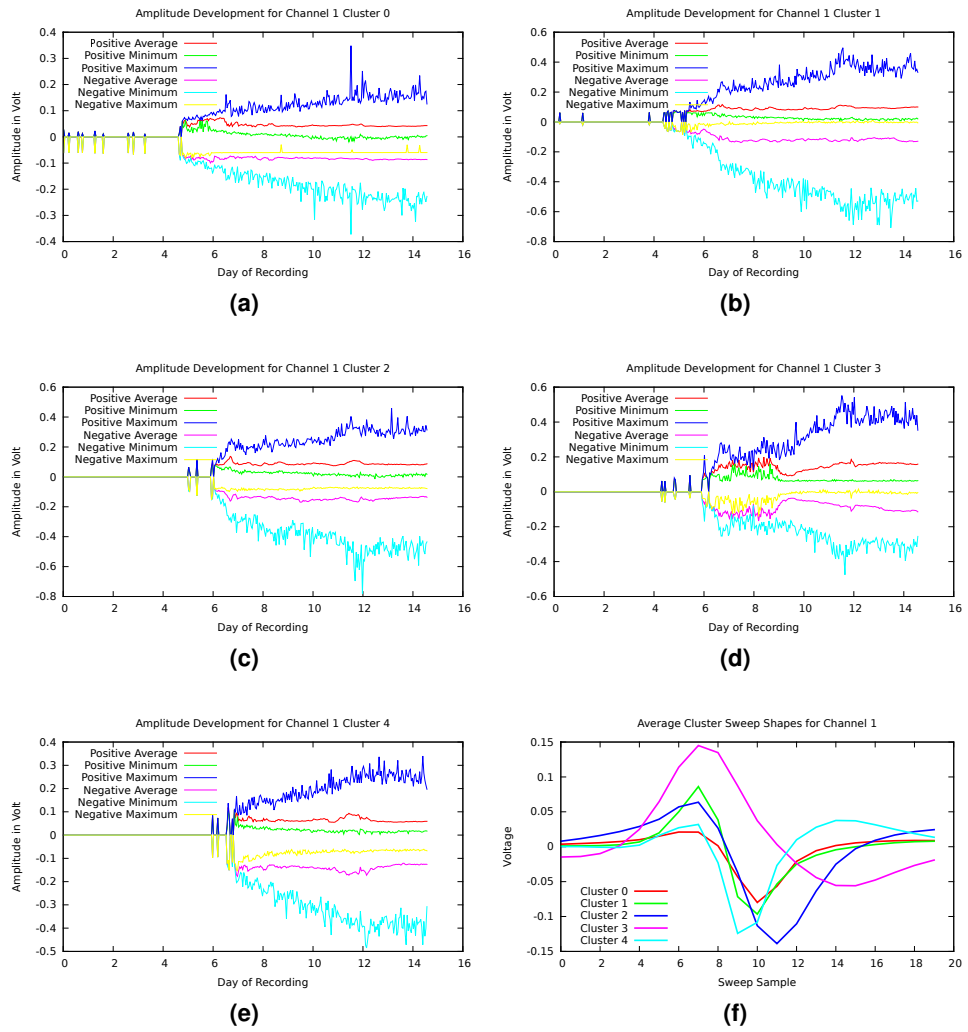


**Figure A.2:** Development of spike amplitudes over time for each cluster in channel 1. (a) to (e) show the amplitudes for the individual clusters. (f) contains the average spike sweeps of the clusters for reference.

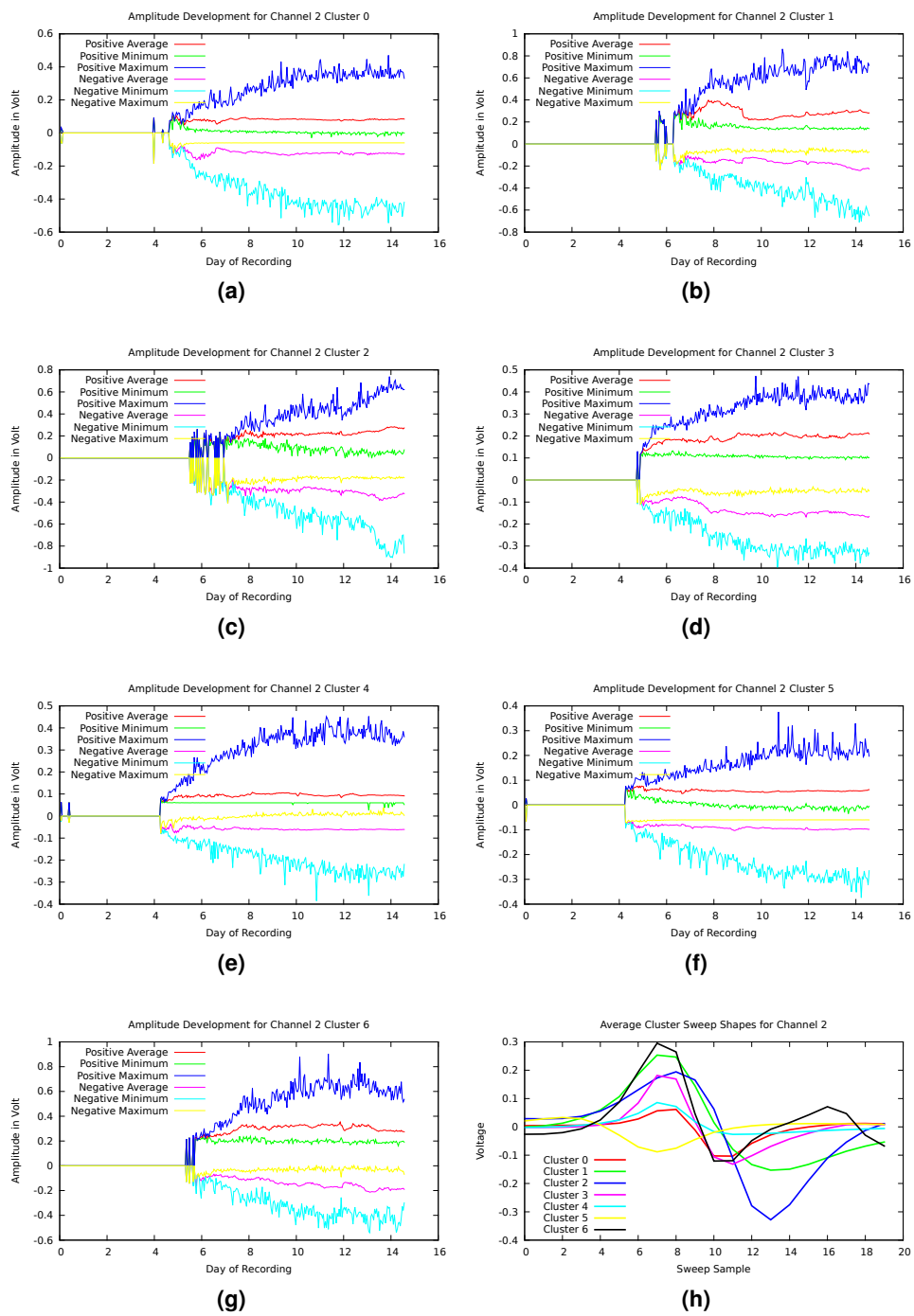


**Figure A.3:** Development of spike amplitudes over time for each cluster in channel 2. (a) to (g) show the amplitudes for the individual clusters. (h) contains the average spike sweeps of the clusters for reference.

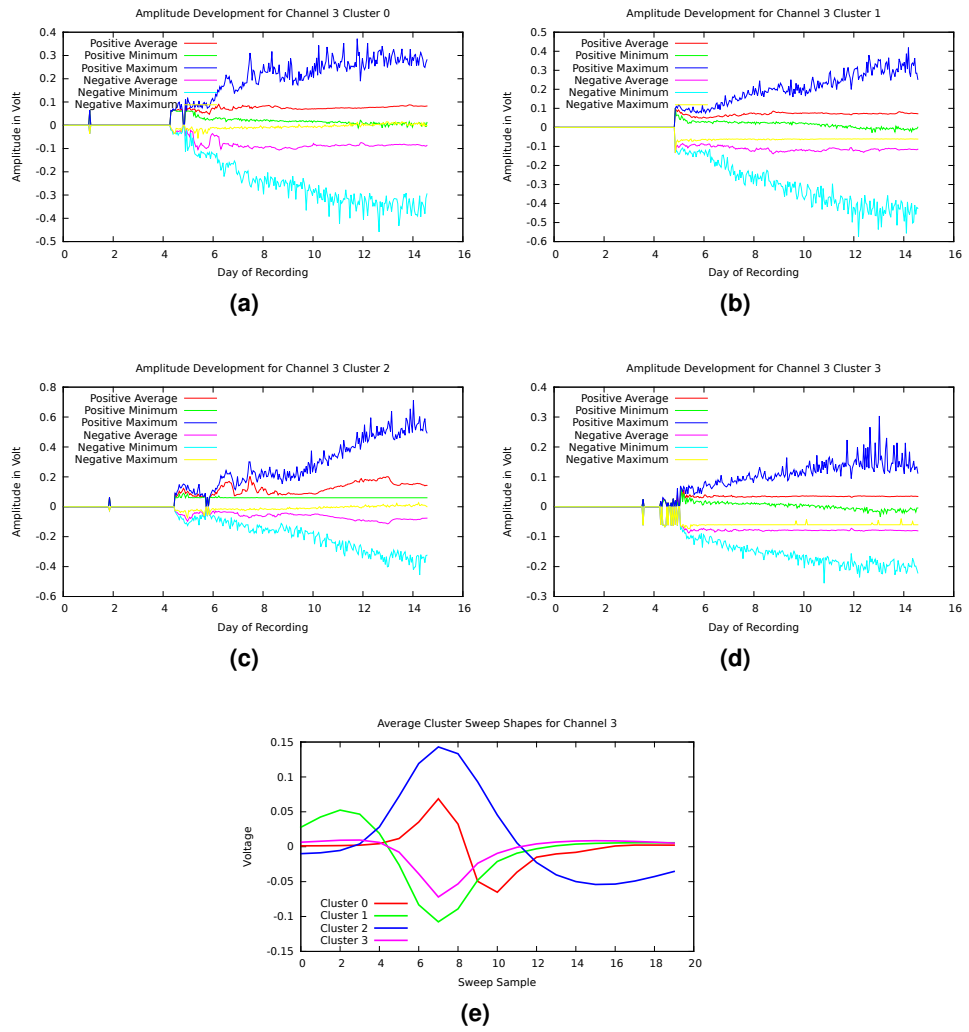


**Figure A.4:** Development of spike amplitudes over time for each cluster in channel 3. (a) to (d) show the amplitudes for the individual clusters. (e) contains the average spike sweeps of the clusters for reference.

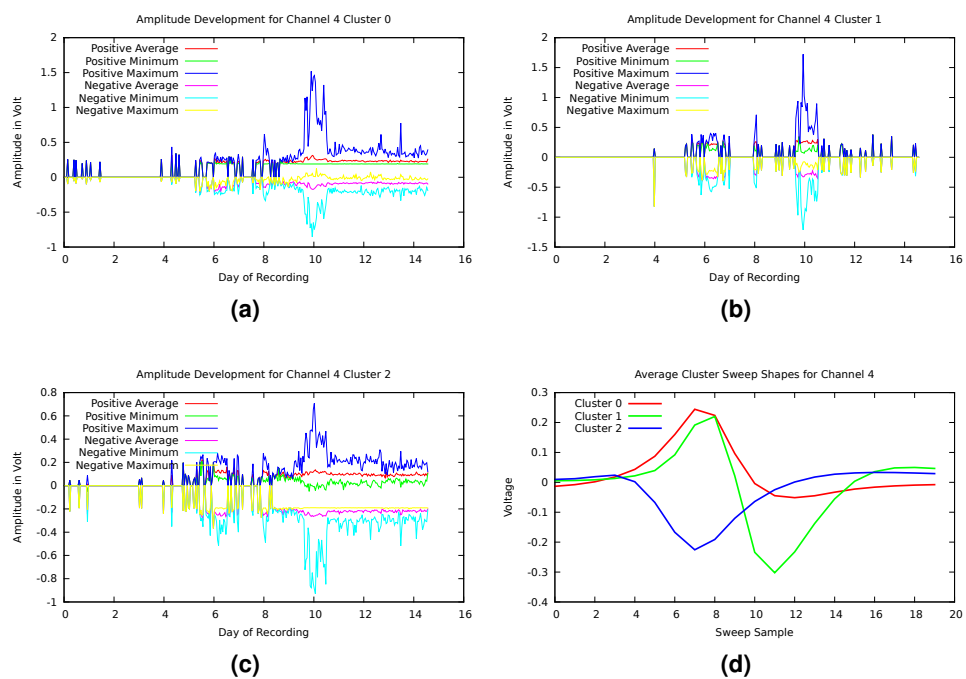


**Figure A.5:** Development of spike amplitudes over time for each cluster in channel 4. (a) to (c) show the amplitudes for the individual clusters. (d) contains the average spike sweeps of the clusters for reference.



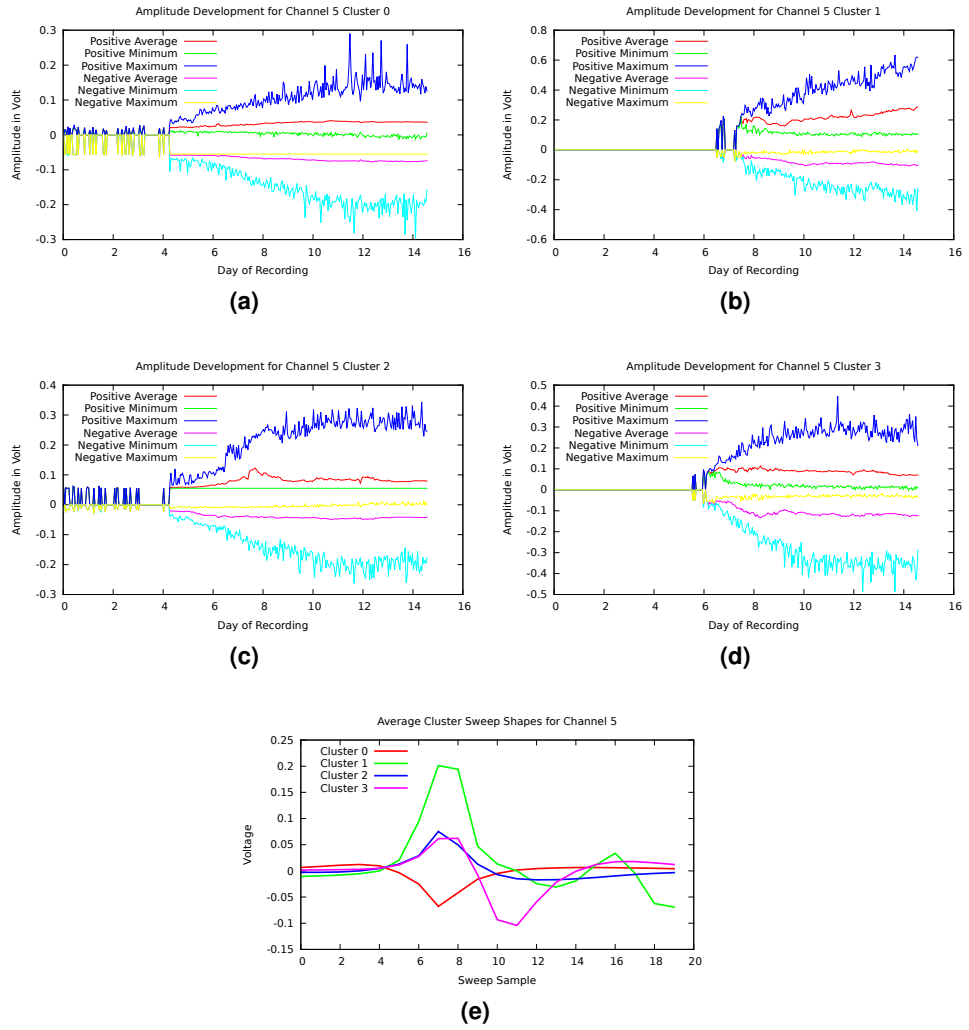


**Figure A.6:** Development of spike amplitudes over time for each cluster in channel 5. (a) to (d) show the amplitudes for the individual clusters. (e) contains the average spike sweeps of the clusters for reference.

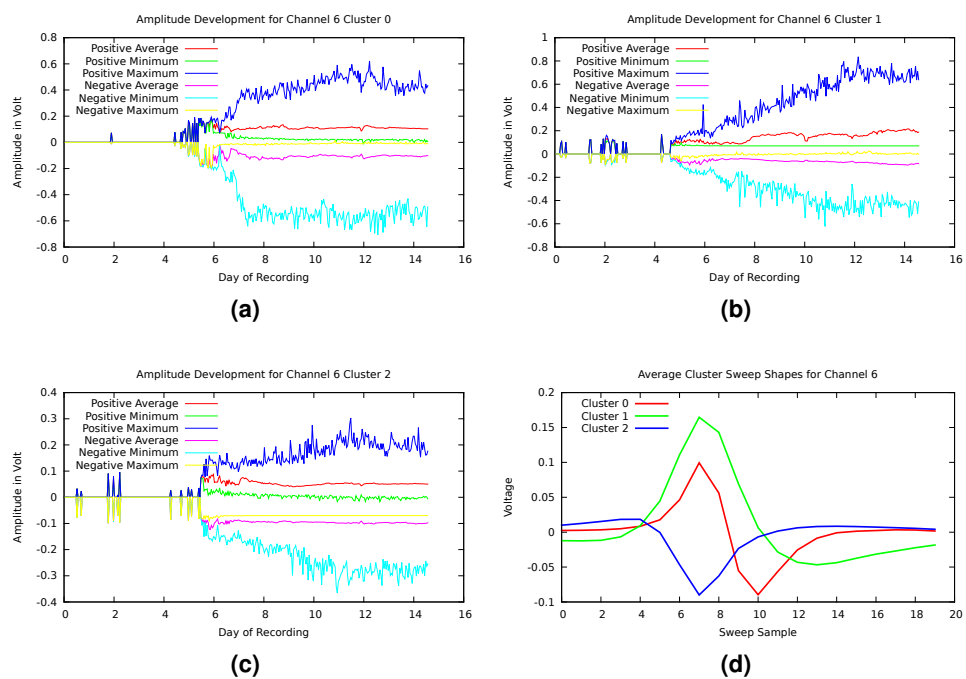


**Figure A.7:** Development of spike amplitudes over time for each cluster in channel 6. (a) to (c) show the amplitudes for the individual clusters. (d) contains the average spike sweeps of the clusters for reference.

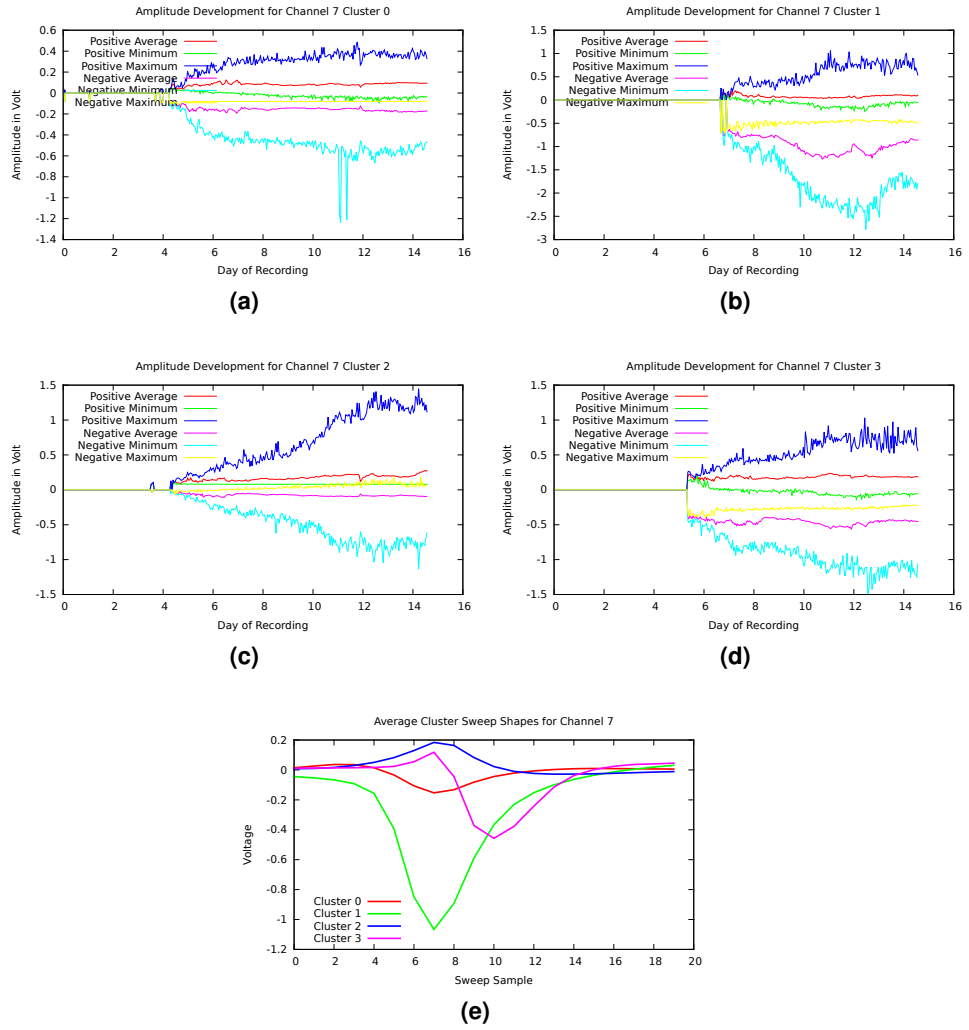


**Figure A.8:** Development of spike amplitudes over time for each cluster in channel 7. (a) to (d) show the amplitudes for the individual clusters. (e) contains the average spike sweeps of the clusters for reference.